Probing the Chemical Stability and Adsorption Properties of Molecule|Metal Oxide Architectures under Conditions of Photoelectrochemical Water Oxidation.

by

Samuel L. Esarey

A dissertation submitted in partial fulfillment
of the requirements for the degree of
Doctor of Philosophy
(Chemistry)
in the University of Michigan
2018

Doctoral Committee:

Associate Professor Bart M. Bartlett, Co-Chair
Professor Levi T. Thompson, Co-Chair
Associate Professor Stephen Maldonado
Professor Melanie S. Sanford

Samuel L. Esarey
slesarey@umich.edu
ORCID iD: 0000-0002-1117-6891

Dedicated to those who struggle with depression.

Don't let anyone let you lose track of who you are, or what you desire to become.

Even if that person is yourself.

Because then, nothing can stop you.

Acknowledgments

This journey led me to do a lot of soul searching throughout these five years. But I couldn't do it without the help and support of those who truly care about me.

First, I would like to thank my committee – Bart Bartlett, Melanie Sanford, Stephen Maldonado, and Levi Thompson, for your guidance throughout these last 5 years professionally and getting me to this moment. I appreciate all of the work you have put in to helping me get to this point.

To Patti Esarey, who raised me as a single mother for most of my childhood. From starting your work life in a cafeteria and a nursing home just to support her children at home, taking classes in your spare time, to the great job you have now at a local urgent care. You have raised 3 wonderful children with higher level degrees, and careers that we all enjoy – thanks you the support you gave all of us when we were little. You give me life and drive me to succeed with the confidence I need to push through any obstacle. You were there in my brightest and darkest moments, and knew exactly what to say to me. I'm so proud of the mother you are, proud to be your son, and am excited to take my Ph.D. back home to Pittsburgh, PA to work for PPG.

To the rest of my family, Brooke, Justin, John, and Isabel Colón-Bernal. You all have seen me go through so much, and I would not be here if I didn't have you in my life to push me toward my goals, to listen to my grief, and to listen to my triumphs. You have all contributed in your own unique way, and I could not thank you enough for what each of you contributed in my journey to this point. In particular, Isabel. I could write a book thanking you for everything you have brought me since we met in graduate school. You are a fierce friend, and a faithful companion that I will

cherish for a lifetime. The joy that you and Emily have brought Reese and I is unforgettable. I will never forget our time here, and look forward to the time we spend together in the future.

To the friends I made in graduate school, Kyle Williams, Kyle Ferguson, Jake Boissonnault, Jacob Lutter, Nate Ulrich & Molly Bilderback Ulrich, Frances & Megan Dudek, and Jeremy Kallick. In your own ways, you were the direct support I needed to get through this journey. Seeing each of you, hanging out on the porch drinking beers and reminiscing of the game nights we had, celebrating our birthdays at midnight at Denny's for our free grand slams, playing with our dogs at the dog park. These are things I will never forget, and I will cherish our friendship forever.

There are two great mentors I've had in my academic pursuits without whom I would not be writing this thesis. First, Mr. Graig Marx, the hot-shot out of Duquesne University. Your drive to teach me and show me the enthusiasm you have for chemistry may have gotten me interested in this field, but your passion to help people, including me, helped me travel down the path that led me to this moment. Your Advanced Research course at Blairsville High School was what got me interested in pursuing research, even if you did offer it to me like you were offering me drugs in a back alley. To think that you could design such a course in a low-income rural community with few students truly passionate about science is incredible, and I'm proud to call myself one of your first students. Second, Prof. Jordan E. Katz, my research advisor at Denison University. Oddly enough, I was also one of your first students as well. I was the lone sophomore in your upper level analytical chemistry course, which I tried desperately to get into. The interactions we had in class led me to join your research group after your first year as an assistant professor in 2011. You introduced me to the idea of solar water splitting, an idea that I took with me all the way to this thesis. You gave me the independence to explore research how I wanted to, with the proper

guidance to let me learn how to conduct research on my own. It is this experience with you that led me to my internship at NASA Glenn Research Center in 2012, and a Ph.D. in chemistry at the University of Michigan.

To my best friend, David Calhoun. You breathed life into me the last year of college when we lived together our senior year. You showed me how to get out of my anti-social ways, to have fun, and led me to become to person I am. I will never forget our friendship and look forward to hearing about all your future successes in teaching and beyond.

To the Bartlett lab, past and present – Ben, Kayla, Emily, Charles, Jimmy, Frances, Adam, Aaron, Andy, Kori, John, and Dan, You guys helped me get through tough scientific challenges, double-checked my derivations, and gave me sound advice on my experiments and in personal matters. All of which I am eternally grateful for, and hope that you continue to do for those around you and those who join in the future. I am the professional that I have become in large part because of your help and guidance.

Finally, to Reese. You may never read this, or read anything, or know what "reading" is – because you're a dog. But you did what no one else could do – you saved me from myself. There were colleagues of mine who questioned my decision to adopt, and thus questioned my dedication to the Ph.D. However, it should be clear from this thesis that my success started *after* your adoption in 2015. Although there is a large stigma in academia regarding mental health, the intense focus I had on a work-life balance is what made me successful both in tackling my personal mental health concerns and my academic pursuits. You, Reese, played the most important role in that aspect of my life. I do not regret the decision to adopt you in graduate school. We all need our ways of coping, and this was mine. And it worked.

Table of Contents

List of Tables

List of Figures

List of Illustrations

List of Abbreviations

α-Fe_2O_3	hematite, alpha-iron oxide
Ag/AgCl	silver/silver chloride reference electrode
$BiVO_4$	bismuth vanadate
bpmcn	(1S,2S)-N,N' dimethyl-N,N'-bis(2-pyridinylmethyl)cyclohexane-1,2-diamine)
CB	conduction band
$CuWO_4$	copper tungstate
CV	cyclic voltammetry
EDS	electron dispersive X-ray spectroscopy
E_{red}	electrochemical reduction potential
E_g	band gap energy
$FeCl_2$	iron(II) chloride
α-FeOOH	goethite, alpha-iron (oxy)hydroxide
a-FeOOH	amorphous iron (oxy)hydroxide
Hg/HgO	mercury/mercuric oxide reference electrode (1 M NaOH)
HOMO	highest occupied molecular orbital
ICP-MS	inductively coupled plasma mass spectrometry
LSV	linear sweep voltammetry
LUMO	lowest unoccupied molecular orbital
MO_X	metal oxide
MS	mass spectrometry
NaOH	sodium hydroxide
NHE	normal hydrogen electrode
OER	oxygen evolution reaction
PCET	proton-coupled electron transfer
PEC	photoelectrochemical
RHE	reversible hydrogen electrode

SEM	scanning electron microscopy
TiO_2	titanium oxide
UV	ultraviolet
VB	valence band
WO_3	tungsten oxide
WOC	water oxidation catalyst
XPS	X-ray photoelectron spectroscopy
XRD	X-ray diffraction

List of Appendices

Abstract

Photoelectrochemical (PEC) water splitting is one viable method for harvesting and storing solar energy, serving as a benign alternative to fossil fuels as a way of powering society sustainably. It involves the conversion of water to O_2 and H_2 gas to be used as a portable fuel. However, many cheap, binary metal oxides like TiO_2, WO_3, and α-Fe_2O_3 don't have the ideal properties needed for the first step of oxidizing water, such as high Faradaic efficiency, absorb visible light, high stability at a wide range of pH, or high rates of reaction and high external quantum efficiencies.

On the other hand, homogeneous water oxidation catalysts (WOCs) are much better suited to oxidize water selectively at low overpotential compared to metal oxide semiconductors. They are easily tunable based on the ligand design and can achieve high turnover numbers. However, they are not capable of oxidizing water without the use of an external energy source. In this way, they can serve as a coating on top of a light-absorbing semiconductor that suffers from low Faradaic efficiency. In addition, molecular dyes such as $[Ru(bpy)_3]^{2+}$ can serve to increase visible light absorption on metal oxide semiconductors that suffer from low visible light absorption without significantly hindering their catalytic activity for water oxidation.

Many researchers have designed devices that functionalize metal oxide photoanodes with WOCs or dyes, but they also suffer from instability of the molecular|solid-state interaction due to either anchoring group desorption or instability, and/or catalyst/chromophore decomposition during water oxidation in a PEC cell. Few have probed the inherent stability of the WOC that they anchor to the surface toward the conditions in which it experiences in a PEC cell, such as illumination in the presence of oxygen, and acidic or basic conditions.

This thesis will quantify these phenomenon as a means of getting to the heart of the problem, in order to determine ways to improve the system. First, I explore the binding constants and adsorption/desorption kinetics associated with phosphonic acid and hydroxamic acid on two common photoanodes for water oxidation, TiO_2 anatase and WO_3. In this section, I discuss hydroxamic acid as a more suitable anchor for TiO_2 anatase under neutral and basic conditions,

while showing that phosphonic acid is primarily only suitable for highly acidic conditions on TiO_2 and WO_3. I will then dive into a deep discussion on the inherent chemical stability of a known WOC, $Fe(bpmcn)Cl_2$ toward typical water oxidation conditions in a PEC cell – visible light in the presence of O_2, and acidic and basic conditions. In all three cases, the non-heme iron complex shows reactivity with different rate constants associated with each phenomenon. In acid and base, the $Fe(bpmcn)Cl_2$ dissociates into $[Fe(H_2O)_6]^{2+}$ in acidic conditions, or becomes oxidized in air or electrochemically in basic conditions to become a-FeOOH(s). Here, I present the case that the basic precipitation of $Fe(bpmcn)Cl_2$ to form a-FeOOH allows for a controlled, anisotropic morphology that leads to an electrochemically active powder for water oxidation.

Finally, I discuss at the end of the thesis potential areas in which you could move forward with this information. This discussion includes the pursuit of new anchoring groups better suited for the neutral to basic regime other than hydroxamic acid.

Chapter 1
Introduction

1.1 The Building Evidence Necessitating Sustainable Renewable Energy

There are well-supported scientific arguments that necessitate research toward replacing fossil fuels as society's primary energy source with sustainable, renewable energy. One argument is the exponential build-up of carbon dioxide, the gaseous by-product from burning coal, natural gas, and gasoline. The chemical reaction for the general combustion of hydrocarbons found in fossil fuels in the presence of oxygen is presented in Eqn. 1.1.

$$2C_nH_{2n+2} + (3n+1)O_2 \rightarrow 2nCO_2 + (2n+2)H_2O \qquad \text{Eqn. 1.1}$$

Producing CO_2 on a global scale is concerning due to the strong IR-active vibrational modes of CO_2, subsequently trapping IR radiation that we feel as heat. Hundreds of thousands of years of data collected from Dome C ice cores in Antarctica regarding global concentration of CO_2 in (ppm)[1] in the atmosphere and global average temperature fluctuations (in ºC from a 1,000 year average)[2] have definitively demonstrated a high correlation between the two variables, shown in Figure 1.1a. While the highest the concentration of CO_2 prior to the industrial revolution has only reached ~310 ppm in Earth's recorded history prior to the Industrial Revolution, we have observed the concentration of CO_2 steadily increase to over 400 ppm since 1880 (Figure 1.1b).[3] Subsequently, a trend toward a global average temperature of 2 ºC above the 20th century average is also observed.[4]

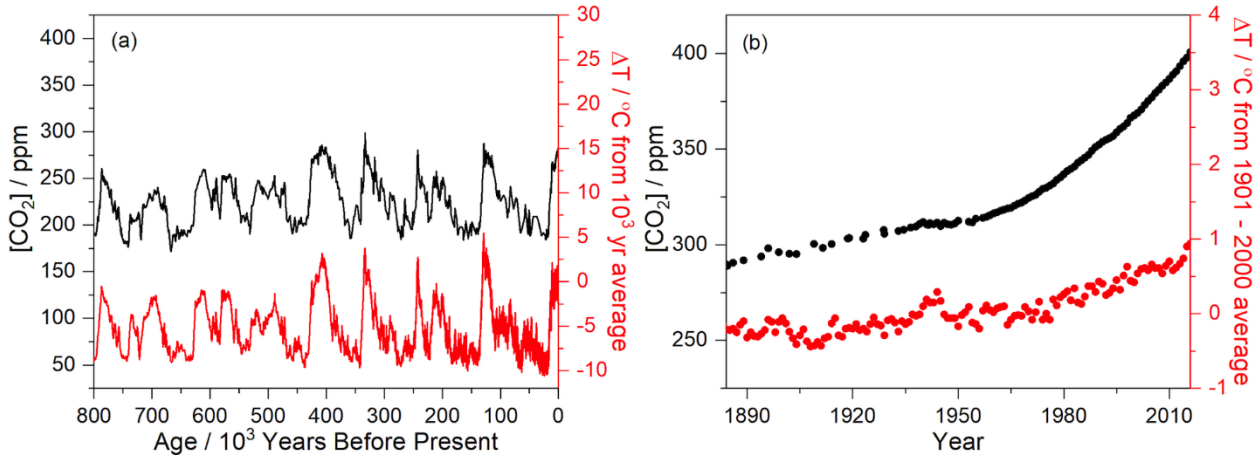

Figure 1.1. (a) $[CO_2]$ in ppm and ΔT in ºC (from an average of the last 1000 years) in the previous 800 kyr, and (b) $[CO_2]$ in ppm and ΔT in ºC (from the 20th century average) between 1884 – 2015.

It is worrisome what the predicted consequences a significant rise in CO_2 can have and what will follow, with implications on global climate including but not limited to, rising sea levels, increasing ocean acidity, extreme weather patterns and fluctuations, and rising average global surface temperatures.[5–8] Although specific details on these consequences will not be discussed in here, they are invoked to propose that alternative energy harvesting and storage mechanisms absent of carbon dioxide as a major byproduct are paramount.

Climate effects of CO_2 emissions aside, a second major argument for sustainable, renewable energy involves the exponentially increasing global demand for energy observed and predicted within the next 100 years. Although the current most economically viable option for energy consumption is the use of fossil fuels such as oil and coal,[9] they are inherently a finite resource. Long-chain hydrocarbons buried within the earth take millions of years to form yet are consumed for our energy purposes at a much faster rate. With the world population and energy demand rising exponentially, and the correlation between per capita energy demand and per capita gross domestic product (GDP),[10] the predicted energy requirements necessary to meet this demand will reach 47.9 PWh, or 173 EJ/yr , by the year 2050.[11–13] We must guarantee an energy source that can sustain this predicted demand without a drastically negative influence on the price of energy.

Of the main forms of renewable energy sources used, such as hydrothermal, geothermal, solar energy, and wind, solar energy is particularly attractive due to the amount of energy that reaches the earth's surface. In just one day, 10,320 EJ reaches the surface after accounting for scattering and absorption by the atmosphere, two orders of magnitude more than the projected

global energy consumption in the year 2050.[9,11,12] However, an obvious concern with solar energy is the inherent intermittence nature of sunlight. In that regard, it is important to not just harness solar energy during daylight, but also to store that energy for use when the sun is not available. In addition, peak energy consumption times (~5–8 PM in the United States)[14] do not line up well with the highest intensity of sunlight (~10 AM–3 PM),[15] as shown in Figure 1.2. Without a reliable way to store the harvested energy, much of this energy would go unused, while high energy demand would be matched with low supply.

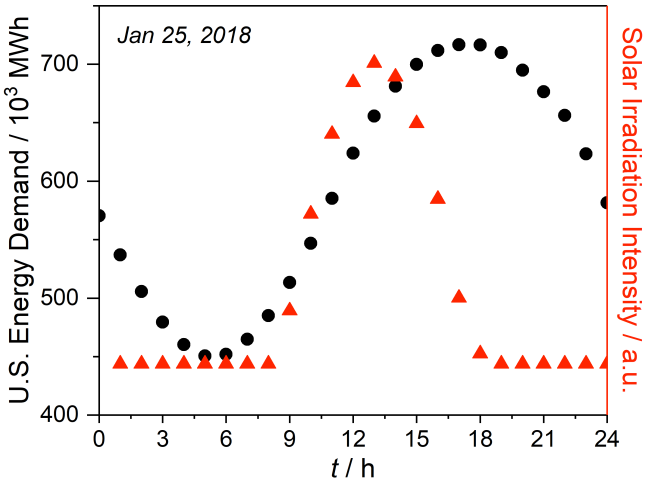

Figure 1.2. Plot of (black) U.S. energy demand on January 25, 2018 overlaid with (red) solar irradiation measured in Detroit, MI in 1990.

For solar energy to contribute significantly to energy consumption, significant advancements must be made in technology to not only harness, but also store solar energy. Efforts are currently being made to not just develop technology to harness solar energy, but also reliably store it.

1.2 Solar Energy Conversion, Solar Water Splitting, and Photoelectrochemical Cells

One known way of converting solar energy to usable electricity is through polycrystalline Si-based photovoltaic (PV) cells. The first Si-based PV was fabricated in the 1950s by Bell Laboratory, subsequently put on the market in the 1970s, and recently has achieved external quantum efficiencies of ~20%.[16] However, the cost of current commercial Si photovoltaics at that efficiency are significantly hindered by the amount of energy needed for the 99.999999999% purity of the trichlorosilane precursors used to make the extremely pure Si crystalline material in the cell, which is created through the reduction of $HSiCl_3$ with H_2 at high temperature.[17] In order

to be more cost effective, cost reduction requires a different approach, even if that approach involves a different material to harvest sunlight. In addition, photovoltaic cells require a separate mechanism to store this energy. However, lithium-ion batteries currently cost too much per unit energy for grid-scale storage, with current DoE goals of approximately \$125 kWh^{-1}. Replacements for lithium are still in the research phase.[18] Although this technology still holds great promise for the future, a more direct approach for solar energy conversion and storage lies in the splitting of water into oxygen and hydrogen fuel.

In 1972, Fujishima & Honda published an article in *Nature* describing solar water splitting through a photoelectrochemical (PEC) cell, with TiO_2 as the photoanode and a platinum counter electrode, to produce oxygen and hydrogen (see Eqn. 1.2 – 1.4).[19] For heterogeneous photocatalysts and photoanodes, water oxidation is accomplished primarily on metal oxide semiconductors including but not limited to TiO_2 anatase, WO_3, α-Fe_2O_3, $CuWO_4$, and $BiVO_4$.[20–28] In these examples, all are used as photoanodes in a 3-electrode PEC cell, described in Scheme 1.1. Here, light comes in to the cell through a quartz window to illuminate a photoanode working electrode, generating an electron-hole pair in the material. In an *n*-type semiconductor anode and under a closed circuit system, the holes are located in the valence band of the material, which you can think of as the solid-state analogue to the highest-occupied molecular orbital in a small molecule. The holes generated go toward the surface of the anode to participate in the oxidation of water to form oxygen and protons. The excited electrons, on the other hand, exist within the conduction band of the material, or the solid-state analogue to the lowest-unoccupied molecular orbital of a small molecule. These excited electrons go toward the electrical back contact and are collected by the potentiostat (represented by circle in Scheme 1.1) and then sent to the counter electrode (cathode) for the reduction of protons to hydrogen gas.

$O_2(g) + 4H^+ + 4e^- \rightarrow 2H_2O$	$E^o_{red} = -1.23$ V vs NHE	Eqn. 1.2
$4H^+ + 4e^- \rightarrow 2H_2(g)$	$E^o_{red} = 0.00$ V vs NHE	Eqn. 1.3
$2H_2O \rightarrow O_2(g) + 2H_2(g)$	$E^o_{rxn} = 1.23$ V vs NHE	Eqn. 1.4

The energy that can be stored in the bonds of $O_2(g)$ and $H_2(g)$ is 237 kJ per mole of water split, but still requires an overpotential or activation energy in order to drive the reaction. In fact, the bottleneck of this reaction is considered the oxidation of water to O_2 and H^+, as it is kinetically

challenging to create an O–O bond from two water molecules, with multiple highly reactive intermediates.[29,30] Since the initial publication of the Fujishima & Honda paper, countless researchers have worked to improve this technology toward overall solar water splitting with visible light near neutral pH, both on heterogeneous and homogeneous light absorbers and catalysts.

Scheme 1.1. Photoelectrochemical (PEC) Cell of Photoanode Working Electrode Designed for Solar Water Splitting.

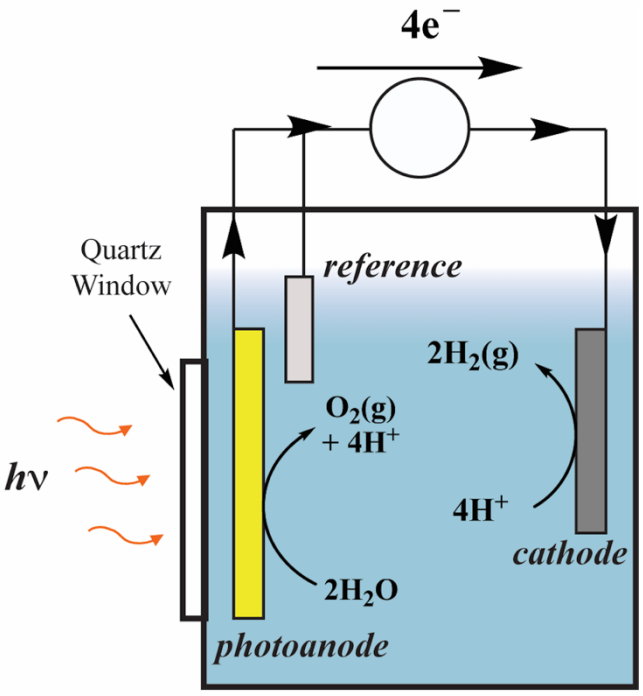

Overall: $2H_2O(l) \rightarrow O_2(g) + 2H_2(g)$

1.3 Heterogeneous, Homogeneous, and Molecular|Solid-State Water Oxidation Catalysis

Continuing with PEC cells, two common photoanodes used in the literature for water oxidation are TiO_2 anatase, and monoclinic WO_3. An example of the valence and conduction band edges of TiO_2 anatase and WO_3 materials in relation to electrochemical reduction potentials for solar water splitting are shown in Scheme 1.2. Two key aspects of Scheme 1.2 are the band positions and the band gap. While the energy gap between the valence band maximum and the conduction band minimum dictates the wavelength of light that the material can absorb, the position in energy of these band edges dictates what electrochemical redox reactions the material can participate in. Ideally, a metal oxide suitable for overall solar water splitting would have a valence band maximum more positive in electrochemical potential than the redox potential for

water oxidation (1.23 V vs NHE), a conduction band minimum more negative than the reduction potential of protons to hydrogen gas (0.00 V vs NHE), and a band gap energy, E_g, of 1.8 eV < E_g < 3.1 eV. Shown in Scheme 1.2, the band gap of TiO_2 is ~3.2 eV, while the band gap of WO_3 is ~2.7 eV.[31] In these examples, the valence band edge of the semiconductor is positioned to provide oxidizing power to drive water oxidation from a thermodynamic perspective, with a conduction band positioned to absorb visible light and UV light to generate the excited state electron-hole pair to drive the reaction from a thermodynamic perspective.

Scheme 1.2. **Valence and Conduction Band Positions for TiO_2 Anatase and WO_3 Compared to Water Oxidation and Proton Reduction Potentials at pH 0.**

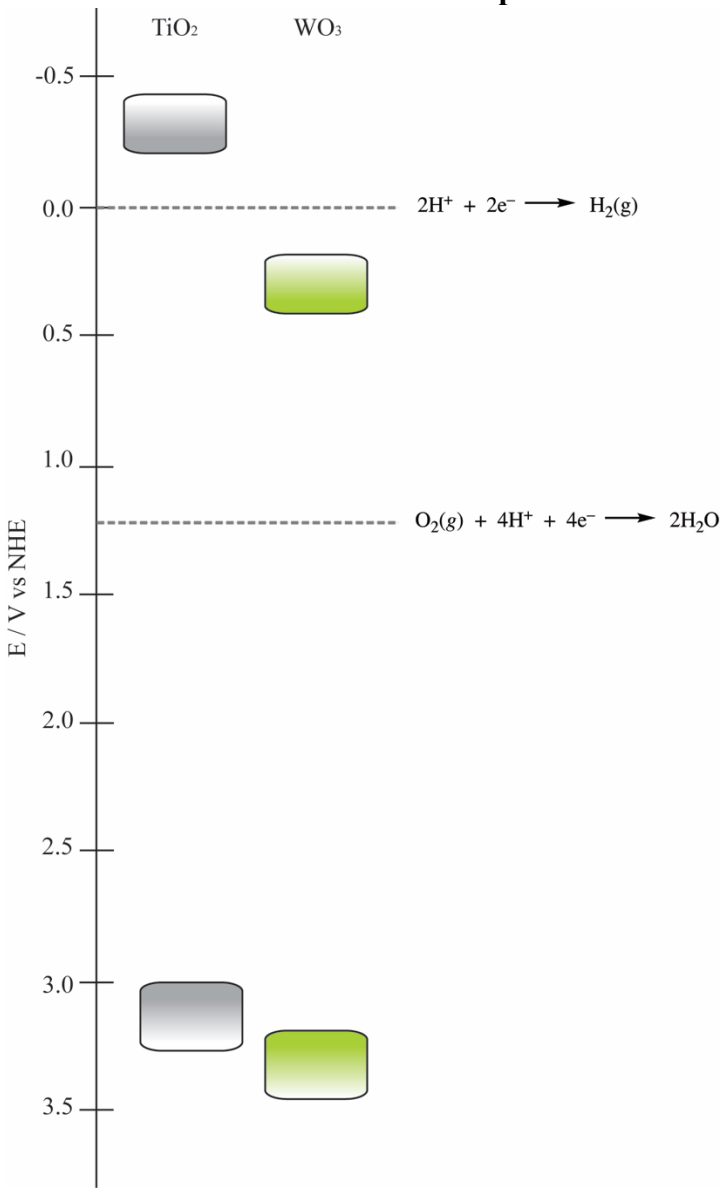

It is clear from Scheme 1.2 that both TiO_2 and WO_3 are thermodynamically suitable for the oxidation of water, but only the conduction band of TiO_2 anatase is in a suitable location for the reduction of protons when an electron is excited into the conduction band from photon absorption.

To fully describe the design of new OER catalysis, the semiconductor/liquid interface in a PEC cell must be discussed. An illustration of this process is shown in Scheme 1.3. When an *n*-type semiconductor anode is placed into a buffered solution of water, there is an inherent mismatch in the redox potential of the active species in solution (H_2O/O_2 = 1.23 V vs NHE) and the Fermi level, E_F, of the semiconductor. The Fermi level is defined as the average energy of available electrons in a specific phase, which depends on the work function of the electrode. So, at absolute zero, $E_F = E_g/2$. Ideally, in order for the semiconductor to be at equilibrium with the solution in the dark such that no electrons are moving, the condition $E_F = E_{H_2O/O_2}$ should be met. In an *n*-type semiconductor, this requires electrons to move from the solid to the liquid, depleting the surface of the material of electrons and thus lowering the E_F. Practically speaking, E_F and E_{H_2O/O_2} never truly reach equilibrium, causing the deprotonation of surface-bound water molecules to compensate for charge. This amount of charge changes as a function of pH and Lewis acidity of the metal oxide, and ultimately dictates the point of zero charge (PZC) for a metal oxide semiconductor in water. It is important to point out that there is no significant change in the redox potential of the redox species in solution, E_{H_2O/O_2}, during equilibration as compared to the change in E_F at the surface of the semiconductor. Here, the E_F becomes more positive and moves toward E_{H_2O/O_2}. This transfer of electrons out of the solid creates an overall positive charge within the material at the surface, forcing negatively charged ions within the solution to compensate the positive charge. The region in which there is a depletion of electrons within the material near the surface is called the depletion region. Meanwhile, the build-up of negative charge within the electrolyte to balance the positive charge on the surface makes up the Helmholtz double layer. This double layer consists of layers of ions more concentrated than they are in the bulk solution, with the first layer being more densely packed negatively charged ions than the second layer.

Once the E_F has reached equilibrium with the solution and a photon is absorbed by the material, another electrochemical potential mismatch occurs. In this moment, an electron, e^-, is excited into the conduction band and lies at the conduction band minimum, leaving behind a hole, h^+, at the valence band maximum. These electron-hole pairs generate free charge carriers that drive electrochemical reactions near the surface. For an *n*-type semiconductor photoanode, the

holes accumulate near the surface of the material and create an overall positive charge at the surface. For TiO_2 anatase and WO_3, a photon of sufficient energy (< 390 nm for TiO_2 anatase, and < 460 nm for WO_3) must be absorbed by the material in order to drive water oxidation.[32,33] All of this generates an electric field at the anode surface orthogonal to the surface, forcing electrons toward the semiconductor/liquid junction. When the anode and cathode are connected by an external circuit like a potentiostat, water bound to the surface (typically under an additional applied bias from a potentiostat or other external energy source to aid in the process) then donates electrons to fill the holes in the valence band of the material, generating O_2(g) and protons at the surface of the material.[32,33] This chemical reaction forces a current to be generated due to the photo-excited electrons leaving the material, and the holes being filled by electrons from water. In an ideal case, because photons are constantly absorbed by the material, transferring electrons from the valence band to the conduction band and electrons from water filling the holes left behind in the valence band, E_F will no longer equal that of E_{H_2O/O_2}, leaving a permanent electric field that constantly drives the oxidation of water. In addition, all current recorded by the potentiostat is ideally derived from the electrons used in the oxidation of water, making the material have 100% Faradaic efficiency for water oxidation; however, some materials such as WO_3 do not have 100% Faradaic efficiency for water oxidation, primarily attributed to either incomplete oxidation of water to form peroxide intermediates, or the oxidation of the electrolyte such as Cl^-, PO_4^{3-}, or SO_4^{2-}.[34,35]

Homogeneous water oxidation catalysts, on the other hand, allow water oxidation to occur on the molecular level with fine tenability of reactivity as a function of the metal center and design of the ligand backbone. Recent examples in the literature of molecular water oxidation catalysts are shown in Scheme 1.4.[36–38] While their mechanisms vary between unimolecular and bimolecular in nature, they also vary in turnover number (TON, mol O_2 mol^{-1} catalyst) and turnover frequency (TOF, mol O_2 mol^{-1} catalyst s^{-1}) depending on the metal center, lability and basicity of the ligand, and stability toward oxidative and corrosive conditions. Because of these variables, TONs can range from ~1 to ~10,000 and TOFs can vary from 0.14 s^{-1} for Fe(bpmcn)Cl_2[36] to 107 s^{-1} for single-site derivatives of the Ru(bpa)$(pic)_2$ catalyst[39] and an astounding 50,000 s^{-1} for bidentate derivatives (two catalysts required per O_2 generated) when measured electrochemically at pH 10.[40]

Scheme 1.3. Idealized band diagram illustration of semiconductor/liquid interface for an n-type semiconductor in buffered water in dark (a) before and (b) after equilibrium, and (c) under illumination

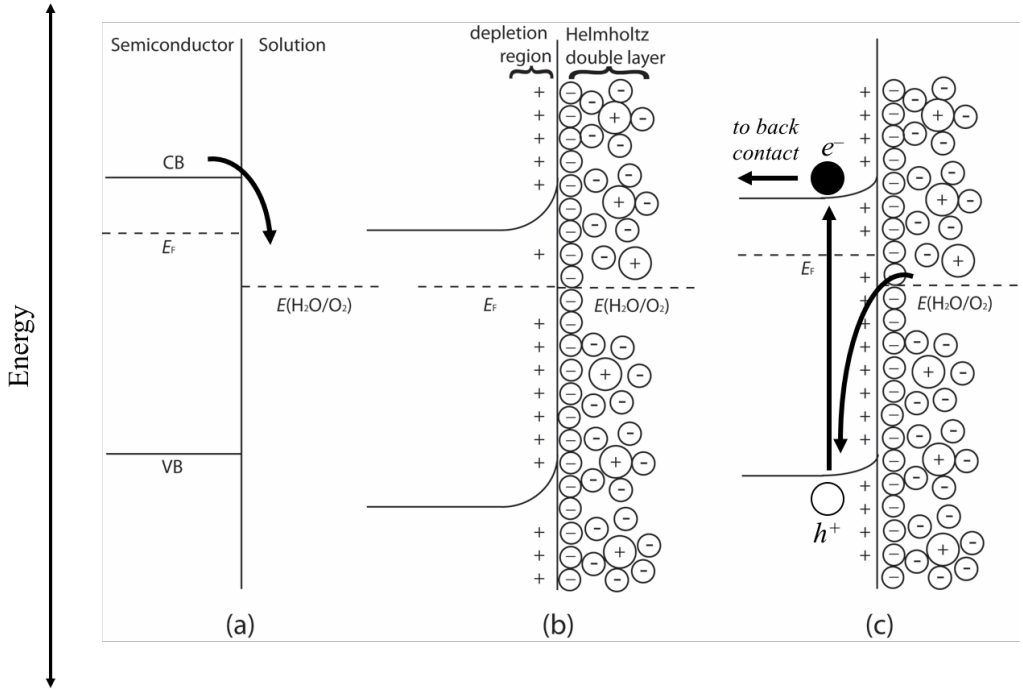

Scheme 1.4. Examples of Known Water Oxidation Catalysts Commonly Found in the Literature.

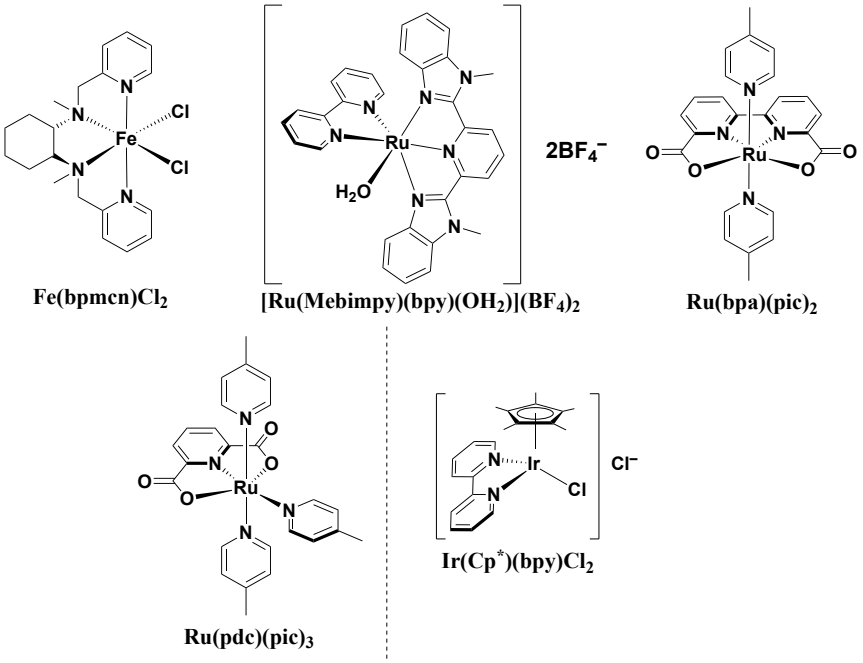

However, TONs are typically small for $Ru(bda)(pic)_2$ derivatives, lasting only ~5-10 minutes prior to full decomposition of the catalyst (TON $\lesssim$ 100). For $Fe(bpmcn)Cl_2$ and $Ru(Mebimpy)(bpy)(BF_4)_2$, both single-site catalysts, their TONs are typically higher, ranging from ~1000 – 11,000 once the complex has been immobilized on a conductive metal oxide substrate such as fluorine-doped tin oxide (FTO).[36,41] In fact, it has been shown that immobilizing homogeneous water oxidation catalysts onto metal oxide surfaces increases the lifetime of the complexes, albeit with diminished TOF.[41] The active species of these various Fe, Ru, or Ir-based catalysts typically involve a $M^{IV}=O/M^{V}=O$ (unimolecular) or M^{IV}-O–O-M^{IV} (bimolecular) intermediate with an electrochemical potential ~1.5 V vs NHE to generate the active species. An example of the known mechanism behind catalytic water oxidation using $Fe(bpmcn)Cl_2$ is reported in Figure 1.3, a catalyst that will be discussed in Chapters 3 and 4. For $Fe(bpmcn)Cl_2$, the mechanism for water oxidation involves the nucleophilic attack of the $L_4Fe^{V}=O$ intermediate, forming the kinetically challenging O–O bond as an L_4Fe^{III}-OOH state prior to the further oxidation of the iron center and the subsequent elimination of O_2 to return to the $L_4Fe^{IV}=O$ ground state.

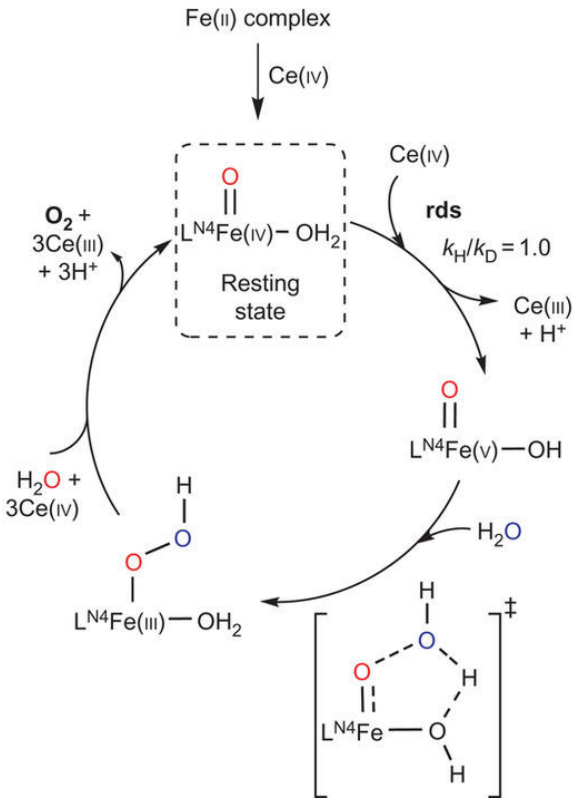

Figure 1.3. Proposed mechanism for the oxidation of water by the $Fe(bpmcn)Cl_2$ catalyst with Ce^{4+} as the sacrificial oxidant. Adapted from ref. 36 with permission from Nature Publishing Group.

Although the complexes listed in Scheme 1.4 are highly selective for water oxidation and can be easily tuned for high rates of reaction, they require a sacrificial oxidant in order to achieve the active species for water oxidation. Typical oxidants are Ce^{4+}, $S_2O_8^{-}$, or IO_4^{-},[36,38,42] and are energy-intensive to synthesize and are wasteful by nature. Replacing a sacrificial oxidant with a potentiostat applying electrochemical bias to generate the active species is also common, but the energy still must come from an external energy source that are often powered by non-renewable resources. However, semiconductor materials with highly positive valence band energies such as TiO_2 or WO_3 could serve as an intermediary to use UV or visible light to generate the active species without the need for wasteful, high energy sacrificial intermediates. In pursuit of replacing sacrificial reagents, many have explored tethering molecular oxygen evolution reaction (OER) catalysts to surfaces of common binary metal oxides such as TiO_2 anatase, WO_3, and α-Fe_2O_3.[37,48–52] Common issues with these semiconductors include the poor selectivity for water oxidation and electron transfer kinetics of WO_3 and α-Fe_2O_3, respectively,[27,45–47] or poor absorption of lower-energy visible light like that of TiO_2 anatase. Given that sunlight that hits the earth's surface is only 4% UV, it is critical to design PEC cells that absorb more of the visible spectrum (see Figure 1.4.). Therefore, those that have attempted to tether molecular catalysts to surfaces of TiO_2 have also anchored $[Ru(bpy)_3]^{2+}$,[48–51] a well-known molecular dye with a symmetry-allowed metal-to-ligand charge transfer event from the d_{z^2} orbital of the Ru^{2+} center (HOMO) to the conjugated π-system of the bipyridine ligands (LUMO) caused by the absorption of visible light (λ_{max} = 455 nm, $\varepsilon = 10^4\ M^{-1}\ cm^{-1}$).[52] This dye is particularly useful for increasing the visible light absorption of TiO_2 due to the proper alignment of the excited state energy in relation to the TiO_2 conduction band edge (–0.2 V vs NHE).[31]

The most common anchoring group used to tether most molecular catalysts or dyes to the surface of TiO_2 or WO_3 is phosphonic acid, R-PO_3H_2 due to its high stability in acidic conditions and ease of synthesis.[48,49,53,54] However, the instability of this molecular|solid-state system under illumination during catalysis is primarily attributed to either chromophore decomposition and desorption of the anchoring group in water at neutral or basic pH. Much is known regarding the photochemical and electrochemical instability of both $[Ru(bpy)_3]^{2+}$ and the phosphonate anchor, primarily in dye-sensitized solar cell devices and in aqueous conditions. A primary goal of researchers in this field is to stabilize this system and its hydrolysis-prone anchor.[55–57] To that end,

there are even reports of burying the complexes in insulating materials to prevent water or hydroxyl groups from attacking the anchor. However, this strategy reduces the observed photocurrent.[58]

Further, not much is reported on the inherent stability of molecular OER catalysts to the conditions typically found in water oxidation – visible light, oxygen, acid, and base. Our group recently developed such a molecular/solid-state electrode, **Fe**|WO_3, where the iron species is the non-heme iron WOC, Fe(tebppmcn)Cl_2 (tebppmcn = tetraethyl *N,N′*-bis(2-methylpyridyl-4-phosphonate)-*N,N′* dimethylcyclohexyl-diamine), with a phosphonate anchoring group to attach the molecule to a tungsten oxide surface.[42] The intent of creating this system was to eliminate the need for a sacrificial reagent to oxidize the iron complex, while also improving the OER efficiency for WO_3 in a PEC cell. Indeed, we observe a 60% increase in the photocurrent generated, coupled with a 30% increase in the OER efficiency over the first three hours of operation. Using an iron complex is preferable to more common ruthenium complexes commonly used in dye-sensitized solar cells, PEC cells, and photoelectrosynthesis cells because of their significantly lower cost. However, the true active species and the fate of the iron complex could not be identified with confidence, as the molecule was no longer observed spectroscopically or electrochemically on the surface of WO_3 after 3 hours of operation in aqueous sulfate solution at pH 3 under low loadings (15 nmol/cm^2). Similar disappearances of other Ru-based complexes have also been observed, and decomposition is typically ascribed either to hydrolysis of the anchoring group, forcing the molecule to leave the surface, or to chromophore decomposition.[48–50] Again, many of these reports use phosphonate as the anchor. No quantitative understanding of the interactions between phosphonate and TiO_2 anatase or WO_3 in aqueous media at various pH has been reported. In addition, many of the aforementioned homogeneous catalysts have reported ligand dissociation of the η^1 ligands as the primary deactivation pathway. To that end, it is crucial to quantify the stability of both anchoring group and molecular catalyst choice for tethering to TiO_2 and WO_3. Specifically, it will be important to critically analyze the stability of the molecular|solid-state interactions "from the ground up", starting at the metal oxide-anchor interaction and ending at the stability of the catalyst. Starting from the metal oxide semiconductor, it will be important to find an anchoring group that binds strongly to the metal oxide at the particular pH in which the semiconductor is stable and best suited for water oxidation. After quantifying that interaction and finding a suitable anchor, it is then important to choose a molecular dye or WOC that is also stable to the conditions in which it will be exposed in a PEC cell.

1.4 Scope of this Thesis

This thesis will focus on providing quantitative data outlining thermodynamic and kinetic processes governing stability of a molecular/solid-state photoanode both from the perspective of the anchor and the molecular catalyst. Chapter 2 will cover the quantified binding and desorption kinetics and thermodynamics of phosphonate- and hydroxamate-anchored $[Ru(bpy)_3]^{2+}$ to the two common semiconductors mentioned earlier in this introduction, TiO_2 anatase and WO_3. The chapter will ultimately discuss the ideal conditions suitable for either anchoring group with respect to metal oxide choice and pH range. Chapters 3 and 4 will then cover the chemical stability of $Fe(bpmcn)Cl_2$, a non-heme OER catalyst that we have explored previously in our group,[42] with regards to visible light, oxygen, and pH (acidic vs basic). This chapter will discuss the reactivity of the molecular catalyst in the Fe^{II} state toward these variables, their decomposition products, and how they could potentially be useful in other applications other than water oxidation. Finally, Chapter 5 will take a detour from this field and discuss my year-long study on changing the format of CHEM 125/126 General Chemistry Laboratory instruction in the University of Michigan Department of Chemistry. The chapter will highlight motives of the project, the changes in format I pursued, the response from students in two separate sections of ~22 students each, and the ultimately make suggestions on how this format could be translated to the larger scale within the department over a long period of time. Following the thesis, there are appendices containing supporting data pertinent to each chapter. They are separated by chapter and appendix A-E is each for Chapter 2-5, respectively. The appendix figures are referenced throughout each chapter.

1.5 References

(1) Lüthi, D., M. Le Floch, B. Bereiter, T. Blunier, J.-M. Barnola, U. Siegenthaler, D. Raynaud, J. Jouzel, H. Fischer, K. Kawamura, and T.F. Stocker. 2008. High-resolution carbon dioxide concentration record 650,000-800,000 years before present. Nature, Vol. 453, pp. 379-382, 15 May 2008.

(2) Jouzel, J., V. Masson-Delmotte, O. Cattani, G. Dreyfus, S. Falourd, G. Hoffmann, B. Minster, J. Nouet, J.M. Barnola, J. Chappellaz, H. Fischer, J.C. Gallet, S. Johnsen, M. Leuenberger, L. Loulergue, D. Luethi, H. Oerter, F. Parrenin, G. Raisbeck, D. Raynaud, A. Schilt, J. Schwander, E. Selmo, R. Souchez, R. Spahni, B. Stauffer, J.P. Steffensen, B. Stenni, T.F. Stocker, J.L. Tison, M. Werner, and E.W. Wolff. 2007. Orbital and Millennial Antarctic Climate Variability over the Past 800,000 Years. Science, Vol. 317, No. 5839, pp.793-797, 10 August 2007.

(3) C. D. Keeling, S. C. Piper, R. B. Bacastow, M. Wahlen, T. P. Whorf, M. Heimann, and H. A. Meijer, Atmospheric CO_2 and $^{13}CO_2$ exchange with the terrestrial biosphere and oceans

from 1978 to 2000: observations and carbon cycle implications, pages 83-113, in "A History of Atmospheric CO_2 and its effects on Plants, Animals, and Ecosystems", editors, Ehleringer, J.R., T. E. Cerling, M. D. Dearing, Springer Verlag, New York, 2005.

(4) Jones, P. D., M. New, D. E. Parker, S. Martin, and I. G. Rigor (1999), Surface Air Temperature and its Changes Over the Past 150 Years, *Rev. Geophys.*, 37(2), 173—199. Raw data set taken from Global Surface Temperature Anomalies. https://www.ncdc.noaa.gov/monitoring-references/faq/anomalies.php (accessed Jan. 26, 2018).

(5) Solomon, S.; Plattner, G.-K.; Knutti, R.; Friedlingstein, P., *PNAS* **2009**, *106*, 1704 – 1709.

(6) Lobell, D.B.; Schlenker, W.; Costa-Roberts, J., *Science* **2011**, *333*, 616 – 620.

(7) Feely, R.A.; Doney, S.C.; Cooley, S.R., *Oceanography* **2009**, *22,* 37 – 47.

(8) Lenton, T.M.; Held, H.; Kriegler, E.; Hall, J.W.; Lucht, W.; Rahmstorf, S.; Schellnhuber, H.J., *PNAS* **2008**, *105*, 1786 – 1793.

(9) United Nations Development Program (2003). World Energy Assessment Report: Energy and the Challenge of Sustainability (United Nations, New York).

(10) Kadoshin, S.; Nishiyama, T.; Ito, T., *Appl. Energy* **2000**, *67*, 407 – 417.

(11) World Energy Council 2013, World Energy Scenarios: Composing Energy Futures to 2050, London 2013.

(12) Lewis, N.S.; Nocera, D.G., Powering the Planet: Chemical Challenges in Solar Energy Utilization. *Proc. Natl. Acad. Sci.* **2006**, *103*, 15729 – 15735.

(13) Turner, J.A. A Realizable Renewable Energy Future, .*Science*, **1999**, *285*, 687 – 689.

(14) U.S. Electric System Operating Data. United States Energy Information Administration. https://www.eia.gov/beta/realtime_grid/?src=l2#/summary/demand?end=20160725&start=20160625 (accessed Jan. 26, 2018).

(15) The National Solar Radiation Data Base 1961-1990 (NSRDB). http://rredc.nrel.gov/solar/old_ data/nsrdb/1961-1990/ (accessed Jan 26, 2018).

(16) Saga, T., Advances in Crystalline Silicon Solar Cell Technology for Industrial Mass Production. *NPG Asia Mater.* **2010**, *2*, 96 – 102.

(17) Green, M.A., Crystalline Silicon Solar Cells. In *Clean Electricity from Photovoltaics,* 2nd ed; Archer, M.D., Green, M.A. Ed.; Imperial College Press, London, 2014; 87 – 137.

(18) Blomgren, G.E., The Development and Future of Lithium Ion Batteries, *J. Electrochem. Soc.* **2017**, *164*, A5019 – A5025.

(19) Fujishima, A.; Honda, K., Electrochemical Photolysis of Water at a Semiconductor Electrode, *Nature*, **1972**, *238*, 37 – 38.

(20) Schneider, J.; Matsuoka, M.; Takeuchi, M.; Zhang, J.; Horiuchi, Y.; Anpo, M.; Bahnemann, D. W. Understanding TiO2 Photocatalysis: Mechanisms and Materials. *Chem. Rev.* **2014**, *114*, 9919–9986.

(21) Chen, X.; Mao, S. S. Titanium Dioxide Nanomaterials: Synthesis, Properties, Modifications, and Applications. *Chem. Rev.* **2007**, *107*, 2891–2959.

(22) Shankar, K.; Basham, J. I.; Allam, N. K.; Varghese, O. K.; Mor, G. K.; Feng, X.; Paulose, M.; Seabold, J. A; Choi, K.-S.; Grimes, C. A. Recent Advances in the Use of TiO2 Nanotube and Nanowire Arrays for Oxidative Photoelectrochemistry. *J. Phys. Chem. C* **2009**, *113*, 6327–6359.

(23) Kim, J. K.; Shin, K.; Cho, S. M.; Lee, T.-W.; Park, J. H. Synthesis of Transparent Mesoporous Tungsten Trioxide Films with Enhanced Photoelectrochemical Response:

Application to Unassisted Solar Water Splitting. *Energy & Environmental Science*, 2011, *4*, 1465.
(24) Santato, C.; Odziemkowski, M.; Ulmann, M.; Augustynski, J. Crystallographically Oriented Mesoporous WO3 Films: Synthesis, Characterization, and Applications. *J. Am. Chem. Soc.* **2001**, *123*, 10639–10649
(25) Lhermitte, C. R.; Verwer, J. G.; Bartlett, B. M. Improving the Stability and Selectivity for the Oxygen-Evolution Reaction on Semiconducting WO3 Photoelectrodes with a Solid-State FeOOH Catalyst. *J. Mater. Chem. A* **2016**, *4*, 2960–2968.
(26) Ishaq, S.; Sikora, A.; Scheidler, N.; Hambleton, C.; Katz, J.E., Enhancement of Water Oxidation Photocurrent for Hematite Thin Films Electrodeposited with Polyvinylpyrrolidone, *J. Electrochem. Soc.* **2016**, *163*, F1330 – F1336.
(27) Yourey, J. E.; Bartlett, B. M. Electrochemical Deposition and Photoelectrochemistry of $CuWO_4$ a Promising Photoanode for Water Oxidation. *J. Mater. Chem.* **2011**, *21*, 7651.
(28) Kim, T.W.; Ping, Y.; Galli, G.A.; Choi, K.S., Simultaneous Enhancements in Photon Absorption and Charge Transport of Bismuth Vanadate Photoanodes for Solar Water Splitting, *Nature Commun.* **2015**, *6* (8769) 1 – 10.
(29) Muuronen, M.; Parker, S.M.; Berardo, E.; Le, A.; Zwiinenburg, M.A.; Furche, F., Mechanism of Photocatalytic Water Oxidation on Small TiO_2 Nanoparticles, *Chem. Sci.* **2017**, *8*, 2179 – 2183.
(30) Chen, J.; Li, Y.-F.; Sit, P.; Selloni, A., Chemical Dynamics of the First Proton-Coupled Electron Transfer of Water Oxidation on TiO_2 Anatase, *J. Am. Chem. Soc.* **2013**, *135*, 18774 – 18777.
(31) Mills, A.; Hunte, S.L., An Overview of Semiconductor Photocatalysis, *J. Photochem. Photobiol. A.,* **1997**, *108*, 1 – 35.
(32) Tan, M.X.; Laibinis, P.E.; Nguyen, S.T.; Kesselman, J.M.; Stanton, C.E.; Lewis, N.S., Principles and Applications of Semiconductor Photoelectrochemistry, In *Progress in Inorganic Chemistry*, Karlin, K.D., Ed.; John Wiley & Sons, Inc., New York, 1994; Vol. 41; p 21
(33) Bard, A.J.; Faulkner, L.R., Electrocheical Methods: Fundamentals and Applications, Harris, D.; Swain, E.; Robey, C.; Aiello, E., Ed.; John Wiley & Sons, Inc., New York, 2001; 2nd ed.
(34) Hill, J.C., Choi, K.-S., Effect of Electrolytes on the Selectivity and Stability of n-type WO_3 Photoelectrodes for Use in Solar Water Oxidation, *J. Phys. Chem. C.* **2012**, *116*, 7612 – 7620.
(35) Mi, Q.; Coridan, R.H., Brunschwig, B.S.; Gray, H.B.; Lewis, N.S., Photoelectrochemical Oxidation of Anions by WO_3 in Aqueous and Nonaqueous Electrolytes, *Energy Environ. Sci.* **2013**, *6*, 2646 – 2653.
(36) Fillol, J.L.; Codolà, Z.; Garcia-Bosch, I.; Gómez, L.; Pla, J.J.; Costas, M., Efficient Water Oxidation Catalysts Based on Readily Available Iron Coordination Complexes, *Nature Chem.* **2011**, *3*, 807 – 813.
(37) Tong, L.; Thummel, R.P., Mononuclear Ruthenium Polypyridine Complexes that Catalyze Water Oxidation, *Chem. Sci.* **2016**, *7*, 6591 – 6603.
(38) Kärkäs, M.D.; Verho, O.; Johnston, E.V.; Åkermark ,B., Artificial Photosynthesis: Molecular Systems for Catalytic Water Oxidation, *Chem. Rev.* **2014**, *114*, 11863 – 12001.

(39) Shaffer, D.W.; Xie, Y.; Szalda, D.J.; Concepcion, J.J., Lability and Basicity of Bipyridine-Carboxylate-Phosphonate Ligand Accelerate Single-Site Water Oxidation by Ruthenium-Based Molecular Catalysts, *J. Am. Chem. Soc.* **2017**, *139*, 15347 – 15355.
(40) Matheu, R.; Ertem, M.Z.; Benet-Buchholz, J.; Coronado, E.; Batista, V.S.; Sala, X., Llobet, A., *J. Am. Chem. Soc.* **2015**, *137*, 10786 – 10795.
(41) Chen, Z.; Concepcion, J.J., Jurss, J.W.; Meyer, T.J., Single-Site, Catalytic Water Oxidation on Oxide Surfaces, *J. Am. Chem. Soc.* **2009**, *131*, 15580 – 15581.
(42) Klepser, B.M.; Bartlett, B.M., Anchoring a Molecular Iron Catalyst to Solar-Responsive WO_3 Improves the Rate and Selectivity of Photoelectrochemical Water oxidation, *J. Am. Chem. Soc.*, **2014**, *136*, 1694 – 1697.
(43) Zhong, D.K.; Zhao, S.; Polyansky, D.E.; Fujita, E., Diminished Photoisomerization of Active Ruthenium Water Oxidation Catalyst by Anchoring to Metal Oxide Electrodes, *J. Catal.* **2013**, *307*, 140 – 147.
(44) Li, W.; He, D.; Sheehan, S.W.; He, Y.; Thorne, J.E.; Yao, X.; Brudvig, G.W.; Wang, D., Comparison of Heterogenized Molecular and Heterogenous Oxide Catalysts for Photoelectrochemical Water Oxidation, *Energy Environ. Sci.* **2016**, *9*, 1794 – 1802.
(45) Klahr, B.; Gimenez, S.; Fabregat-Santiago, F.; Hamann, T.; Bisquert, J., Water Oxidation at Hematite Photoelectrodes: The Role of Surface States, *J. Am. Chem. Soc.* **2012**, *134*, 4294 – 4302.
(46) Liu, R.; Lin, Y.; Chou, L. Y.; Sheehan, S. W.; He, W.; Zhang, H.; Hou, H. J. M.; Wang, D. Water Splitting by Tungsten Oxide Prepared by Atomic Layer Deposition and Decorated with an Oxygen-Evolving Catalyst. *Angew. Chem. Int. Ed.* **2011**, *50*, 499.
(47) Lillard, R. S.; Kanner, G. S.; Butt, D. P. The Nature of Oxide Films on Tungsten in Acidic and Alkaline Solutions. *J. Electrochem. Soc.* **1998**, *145*, 2718.
(48) Ashford, D.L., Lapides, A.M., Vannucci, A.K.; Hanson, K.; Torelli, D.A., Harrison, D.P., Templeton, J.L.; Meyer, T.J., Water Oxidation by an Electropolymerized Catalyst on Derivatized Mesoporous Metal Oxide Electrodes, *J. Am. Chem. Soc.*, **2014**, *136*, 6578 – 6581.
(49) Lapides, A.M., Sherman, B.D.; Brennaman, M.K., Dares, C.J., Skinner, K.R., Templeton, J.L., Meyer, T.J., Synthesis, Characterization, and Water Oxidation by a Molecular Chromophore-Catalyst Assembly Prepared by Atomic Layer Deposition. The "Mummy" Strategy., *Chem. Sci.*, **2015**, *6*, 6398 – 6406.
(50) Song, W.; Vannucci, A.K.; Farnum, B.H.; Lapides, A.M.; Brennaman, M.K.; Kalanyan, B.; Alibabaei, L.; Concepcion, J.J.; Losego, M.D.; Parsons, G.N.; Meyer, T.J., Visible Light Driven Benzyl Alcohol Dehydrogenation in a Dye-Sensitized Photoelectrsynthesis Cell, *J. Am. Chem. Soc.* **2014**, *136*, 9773 – 9779.
(51) Gao, Y.; Ding, X.; Liu, J.; Wang, L.; Lu, Z.; Li, L.; Sun, L., Visible Light Driven Water Splitting in a Molecular Device with Unprecedentedly High Photocurrent Density, *J. Am. Chem. Soc.* **2013**, *135*, 4219 – 4222.
(52) Kumar, P.; Joshi, C.; Srivastava, A.K.; Gupta, P.; Boukherroub, R., Jain, S.L., *ACS Sustainable Chem. Eng.* **2016**, *4*, 69 – 75.
(53) Zhang, L.; Cole, J.M., Anchoring Groups for Dye-Sensitized Solar Cells, *ACS App. Mater. Interfaces* **2015**, *7*, 3427 – 3455.
(54) Materna, K.L.; Crabtree, R.H.; Brudvig, G.W., Anchoring Groups for Photocatalytic Water Oxidation on Metal Oxide Surfaces, *Chem. Soc. Rev.* **2017**, *46*, 6099 – 6110.

(55) Bachinger, A.; Kickelbick, G.; Photocatalytic Stability of Organic Phosphonates and Phosphates on TiO_2 Nanoparticles, *App. Catal. A-Gen* **2011**, *409*, 122 – 132.
(56) Hyde, J.T.; Hanson, K.; Vannucci, A.K.; Lapides, A.M.; Alibabaei, L.; Norris, M.R.; Meyer, T.J.; Harrison, D.P., Electrochemical Instability of Phosphonate-Derivatized, Ruthenium(III) Polypyridyl Complexes on Metal Oxide Surfaces, *ACS Appl. Mater. Interfaces* **2015**, 79554 – 9562.
(57) Wee, K.-R.; Brennaman, K.; Alibabaei, L.; Farnum, B.H.; Sherman, B.; Lapides, A.M.; Meyer, T.J., Stabilization of Ruthenium(II) Polypyridyl Chromophores on Nanoparticle Metal-Oxide Electrodes in Water by Hydrophobic PMMA Overlayers, *J. Am. Chem. Soc.* **2014**, *136*, 13514 – 13517
(53) Wang, D.; Sheridan, M.V.; Shan, B.; Farnum, B.H.; Marquard, S.L.; Sherman, B.D.; Eberhart, M.S.; Nayak, A.; Dares, C.J.; Das, A.K.; Bullock, R.M.; Meyer, T.J., Layer-by-Layer Molecular Assemblies for Dye-Sensitized Photoelectrosynthesis Cells Prepared by Atomic Layer Deposition, *J. Am. Chem. Soc.* **2017**, *139*, 14518 – 14525.

Chapter 2

Determining the Binding Constants and Desorption Kinetics of Phosphonate- & Hydroxamate-anchored $[Ru(bpy)_3]^{2+}$ on Anatase TiO_2 & WO_3 as a Function of pH in Water

Portions of this chapter have been published:

Esarey, S.L.; Bartlett, B.M., *In Revision.*

2.1 Introduction

Water-stable anchoring groups for tethering molecular water oxidation catalysts to increase the selectivity or rate of the oxygen-evolution reaction or dyes to increase visible light absorption have been extensively pursued.[1–14] The primary applications of these systems are dye-sensitized solar cells, photoelectrochemical cells, or photoelectrosynthesis cells. While there are many examples, one of the most commonly used anchoring groups used is phosphonic acid due to its higher stability in aqueous media compared to carboxylate, ease of synthesis, and reasonable rate and collection efficiency of electron injection from the molecule to a metal oxide semiconductor.[15–19] However, this anchoring strategy is still insufficient for long-term applications toward water splitting cells, particularly near neutral pH to basic conditions, where the overpotential for oxygen evolution decreases, since carboxylate desorbs. Hydroxamic acid has been proposed as an alternative anchoring group for both dye-sensitized solar cells and photoelectrochemical water splitting cells.[5,11] The asymmetry of the anchoring group has been shown to lead to higher electron injection rates (< 100 fs), and the resistance to hydrolysis suggests it is more stable in basic conditions compared to the other common anchoring groups.[11] However, few examples have experimentally probed the stability of hydroxamate as the anchoring group in water.[5] Given that semiconductors such as TiO_2 and α-Fe_2O_3 are basic oxides,[20,21] any tethered molecular dyes and/or catalysts on these surfaces must also be stable in base. In contrast, WO_3 is an acidic oxide that is only stable at pH < 5,[22] so finding an anchor that is more stable in acid is

also desirable. *The major scientific questions explored in this chapter are* (1) which anchor (phosphonate or hydroxamate) is best suited for acidic, neutral, and basic conditions? (2) how does changing the metal oxide acidity affect the stability and desorption mechanism of each anchor? (3) how does the mechanism of desorption change as a function of pH? Notably, the binding constant of carboxylic acid to TiO_2 has already been measured, and it is two orders of magnitude lower than phosphonate ($K_B \sim 10^3$ and $\sim 10^5$, respectively). Moreover, the rate of desorption is ten-fold faster for carboxylic acid compared to phosphonic acid ($k_d = \sim 10^{-4}$ s^{-1} and $\sim 10^{-5}$ s^{-1}, respectively).[2,23,24]

As discussed in Chapter 1, $[Ru(bpy)_3]^{2+}$ is commonly employed in the dye-sensitized solar cell community. The most common anchoring group used to tether $[Ru(bpy)_3]^{2+}$ to the surface of TiO_2 is phosphonic acid, R-PO_3H_2, and well-established synthetic techniques for synthesizing Ru(4,4'-PO_3H_2-2,2'-bpy)$(bpy)_2Cl_2$ **(Ru-P)**, are readily available (Scheme 1). However, the instability of this complex under illumination during catalysis is primarily attributed to chromophore decomposition and desorption of the anchoring group in water at neutral or basic pH. Much is known regarding the photochemical and electrochemical instability of both $[Ru(bpy)_3]^{2+}$ and the phosphonate anchor, primarily in dye-sensitized solar cell devices and in aqueous conditions with the primary goal of stabilizing this complex and its hydrolysis-prone anchor.[14,25–33] To that end, there are even reports of burying the complexes in insulating materials to prevent water or hydroxyl groups from attacking the anchor, but this strategy reduces the observed photocurrent.[13] On the other hand, attaching Ru(4,4'-$(C(O)N(OH))_2$-2,2'-bpy)$(bpy)_2Cl_2$ (**Ru-H**) to semiconductor metal oxides has not been reported (see Scheme 2.1)

Scheme 2.1. Chemical structure of **Ru-P** and **Ru-H**.

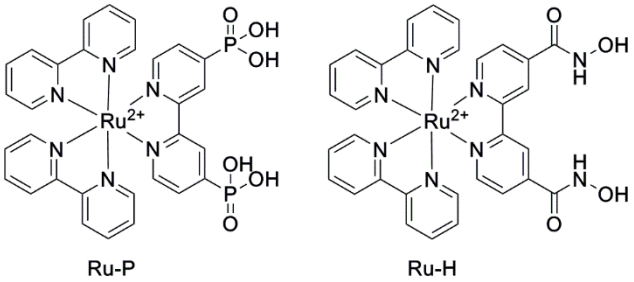

In this chapter, we employ the Langmuir model to describe adsorption to a semiconductor surface, governed by the equation[2]

$$\frac{\text{mol}_{\text{ads}}}{\text{mol}_{\text{ads,max}}} = \frac{K_B c}{1 + K_B c} \qquad \text{Eqn. 2.1}$$

where $mol_{ads}/mol_{ads,max}$ is the fractional surface coverage of the dye bound to the surface of the metal oxide compared to the maximum number of moles associated at the surface, K_B is the binding constant of the dye and c is the concentration of remaining dye dissolved in solution, in M. This model assumes a complete monolayer with fractional occupancy of the surface and that adsorbed molecules are non-interacting. Further, we measure the surface charge as a function of pH. We present data suggesting electrostatic repulsion is primarily responsible for the adsorption/desorption properties of phosphonate and hydroxamate, as well as the rates of desorption from pH 1 – 7 for both anchoring groups on both TiO_2 and WO_3. These metal oxides are chosen for this manuscript due to their common use in molecular/solid-state photoanodes in photoelectrochemical and photoelectrosynthesis cells as described earlier, with stabilities that are either isolated to the acidic regime (WO_3) or are stable throughout pH 1 – 14 (TiO_2). For the purposes of this chapter, we only consider how the anchor binds and desorbs in the dark.

2.2 Experimental Methods

General considerations. *Cis*-dichlorobis(2,2'-bipyridine)ruthenium ($Ru(bpy)_2Cl_2$) was purchased from Strem Chemicals, Inc. Triethylamine, diethyl phosphite, 3,4-dihydro-2-pyran, and 2,2'-bipyridine-4,4'-dicarboxylic acid were purchased from Sigma Aldrich. Phosphoric acid (85%) was purchased from Fisher Scientific. Thionyl chloride was purchased from TCM America. Trimethylsilyl bromide (Me_3SiBr) and diisopropylethylamine were purchased from Chem-Impex Int. Co. *N*-hydroxyphthalimide was purchased from Acros, Inc. 4,4'-dibromo-2,2'-bipyridine and tetrakis(triphenylphosphine)palladium(0) were purchased from Ark Pharm, Inc. Titanium dioxide anatase, < 25nm particles were purchased from Sigma Aldrich, and used without purification. Tungsten oxide particles < 100nm were purchased from Sigma Aldrich, and used without purification. Diisopropylethylamine was previously dried over sodium hydroxide and distilled under nitrogen onto 4 Å molecular sieves prior to use. All other chemicals and solvents were used without purification. For all experiments involving

water, Millipore 18.2 MΩ H_2O was used. NMR spectroscopy was performed with either a Varian MR400 spectrometer equipped with a 5 mm PFG AutoX Dual Broadband probe, or a Varian VNMRS500 equipped with a 5 mm PFG OneNMR probe. UV-Vis spectroscopy was conducted using a Varian Cary 5000 spectrophotometer. ATR-FTIR spectroscopy was collected on a Nicolet iS50 FT-IR with an attenuated total reflectance accessory equipped. Raman spectroscopy was collected on a Reinshaw inVia spectrometer with a 532 nm laser and RenCam CCD detector. Powder X-ray diffraction data was collected on a PANalytical Empyrean Series 2 diffractometer with an X'Celerator detector and Data Collector application software. Scanning electron microscopy images were collected on a JEOL-7800FLV scanning electron microscope equipped with an Oxford X-Man^N silicon drift detector (Oxford Instruments) and a (Oxford NordlysMax2) detector. BET isotherms for determining surface area of powder samples were collected with a NOVA 4200e using N_2 gas. DFT calculations were performed in Gaussian 09 with the PBE0 functional and 6-31G(d,p) basis set, with Stuttgard/Dresden (SDD) effective core potential (ECP) basis set on the central Ru^{2+} atom, in vacuum.[46] Elemental analysis of CHN were completed by Atlantic Microlabs, and Ru elemental analysis collected using a Perkin-Elmer Nexion 2000 ICP-MS with a Ru ICP standard (1000 ppm) purchased from GFS Chemicals.

Synthesis of 4,4'-bis(diethylphosphonate)2,2'-bipyridine. This synthesis has been previously reported in the literature.[27] Briefly, 4,4'-dibromo-2,2'-bipyridine (1.80 g, 5.75 mmol), tetrakis(triphenylphosphine)palladium(0) (0.67 g, 0.58 mmol), diethyl phosphite (1.9 mL, 14.7 mmol), and dry triethylamine (1.9 mL, 13.8 mmol) were added to a dry 100 round bottom flask under N_2. Dry toluene (50 mL) was dispensed to the flask, and the solution was heated to reflux under N_2 for four hours. A brown color appeared from the yellow solution soon after heating the solution. After the reaction was complete, the solution was filtered through a medium glass fritted filter hot, and the toluene was removed under reduced pressure. 50 mL of hexanes were then added to the round bottom flask, and the solution was refluxed for 20 minutes under N_2 to extract the desired product from the brown residue. The solution was then filtered and the resulting filtrate was re-heated and allowed to cool to room temperature to produce pure recrystallized product as dull yellow needles Yield: 1.05 g (43%) yield). ^{1}H NMR (500 MHz, $CDCl_3$,): δ 8.82 (t, 2H), 8.76 (d,

1H), 7.71 (dd, 2H), 4.18 (m, 4H), 1.35 (m, 6H). ^{13}C NMR (500 MHz, $CDCl_3$): δ 149.7, 139.7, 137.9, 125.8, 122.9, 62.9, 16.5. ^{31}P NMR (500 MHz, $CDCl_3$): δ 14.7 ppm.

Synthesis of Ru(4,4'-bis(phosphonic acid)2,2'-bipyridine)(2,2'-bipyridine)$_2$ chloride (Ru-P). The synthesis of this complex has been modified from a previously reported synthesis in the literature.[27] Briefly, 4,4'-bis(diethylphosponate)2,2'-bipyridine (0.49 g, 1.1 mmol) and *cis*-dichlorobis(2,2'-bipyridine)ruthenium(II) (0.56 g, 1.1 mmol) were added to a 250 mL round bottom flask charged with 80 mL of a 1:1 mixture of ethanol and Millipore water. The solution was heated to reflux overnight, then condensed under reduced pressure, washed with a small amount of diethyl ether, and dried under high vacuum to remove all solvent. The residue was dissolved in 40 mL of dry acetonitrile under N_2, and 1.5 mL of Me_3SiBr (10 eq.) was added to the solution. The solution was refluxed under N_2 for 24 hours to ensure complete reaction of the ethoxy-groups from the phosphonate. The solution was then condensed under reduced pressure, and redissolved in 20 mL of methanol. After 30 minutes of stirring, the solution was condensed under reduced pressure and redissolved in 5 mL of methanol. 50 mL of acetone was added to crash out the desired product and filtered from solution. The resulting red-orange powder was wased with acetone, acetonitrile, and diethyl ether, and then dried under high vacuum to yield the desired product. Yield: 0.764 g (83% yield). ^{1}H NMR (500 MHz, D_2O): δ 8.73 (d, 2H), 8.49 (d, 4H), 8.01 (t, 4H), 7.9 (t, 2H), 7.75 (dd, 4H), 7.53 (dd, 2H), 7.33 (m, 4H). ^{13}C NMR (500 MHz, D_2O): δ 156.8, 151.3, 145.7, 144.3, 137.7, 127.5, 127.1, 124.6, 123.9. ^{31}P NMR (500 MHz, D_2O): δ 7.1 ppm. Elemental Analysis for $C_{30}H_{26}N_6O_6Cl_2P_2Ru \bullet 6H_2O \bullet HBr$: (Calc.) Ru: 11.02, C: 39.28, H: 3.41, N: 9.16, (Exp.) Ru: 11.0, C: 38.46, H: 3.40, N: 8.85.

Synthesis of O-(tetrahydro-2H-pyran-2-yl)hydroxylamine (NH_2OTHP). N-hydroxyphthalimide (10.0 g, 61.3 mmol) was added to a solution composed of 70 mL of dichloromethane and 80 mL of 1,4-dioxane. 3,4-dihydro-2H-pyran (6.16 mL, 67.5 mmol) was then dispensed to the stirring solution, followed by p-toluenesulfonic acid (220 mg, 1.2 mmol). The solution was vigorously stirred in air for 2 hours. 100 mL of a saturated sodium bicarbonate solution was then slowly added and stirred to yield an orange color in the solution. The organic layer was extracted as the bottom layer, then washed with 100

mL of brine before drying over Na_2SO_4, filtering, and condensing under reduced pressure. The resulting powder was suspended in 30 mL of dry benzene under N_2. Methylhydrazine (2.12 mL, 41 mmol) was added to the solution, and refluxed under N_2 for 15 minutes. The solution was cooled to room temperature and filtered through Celite to remove white precipitate. The solution was condensed under reduced pressure and distilled under vacuum (70^0C) to yield a colorless oil that turned solid upon leaving in a -20^0C freezer. Yield: 3.91 g (54% yield). ^{1}H NMR (400 MHz, $CDCl_3$): δ 5.45 (s, 2H), 4.66 (t, 1 H), 3.86 (m, 1H), 3.54 (m, 1H), 1.7 (m, 2H), 1.51 (m, 4H). ^{13}C NMR (400 MHz, $CDCl_3$): δ 102.52, 62.52, 28.90, 25.33, 19.67. ESI-MS$^+$: $[NH_2OTHP+H]^+$ = 118.09 m/z

Synthesis of N4,N4'-bis(tetrahydro-2H-pyran-2-yl)oxy)-[2,2'-bipyridine]-4,4'-dicarboxamide. [2,2'-bipyridine]-4,4'-dicarboxylic acid (507 mg, 2.08 mmol) was added to a 100 mL Schlenk flask containing 30 mL of thionyl chloride. The reaction was refluxed overnight under N_2 before the starting material was fully dissolved. The thionyl chloride was then bubbled through a saturated sodium carbonate solution until dry (Caution: at this scale, there is an increased inhalation hazard. It is advised to purge the aqueous solution with nitrogen before disposing of it to remove dissolved SO_2 formed from the quenching process). The resulting powder was dried under high vacuum under heat to remove any remaining solvent before 20 mL of dry dichloromethane and 1.0 mL of dry diisopropylethylamine was added to the flask. Separately, *O*-(tetrahydro-2H-pyran-2-yl)hydroxylamine (532 mg, 4.54 mmol) was added to 20 mL of dry dichloromethane and 1.0 mL of dry diisopropylethylamine. The two solutions were mixed in the 100 mL Schlenk flask under N_2, and the solution was allowed to stir overnight under N_2. This yielded a red solution, which was condensed under reduced pressure. The resulting material was purified via flash chromatography using a gradient eluent from 100:0 dichloromethane/methanol to 95:5 dichloromethane/methanol, yielding an off-white powder. Yield: 845 mg (93%). ^{1}H NMR (400 MHz, $CDCl_3$): δ 12.13 (s, 2H), 8.89 (d, 2H), 8.72 (s, 2H), 7.8 (s, 2H), 5.06 (s, 2H), 4.08 (t, 2H), 3.57 (d, 2H), 1.75 (m, 6H), 1.57 (m, 6H). ^{13}C NMR (400 MHz, $CDCl_3$): δ 162.4, 155.3, 150.2, 140.9, 122.0, 118.2, 101.1, 61.3, 27.8, 24.7, 18.1. ESI-MS$^+$: $[bpy\text{-}Hyd+H]^+$ = 443.19 m/z

Synthesis of Ru(4,4'-bis(hydroxamic acid)2,2'-bipyridine)(2,2'-bipyridine)$_2$ chloride (Ru-H). *cis*-Bis(2,2'-bipyridine)dichlororuthenium(II) hydrate (355 mg, 0.682 mmol) and N4,N4'-bis(tetrahydro-2H-pyran-2-yl)oxy)-[2,2'-bipyridine]-4,4'-dicarboxamide (302 mg, 0.682 mmol) were dissolved in 40 mL of 200 proof ethanol and refluxed in air overnight. The color changed from purple to red after refluxing. The solution was then condensed under reduced pressure and the resulting red powder was dissolved in 10 mL of 0.2 M HCl for 1 hour to deprotect the hydroxamate. The solution was then condensed under reduced pressure and the final product was recrystallized from slow addition of diethyl ether into methanol as a red powder. Yield: 500 mg (97% yield). ^{1}H NMR (500 MHz, D_2O): δ 8.92 (dd, 2H), 8.56 (d, 4H), 8.04 (m, 6H), 7.78 (d, 4H), 7.67 (dd, 2H), 7.4 (t, 4H). ^{13}C NMR (500 MHz, D_2O): δ 168.4, 163.8, 157.6, 156.8, 156.6, 152.4, 151.3, 151.2, 141.0, 139.4, 138, 127.3, 127.2, 124.8, 124.2, 124.1, 122.2, 121.9. Elemental Analysis for $C_{32}H_{26}N_8O_4Cl_2Ru \bullet 3H_2O$ (Calc.) Ru: 12.72, C: 48.37, H: 3.81, N: 14.10, (Exp.) Ru: 13.14, C: 48.20, H: 3.96, N: 13.10.

UV-Vis titration of Ru-P. This method has been previously demonstrated in the literature to determine the pK_a of anchoring groups on Ru-based dyes, and was used to identify the pK_a of the most acidic proton on Ru-P[28–31]. Briefly, a 100 mL solution of 0.15 mM **Ru-P** was brought to pH 0.92 with HNO_3, and a UV-Vis spectra was taken of the solution. The pH was then adjusted to higher pH values in small increments by using either 10 M, 1 M or 0.1 M NaOH, using as needed to keep the relative volume from changing significantly and not significantly altering the concentration of the **Ru-P** in solution. UV-Vis spectra were taken after the pH reached equilibrium with each incremental rise of the pH until a final pH near 11 was reached. Deprotonation of the anchoring group that results in a spectral shift in the absorption profile allows us to reveal the equivalence point of the graph as the pKa of that particular proton.

Acid-base titration of Ru-P and Ru-H complexes. A 10mL solution of 0.55 mM **Ru-P** or **Ru-H** was titrated with a standardized 0.05 M NaOH solution, taken from pH 3.17 to 10.4. The solution was standardized by titrating the NaOH solution in the presence of methyl red indicator with 1.2 mM potassium hydrogen phthalate. Small aliquots of NaOH

were added to the stirring solution of the ruthenium complex and the pH was allowed to reach equilibrium between each aliquot.

Mass Titration of TiO_2 anatase particles. This method was adopted from a previously reported procedure in the literature. Various 20 mL solutions of 0.3 M $NaNO_3$ were stirred overnight under N_2 (after being previously degassed) with various quantities of TiO_2 anatase particles ranging from 0.06 g to 2.4 g. Upon stirring overnight to allow the solution to reach equilibrium with the surface, the pH was measured with a pH meter to yield the resulting pH. The equilibrium pH in which the proton concentration was not significantly altered by changing the mass of the TiO_2 anatase particles in solution was shown to be the point of zero charge.

Generating Langmuir plots for Ru-P|TiO_2 & Ru-H|TiO_2. A 5.00 mL stock solution of 3 mM **Ru-P** was prepared for each solution tested: 200 proof ethanol, pH 1 HNO_3, pH 3 0.1 M Na_2SO_4, pH 6 0.1 M NaP_i. pH 8 0.1 M NaP_i, and pH 10 0.1 $Na_2B_4O_7$ Over 6 scintillation vials, a 5.00 mL solution of **Ru-P** or **Ru-H** made from various dilutions of the stock solution (100 µL to 2.00 mL) were stirred in the presence of 10 mg of TiO_2 anatase particles for each solution. The solutions were allowed to stir overnight in the dark before being centrifuged at 4000 rpm to remove the particles. In some cases, the solution was then filtered through a 0.2 µm syringe filter to remove any remaining particulates. A UV-Vis spectrum was then taken of each supernatant, diluting to 1:5 or 1:10 depending on the final equilibrium concentration of **Ru-P** or **Ru-H** in solution. Calibration curves were also taken of the stock solution (taking at least 3 points) in order to determine the extinction coefficient. Data are modelled to Eqn 2.1 using the Origin Pro 2017 graphing and analysis software package.

Synthesis of TiO_2 films via sol-gel paste. FTO slides were cleaned by sonicating in a solution of Fisherbrand Sparkleen® detergent for 30 minutes, then rinsed with water and sonicated in ethanol, acetone, and hexanes for 20 minutes each. The slides were then rinsed thoroughly with hexanes before being dried under a stream of nitrogen. TiO_2|FTO slides were made by a sol-gel method. Briefly, 250 mL of MilliQ water and 80 mL of glacial

acetic acid were mixed at room temperature. The solution was then brought to -5ºC with a brine/ice bath, and 37 mL of titanium(IV) tetraisopropoxide and 20 mL of 2-propanol were added to the solution over 5 minutes. The solution was returned to room temperature below slowly heating to 80 ºC under air overnight. The solution was sonicated for 10 minutes before 26 mL was split between two Teflon liners (13 mL in each liner). The solutions were sealed and heated to 180 ºC for 12 hours in a stainless steel pressure vessel with a ramp rate of 1.3 ºC/min. The solutions were sonicated, combined, and condensed to ~10 mL. 325 mg hydroxypropyl cellulose was then added and the solution was allowed to stir for 24 hours, creating a opaque white paste. 25 μL of this paste was spin-coated onto a 1 cm^2 area of FTO (sectioned off with Kapton tape) at 2000 rpm for 1 minute, dried for 1 hour in air, and annealed at a ramp rate of 5 ºC/min to 500 ºC for 4 hours. Film thicknesses were estimated to be ~1.6 μm via SEM cross-sectional images.

Potentiometric titration of TiO_2 electrodes. A TiO_2 electrode on an FTO-coated glass substrate was created with copper wire, thin glass tubing, and Hysol epoxy resin. The electrode was placed in 200 mL of 0.1 M NaCl in aqueous pH 2 HCl. The solution was degassed with N_2 for 30 minutes, then the pH was adjusted with a syringe pump programmed at 1.00 mL h^{-1} with 1 M NaOH. The process was repeated for 0.2 M and 0.3 M NaCl, where the pH at which the three titration curves intersect is considered the point of zero charge.

Synthesis of WO_3 films via sol-gel paste. FTO slides were cleaned by sonicating in a detergent for 30 minutes, then rinsed with water and sonicated in ethanol, acetone, and hexanes for 20 minutes each. The slides were then rinsed thoroughly with hexanes before being dried under a stream of nitrogen. WO_3 slides were made with a procedure previously reported in the literature.[32] Briefly, 3.294 g of sodium tungstate dihydrate was dissolved in 20 mL of DI water. This solution was poured into a Dowex ion exchange column previously treated with 6 M HCl and washed with Milli-Q water until the pH of the eluent returned to neutral. The yellow/green eluent was collected into a stirring solution of 20 mL absolute ethanol until the tungstic acid was no longer visibly eluting from the column. The solution was then condensed back to 20 mL under reduced pressure, which yielded an

opaque yellow slurry. 6.6 g of PEG 300 was added to the solution as a stabilizer and stirred vigorously in the dark. 25 μL was dispensed onto a 1 cm^2 area of FTO (sectioned off by Kapton tape) at 2500 rpm for 30 seconds, and annealed in a preheated oven at 500ºC for 30 minutes. The procedure for deposition was repeated 10 times to achieve films of desired thickness, which was measured to be ~2 μm.

Kinetics plots for rates of desorption. TiO_2 or WO_3 slides were soaked in a 2 mM solution of either **Ru-P** or **Ru-H** in 200 proof ethanol (enough to only soak the TiO_2) in the dark overnight. The slides were then soaked in 200 proof ethanol for 12 hours to remove any residual unbound **Ru-R** before being dried over a stream of nitrogen. These films were then made into electrodes and placed in 25 mL of various aqueous solutions from pH 1 HNO_3 to pH 10 $Na_2B_4O_7$. Cyclic voltammograms were recorded in the dark every 5 minutes, and the total charge passed from the $Ru^{3+/2+}$ redox couple quantified the total number of molecules bound to the surface. This charge was converted to nmol **Ru-R**/cm^2 ($\Gamma_{Ru\text{-}R}$), and was found to desorb via a second-order dependence on **Ru-R**. Kinetics plots were modelled either as a first-order or second-order rate plots.

2.3 Characterization of Ru-P and Ru-H

Ru-P and **Ru-H** starting materials and the complexes were characterized by NMR spectroscopy (Figure A1 – A12). The synthetic scheme for the novel Ru-H synthesis is presented in Scheme 2.2, with an overall yield of 90% from original 2,2'-bipyridine-4,4'-dicarboxylic acid starting material.

Scheme 2.2. Synthesis route of novel Ru-H complex

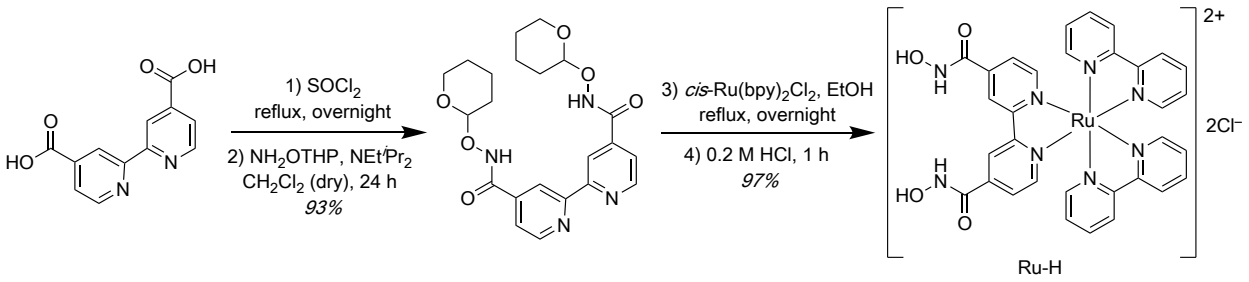

For the complexes only, we recorded FTIR- (Figure 2.1), and Raman spectra (Figure 2.2). The P-OH and C=O amide stretches near ~1700 – 1800 cm^{-1} are apparent in the FTIR spectra, and support the successful synthesis of either **Ru-P** and **Ru-H**. Further, the the N–

O mode near 1500 cm^{-1} in the FTIR and C–N mode in the Raman spectrum near 1350 cm^{-1} of Ru-H correspond to hydroxamic acid, indicating the anchor is in-tact and not reacted to form an amide bond as has been previously reported in other synthetic routes.[33] The elemental analyses show that **Ru-P** forms as a hexahydrate hydrogen bromide salt, which is similar to the known formation of its trimethylsilybromide salt[34] and **Ru-H** forms as its trihydrate salt.

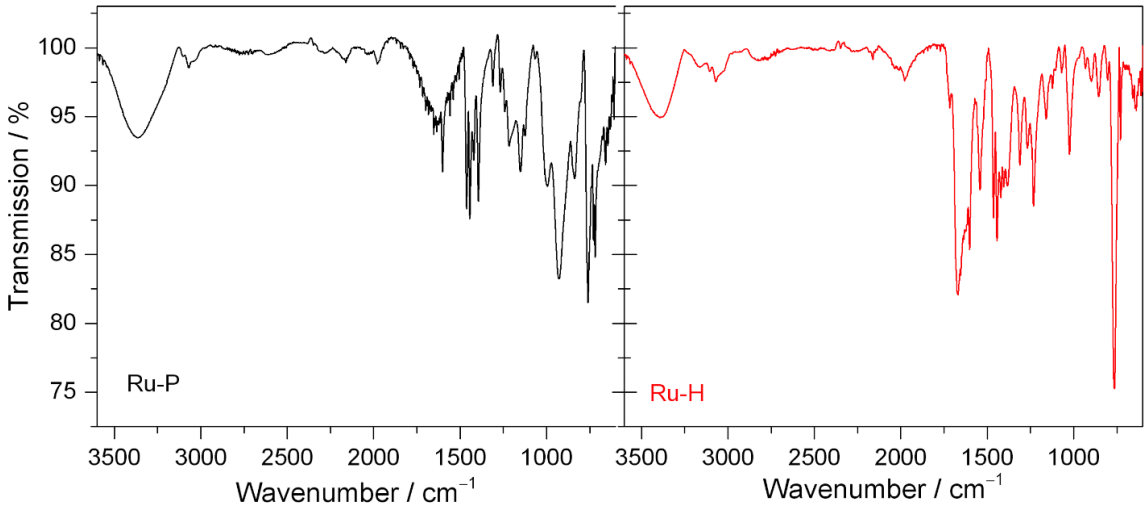

Figure 2.1. FT-IR spectra of (left) **Ru-P** and (right) **Ru-H**

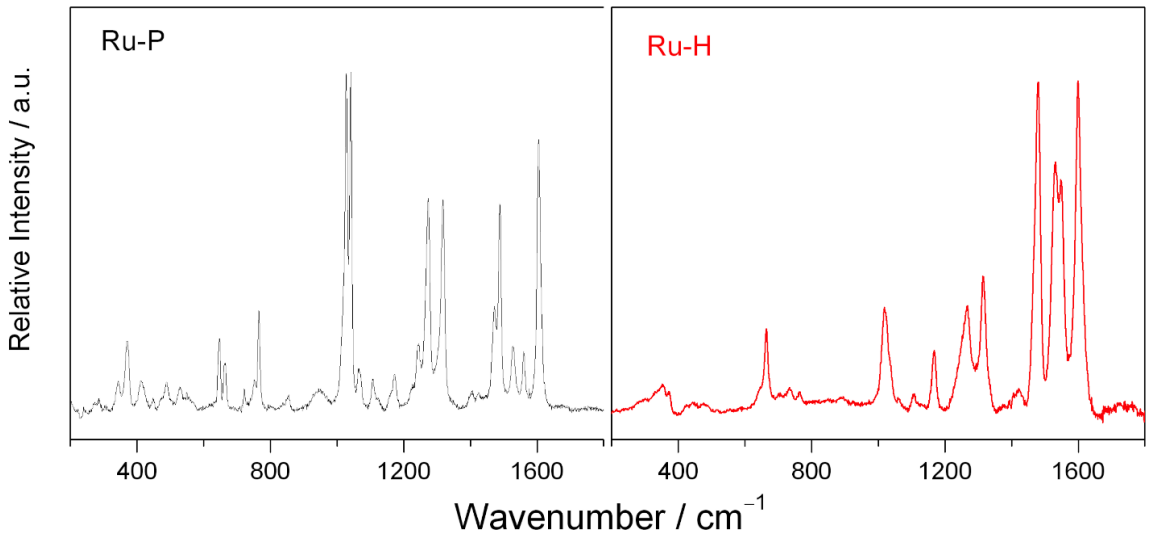

Figure 2.2. Raman spectra of (left) **Ru-P** and (right) **Ru-H** taken with a 532 nm laser at 5% power.

UV-Vis spectra show similarities in the MLCT absorption bands for both complexes (Figure 2.3) between 350 – 600 nm. The highest intensity MLCT band for **Ru-H** extends toward longer wavelengths (λ_{max} = 466 nm, ε= 12,700 M^{-1} cm^{-1}) compared to **Ru-P** (λ_{max}

= 455 nm, ε= 14,000 M^{-1} cm^{-1}). These extinction coefficients were used to determine total concentration of dye remaining in solution after exposure to TiO_2 or WO_3.

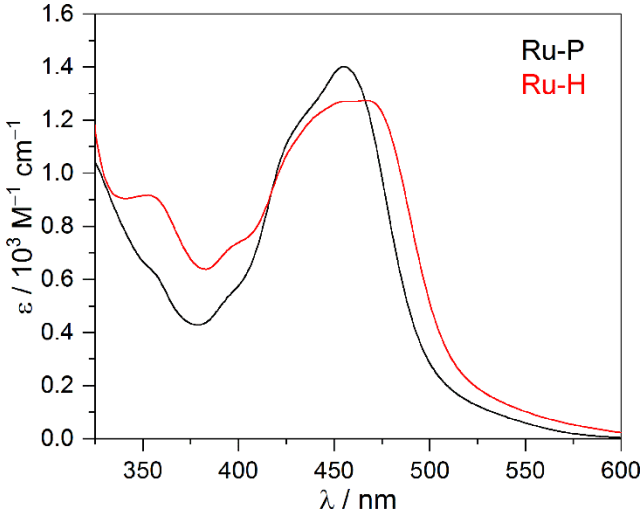

Figure 2.3. UV-Vis spectra of 0.1 M **Ru-P** (black) and **Ru-H** (red) in ethanol highlighting the MLCT band of each dye.

TiO_2 and WO_3 powders for Langmuir plot measurements have surface areas (determined by BET analysis of N_2 sorption isotherms) of 82.15 m^2/g and 8.159 m^2/g respectively (Figures A13 & A14). These values allow us to quantify the amount of complex bound to the surface of these particles independent of surface area. pK_a values for **Ru-P** were measured as p$K_{a,1}$ ≈ p$K_{a,2}$ = 1.6, p$K_{a,3}$ = 3.5, and p$K_{a,4}$ = 5.1 (Figure A15). pK_a values within the relevant pH ranges of operation for **Ru-H** are p$K_{a,1}$ = 6.5, p$K_{a,2}$ = 9.1, and p$K_{a,3}$ ≈ 11. p$K_{a,4}$ is above 12, and could not be accurately measured with a simple acid-base titration (Figure A16). Raman spectra of **Ru-P** and **Ru-H** bound to either TiO_2 or WO_3 are shown in Figure 2.4. These spectra show the dye is indeed the surface.

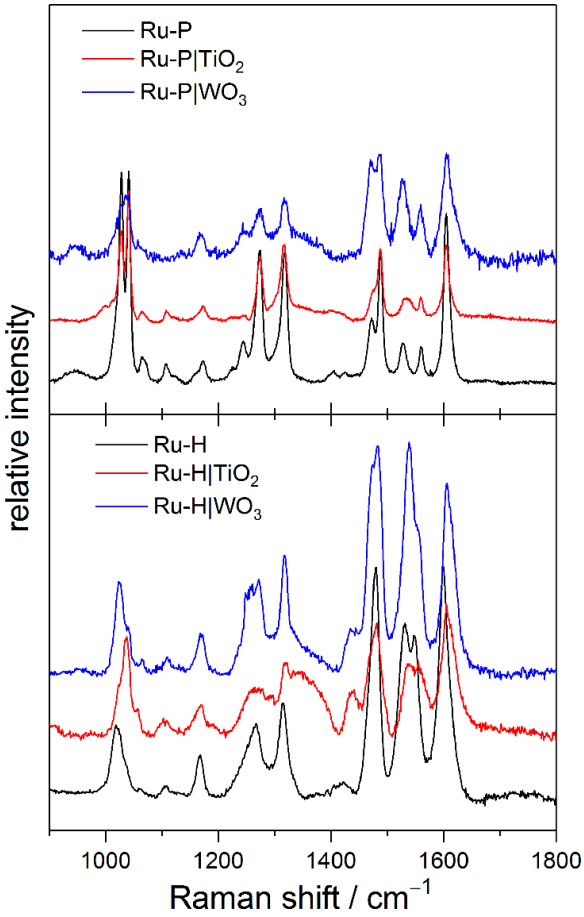

Figure 2.4. Raman spectra of **Ru-P** (a) and **Ru-H** (b) as the pure powder (black), bound to TiO_2 (red), and bound to WO_3 (blue).

2.4 Binding Constant Measurements Using the Langmuir Model

Given the starting concentration of **Ru-R (Ru-P or Ru-H)** and the measured final concentration of the dye after exposure to the metal oxide, we generate Langmuir plots of dye adsorbed (mol_{ads}) vs solution concentration, $[\mathbf{Ru\text{-}R}]_{eq}$. An example of the Langmuir plots for **Ru-P**|TiO_2 and **Ru-H**|TiO_2 in pH 1 HNO_3 are shown in Figure 2.5. The binding constant for phosphonic acid is ~2 orders of magnitude higher than that of hydroxamic acid when anchoring $[Ru(bpy)_3]^{2+}$ onto TiO_2. Langmuir plots fit with equation 1 are presented as Figure A17 – A20, Although WO_3 can only be modelled for pH ≤ 4, TiO_2 is stable across the entire pH range. A table of binding constants K_B is provided in Table 2.1.

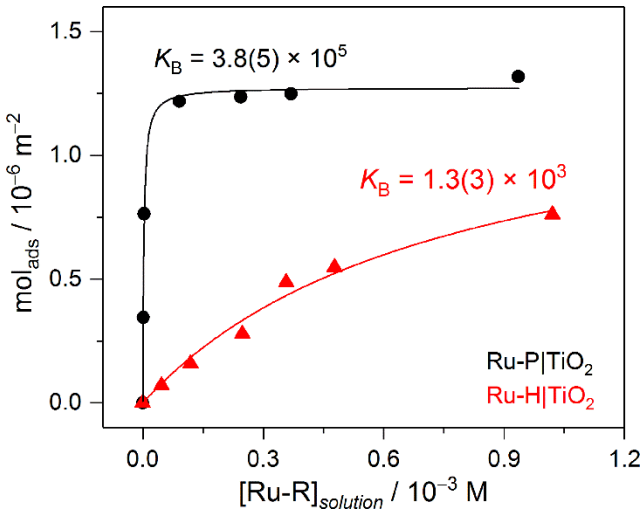

Figure 2.5. Langmuir plot of **Ru-P** (black circles) and **Ru-H** (red triangles) on TiO_2 anatase in pH 1 HNO_3 solution.

Table 2.1. K_B for **Ru-P** and **Ru-H** on TiO_2 and WO_3 at various pH.

K_B on anatase TiO_2		
pH	**Ru–P**	**Ru–H**
1	3.8(5) × 10^5	1.3(3) × 10^3
2	2.0(6) × 10^5	--
3	1.0(5) × 10^4	2.4(8) × 10^3
4	2.9(3) × 10^3	--
5	4(2) × 10^2	--
6	8.7(7) × 10^1	1.2(3) × 10^3
8	3.1(2) × 10^1	1.5(4) × 10^3
10	4.3(3) × 10^1	7(3) × 10^3
K_B on WO_3		
pH	**Ru–P**	**Ru–H**
1	4(2) × 10^4	8(1) × 10^2
2	4(1) × 10^4	2.2(4) × 10^3
3	1.2(3) × 10^4	9(2) × 10^3
4	7(4) × 10^2	2(2) × 10^4

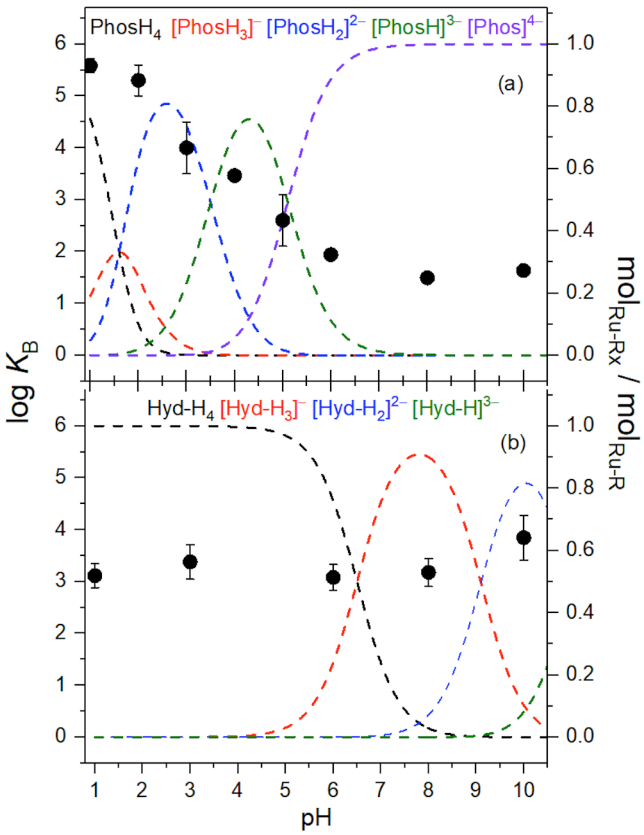

Figure 2.6. Log(K_B) of both **Ru-P**|TiO_2 (a) and **Ru-H**|TiO_2 (b) vs pH on TiO_2 (dark symbols, •) as compared to the speciation of either anchor as a function of pH. The left axis is log(K_B) of the anchor on TiO_2, and the right axis describes the ratio of each protonation state ($mol_{Ru\text{-}X}$) per total fractional surface coverage of the dye ($mol_{Ru\text{-}R}$). **Ru-R** refers to either **Ru-P** or **Ru-H**.

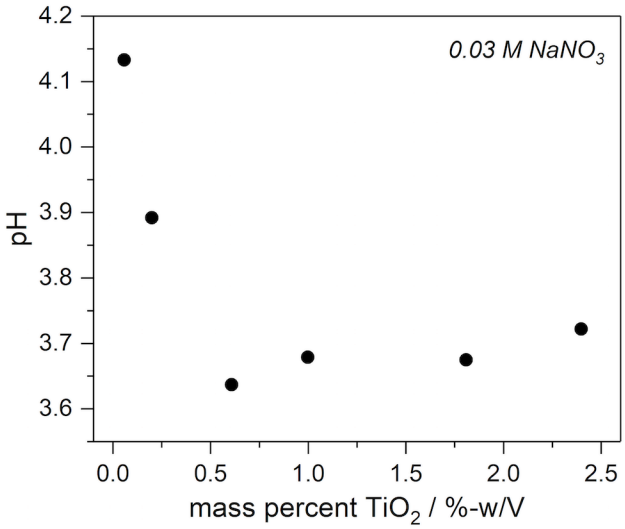

Figure 2.7. Mass titration of TiO_2 in 100 mL of degassed 0.03 M $NaNO_3$ under N_2 as a function of mass-percent TiO_2, showing PZC = 3.65.

We observe only small changes to K_B **Ru-P** and **Ru-H** on TiO_2 anatase when comparing the conjugate bases of different acids at pH 1; all are on the order of 10^5. For example, K_B of **Ru-P** in H_2SO_4, HNO_3, and HCl are and H_2SO_4 are $2.4(6) \times 10^5$, $3.8(5) \times 10^5$, and $9(2) \times 10^5$, respectively. These Langmuir plots are presented in the supporting information in Figure A21. These very subtle differences may arise from conjugate base biding to the surface, and a practical consideration is that HCl is not commonly used in photoelectrochemical water oxidation since $Cl^-(aq)$ is readily oxidized to $Cl_2(g)$ on WO_3 photoanodes.[35]

Comparing the binding constant and the pK_a of **Ru-P** as a function of pH is illustrated in Figure 2.6. Phosphonate has a binding constant on TiO_2 of ~10^5, matching well with reported values at these conditions.[36] As pH increases, K_B decreases, which is directly related to the speciation of the anchor on **Ru-P**. That is, as the ligand becomes increasingly anionic, K_B decreases. At the point of zero charge (PZC) on TiO_2 (3.7, see Figure 2.7), ~98% of **Ru-P** possesses at least a –2 charge on the anchored bipyridine ligand. As both the surface of TiO_2 and the phosphonic acid are deprotonated at increasing pH, we observe a 2 order of magnitude decrease in the binding constant, which we attribute to the electrostatic repulsion of the anionic ligand and the negatively charged surface.

It is important to point out that an overall neutral charge on the surface does *not* mean that negative charge does not exist on the surface; rather, the *sum* of the positive *and* negative charges on the surface equals zero. These charges arise due to either surface Ti-OH (hydroxide) or Ti–O–Ti (ether-like) linkages, which may potentially bind differently to the anchor. The equilibrium of protonation states on the surface of TiO_2 has been established, with the two major equilibria listed below:[37]

$$TiOH_2^{+0.67} + OH^- \rightleftharpoons TiOH^{-0.33} \qquad \text{Eqn. 2.2}$$

$$Ti_2OH^{+0.33} + OH^- \rightleftharpoons Ti_2O^{-0.67} \qquad \text{Eqn. 2.3}$$

Although we cannot distinguish between phosphonic acid surface binding geometries, our data implies that phosphonic acid binds preferentially to the *protonated* surface (Ti–OH_2 and Ti–OH–Ti) over Ti–OH or Ti–O–Ti species. However, given that there are certain pH values within Figure 4 that have primarily two dominant protonation states, we can employ a Langmuir model at those pH that govern a binary mixture.[38,39]

$$\frac{mol_{ads,i}}{mol_{max}} = \frac{K_{B,1}[Ru\text{-}R]_1}{1+K_{B,1}[Ru\text{-}R]_1 + K_{B,2}[Ru\text{-}R]_2} \quad \text{Eqn. 2.4}$$

where *i* is designated as one of the two possible protonation states at a particular pH that exists in significant quantity (≥ 0.1**[Ru-R]$_{eq}$**). This model assumes the same parameters as the single mixture Langmuir model, but also adds the assumption that the maximum number of moles that can bind to the surface is equal for both compounds within the mixture. In other words, we assume that all protonation states have access to the same maximum number of binding sites at a given pH, but that the maximum number of binding sites only varies as a function of pH. While this assumption has been challenged for gas sorption between two different gasses,[40,41] it is reasonable that this assumption is valid for our system given that only the protonation state of the **Ru-R** dye is changing. Therefore, replotting the Langmuir plot at pH 1, 3, 5, and 8 against the model outlined in eqn. (5) should allow us to extrapolate the various K_B values to the proper order of magnitude. Replotted Langmuir plots with the binary mixture equation (5) are listed in Appendix A, with the results listed in Table 2.2.

Table 2.2. Binding constants for **Ru-P$_{xH}$** on TiO_2 where *x* is the number of protons on the anchors.

x	K_B
4	$4.9(7) \times 10^5$
3	$4(5) \times 10^4$
2	$1.3(4) \times 10^4$
1	$6.9(4) \times 10^2$
0	$3.1(2) \times 10^1$

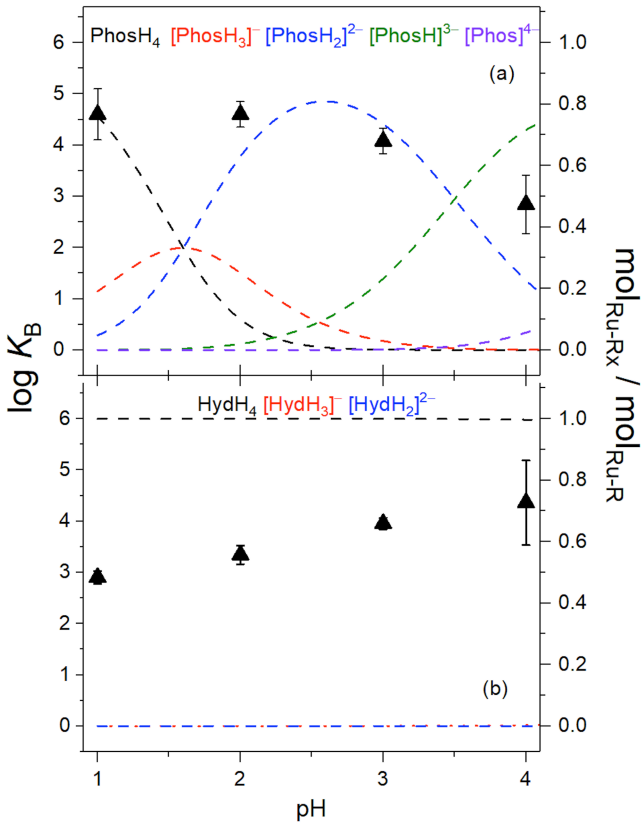

Figure 2.8. Log(K_B) of both **Ru-P**|WO_3 (a) and **Ru-H**|WO_3 (b) vs pH (▲) as compared to the p*K*a values of either anchor. Here, the left axis is describing the log(K_B) of the anchor on TiO_2, whereas the right axis describes the ratio of each protonation state ($mol_{Ru\text{-}X}$) per total fractional surface coverage of the dye ($mol_{Ru\text{-}R}$). **Ru-R** refers to either **Ru-P** or **Ru-H**.

The Langmuir plots of **Ru-P**|WO_3 and **Ru-H**|WO_3 in Figure 2.8 show that K_B decreases by about an order of magnitude for **Ru-P** (from 10^5 to 10^4) at pH 1 in moving from TiO_2 to WO_3. We attribute this change in binding constant to the difference in surface environment between the two semiconductors, possibly due to lower PZC of WO_3 (~0.5) compared to the PZC of anatase TiO_2 (~3.7) leaving differences in overall charge on the surfaces. Similarly, differences in Lewis acidity between the two metal ions could lead to differences in binding constant, where Ti^{4+} serves as a better Lewis acid for the binding of **Ru-P** or **Ru-H** compared to W^{6+}. Second, a decrease in binding constant is still observed for **Ru-P**|WO_3 at pH 4, even though the PZC of WO_3 is pH < 0.5.[42] This observation indicates that the build-up of negative charge due to the higher acidity of phosphonic acid leads to the decrease in binding constant on an overall negatively charged surface. Given the weaker acidity of hydroxamic acid protons (pK_{a1} = 6.5), it is not surprising that K_B is

pH-independent on WO_3 for pH $\leq$ 4. Control experiments at pH 1 for both TiO_2 and WO_3 with *unanchored* $[Ru(bpy)_3]^{2+}$ indicate that adsorption to the surface is indeed *chemisorption (*Figure A22), as physisorption is ~3 and ~5 orders of magnitude lower in binding constant versus **Ru-H** and **Ru-P**, respectively. pH 1 was chosen for this control experiment since both anchors bind strongly to both surfaces at that pH.

2.5 Characterization and Electrochemistry of Ru-R|MO_x Electrodes in Water and Acetonitrile

Diffuse reflectance UV-Vis spectra for both complexes bound to TiO_2 and WO_3 are reported in Figure 2.9. The prominent MLCT bands demonstrate that **Ru-P** and **Ru-H** are bound to the surface of each metal oxide. In order to measure the rates of desorption accurately at significantly low quantities on the surface with little outside interference or perturbation of the system, we employ cyclic voltammetry (CV) to quantify both the fractional surface coverage of the dye on the films, and the rates of desorption over time. Voltammetry also allows us to probe the desorption kinetics of the metal complex after it has undergone oxidation and reduction on the surface of the metal oxide.

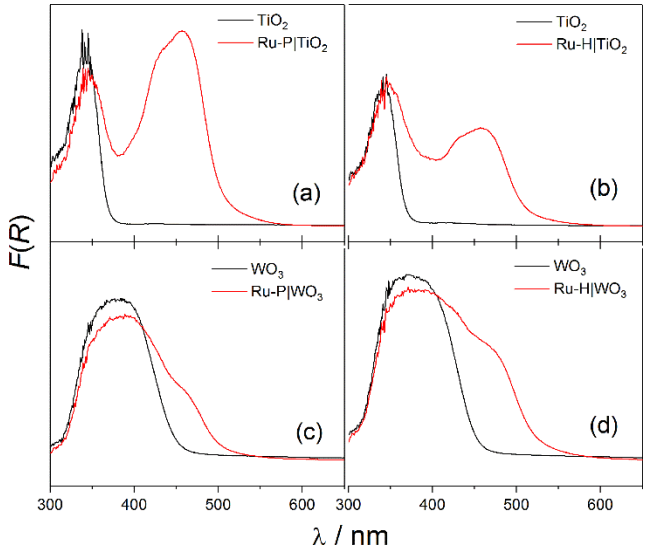

Figure 2.9. UV-Vis spectra of (a) **Ru-P**|TiO_2, (b) **Ru-H**|TiO_2, (c) **Ru-P**|WO_3, and (d) **Ru-H**|WO_3 after soaking films in ~1.5 mL 0.2 mM of either **Ru-P** or **Ru-H** in ethanol.

Limitations of this method primarily arose past pH 7, when the potential for the pH *dependent* water oxidation (1.23 V vs RHE) overlapped with that of the pH *independent* $Ru^{3+/2+}$ couple of **Ru-P** (1.4 V vs NHE) and **Ru-H** (1.45 V vs NHE). By integrating the

anodic wave of the cyclic voltammogram and correcting for surface area, we can deduce the quantity of chemisorbed **Ru-R** and quantify the rate constant for its desorption. An example of cyclic voltammograms of **Ru-P** and **Ru-H** on TiO_2 is shown in Figure 2.10. the Linear relationship between scan rate (ν) and peak current (i_p), in acetonitrile with 0.1 M Bu_4NPF_6 as an electrolyte, confirms that **Ru-R** is chemisorbed to be chemically bound to the surface (Figure A23). It is assumed that any change in chemisorption moving from acetonitrile to water is governed by the mechanism of desorption, and that all **Ru-R** is chemisorbed at the start of each CV scan. CV scans and their respective second-order plots are listed in Figures A24 and A25, respectively.

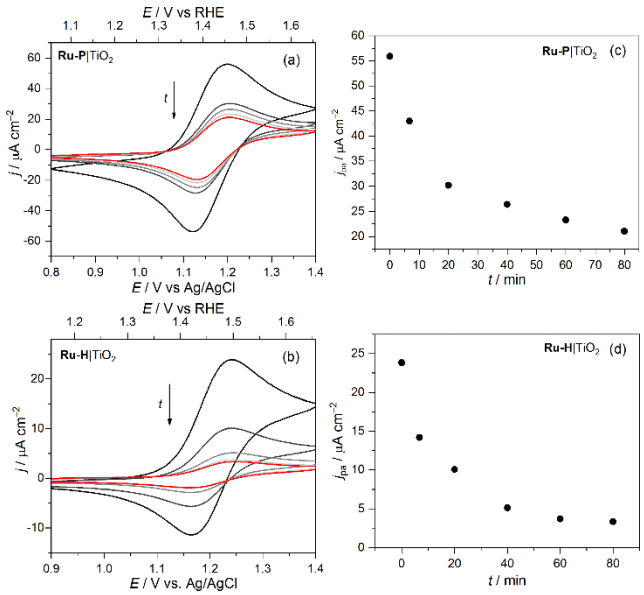

Figure 2.10. Representative cyclic voltammograms of (a) **Ru-P**|TiO_2 and (b) **Ru-H**|TiO_2 in pH 1 HNO_3 with a scan rate of 25 m V s^{-1}, where the time interval between CV scans is ~20 minutes for clarity. The anodic peak current as a function of time, j_{pa} for (c) **Ru-P**|TiO_2 and (d) **Ru-H**|TiO_2 are also presented.

Surface functionalized **Ru-P**|TiO_2, **Ru-H**|TiO_2, **Ru-P**|WO_3, and **Ru-H**|WO_3 yield cyclic voltammogram scans with differences in peak currents of the anodic and cathodic peaks, $\Delta i_p > 0$. While a linear relationship between i_p and v exists for both surfaces, indicating a surface-bound species (Figure A23), the difference in peak currents can be explained by the poor kinetics for charge transfer from the dye to the metal oxide surface, as shown in Figure . CV scans of a 0.01 M $[Ru(bpy)_3]^{2+}$ solution in pH 1 HNO_3 with a TiO_2 anatase or WO_3 working electrode, Pt counter electrode, and Ag/AgCl reference electrode show significantly broadened scans compared to a glassy carbon working

electrode. Therefore, the significantly sharper CV scans of **Ru-P**|TiO_2, **Ru-H**|TiO_2, **Ru-P**|WO_3, and **Ru-H**|WO_3 with closer i_{pa} and i_{pc} versus an unanchored $[Ru(bpy)_3]^{2+}$ solution further support a chemisorption over a physisorption of dye to the metal oxide surface.

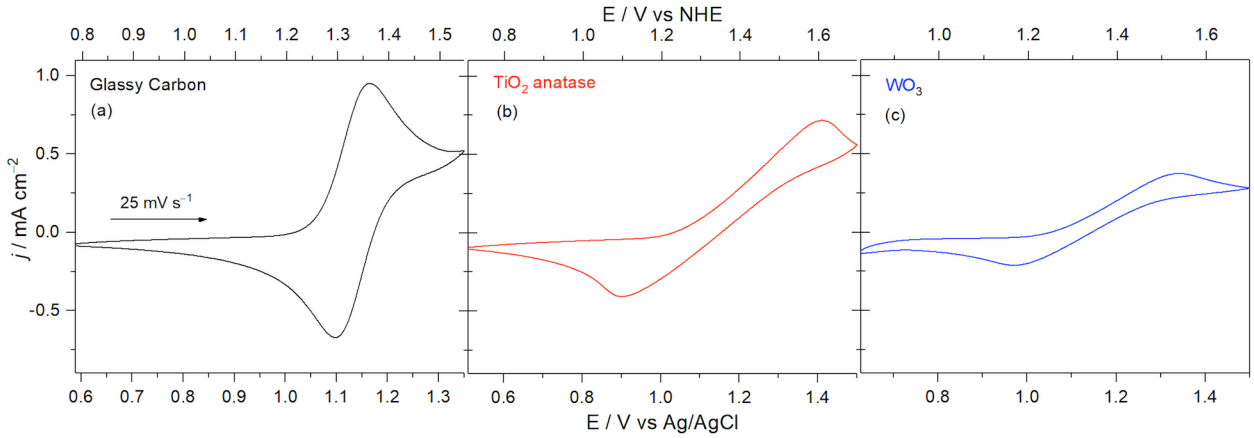

Figure 2.11. Cyclic voltammograms of a 0.01 M $[Ru(bpy)_3]^{2+}$ solution in pH 1 HNO_3 with (a) glassy carbon, (b) TiO_2 anatase, and (c) WO_3 working electrode, a Pt counter electrode, and Ag/AgCl reference electrode. Scan rates are 25 mV s^{-1} with a positive initial polarity.

Comparing the fractional surface coverage of **Ru-P** and **Ru-H** on either TiO_2 or WO_3 (Table 2.3) suggests that our films are close to a monolayer of dye, as has been reported.[6,19,23,43] Note that the surface coverage of **Ru-P** onto WO_3 is an order of magnitude lower than other electrodes, indicating the overall number of bound, electrochemically active **Ru-P** on WO_3 is significantly lower. Thus, measurable quantities of **Ru-R** (via cyclic voltammetry) seem to be dependent on both anchor *and* surface metal identity, where the decrease in binding sites from TiO_2 to WO_3 for **Ru-H** is only 33%. However, ICP-MS analysis of **Ru-P**|TiO_2, **Ru-H**|TiO_2, **Ru-P**|WO_3, and **Ru-H**|WO_3 solutions after fully desorbing the dye in a 1.0 M NaOH solution yields values 2 – 10 times higher than dye electrochemically measured by CV. This result suggests portions of the metal oxide surface that are either not chemically bound to the surface and are instead physisorbed through a bilayer of the dye via intermolecular interactions, or are chemically bound to a portion of the surface that are not electrochemically active. Determining the order in which the dye desorbs should distinguish between these two possibilities. Results of these experiments are discussed in Section 2.6.

Table 2.3. Average fractional surface coverage of **Ru-R** ($\Gamma_{Ru\text{-}R}$) on both TiO_2 and WO_3 based on integrating the first anodic wave of the cyclic voltammograms from pH 1 – 7, compared to **Ru-R** bound to each metal oxide measured through ICP-MS.

Electrode	Charge passed / 10^{-4} C	$\Gamma_{Ru-R,\,CV}$ / 10^{-5} mol m^{-2}	$\Gamma_{Ru-R,\,ICP}$ / 10^{-5} mol m^{-2}	Surface Coverage / molecules m^{-2}
Ru-P|TiO_2	6.2	6.5	44	2.6×10^{20}
Ru-P|WO_3	0.65	0.63	6.9	4.2×10^{19}
Ru-H|TiO_2	5.0	4.8	7.6	4.6×10^{19}
Ru-H|WO_3	3.2	3.2	7.6	4.6×10^{19}

However, further inspection of CV scans of **Ru-H** on TiO_2 and WO_3 reveal a large, quasi-reversible anodic current that converged to the reversible $Ru^{3+/2+}$ couple. For voltammogramms reported in Figure A24, the second scan is used to quantify Ru^{2+} on the surface given this anodic wave is not observed after the first scan at a scan rate of 25 mV s^{-1}. This effect was also observed in 0.1 M Bu_4NPF_6 in acetonitrile, which indicates that the irreversible oxidation scans are seemingly independent of solvent. However, multiple scans taken after ~15 – 60 minutes of time reveal that at least part of this anodic wave reappears when resting in solution under no applied bias in the dark, and in the case of TiO_2 most of it reappears (Figure 2.12). **Ru-H** was returned to Ru^{2+} at the end of each voltammetry experiment.

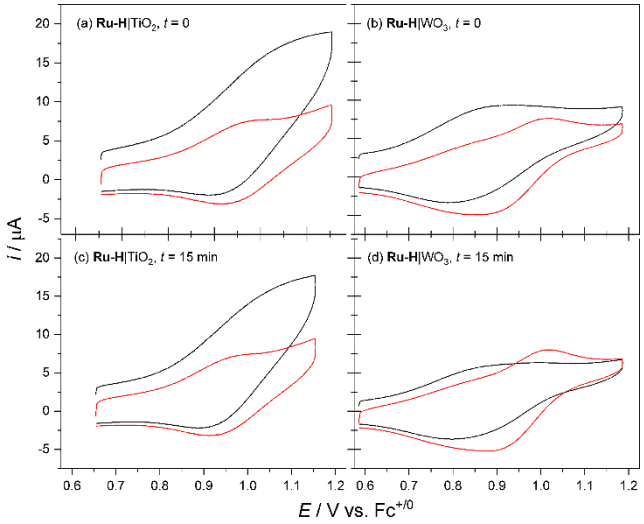

Figure 2.12. Cyclic voltammograms of (a) **Ru-H**|TiO_2 and (b) **Ru–H**|WO_3 recorded in after immersing films 0.1 M Bu_4NPF_6 CH_3CN t = 0 (black); (c) **Ru-H**|TiO2 and (d) **Ru–H**|WO_3 re-recorded after a 15-minute delay (t = 15 min). During each cyclic voltammogram, five sweeps were recorded with a scan rate of 100 mV s^{-1}. For clarity, only the first (black) and the fifth (red) sweep are illustrated.

Indeed, DFT calculations of this complex reveal that electron density in the HOMO includes contributions from d_{z^2} of Ru^{2+} and the π system of the of the bipyridine ligand in **Ru-P**, but lies both on the d_{z^2} Ru^{2+} center and π-bonds on one of the hydroxamate ligands of **Ru-H** (Figure 2.13). It is therefore possible that the hydroxamate is still protonated when on the surface of either semiconductor metal oxide, and undergoes a proton-coupled electron transfer (PCET) under positive bias to oxidize Ru^{2+}. It has been shown that hydroxamate primarily binds to Ti^{4+} in a monodentate fashion,[44] allowing this pathway toward PCET oxidation to occur at the most acidic proton on hydroxamic acid (pK_{a1} = 6.5). At pH < 6, hydroxamic acid is still protonated when bound to the surface. However, at pH > 6.5, the first proton on the hydroxamic acid is removed, leaving behind a negatively charged conjugate base anchored to the surface of the metal oxide. The slow return of the large anodic wave that can then be subsequently re-oxidized independent of either water or acetonitrile, coupled with computational evidence for the hydroxamate largely incorporated into the HOMO of **Ru-H** suggests that the anchor itself is redox active in a quasi-reversible manner, as shown in Scheme 2.3, where the oxidation of hydroxamic acid has been proposed in solution as described previously.[45]

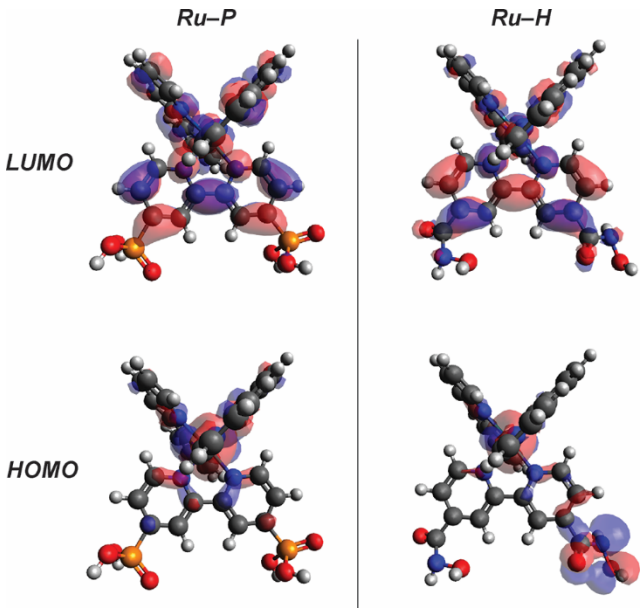

Figure 2.13. Projections of the HOMO and LUMO for **Ru-P** (left) and **Ru-H** (right) calculated using the Gaussian 09 DFT model with the PBE0 functional and 6-31G(d,p) basis set, with Stuttgard/Dresden (SDD) effective core potential (ECP) basis set on the central Ru atom, in vacuum.[46]

Scheme 2.3. Proposed reaction of quasi-reversible oxidation of hydroxamate anchor on **Ru-H** bound to a metal oxide.

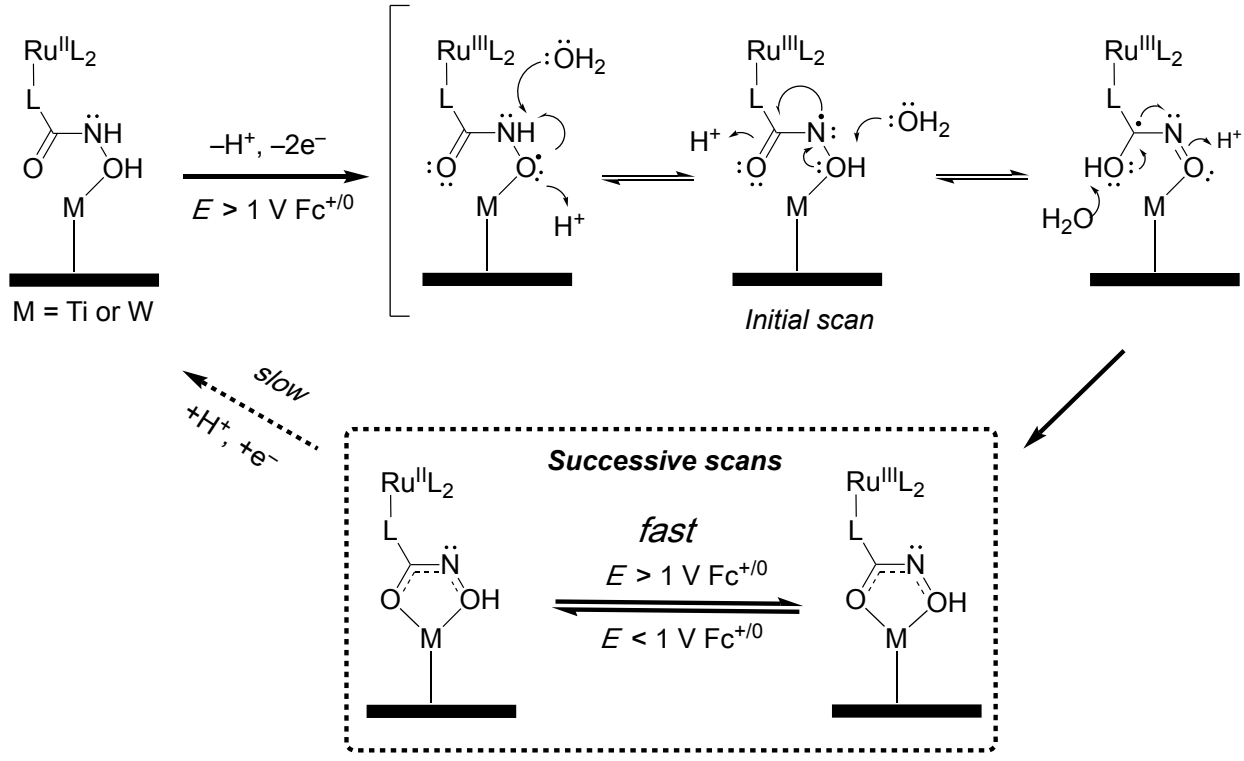

Closer inspection of Figure 2.12b shows that the peak shape changes as we continue scanning on **Ru-H**|WO_3. We attribute this change in the anodic wave peak shape to the slight increase in the $Ru^{2+/3+}$ potential once the hydroxamic acid ligand has been oxidized. However, the shift in the anodic wave toward more positive potentials after initial oxidation of the hydroxamic acid ligand is not observed on TiO_2, rather the electrochemical potential of **Ru-H** before and after oxidation occur at approximately the same electrochemical potential. This result suggests that **Ru-H** may bind differently to the two semiconductors. Regrettably, efforts to observe changes in the C—N or C=O stretches by Raman spectroscopy were unsuccessful due to small quantities of **Ru–H** adsorbed to the surface. (see Figure A26).

The initial CV scans in Figure 2.10 shows current arising from both quasi-reversible hydroxamic acid oxidation and reversible Ru^{2+} oxidation. However, the fifth scan shows only the reversible $Ru^{3+/2+}$ wave. Therefore, integrating the initial anodic wave should reveal twice as much charge passed as that of the last scan. Indeed, for **Ru-H**|TiO_2, we observe 3.27 μC of charge passed initially, double that of the last scan, 1.65 μC. Likewise, for **Ru-H**|WO_3, we observe 3.46 μC, about double that of the last scan, 1.66 μC. These data hint that one hydroxamic acid anchor on **Ru-H** is susceptible to a quasi-reversible oxidation. Successive CV scans of 0.01 M **Ru-H** in pH 1 HNO_3 recorded on a glassy carbon electrode (Pt counter, Ag/AgCl reference) shows two separate oxidations on the dye – one that is irreversible at 1.35 V vs NHE, and one reversible couple at 1.43 V vs NHE (Figure 10). With continued cycling, we notice that the irreversible peak at 1.35 V vs NHE slowly disappears, leaving only the $Ru^{3+/2+}$ redox event at 1.43 V vs NHE (red). This irreversible wave that disappears over successive scans is consistent with the CV scans presented in Figure 8, where the two oxidations are no longer resolved and instead occurr at roughly the same potential. We propose that the oxidation at 1.35 V arises from hydroxamate ligand oxidation, which is reasonable since the hydroxamic acid anchor accounts for ~50% of the electron density in the HOMO. This oxidation is followed by a reorganization of the dye to allow for a resonance-stabilized hydroxamate anion to bind to the metal oxide surface in bidentate fashion. This irreversible wave returns after long times (>15 minutes) if the system rests at open circuit in acid to reprotonate the anchor. The low surface coverage and long times scales preclude observing this proposed phenomenon directly by vibrational spectroscopy.

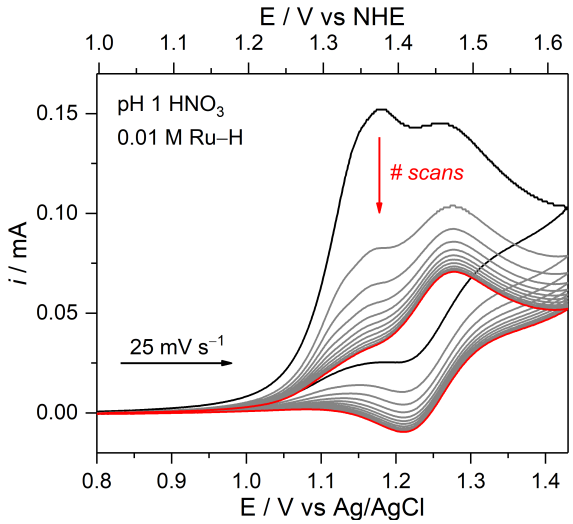

Figure 2.14. Cyclic voltammogram of a 0.01 M Ru-H solution in pH 1 HNO_3 with a glassy carbon (GC) working electrode, Pt counter electrode, and Ag/AgCl (sat'd KCl) reference electrode. Scan rate = 25 mV s^{-1}, showing 12 consecutive CV scans over time.

2.6 Desorption Kinetics of Ru-R|MO_x in Aqueous Media

CV was used to generate kinetics plots that show a second-order dependence on **Ru-R**. The linear least squares regression analysis (R^2) of these fits is better than the corresponding first-order treatment of the data. Second-order in **Ru-R** desorption is observed even after soaking the films in ethanol for at least 12 hours. We propose second-order desorption by two possible mechanisms for $[Ru(bpy)_3]^{2+}$ derivatives (Scheme 2.4).

Scheme 2.4. Possible mechanisms of **Ru-R** second-order desorption, either through (a) the physisorption of one Ru-R complex onto a chemisorbed **Ru-R** to TiO_2 or WO_3, or (b) the concerted desorption of two chemisorbed **Ru-R** species.

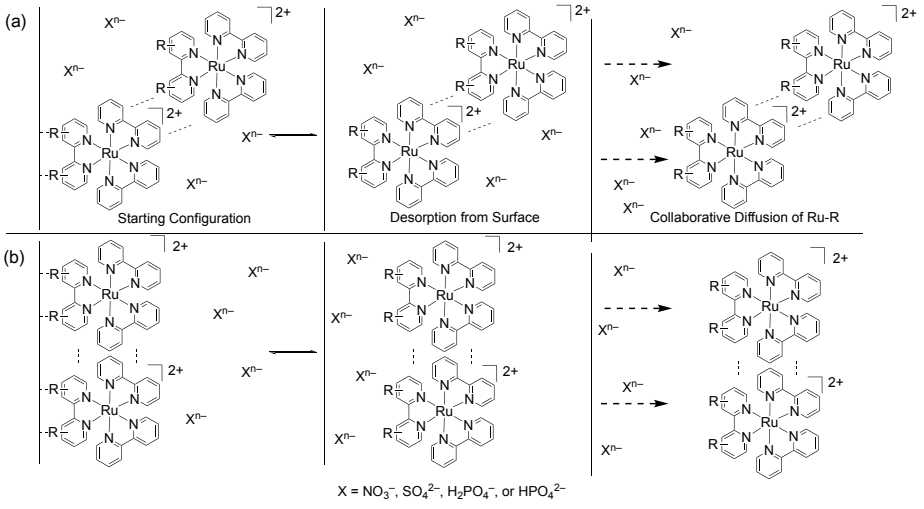

In Scheme 2.4a, soaking the films in an ethanolic solution of **Ru-R** creates a bilayer in which one **Ru-R** layer is bound to the surface and the other is physisorbed through possible π-stacking with the bound dye. However, both dye molecules can reside in the electrical double layer, allowing both layers to possibly be electrochemically active to give the second-order dependence observed by CV. This mechanism suggests that the physisorbed second layer of dye does not desorb from the surface in ethanol, and that *both* chemi- and physisorbed dyes desorb from the surface in a concerted effort. This mechanism also requires forming the bilayer in the Langmuir plots, and would overestimate the binding constant. Recall that Langmuir plots of unanchorable $[Ru(bpy)_3]^{2+}$ binding to the surface of either TiO_2 and WO_3 at pH 1 show little to no physisorption directly to the metal oxide (Figure A22) compared to the chemically adsorbed, anchored **Ru-R** species. The second mechanism, illustrated in Scheme 2.4b, involves two **Ru-R** molecules chemisorbed to the surface that detach concertedly due to ionic interactions with the surface in water. It is possible that all molecules are chemisorbed to the surface through the anchor, but that desorption of one molecule forces the desorption of another at a surface. To distinguish between these two mechanistic possibilities, we increased the ionic strength by adding salt to the ethanolic soaking solution to perturb the intermolecular interactions between the chemisorbed & physisorbed dyes described in Scheme 2.4a. We also determined the relationship between the size of the cation or anion used to perturb the bilayer as it relates to the fit toward first-order kinetics. After soaking films in ethanolic 0.1 M $LiClO_4$, 0.1 M $NaClO_4$, or 0.1 M Bu_4NClO_4 for 24 hours, we observe a better fit for the first-order dependence of **Ru-H** versus when the film is only soaked in pure ethanol, but it is only a small increase in linearity in the first-order rate plot versus a film that was not pre-exposed to 0.1 M $ACl O_4$ in ethanol (A = Li^+, Na^+, or Bu_4N^+). No major change in the R^2 value for a first-order plot is observed (Figure A27 – A30). Further, there seems to be a small trend in the size of the cation and how well the kinetics fit toward a first-order plot. The trend leans toward the smaller cations allowing better fit to the first-order kinetics, possibly due to the smaller size of the salt being able to more easily fit between the chemisorbed Ru-R layer and the physisorbed Ru-R layer, which allows for better ligand exchange between the original Cl^- anion on the Ru-R bound to the surface with the larger ClO_4^- anion. It is important to note that this trend is very weak, and only explains small changes in the R^2

value between the three cations used. We then pursued the changes in the anion size by using NaX salts (X = ClO_4^- and BAr^F, where BAr^F = tetrakis(3,5-bis(trifluoromethyl)phenyl)borate) (Figures S31 – S34). In the cases where perchlorate was added to the ethanolic soaking solution, the plot showing second-order **Ru-R** desorption rate fits with a higher R^2 value compared to a first-order plot, which implies that a bilayer model is still a better model. Although we seem to perturb bilayer formation at high ionic strength, we do not seem to prevent its formation. Further increasing the steric bulk of the anion in solution and adding aromatic groups that may also stack to the pyridyl rings should further increase the first-order in **Ru-R** behavior in desorption. Indeed, as we increase the steric bulk of the auxiliary salt by adding 0.1 M $NaBAr^F$, this first-order dependence on **Ru-R** desorption becomes even higher (Table A1). These data support the mechanism in Scheme 2.4a, where the bulky anion of the salt yields a surface that is closer to monolayer coverage. We note that in all cases, we observe a slower rate of desorption when a metal salt is used in the ethanolic soaking solution. Nevertheless, through the remainder of this chapter, we describe the desorption rate by second-order kinetics due to the higher R^2 fit to the data. Using cyclic voltammetry to determine rate constants for desorption is limited to pH $\leq$ 7, since WO_3 behaves as an Arrhenius acid and catalytic current for oxygen evolution starts to overlap on TiO_2.

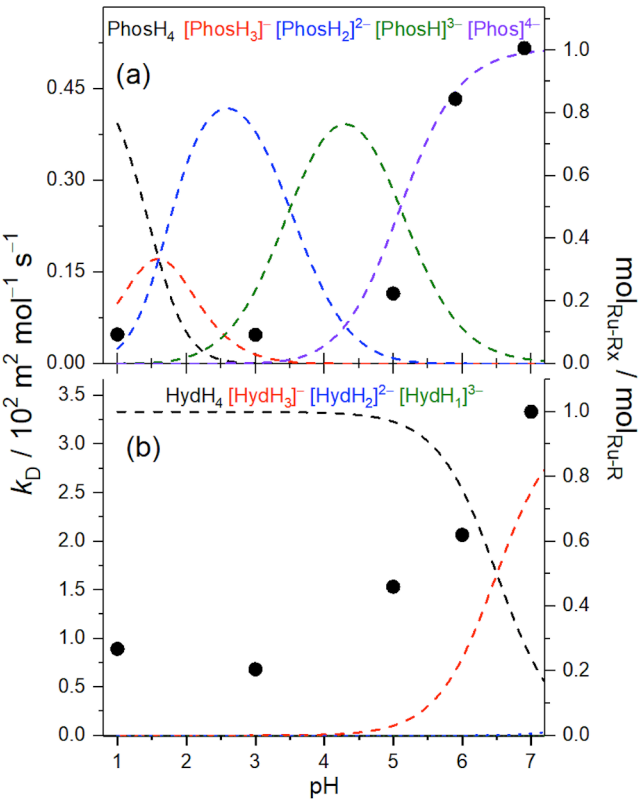

Figure 2.15. k_d of (a) **Ru-P**|TiO_2 and (b) **Ru-H**|TiO_2 as a function of pH (dark symbols ●, left axis), with corresponding speciation for each complex (mol_{Ru-X}) per total fractional surface coverage of the dye (mol_{Ru-R}) on the right axis. **Ru-R** refers to either **Ru-P** or **Ru-H**.

As shown in Figure 2.15a, the rate constant for **Ru-P** is relatively unaffected by the deprotonation of the first three P-OH groups on the anchor. But, we see a five-fold increase in rate constant when the last proton is removed above pH 4. Although this rate constant under acidic conditions matches well with other reports,[23] the rate constant is dependent on the relative protonation states of the anchor. This trend also holds for hydroxamic acid (Figure 2.15b), with a four-fold increase in k_d of **Ru-H** from pH 1 to pH 7). The rate constants as a function of pH is provided in Table 2.4. The increase in rate constant observed in **Ru-P**|TiO_2 and **Ru-H**|TiO_2 was plotted against the hydroxide ion concentration,[OH^-], to determine influence of pH. Desorption is less than 0.3 order for **Ru-P** and less than 0.2 order of [OH^-] in Ru-H, which rounds down to zeroth order (***Figure A35).*** We attribute the lack of [OH^-] dependence to the change in protonation state at the surface as we approach and surpass the pK_a values of the hydroxamate anchor (pK_{a1} = 6.5, pK_{a2} = 9.1), which would give rise to a larger electrostatic repulsion between the anionic

complex and the negatively charge surface, thereby increasing the rate of desorption. However, this electrostatic repulsion occurs because of the increased pH, which explains some small dependence on [OH^-] for desorption kinetics.

Table 2.4. Observed second-order rate constants for **Ru-P** and **Ru-H** desorption from TiO_2.

	k_{obs} / m^2 mol^{-1} s^{-1}	
pH	**Ru-P**	**Ru-H**
1	4.78(8)	$8.93(8) \times 10^1$
3	4.7(1)	$6.83(8) \times 10^1$
5	$1.15(2) \times 10^1$	$1.53(5) \times 10^2$
6	$4.33(3) \times 10^1$	$2.07(5) \times 10^2$
7	$5.2(1) \times 10^1$	$3.33(7) \times 10^2$

The increasing negative charge on the anchor coupled with the PZC of 2.5 (Figure A36) for the TiO_2 electrodes results in electrostatic repulsion of the complex from the surface, leading to this increased rate of desorption. It is clear higher deprotonation states of **Ru-P** are responsible for the significant increase in desorption rate. Thus, it is crucial to create anchors that binds as neutral weak acids to avoid electrostatic repulsion with the negatively charged surface to slow the desorption from the metal oxide surface.

For WO_3, it appears that changes in pH does not significantly alter the rate of desorption for either anchor, even when changing electrolytes at pH 1 – 4 (Figure 2.16). We propose that small changes in ionic strength when moving from the nitrate anion at pH 1 to the various protonation states of sulfate and phosphate above pH 2 do not play a significant role in the desorption of either anchor from WO_3 under acidic conditions. When comparing the rate constants for desorption of **Ru-P** to **Ru-H** on WO_3, we observe smaller differences between the two anchors. It is important to point out that **Ru-H** desorbs most slowly from WO_3 than compared to the other three combinations we tested, **Ru-P** on WO_3, or **Ru-R** on TiO_2.

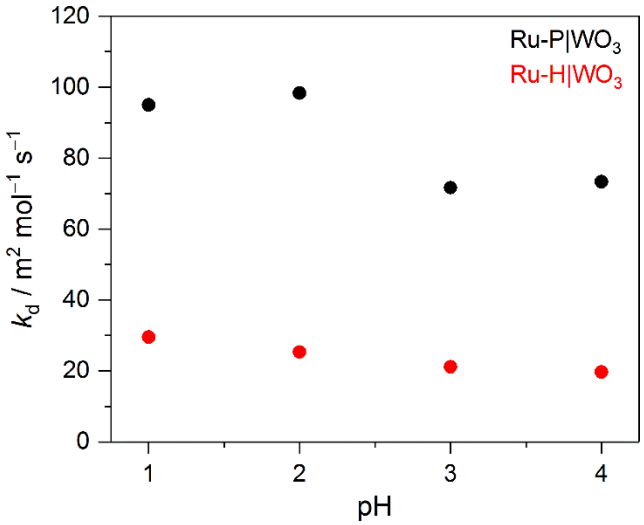

Figure 2.16. k_d vs pH of (black) **Ru-P**|WO_3 and (red) **Ru-H**|WO_3 as a function of pH from 1 – 4.

2.7 Conclusions

Through Langmuir isotherms cyclic voltammetry, we have proposed a mechanism for desorption of modified $[Ru(bpy)_3]^{2+}$ anchored by phosphonate or hydroxamate to the surface of anatase TiO_2 and monoclinic WO_3. We show that phosphonate has a stronger binding constant to WO_3 and TiO_2 under acidic conditions (pH < 5), while hydroxamate is suitable for TiO_2 at pH ≥ 5. However, kinetics governing phosphonic acid desorption from WO_3 do not complement the increased binding constant versus hydroxamic acid, as hydroxamic acid desorbs at a slower rate compared to phosphonic acid. This mismatch leads us to ultimately consider concerns about the overall stability for either anchor discussed herein for WO_3.

Phosphonic acid binding is pH-dependent and its desorption as second-order in **Ru-P**, leading to rapid desorption near neutral pH, an drawback not observed with hydroxamic acid. However, the hydroxamate anchor is prone to oxidation under an applied bias. Oxidation of the hydroxamate did not seem to cause measurable degradation via cyclic voltammetry to the dye on the surface since no significant loss in current is observed after allowing the complex to relax back to its original reduced **Ru^{II}-H** state. Finally, a sufficiently tight-binding anchor with pK_a values similar to or higher than hydroxamate-anchored molecules must be pursued to reach binding constants at least $\sim 10^5$ for the anchor to be a viable long-term option in neutral/basic conditions. Silatrane has been proposed as

an alternative to the anchors discussed in this manuscript, with the deprotected silyltriol expected to have a pK_{a1} ~10[47] and reported stability on TiO_2 up to pH 11.[48]

2.8 References

(1) Zhang, L.; Cole, J.M., Anchoring Groups for Dye-Sensitized Solar Cells, *ACS Appl. Mater. Interfaces,* **2015**, *7*, 3427 – 3455.

(2) Kilsa, K.; Mayo, E.I.; Brunschwig, B.S.; Gray, H.B.; Lewis, N.S.; Winkler, J.R., Anchoring Group and Auxiliary Ligand Effects on the Binding of Ruthenium Complexes to Nanocrystalline TiO_2 Photoelectrodes, *J. Phys. Chem. B* **2004**, *108*, 15640 – 15651.

(3) Mosconi, E.; Selloni, A.; De Angelis, F., Solvent Effects on the Adsorption Geometry and Electronic Structure of Dye-Sensitized TiO_2 : A First-Principles Investigation, *J. Phys. Chem. C* **2012**, *116*, 5932 – 5940.

(4) Bahers, T.L.; Pauporté, T.; Labat, F.; Lefevre, G.; Ciofini, I., Acetylacetone, an Interesting Anchoring Group for ZnO-Based Organic-Inorganic Hybrid Materials : A Combined Experimental and Theoretical Study, *Langmuir*, **2011**, *27*, 3442 – 3450.

(5) Brewster, T.P.; Konezny, S.J.; Sheehan, S.W.; Martini, L.A.; Schmuttenmaer, C.A.; Batista, V.; Crabtree, R.H., Hydroxamate Anchors for Improved Photoconversion in Dye-Sensitized Solar Cells, *Inorg. Chem.* **2013**, *52*, 6752 – 6764.

(6) Martini, L.A.; Moore, G.F.; Milot, R.L.; Cai, L.Z.; Sheehan, S.W.; Schmuttenmaer, C.A.; Brudvig, G.W.; Crabtree, R.H., Modular Assembly of High-Potential Zinc Porphyrin Photosensitizers Attached to TiO_2 with a Series of Anchoring Groups, *J. Phys. Chem. C* **2013**, *117*, 14526 – 14533.

(7) English, C.R.; Bishop, L.M.; Chen, J.; Hamers, R.J., Formation of Self-Assembled Monolayers of π-Conjugated Molecules on TiO_2 Surfaces by Thermal Grafting of Aryl and Benzyl Halides, *Langmuir,* **2012**, *28*, 6866 – 6876.

(8) Hirva, P.; Haukka, M., Effect of Different Anchoring Groups on the Adsorption of Photoactive Compounds on the Anatase (101) Surface, *Langmuir,* **2010***, 26*, 17075 – 17081.

(9) Cong, J.; Yang, X.; Liu, J.; Zhao, J.; Hao, Y.; Wang, Y.; Sun, L., Nitro Group as a New Anchoring Group for Organic Dyes in Dye-Sensitized Solar Cells, *Chem. Commun.,* **2012**, *48*, 6663 – 6665.

(10) Luitel, T.; Zamborini, F.P.; Covalent Modification of Photoanodes for Stable Dye-Sensitized Solar Cells, *Langmuir,* **2013**, *29*, 13582 – 13594.

(11) Li, W.; Rego, L.G.C.; Bai, F.-Q.; Wang, J.; Jia, R.; Xie, L.-M.; Zhang, H.-X., What Makes Hydroxamate a Promising Anchoring Group in Dye-Sensitized Solar Cells? Insights from Theoretical Investigation, *J. Phys. Chem. Lett*, **2014**, *5*, 3992 – 3999.

(12) Ashford, D.L.; Lapides, A.M.; Vannucci, A.K.; Hanson, K.; Torelli, D.A.; Harrison, D.P.; Templeton, J.L.; Meyer, T.J., Water Oxidation by an Electropolymerized Catalyst on Derivatized Mesoporous Metal Oxide Electrodes, *J. Am. Chem. Soc.*, **2014**, *136*, 6578 – 6581.

(13) Lapides, A.M.; Sherman, B.D.; Brennaman, M.K.; Dares, C.J.; Skinner, K.R.; Templeton, J.L.; Meyer, T.J., Synthesis, Characterization, and Water Oxidation by a Molecular Chromophore-Catalyst Assembly Prepared by Atomic Layer Deposition. The "Mummy" Strategy, *Chem. Sci.*, **2015**, *6*, 6398 – 6404.

(14) Bachinger, A.; Kickelbick, G.; Photocatalytic Stability of Organic Phosphonates and Phosphates on TiO_2 Nanoparticles, *App. Catal. A-Gen* **2011**, *409*, 122 – 132.
(15) Sheridan, M.V.; Sherman, B.D.; Coppo, R.L.; Wang, D.; Marquard, S.L.; Wee, K.-R.; Iha, N.Y.M.; Meyer, T.J., Evaluation of Chromophore and Assembly Design in Light-Driven Water Splitting with a Molecular Water Oxidation Catalyst, *ACS Energy Lett.* **2016**, *1*, 231 – 236.
(16) Queffélec, C.; Petit, M.; Janvier, P.; Knight, D.A.; Bujoli, B., Surface Modification Using Phosphonic Acid and Esters, *Chem. Rev.* **2012**, *112*, 3777 – 3807.
(17) Kirner, J.T.; Finke, R.G., Sensitization of Nanocrystalline Metal Oxides with a Phosphonate-Functionalized Perylene Diimide for Photoelectrochemical Water Oxidation with a CoO_x Catalyst, *ACS Appl. Mater. Interfaces* **2017**, *9*, 27625 – 27637.
(18) Ashford, D.L.; Brennaman, M.K.; Brown, R.J.; Keinan, S.; Concepcion, J.J.; Papanikolas, J.M.; Templeton, J.L.; Meyer, T.J.,Varying the Electronic Structure of Surface-Bound Ruthenium(II) Polypyridyl Complexes, *Inorg. Chem.* **2014**, *54*, 460 – 469.
(19) Gao, Y.; Ding, X>; Liu, J.; Wang, L.; Lu, Z.; Li, L.; Sun, L., Visible Light Driven Water Splitting in a Molecular Device with Unprecedentedly High Photocurrent Density, *J. Am. Chem. Soc.* **2013**, *135*, 4219 – 4222.
(20) Kennedy, J.H.; Frese Jr., K.W., Photooxidation of Water at α–Fe_2O_3 Electrodes, *J. Electrochem. Soc.* **1978**, *125*, 709 – 714.
(21) Klahr, B.; Gimenez, S.; Fabregat-Santiago, F.; Hamann, T.; Bisquert, J., Water Oxidation at Hematite Photoelectrodes: The Role of Surface States, *J. Am. Chem. Soc.* **2012**, *134*, 4294 – 4302.
(22) Lhermitte, C.R.; Verwer, J.G.; Bartlett, B.M., Improving the Stability and Selectivity for the Oxygen-Evolution Reaction on Semiconducting WO_3 Photoelectrodes with a Solid-State FeOOH Catalyst, *J. Mater. Chem. A*. **2016**, *4*, 2960 – 2968.
(23) Hanson, K.; Brennaman, M.K.; Luo, H.; Glasson, C.R.K.; Concepcion, J.J.; Song, W.; Meyer, T.J. Photostability of Phosphonate-Derivatized, Ru^{II} Polypyridyl Complexes on Metal Oxide Surfaces, *ACS Appl. Mater. Interfaces* **2012**, *4*, 1462 – 1469.
(24) Gusak, V.; Nkurunziza, E.; Langhammer, C.; Kasemo, B., Real-Time Adsorption and Desorption Kinetics of Dye Z907 on a Flat Mimic of Dye-Sensitized Solar Cell TiO_2 Photoelectrodes, *J. Phys. Chem. C* **2014**, *118*, 17116 – 17122.
(25) Hyde, J.T.; Hanson, K.; Vannucci, A.K.; Lapides, A.M.; Alibabaei, L.; Norris, M.R.; Meyer, T.J.; Harrison, D.P., Electrochemical Instability of Phosphonate-Derivatized, Ruthenium(III) Polypyridyl Complexes on Metal Oxide Surfaces, *ACS Appl. Mater. Interfaces* **2015**, 79554 – 9562.
(26) Wee, K.-R.; Brennaman, K.; Alibabaei, L.; Farnum, B.H.; Sherman, B.; Lapides, A.M.; Meyer, T.J., Stabilization of Ruthenium(II) Polypyridyl Chromophores on Nanoparticle Metal-Oxide Electrodes in Water by Hydrophobic PMMA Overlayers, *J. Am. Chem. Soc.* **2014**, *136*, 13514 – 13517.
(27) Norris, M.R.; Concepcion, J.J.; Glasson, C.R.K.; Fang, G.F., Lapides, A.M.; Ashford, D.L.; Templeton, J.L.; Meyer, T.J., *Inorg. Chem.*, **2013**, *52*, 12492 – 12501.
(28) Zhong, Z.; Postnikova, B.J.; Hanes, R.E.; Lunch, V.M.; Anslyn, E.V., *Chem. Eur. J.*, **2004**, *11*, 2385 – 2394.
(29) Reijenga, J.; Hoof, A.v.; Loon, A.v.; Teunissen, B., *Anal. Chem. Insights*, **2013**, *8*, 53 – 71.
(30) Wigler, P.W.; Wilson, L.E., *Anal*. Biochem. **1966**, *15*, 421 – 425.

(31) Xie, P.-H.; Hou, Y.-J.; Zhang, B.-W.; Cao, Y.; Wu, F.; Tian, W.J.; She, J.-C., *J. Che. Soc., Dalt. Trans.* **1999** (23), 4217 – 4221.
(32) Lhermitte, C.R.; Verwer, J.G.; Bartlett, B.M., *J. Mater. Chem. A* **2016**, *4*, 2960 – 2968.
(33) McNamara, W.R.; Milot, R.L.; Song, H.; Snoeberger III, R.C.; Batista, V.S.; Schmuttenmaer, C.A.; Brudvig, G.W.; Crabtree, R.H., Water-Stable, Hydroxamate Anchors for Functionalization of TiO_2 Surfaces with Ultrafast Interfacial Electron Transfer, *Energy Environ. Sci.* **2010**, *3*, 917 – 923.
(34) Auberson, Y.P.; Allgeier, H.; Bischoff, S.; Lingenhoehl, K.; Moretti, R.; Schmutz, M., 5-Phosphonomethylquinoxalinediones as Competitive NMDA Receptor Antagonists with a Preference for the Human 1A/2A Rather than 1A/2B Receptor Composition, *Bioorganic Med. Chem. Lett.* **2002**, *12*, 1099 – 1102.
(35) Mi, Q.; Zhanaidarova, A.; Brunschwig. B. S.; Gray, H. B.; Lewis, N. S. A Quantitative Assessment of the Competition between Water and Anion Oxidation at WO_3 Photoanodes in Acidic Aqueous Electrolytes. *Energy Environ. Sci.* **2012**, *5*, 5694-5700
(36) Gillaizeau-Gauthier, I.; Odobel, F.; Alebbi, M.; Argazzi, R.; Costa, E.; Bignozzi, C.A.; Qu, P., Meyer, G., Phosphonate-Based Bipyridine Dyes for Stable Photovoltaic Devices, *Inorg. Chem.* **2001**, *40*, 6073 – 6079.
(37) Panagiotou, G.D.; Petsi, T.; Bourikas, K.; Garoufalis, C.S.; Tsevis, A.; Spanos, N.; Kordulis, C.; Lycourghiotis, A., Mapping the Surface (Hydr)oxo-Groups of Titanium Oxide and its Interface with an Aqueous Solution: The State of the Art and a New Approach, *Advances in Colloid and Interface Science* **2008**, *142*, 20-42.
(38) Tompkins, F.G.; Young, D.M., The Adsorption of Gas Mixtures, *Trans. Faraday Soc.* **1951**, *47*, 88 - 96
(39) LeVan, M.D.; Vermeulen, T., Binary Lagnmuir and Freundlich Isotherms for Ideal Adsorbed Solutions *J. Phys. Chem.* **1981**, *85*, 3247 - 3250
(40) Kemball, C.; Rideal, E.K.; Guggenheim, E.A., Thermodynamics of Monolayers, *Trans. Faraday Soc.* **1948**, *44*, 948 – 954.
(41) Broughton, D.B., Adsorption Isotherms for Binary Gas Mixtures, *Ind. Eng. Chem.* **1948**, *40*, 1506 – 1508.
(42) El Wakkad, S.E.S.; Rizk, H.A., The Polytungstates and the Colloidal Nature and the Amphoteric Character of Tungstic Acid, *J. Phys. Chem.* **1957**, *61*, 494 – 497.
(43) Klepser, B.M.; Bartlett, B.M., Anchoring a Molecular Iron Catalyst to Solar-Responsive WO_3 Improves the Rate and Selectivity of Photoelectrochemical Water Oxidation, *J. Am. Chem. Soc.* **2014**, *136*, 1694 – 1697.
(44) Brennan, B.J.; Chen, J.; Rudshteyn, B.; Chaudhuri, S.; Mercado, B.Q.; Batista, V.S.; Crabtree, R.H.; Brudvig, G.W., Molecular Titanium-Hydroxamate Complexes as Models for TiO_2 Surface Binding, *Chem. Commun.* **2016**, *52*, 2972 – 2975.
(45) Goldstein, S.; Samuni, A., Oxidation Mechanism of Hydroxamic Acids Forming HNO and NO: Implications for Biological Activity. *Adv. Inorg. Chem.* **2015**, *67*, 315 – 333.
(46) Fredin, L.A.; Allison, T.C., Predicting Structures of Ru-Centered Dyes: A Computational Screening Tool, *J. Phys. Chem. A* **2016**, *120*, 2135 – 2143.
(47) Perrin, D.D. Ionization Constants of Inorganic Acids and Bases in Aqueous Solution, *Second Edition, Pergamon*, Oxford, **1982**.
(48) Materna, K.L.; Crabtree, R.H.; Brudvig, G.W., Anchoring Groups for Photocatalytic Water Oxidation on Metal Oxide Surfaces *Chem. Soc. Rev.* **2017**, *46*, 6099 – 6110.

Chapter 3

Determining the Fate of a Non-heme Iron Oxidation Catalyst Under Illumination, Oxygen, and Acid

Portions of this chapter have been published:

Esarey, S.L.; Holland, J.C.; Bartlett, B.M., *Inorg. Chem.* **2016**, *55*, 11040 – 11049

3.1 Introduction

Our group recently developed such a molecular/solid state electrode, **Fe**|WO_3, where the iron species is the nonheme iron WOC, Fe(tebppmcn)Cl_2 (tebppmcn = tetraethyl *N*,*N*′-bis(2 methylpyridyl-4-phosphonate)-*N*,*N*′ dimethylcyclohexyl- diamine), with a phosphonate anchoring group to attach the molecule to a tungsten oxide surface (Scheme 1).[1] However, the true active species and the fate of the iron complex could not be identified with confidence, as the molecule was no longer observed spectroscopically or electrochemically on the surface of WO_3 after 3 hours of operation in aqueous sulfate solution at pH 3 under low loadings (15 nmol/cm^2). Similar disappearances of other Ru-based complexes have also been observed, and decomposition is typically ascribed either to hydrolysis of the anchoring group, forcing the molecule to leave the surface, or to chromophore decomposition.[2–6] In addition, many of the aforementioned homogeneous catalysts have reported ligand dissociation of the η^1 ligands as the primary deactivation pathway.[7–10]

Scheme 3.1. Chemical structures of previously reported Fe-based WOC systems. Reprinted (adapted) with permission from Esarey, S.L.; Holland, J.C.; Bartlett, B.M., *Inorg. Chem.* **2016**, *55*, 11040 – 11049. Copyright 2016 American Chemical Society.

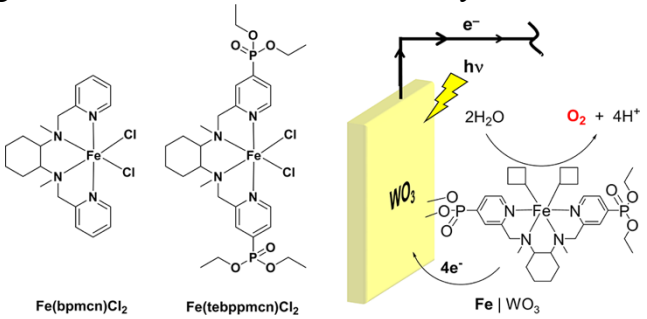

Specifically, Hong et al. have probed Fe(bqen)OTf$_2$ and Fe(bqcn)OTf$_2$ (bqen = *N*,*N*′-dimethyl-*N*,*N*′-bis(8-quinolyl) -ethane-1,2-diamine, bqcn = *N*,*N*′ dimethyl-*N*,*N*′-bis(8-quinolyl)-cyclohexane-1,2-diamine), other non-heme iron WOCs, for their decomposition during the OER using Ce^{IV}.[11] They concluded that catalyzing the OER by these iron complexes competes with ligand degradation by Ce^{IV} and that iron dissociates during catalysis under acidic conditions. Moreover, under basic conditions, the complex decomposes to an iron hydroxide species that can be used as an OER catalyst in the presence of the photoactive dye, $[Ru(bpy)_3]^{2+}$. This report focuses on the dark reactivity, with no discussion of the direct effects of light on the molecule's stability in water. Reports from other groups have also examined the identity and stability of the active species of non-heme iron, manganese, and ruthenium-based complexes during homogeneous water oxidation using Ce^{IV}, $S_2O_8^{-}$, and IO_4^{-}.[12–16] However, the stability of these complexes in acid as well as under illumination are critical in determining the long-term viability of these catalysts for molecular/solid-state PEC cells.

Outside of WOCs, many chemists have also used these non-heme iron complexes in C–H activation of organic substrates.[17–27] These examples typically rely on $NaIO_4$, H_2O_2, and PhIO as sacrificial oxidants, although there are examples of using CAN for similar reactivity. In many cases, the sacrificial oxidant is typically dissolved in a small amount of water prior to adding it to the reactants. The ideal scenario is to use dissolved O_2 as the oxidant, eliminating the need for waste-forming higher-energy oxidants. There are additional reports of photo-driven oxidation reactions using non-heme iron complexes with O_2 as the oxidant through either adding a dye [17,28,29] or through direct absorption by the iron complex itself.[30] This bodes well for chemists looking to use O_2 as a direct oxygen source for C–H activation using sunlight as the driving force instead of a wasteful, sacrificial component.

Although emphasis has been placed on attaching molecules to surfaces and understanding their desorption, relatively little attention has been paid to how light alters molecular WOCs and what the fate of these catalysts is. This is a problem of particular importance in molecule/electrode architectures. In this chapter, we present data showing that even the un-anchorable complex, Fe(bpmcn)Cl_2 (bpmcn = (1*S*,2*S*)-*N*,*N*′ dimethyl-*N,N*′-bis(2-pyridinylmethyl)cyclohexane-1,2-diamine) is inherently unstable under acidic conditions, and that free ferrous ion is released as a decomposition product. We discuss the effects of oxygen and solar illumination on this complex in acidic water and in non-aqueous conditions. Our results provide further information toward identifying the true active species on the surface of our previously reported Fe|WO_3 electrode,[1] and possibly on other WOCs with similar ligand scaffolds on highly-oxidizing photoactive semiconductor surfaces. We recognize that our findings also have an impact on the use of non-heme iron complexes in organic oxidation reactions in water, as has been proposed in the literature,[31] and we expose how O_2 reacts with iron in the presence of light even under non-aqueous conditions. For the scope of this paper, we will be focusing on the implications toward water oxidation, and will not be directly applying this to organic oxidation reactions.

3.2 Experimental Section

General considerations. $FeCl_2$, bpmcn ligand, and distilled acetonitrile were all stored in an N_2 glovebox prior to synthesis. Acetonitrile was purchased from Fisher Scientific, and was previously dried over powdered 4Å molecular sieves for 3 days prior to distilling over CaH_2 under N_2 and stored on molecular sieves in an N_2 glovebox. Anhydrous $FeCl_2$ (99.5%) was purchased from Alfa Aesar, and used without further purification. Trifluoromethanesulfonic acid (reagent grade, 98%) was purchased from Sigma Aldrich, stored under N_2, and used without further purification. For isotopic labelling experiments, $^{18}O_2$ (97 atom-% ^{18}O, 99% purity) was purchased from Sigma Aldrich. For all experiments involving water, Millipore 18.2 MΩ H_2O was used. Elemental analysis was conducted by Atlantic Microlab, Inc. UV-Vis spectroscopy was conducted using a Varian Cary 5000 spectrophotometer. FTIR spectroscopy was conducted using a ThermoScientific Nicolet 6700, and samples were prepared in dried KBr pellets. Resonance enhanced Raman spectroscopy was conducted in a quartz electron paramagnetic resonance tube and immersed in liquid nitrogen using a custom made cold-finger apparatus. The laser was a 413.1 nm continuous-

wave Kr-ion laser from a Spectra Physics. The detector used for resonance Raman spectroscopy was a Princeton Instruments TriVista Spectrometer System. NMR spectroscopy was performed with Varian MR400 spectrometer equipped with a 5 mm PFG AutoX Dual Broadband probe. Electrospray Ionization Mass Spectrometry (ESI-MS) was conducted using a Micromass AutoSpec Ultima Magnetic Sector mass spectrometer. Characterization data for the synthesized compounds are included in Appendix B as Figures B1-B5.

Synthesis of *N1,N2*-dimethyl-*N1,N2*-bis(pyridin-2-ylmethyl)cyclohexane-1,2-diamine (bpmcn). Synthesis of this compound was taken from a previously reported procedure.[19] Briefly, 1,2-dimethylcyclohexane-1,2-diamine (162 mg, 1.14 mmol) was dissolved in acetonitrile (15 mL) in a round bottom flask. Triethylamine (0.78 mL, 5.6mmol) was charged to the solution, and 2-(chloromethyl)pyridine (374 mg, 2.27 mmol) was added. The solution as brought to reflux in air overnight, then cooled to room temperature and condensed under reduced pressure. The resulting crude solid was dissolved in 30 mL of dichloromethane, and washed with 30 mL of saturated $NaHCO_3$(aq). The organic layer was extracted, and the aqueous layer was washed 2Å~ 30 mL with dichloromethane. The organic layers were collected, dried over Na_2SO_4, filtered, and condensed under reduced pressure to yield a brown oil. The crude product was purified using silica gel chromatrography with 86% EtOAc/10% MeOH/4% NH_4OH to yield the desired product as a light brown oil; yield: 155 mg (0.479 mmol, 42%). ^{1}H NMR ($CDCl_3$): δ (ppm) = 8.47 (d, 2H), 7.55 (d, 4H), 7.09 (m, 2H), 3.84 (q, 4H), 2.63 (d, 2H), 2.27 (s, 6H), 1.97 (2H), 1.75 (d, 2H), 1.27 (m, 2H), 1.14 (t, 2H). ^{13}C NMR ($CDCl_2$): δ (ppm) = 161.6, 148.7, 136.4, 122.9, 121.7, 64.7, 60.6, 36.8, 26.0, 25.9. EA $C_{20}H_{28}N_4$: (calc.) C 74.03, H 8.70, N 17.27 (found) C 73.29, H 8.69, N 16.96 ESI-MS^+: $[bpmcn+H]^+$ = 325.24 m/z^+

Synthesis of Fe(bpmcn)Cl_2. Synthesis of this compound was adapted from a previously reported procedure,[1] and was performed under N_2. Briefly, the bpmcn ligand (162 mg, 0.5 mmol) was dissolved in dry, degassed acetonitrile (5 mL). Separately, a slurry of anhydrous $FeCl_2$ (63.3 mg, 0.5 mmol) in a solution of dry, degassed acetonitrile (5 mL) was made. The bpmcn solution was added to the vigorously stirring $FeCl_2$ solution, and the resulting solution was allowed to stir overnight under N_2. The solution changed from a pale-yellow solution to an opaque yellow-orange solution over the course of the reaction. The resulting yellow suspension was filtered, washed with

acetonitrile, and dried under high vacuum. After synthesis, the powder was stored in the N_2 glovebox in the dark; yield: 172 mg (0.382 mmol, 76%). ^{1}H NMR (CD_3CN): δ (ppm) = 147.0, 108.2, 62.8, 50.6, 50.1, 20.3, 16.0, 1.3, -0.3, -0.4, -8.1, -25.8. EA $C_{20}H_{28}N_4FeCl_2$: (calc.) C 52.20, H 6.35, N 12.17, Cl 15.41 (found) C 52.40, H 6.22, N 12.25, Cl 15.31. ESI-MS$^+$: $[Fe(bpmcn)(OEt)]^+$ = 425.16 m/z$^+$

UV-Vis spectroscopy of Fe(bpmcn)Cl_2 in dry acetonitrile. The sealed quartz vial used in this experiment was previously cleaned with *aqua regia*, and dried prior to use. A 0.2 mM solution of Fe(bpmcn)Cl_2 was made in dry acetonitrile under N_2. Dry acetonitrile under N_2 was used as a baseline for the UV-Vis measurements, and Fe(bpmcn)Cl_2 solutions were prepared immediately prior to measuring the UV-Vis spectra, where the solution was placed into the quartz vial, sealed under N_2. The solution was either kept in the dark or illuminated with 1-sun using a Newport Oriel 150 W Xe lamp equipped with an AM 1.5G filter, and kept under positive N_2 pressure.

Determining stability of Fe(bpmcn)Cl_2 under illumination via ^{1}H NMR spectroscopy. A saturated solution of Fe(bpmcn)Cl_2 was made in the N_2 glovebox with dry d_3-CD_3CN. This solution was then placed in a dry J-Young tube and sealed under N_2 with a Teflon seal. The solution was monitored by ^{1}H NMR spectroscopy while illuminating the NMR tube using a Newport Oriel 150 W Xe lamp at 100 mW cm^{-2} equipped with an AM 1.5G solar filter. The solution was illuminated for a total of 24 hours under N_2.

Exposure of Fe(bpmcn)Cl_2 to O_2 and light for UV-Vis Kinetics. The sealed quartz vial used in this experiment was previously cleaned with *aqua regia*, and dried prior to use. A dilute solution (0.2 mM) of Fe(bpmcn)Cl_2 was made in dry acetonitrile previously saturated with O_2. The solution was placed in a clean sealed quartz cuvette, and exposed to 100 mW cm^{-2} of illumination at the front of the quartz cuvette using a Newport Oriel 150 W Xe lamp with an AM 1.5G filter for 24 hours. The reaction was monitored by UV-Vis spectroscopy. Dry acetonitrile saturated with O_2 was used as a baseline for the UV-Vis measurements, and Fe(bpmcn)Cl_2 solutions were prepared immediately prior to measuring the UV-Vis spectra.

Exposure of Fe(bpmcn)Cl_2 to O_2 and light at Preparative Scale. 50 mg of Fe(bpmcn)Cl_2 was dissolved in 200 mL of dry acetonitrile previously saturated with pure O_2 in a dry 250 mL Erlenmeyer flask. The solution was then placed under positive O_2 pressure with a balloon, and allowed to stir vigorously under 1.5W of illumination using a Newport Oriel 150 W Xe lamp equipped with an AM 1.5G filter. The reaction was monitored by UV-Vis spectroscopy, and took approximately two days given the experimental setup. For this experiment, the entirety of the solution was not capable of being illuminated. The resulting orange solution was condensed under reduced pressure and dried under high vacuum to yield a dark brown solid. The product was characterized without any further purification.

UV-Vis spectroscopy of Fe(bpmcn)Cl_2 in acidic water at various pH. The sealed quartz vial used in this experiment was previously cleaned with *aqua regia*. A 0.2 mM solution of Fe(bpmcn)Cl_2 was made in 0.1 M triflate adjusted to various pH with mixtures of TfOH and TfONa. The TfOH solution was prepared under an inert N_2 atmosphere and degassed prior to adding the metal complex. TfOH solutions under N_2 were used as a baseline for the UV-Vis measurements, and Fe(bpmcn)Cl_2 solutions were prepared immediately prior to measuring the UV-Vis spectra, where the solution was placed into the quartz vial, sealed under N_2. The solution UV-Vis spectra were collected until the change in absorbance over time approached zero.

Electrochemistry. A solution of 2.5mM Fe(bpmcn)Cl_2 was made under N_2 with pH 1 TfOH. This solution was placed in a 3-neck cell equipped with a glassy carbon working electrode, a Pt wire counter electrode, and a Ag/AgCl (sat'd KCl) reference electrode. The cell was sealed under N_2, and connected to a CH Instruments CHI-1000 potentiostat. A macro command was programmed to take measurements every 30 minutes starting at the original open circuit potential, and scan at 100 mV s^{-1} from –0.2 to 1.2 V vs Ag/AgCl with negative polarity. After measuring cyclic voltammograms for 4 hours, 3-equivalents of 2,2'-bipyridine were added and monitored over the same potential range at the same scan rate over 10 minutes.

Oxygen Evolution Reaction Measurements. Oxygen was quantified using a FOSSPOR fluorescence probe using two-point calibration at 20.90% and 0.00% O_2. A 12.5μM solution of Fe(bpmcn)Cl_2 was made either in degassed unbuffered water or in pH 1 TfOH under N_2. The 20-

mL solution was poured into a 3-neck round bottom flask and purged of air with N_2 until the oxygen probe read 0.00%. Data was collected for 10 minutes under N_2 prior to the injection of 0.8mL of 1.25 M CAN (4000 eq., previously degassed with N_2). Measurements were taken until the oxygen evolved had plateaued, typically at the 4-hour mark. For unbuffered solutions, the OER experiment was conducted immediately after the solution was made. For Fe(bpmcn)Cl_2 dissolved in pH 1 TfOH, the solution was allowed to stir under N_2 in the dark for 4 hours prior to the injection of CAN. For Fe(bpmcn)Cl_2 dissolved in acetonitrile under illumination and O_2, the complex was illuminated for 24 hours, then isolated under reduced pressure. A 12.5 μM solution of the final product was made in 20 mL of degassed, unbuffered Millipore water. 0.8 mL of 1.25 M CAN was then added to the solution, and the amount of oxygen in the headspace was measured by the FOSSPOR fluorescence probe. Oxygen measurements and calculations accounted for the solubility of oxygen in water and the overall headspace of the reaction vessel.

Magnetic Susceptibility Measurements. DC susceptibility was measured with a Quantum Design MPMS-XL7 SQUID equipped with an Evercool dewar. Fe(bpmcn)Cl2 pre- and post-exposure to O2 and 1.5 W of light from a Newport Oriel 150 W Xe lamp equipped with an AM 1.5G filter were used for these measurements. The sample was suspended in a known quantity of eicosane and placed in a small polycarbonate capsule. Total moment was measured from 30 K to 300 K every 5 K, and were converted to $\chi_M T$ by accounting for the susceptibility of eicosane and the diamagnetic components of the complex using Pascal's constants.

3.3 Effects of Light and O_2 on Fe(bpmcn)Cl_2

We start with the key control experiment: illuminating Fe(bpmcn)Cl_2 in dry acetonitrile under N_2 for 24 hours shows no observable structural isomerism or decomposition by ^{1}H NMR spectroscopy (Figure B6), as expected. For comparison, structural isomerism from the cis-α conformation to a cis-β conformation would result in the loss of C_2 symmetry (Scheme 3.2), and the ^{1}H NMR spectrum in that case would show twice the number of resonances— from 12 to 24. Also, the cis-β form is not active for catalyzing the OER.[32] In addition, oxidation of Fe^{2+} to Fe^{3+} can result in C–N bond cleavage by oxidative *N*-dealkylation, resulting in hemi-aminal complexes.[33] The lack of drastic chemical shifts in the ^{1}H NMR rules out this reaction under 1 sun

illumination during a 24-hour period. Finally, the UV-Vis spectrum in Figure 1 (red trace) shows that Fe(bpmcn)Cl_2 is stable under completely inert conditions in dry acetonitrile under N_2.

Scheme 3.2. **Possible Conformal Rearrangement of Fe(bpmcn)Cl_2. Reprinted (adapted) with permission from Esarey, S.L.; Holland, J.C.; Bartlett, B.M., *Inorg. Chem.* 2016, *55*, 11040 – 11049. Copyright 2016 American Chemical Society.**

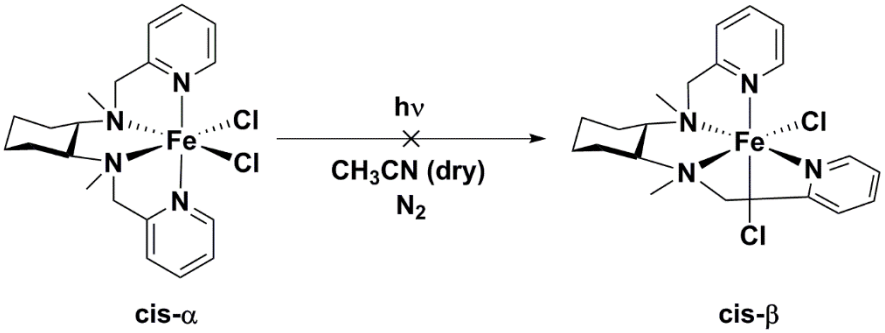

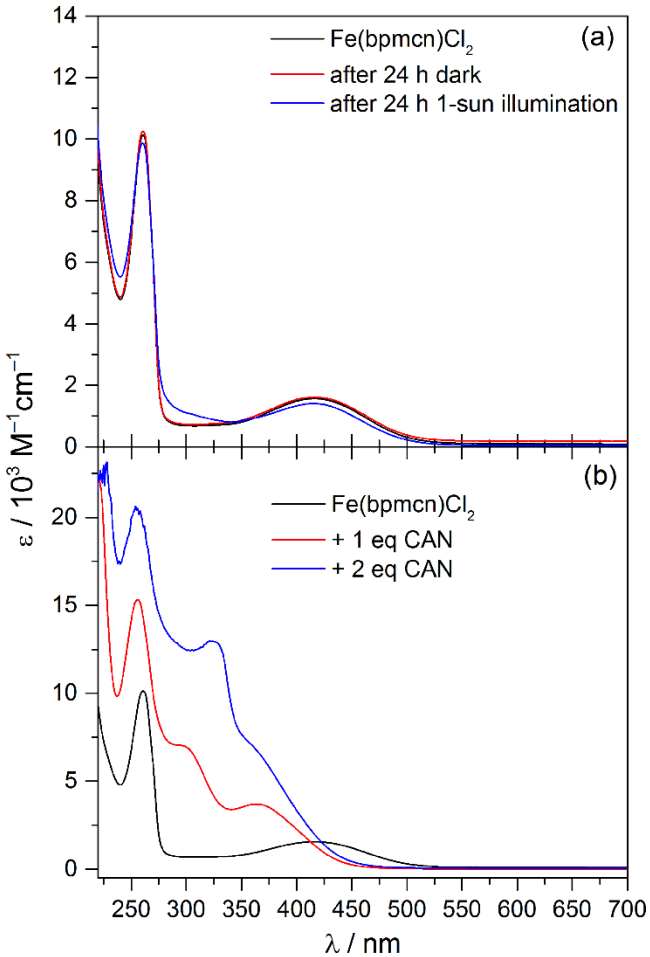

Figure 3.1. (a) UV-vis spectra of Fe(bpmcn)Cl_2 in dry, degassed acetonitrile for $t = 0$ (black) and 24 hrs (red) in the dark and under 1-sun illumination (blue). (b) UV-vis spectra of Fe(bpmcn)Cl_2 in acetonitrile with no added cerium ammonium nitrate (CAN, black), 1 equivalent of CAN (red),

and two equivalence of CAN (blue). Reprinted (adapted) with permission from Esarey, S.L.; Holland, J.C.; Bartlett, B.M., *Inorg. Chem.* **2016**, *55*, 11040 – 11049. Copyright 2016 American Chemical Society.

When exposed to 24 hours of 1-sun illumination (but still under N_2 in acetonitrile), the ^{1}H NMR spectrum is unchanged, but the UV-Vis spectrum presented as the blue trace in Figure 3.1 indicates a small, blue shift in the MLCT band over a 24-hour period. This shift in similar to what is observed in Fe^{2+} in solution as well as Fe^{2+} in enzymes as it slowly photo-oxidizes to Fe^{3+}.[34–36] However, when we add 1 and 2 equivalents of CAN oxidant to a solution of Fe(bpmcn)Cl_2 in acetonitrile, a similar blue shift and the appearance of higher energy bands appear but with molar extinction coefficients that are approximately an order of magnitude higher. Therefore, we surmise that even for illumination times ≥ 24 h, little photo-induced oxidation of Fe^{2+} in the complex is observed, which is consistent with the ^{1}H NMR spectra in Figure B6.

When exposed to a saturated solution of O_2 in dry acetonitrile in the dark, a similar Fe^{2+} oxidation is observed by UV-Vis spectroscopy, illustrated in Figure 3.2. Here, new absorption maxima appear at λ_{max} = 294, 328, and 374 nm, with an isosbestic point at 417 nm. Given that this hypsochromic shift in the UV-Vis spectrum does not occur in the absence of O_2 and light (see Figure 3.1, blue trace), we surmise that O_2 reacts with the complex in the dark, albeit slowly.

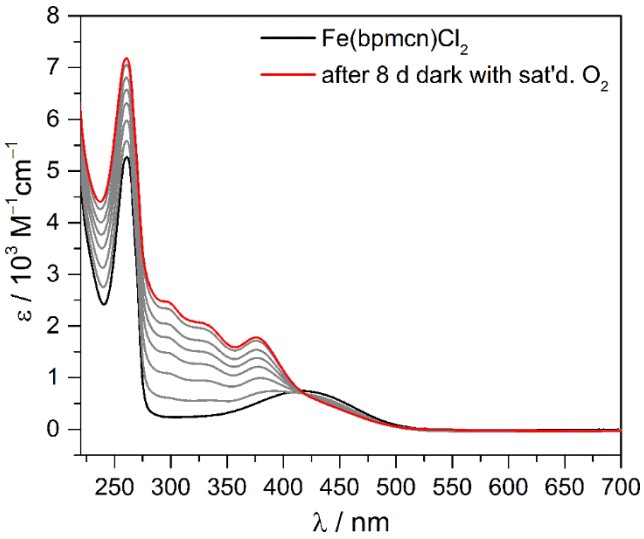

Figure 3.2.UV-vis spectra of a Fe(bpmcn)Cl_2 solution in dry acetonitrile saturated with O_2 over time in the dark. Reprinted (adapted) with permission from Esarey, S.L.; Holland, J.C.; Bartlett, B.M., *Inorg. Chem.* **2016**, *55*, 11040 – 11049. Copyright 2016 American Chemical Society.

Irradiating a dry acetonitrile solution of $Fe(bpmcn)Cl_2$ that is saturated with O_2 results in the onset of a spectral shift in the UV-Vis response, with a new peak appearing at 342 nm. Further, a clear isosbestic point at 419 nm is present in the series of spectra, indicating that only one reaction is proceeding with $Fe(bpmcn)Cl_2$. In separate experiments, spectral changes resulting from iron oxidation upon exposure to either saturated O_2 or to light do not emerge until after 1 day. In contrast, Figure 3.3 shows that when both light and O_2 are present, iron oxidation proceeds with a pseudo-first-order rate constant $k = 3.08(3) \times 10^{-3}$ min^{-1} by monitoring the absorbance at 342 nm (see inset). After 3 h, the reaction rate drops either as we approach equilibrium or as the concentration of O_2 in solution decreases. The changes in ^{1}H NMR chemical shifts and new peaks appearing near 7 ppm after exposure to both O_2 and light corroborate this reactivity (Figure B7). The faster oxidation with both O_2 and light present implies that both sunlight and O_2 react with the iron together.

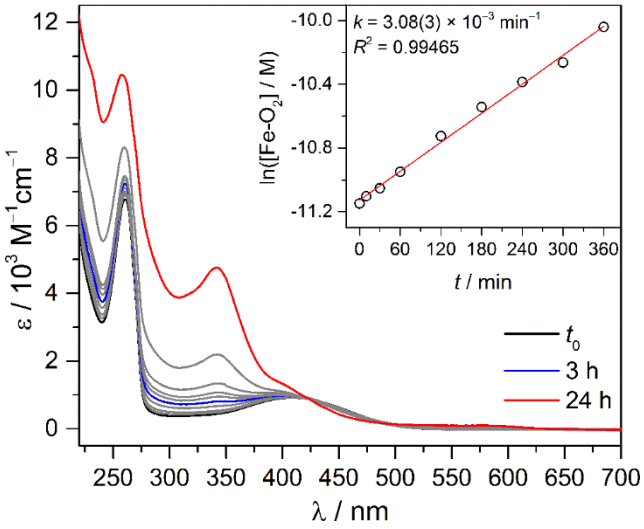

Figure 3.3. UV-vis spectra of a $Fe(bpmcn)Cl_2$ solution in dry acetonitrile under O_2 with 1-sun illumination. Reprinted (adapted) with permission from Esarey, S.L.; Holland, J.C.; Bartlett, B.M., *Inorg. Chem.* **2016**, *55*, 11040 – 11049. Copyright 2016 American Chemical Society.

When we irradiate a dry acetonitrile solution of $Fe(bpmcn)Cl_2$ under O_2 through a 550 nm cutoff filter, only the slow oxidation of the iron from the presence of O_2 is observed over the first 24 h (Figure B8). Then, preparing $Fe(bpmcn)Cl_2$ in acetonitrile with excess H_2O_2 results in an absorption maximum at 340 nm, similar what we observe with both O_2 and light (Figure B9). All three spectra in Figure B9 also show an isosbetic point at 422 nm, suggesting that reacting with H_2O_2 and with O_2 and light result in the similar products. We note that adding H_2O_2 to similarly

structured non-heme iron complexes is commonly used in organic oxidation catalysis, and these oxidations proceed through an Fe^{3+}-peroxo intermediate.[20,21,31,37] In addition, the spectra produced do not correspond to any $FeCl_2$ solvated complex in acetonitrile (Figure B10), discounting ligand dissociation as a potential decomposition pathway. Previous examples of non-heme iron complexes exposed to O_2 at low temperatures have yielded similar UV−vis spectral responses, with the emergence of a strong absorption band between 340 and 350 nm that corresponded to an Fe^{3+}–O_2^- species.[38–41] We therefore surmise that that a Fe^{3+}–O_2^- (superoxo) species is generated with O_2 and light at room temperature.

To corroborate forming a superoxo intermediate, we recorded resonance Raman spectra after illumination with 1.5 W of AM 1.5 G filtered light (Figure 3.4). Spectra were recorded on samples taken directly from solution under illumination (0.5 mM) and frozen immediately in liquid nitrogen (77 K). Cosmic rays were manually removed for clarity in Figure 3.4. A resonance-enhanced vibration near 1051 cm^{-1} appears as a shoulder to the acetonitrile solvent peak for the Fe–$^{16}O_2^-$ complex. As expected, a 56 cm^{-1} shift in this peak occurs when $^{16}O_2$ is replaced with $^{18}O_2$ under illumination, with a peak appearing at 995 cm^{-1}.[39–41] This is strong evidence for an end-on ferric superoxo species generated photochemically in dry organic solvent.

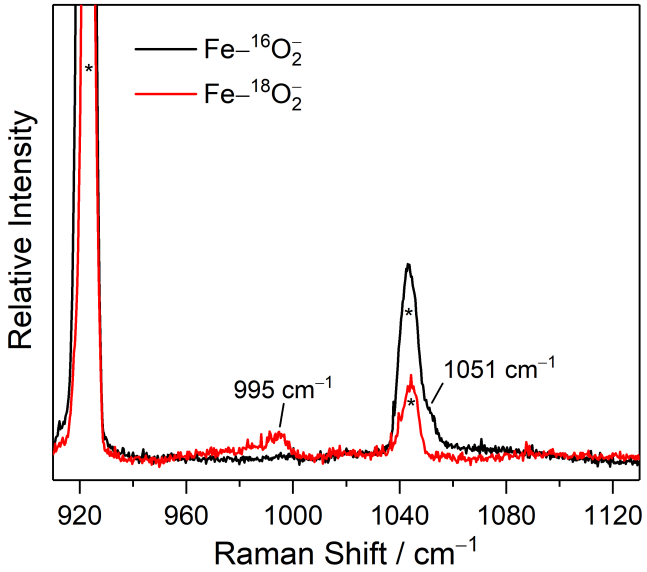

Figure 3.4. Resonance Raman spectra of (black) Fe–$^{16}O_2^-$ and (red) Fe–$^{18}O_2^-$ with a 413 nm laser at 77K. Starred peaks indicate acetonitrile solvent peaks. Reprinted (adapted) with permission from Esarey, S.L.; Holland, J.C.; Bartlett, B.M., *Inorg. Chem.* **2016**, *55*, 11040 – 11049. Copyright 2016 American Chemical Society.

The SQUID magnetometry of the product formed after exposing Fe(bpmcn)Cl_2 to O_2 and light shows a significant decrease in the $\chi_M T$ product from 3.89 cm^3 K mol^{-1} in the freshly prepared sample to 0.59 cm^3 K mol^{-1} (Figure 3.5). This result is indicative of a spin-state change from high-spin Fe^{2+} ($S = 2$) to low-spin Fe^{3+} ($S = 1/2$) that is uncoupled to the superoxo radical. Furthermore, ESI-MS^+ analysis shows fragments at $m/z^+ < 400$ from Fe(bpmcn)Cl_2 exposed to illumination under O_2 for 24 h that are consistent with amide formation on the ligand ($m/z^+ = 339.22$), and C–N bond cleavage ($m/z^+ = 262.19$) (Figure B11). When $^{16}O_2$ is replaced with $^{18}O_2$, clear isotopic labeling is observed in the mass spectra corresponding to the amide formation under soft ionizing conditions (Figure B12). Moreover, FTIR spectra of Fe–$^{16}O_2$ vs Fe–$^{18}O_2$ show this amide bond in the crude material, with a shift in the vibrational signal at 1660 cm^{-1} into the signals from the pyridine ring near 1600 cm^{-1}, consistent with the difference in reduced mass when substituting C—^{16}O with C—^{18}O in the amide bond (Figure B13).

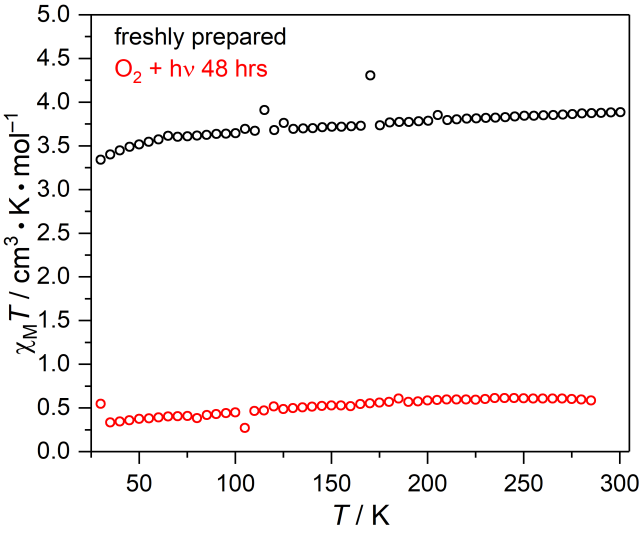

Figure 3.5. Variable-temperature magnetic susceptibility of Fe(bpmcn)Cl_2 (black) pre- and (red) post-exposure to O_2 under 1.5 W of illumination through an AM 1.5G filter. Reprinted (adapted) with permission from Esarey, S.L.; Holland, J.C.; Bartlett, B.M., *Inorg. Chem.* **2016**, *55*, 11040 – 11049. Copyright 2016 American Chemical Society.

Since these products are observed only through exciting electrons from the MCLT band absorption, reactivity must include the Fe-center of the molecular complex. Although we observe iron oxidation through varying spectroscopic techniques, the activity of the resulting complex toward the OER does not completely diminish (Figure 3.6). Rather, oxidation decreases the

turnover number (TON) by only 35% after 3 h and decreases the turnover frequency (TOF, measured by the initial rate) from 3.24 to 2.30 min^{-1}. We conclude that although O_2 binds to the iron complex, the resulting $Fe^{3+}–O_2^-$ is active for catalyzing the OER, but that it slowly oxidizes itself. It is likely that this decomposition leads to the decreased activity of the OER observed in Figure 3.6. Nevertheless, adding CAN to the $Fe^{3+}–O_2^-$ species illustrated in Scheme 3.3 releases O_2 and generates a species active for the OER.

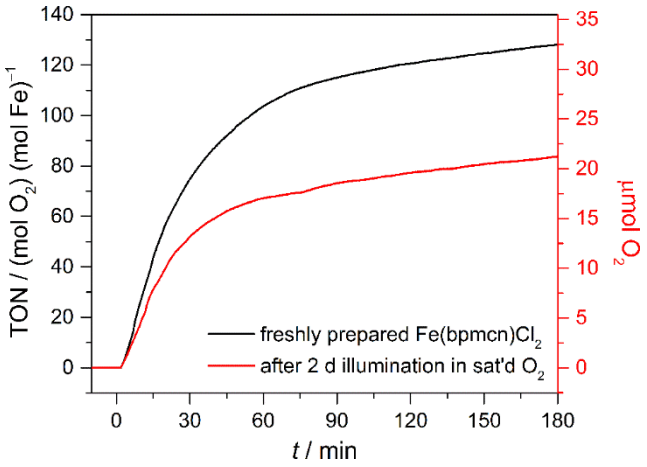

Figure 3.6.OER data collected using an O_2 probe over a solution of 12.5μM Fe(bpmcn)Cl_2 (black) in unbuffered 18.2 MΩ H_2O and (red) after exposing Fe(bpmcn)Cl_2 to O_2 and light for 2 days. 4,000 eq. of CAN were added to the solution to initiate chemical oxidation of water, and the solution pH is ~0.9 after adding excess oxidant. Reprinted (adapted) with permission from Esarey, S.L.; Holland, J.C.; Bartlett, B.M., *Inorg. Chem.* **2016**, *55*, 11040 – 11049. Copyright 2016 American Chemical Society.

Scheme 3.3. Proposed mechanism for photo-initiated binding of O_2 to Fe(bpmcn)Cl_2 in acetonitrile. Reprinted (adapted) with permission from Esarey, S.L.; Holland, J.C.; Bartlett, B.M., *Inorg. Chem.* **2016**, *55*, 11040 – 11049. Copyright 2016 American Chemical Society.

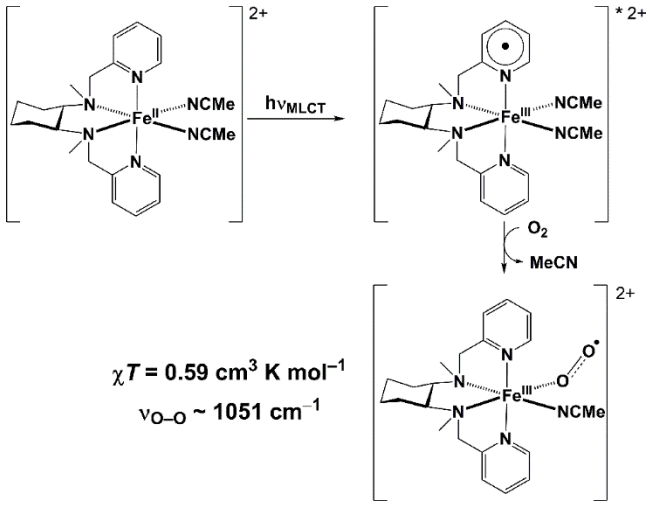

To recap, UV-Vis- and resonance-enhanced Raman spectroscopies, coupled with magnetic susceptibility measurements indicate that Fe(bpmcn)Cl2 reacts to form an end-on Fe^{3+}–O_2^- species in the presence of O_2 at room temperature; the reaction is slow in the dark. Moreover, oxidation of the iron complex solely under illumination yields no reaction. Of note, these non-heme iron complexes have been used previously with H_2O_2 for epoxidation of alkenes and for aliphatic C–H bond oxidation, and visible light coupled with O_2 has shown reactivity for non-heme $\{FeNO\}^7$ complexes in the oxidation of thiolates in organic solvents as described in the introduction. Although this background reaction occurs significantly faster than when $Fe(bpmcn)Cl_2$ is exposed to O_2 and light separately, it still requires at least 24 hours to completely react in solution and it forms ~6 times slower than acid-driven ligand dissociation. This reaction could be accelerated by adding an acid in non-aqueous media to yield an Fe-OOH intermediate for use in organic substrate oxidation. In this regard, further exploration is needed to generate photocatalysis in organic media, using similar reaction conditions as reported herein and examples from the literature such as the recently reported $\{FeNO\}^7$ complexes for thiolate oxidation.[30]

3.4 Effects of Water and Acid. Dissolving $Fe(bpmcn)Cl_2$ in D_2O with 0.1 M deuterated trifluoroacetic acid (*d*-TFA) results in the rapid disappearance of ^{1}H NMR signals downfield of 10 ppm. Instead, the 12 peaks appear between 0 and 10 ppm upon monitoring the reaction for 4 h (Figures B14 and B15), and no deshielded signals indicative of a paramagnetic center remain after 8 h. Furthermore, the final ^{1}H NMR spectra matches closely to that of free bpmcn in the presence of 1 equiv $FeCl_2$ in pH 1 *d*-TFA. In addition, the UV−vis spectra in Figure 3.7a show a decreasing MLCT band at 367 nm over 3 h in the dark in pH 1 trifluoromethanesulfonic acid (TfOH). The existence of a clear isosbestic point at 287 nm suggests that only two species contribute to the absorption spectrum the starting iron complex and a single product. A plot of $\log[Fe(bpmcn)Cl_2]$ vs t for the MLCT band at 367 nm is linear, consistent with a first-order decay with a rate constant of $k_{obs} = 19.8(2) \times 10^{-3}$ min^{-1}.

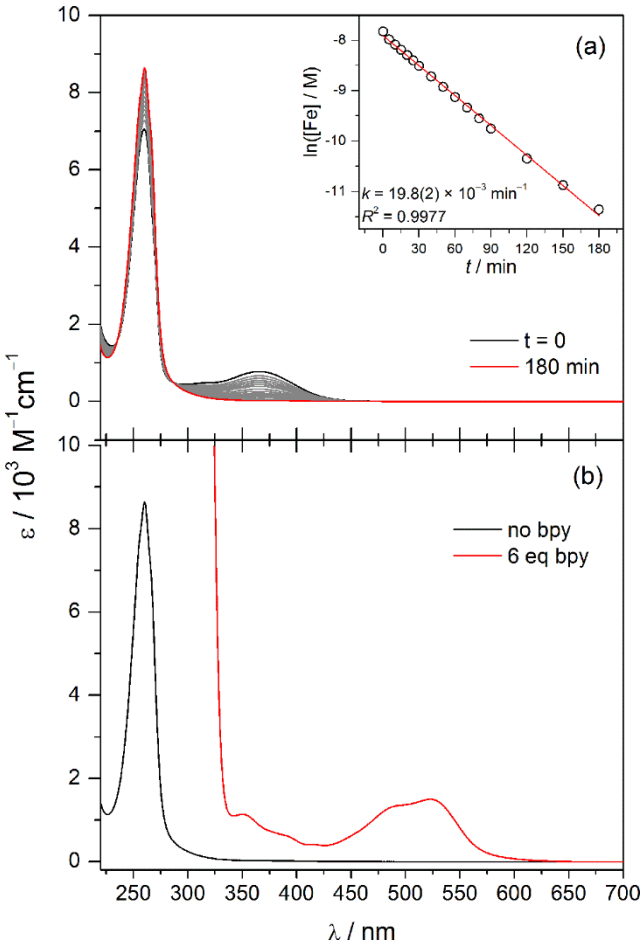

Figure 3.7. (a) $Fe(bpmcn)Cl_2$ in pH 1 TfOH over time from $t = 0$ to 3 hours. (b) UV-vis spectra of $Fe(bpmcn)Cl_2$ after 3 hours in pH 1 TfOH before and after the addition of 2,2'-bipyridine. Reprinted (adapted) with permission from Esarey, S.L.; Holland, J.C.; Bartlett, B.M., *Inorg. Chem.* **2016**, *55*, 11040 – 11049. Copyright 2016 American Chemical Society.

Disappearance of the MLCT band hints at ligand dissociation, leaving behind free bpmcn and $[Fe(H_2O)_6]^{2+}$. To demonstrate that indeed the bpmcn ligand dissociates from Fe^{2+} upon reacting with acid, we added 2,2′-bipyridine to the solution after 3 h. This reaction results in a new UV−vis spectrum in Figure 3.7b with absorbances at 349, 496, and 523 nm, all of which match closely with $[Fe(bpy)_3]^{2+}$.[42] This observation is consistent with what has been observed during the OER catalysis for similar non-heme iron complexes.[11] The increasing absorptivity of the π–π* transition at 261 nm of the ligand is consistent with the inherent higher absorptivity of the free intact bpmcn ligand, and adding 2,2′-bpyridine to a solution of $FeCl_2$ in pH 1 TfOH produced the same result as presented in Figure 3.7 (Figure B16). Moreover, cyclic voltammetry of the pH 1 TfOH solution over time shows a disappearance of the $Fe^{3+/2+}$ reversible wave having $E_{1/2} = 0.578$

V vs Ag/AgCl (0.775 V vs NHE) associated with the Fe(bpmcn)Cl_2 complex over a similar time-scale as the ^{1}H NMR and UV−vis spectroscopy experiments, illustrated in Figure 3.8a. Within 4 h, the $Fe^{3+/2+}$ wave associated with Fe(bpmcn)Cl_2 completely disappears, and a very broad wave centered at ~0.6 V vs Ag/AgCl appears. Figure 3.8b shows that after adding 3 equiv. of 2,2′-bipyridine to this solution, a new clearly distinct and reversible wave with $E_{1/2}$ = 0.886 V vs Ag/AgCl results; this wave is consistent with the $[Fe(bpy)_3]^{2+/3+}$ couple.[43] Together, these data show unequivocally that bpmcn dissociates at pH 1 through the reaction outlined in Scheme 3.4.

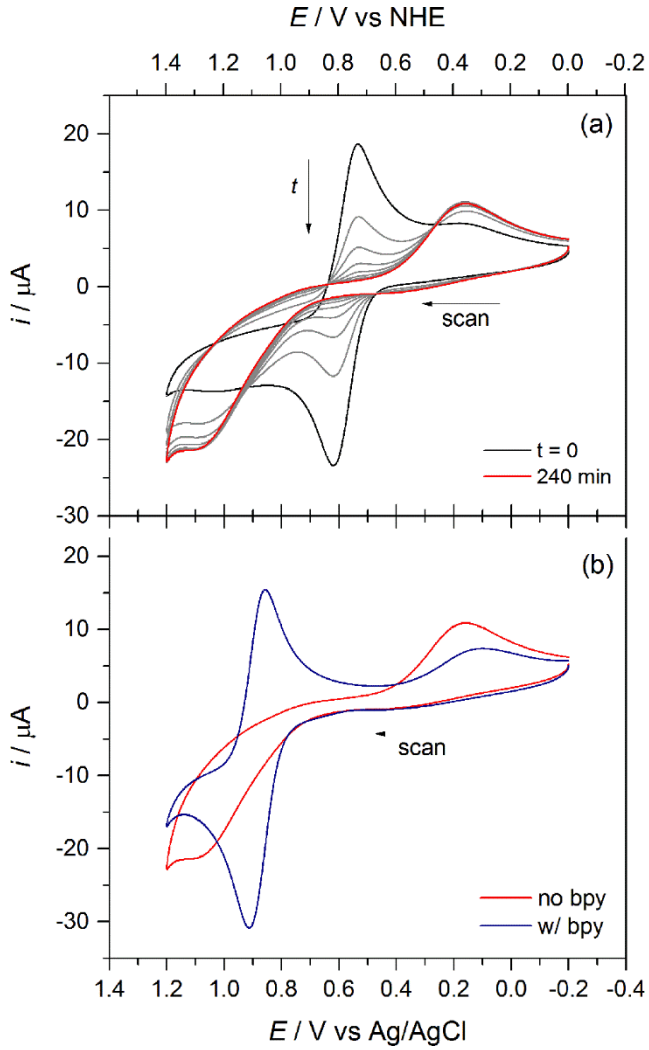

Figure 3.8. (a) Cyclic voltammetry of Fe(bpmcn)Cl_2 in pH 1 TfOH over four-hour block of time. WE: Glassy carbon, CE: Pt wire, RE: Ag/AgCl (sat'd KCl). (b) The same solution (black) after the four-hour mark, (red) prior to, and (blue) after adding 3 eq. of 2,2'-bipyridine to the solution. Reprinted (adapted) with permission from Esarey, S.L.; Holland, J.C.; Bartlett, B.M., *Inorg. Chem.* **2016**, *55*, 11040 – 11049. Copyright 2016 American Chemical Society.

Scheme 3.4. Proposed mechanism for dissociation of Fe^{3+} from bpmcn ligand under acidic conditions. Reprinted (adapted) with permission from Esarey, S.L.; Holland, J.C.; Bartlett, B.M., *Inorg. Chem.* **2016**, *55*, 11040 – 11049. Copyright 2016 American Chemical Society.

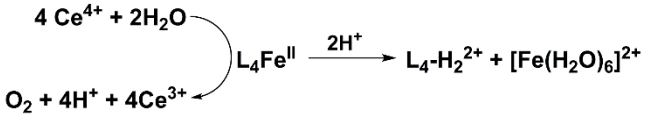

As expected, free Fe^{2+} in solution that results from adding 0.1 M acid (pH 1) yields no OER activity, illustrated in Figure 3.9. However, ligand dissociation is slower when the pH is raised to pH 3, similar to the conditions used for Fe|WO_3 electrodes in our previous work.[1] Monitoring the disappearance of the MLCT band in Figure 3.10a shows that ligand dissociation now occurs over the course of several days, not hours.

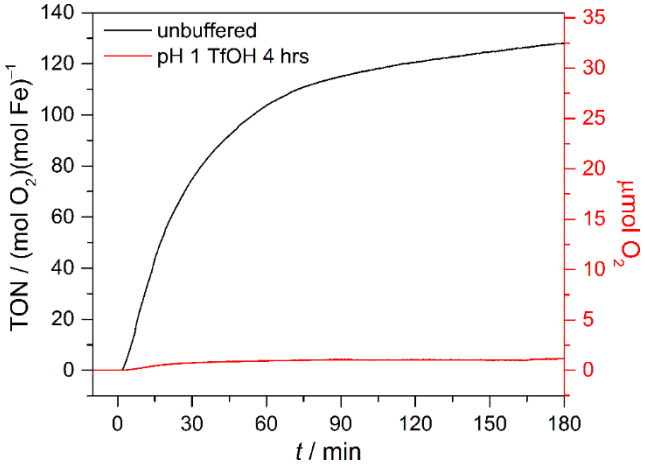

Figure 3.9. OER data collected using an O_2 probe of solution of 12.5 μM Fe(bpmcn)Cl_2 in unbuffered 18.2 MΩ H_2O (black) and in pH 1 TfOH for 4 hours (red). 4,000 eq. CAN were added to the solution to initiate dark oxidation of water, which is marked as $t = 0$ in the plot. The solution pH is ~0.9 after adding excess oxidant. Reprinted (adapted) with permission from Esarey, S.L.; Holland, J.C.; Bartlett, B.M., *Inorg. Chem.* **2016**, *55*, 11040 – 11049. Copyright 2016 American Chemical Society.

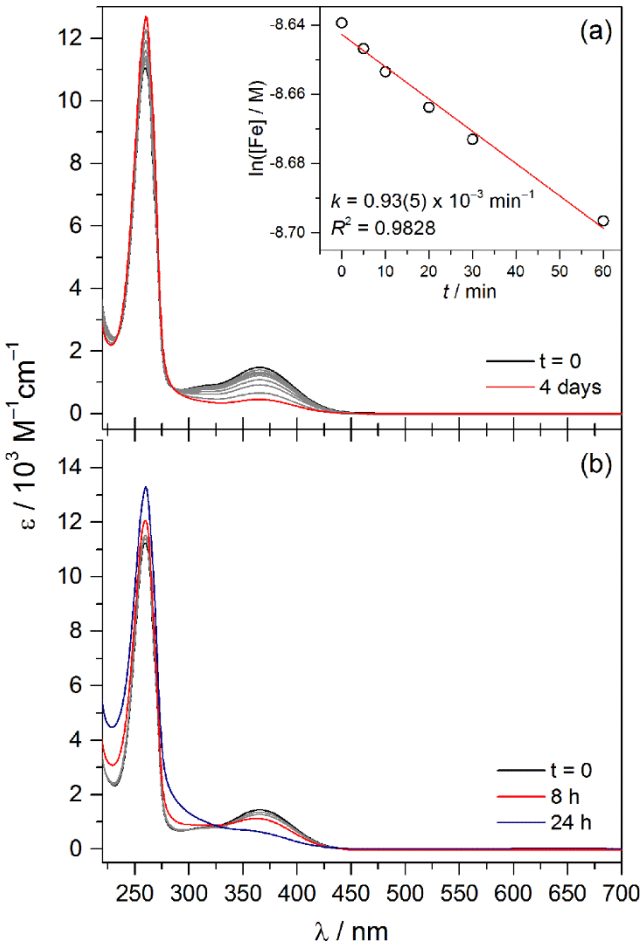

Figure 3.10. UV-vis spectra of Fe(bpmcn)Cl_2 in 0.1 M HOTf/NaOTf pH 3 under N_2 (a) in the dark over 4 days, and (b) under 1-sun illumination under N_2 at (black) t = 0, (red) 8 hours, and (blue) after 24 hours. Reprinted (adapted) with permission from Esarey, S.L.; Holland, J.C.; Bartlett, B.M., *Inorg. Chem.* **2016**, *55*, 11040 – 11049. Copyright 2016 American Chemical Society.

By plotting first-order kinetics for the first hour, the rate constant, kobs = 93(5) × 10^{-5} min^{-1} reflects this increased stability, decreasing by 2 orders of magnitude (inset of Figure 3.10a). With prolonged exposure to sunlight at pH 3, the complex also undergoes acid-driven ligand dissociation and light-driven oxidation occurring simultaneously, presented in Figure 3.10b. The absorption band growing in at ~300 nm can be attributed to the MLCT band absorption from the newly formed Fe^{3+} complex, and the decrease in intensity of the MLCT band from the Fe^{2+} complex can be attributed to ligand dissociation.

Given that Fe(bpmcn)Cl_2 does not exist as an Fe^{2+} in the proposed mechanism of water oxidation, and an increased oxidation state of the iron center would result in a substitutionally inert

intermediate, it is unlikely that ligand dissociation occurs during the OER. However, prolonged exposure of the complex to light, oxygen, and/or acid prior to using it for catalytic water oxidation will significantly reduce the activity of this catalyst due to ligand dissociation–whether as a homogeneous catalyst or when anchored to a semiconductor.

3.5 Conclusions

The complex Fe(bpmcn)Cl_2 is easily oxidized under the action of solar illumination and O_2. It is also prone to ligand dissociation at pH 1. These findings have profound implications on the stability and structural identity of non-heme iron WOCs anchored to semiconductor photoelectrodes such as WO_3. Oxygen in the dark oxidizes Fe(bpmcn)Cl_2 in non-aqueous conditions (acetonitrile) over the course of days, and under illumination, an Fe^{3+}–O_2^- complex forms within a few hours. This new complex remains active for the OER, albeit slower than the original Fe(bpmcn)Cl_2 complex. In contrast, Fe(bpmcn)Cl_2 is inherently unstable in water at pH $\leq$ 3. There, bpmcn dissociates. At pH 3, this reaction is slow, so it may not lead to direct drastic decomposition of anchorable catalysts such as Fe(tebppmcn)Cl_2 tethered to WO_3. Still, several analytically challenging questions remain, such as the possibility of ligand backbone oxidation by WO_3 and identifying the catalytically active species responsible for oxidation of the ligand backbone by WO_3. Nevertheless, this chapter introduces a new possible pathway for degradation of molecular WOCs on semiconductors or solid supports irrespective of anchoring group hydrolysis. We aim to begin a larger discussion of what is feasible in proposing the true active species of molecular/solid-state electrodes in PEC and PES cells over short and long time periods. These considerations are also quite relevant to using non-heme complexes as photocatalysts for oxidizing organic substrates.

3.6 References

(1) Klepser, B. M.; Bartlett, B. M. Anchoring a Molecular Iron Catalyst to Solar-Responsive WO3 Improves the Rate and Selectivity of Photoelectrochemical Water Oxidation. *J. Am. Chem. Soc*. **2014**, *136*, 1694.

(2) Ashford, D. L.; Lapides, A. M., Vannucci, A. K.; Hanson, K.; Torelli, D. A.; Harrison, D. P.; Templeton, J. L.; Meyer, T. J. Water Oxidation by an Electropolymerized Catalyst on Derivatized Mesoporous Metal Oxide Electrodes. *J. Am. Chem. Soc.* **2014**, *136*, 6578.

(3) Lapides, A. M.; Ashford, D. L.; Hanson, K.; Torelli, D. A.; Templeton, J. L.; Meyer, T. J. Stabilization of a Ruthenium(II) Polypyridyl Dye on Nanocrystalline TiO_2 by an Electropolymerized Overlayer. *J. Am. Chem. Soc*. **2013**, *135*, 15450.
(4) Lapides, A. M.; Sherman, B. D.; Brennaman, M. K.; Dares, C. J.; Skinner, K. R.; Templeton, J. L.; Meyer, T. J. Synthesis, Characterization, and Water Oxidation by a Molecular Chromophore-Catalyst Assembly Prepared by Atomic Layer Deposition. The "Mummy" Strategy. *Chem. Sci*. **2015**, *6*, 6398.
(5) Song, W. J.; Vannucci, A. K.; Farnum, B. H.; Lapides, A. M.; Brennaman, M. K.; Kalanyan, B.; Alibabaei, L.; Concepcion, J. J.; Losego, M. D.; Parsons, G. N.; Meyer, T. J. Visible Light Driven Benzyl Alcohol Dehydrogenation in a Dye-Sensitized Photoelectrosynthesis Cell. *J. Am. Chem. Soc.* **2014**, *136*, 9773.
(6) Ashford, D. L.; Brennaman, M. K.; Brown, R. J.; Keinan, S.; Concepcion, J. J.; Papanikolas, J. M.; Templeton, J. L.; Meyer, T. J. Varying the Electronic Structure of Surface-Bound Ruthenium(II) Polypyridyl Complexes. *Inorg. Chem*. **2015**, *54*, 460.
(7) Duan, L. L.; Fischer, A.; Xu, Y. H.; Sun, L. C. Isolated Seven- Coordinate with [HOHOH]—Ligand as an Intermediate for Catalytic Water Oxidation. *J. Am. Chem. Soc*. **2009**, *131*, 10397.
(8) Duan, L.; Bozoglian, F. ; Mandal, S.; Stewart, B.; Privalov, T.; Llobet, A.; Sun, L. A Molecular Ruthenium Catalyst with Water- Oxidation Activity Comparable to That of Photosystem II. *Nature Chem*. **2012**, *4*, 418.
(9) Jiang, Y.; Li, F.; Zhang, B. B.; Li, X. N.; Wang, X. H.; Huang, F.; Sun, L. C. Promoting The Activity of Catalysts for the Oxidation of Water with Bridged Dinuclear Ruthenium Complexes. *Angew. Chem. Int. Ed*. **2013**, *52*, 3398
(10) Gao, Y.; Ding, X.; Liu, J. H.; Wang, L.; Lu, Z. K.; Li, L.; Sun, L. C. Visible Light Driven Water Splitting in a Molecular Device with Unprecedentedly High Photocurrent Density. *J. Am. Chem. Soc*. **2013**, *135*, 4219.
(11) Hong, D.; Mandal, S.; Yamada, Y.; Lee, Y.-M.; Nam, W.; Llobet, A.; Fukuzumi, S. Water Oxidation Catalysis with Nonheme Iron Complexes Under Acidic and Basic Conditions: Homogeneous or Heterogeneous? *Inorg. Chem*. **2013**, *52*, 9522.
(12) Parent, A.R.; Nakazono, T.; Lin, S.; Utsunomiya, S.; Sakai, K., Mechanism of Water Oxidation by Non-Heme Iron Catalysts when Driven with Sodium Periodate. *Dalton Trans*., **2014**, *43*, 12501.
(13) Ma, L.; Wang, Q.; Man, W.-L.; Kwong, H.-K.; Ko, C.-C.; Lau, T.-C., Cerium(IV)-Driven Water Oxidation Catalyzed by a Manganese(V)-Nitrido Complex. *Angew. Chem. Int. Ed*., **2015**, *54*, 5246.
(14) Liu, Y.; Ng, S.-M.; Yiu, S.-M.; Lam, W.W.Y.; Wei, X.-G.; Lau, K.-C.; Lau, T.-C., Catalytic Water Oxidation By Ruthenium(II) Quaterpyridine (Qpy) Complexes: Evidence for Ruthenium(III) Qpy-N,N″-Dioxide as the Real Catalysts. *Angew. Chem. Int. Ed*., **2014**, *53*, 14468.
(15) Chen, G.; Chen, L.; Ng, S.-M.; Man, W.-L.; Lau, T.-C. Chemical and Visible-Light-Driven Water Oxidation by Iron Complexes at pH 7-9: Evidence for Dual-Active Intermediates in Iron-Catalyzed Water Oxidation. *Angew. Chem. Int. Ed*., **2013**, *52*, 1789.
(16) Wu, X.; Li, F.; Zhang, B.; Sun, L., Molecular Complexes in Water Oxidation: Pre-Catalysts or Real Catalysts. *J. Photoch. Photobio. C*, **2015**, *25*, 71.

(17) Mühldorf, B.; Wolf, R. C—H Photooxygenation of Alkyl Benzenes Catalyzed by Riboflavin Tetraacetate and a Non-Heme Iron Catalyst. *Angew. Chem. Int. Ed*. **2016**, *55*, 427.
(18) Costas, M.; A. K. Tipton, A. K.; Chen, K.; Jo, D.-H.; Que Jr., L. Modeling Rieske Dioxygenases: The First Example of Iron-Catalyzed Asymmetric Cis-Dihydroxylation of Olefins. *J. Am. Chem. Soc*. **2001**, *123*, 6722.
(19) Costas, M.; Que, Jr., L. Ligand Topology Tuning of Iron-Catalyzed Hydrocarbon Oxidations. *Angew. Chem. Int. Ed*. **2002**, *41*, 2179.
(20) Cussó, O.; Garcia-Bosch, I.; Ribas, X.; Lloret-Fillol, J.; Costas, M. Asymmetric Epoxidation with H_2O_2 by Manipulating the Electronic Properties of Non-heme Iron Catalysts. *J. Am. Chem. Soc*. **2013**, *135*, 14871.
(21) Mas-Ballesté, R.; Costas, M.; van den Berg, T.; Que, Jr. L. Ligand Topology Effects on Olefin Oxidations by Bio-Inspired [Fe^{II} (N_2Py_2)] catalysts. *Chem. Eur. J*. **2006**, *12*, 7489.
(22) Prat, I.; Mathieson, J. S.; Guell, M.; Ribas, X.; Luis, J. M.; Cronin, L.; Costas, M. Observation of Fe(V)=O using Variable Temperature Mass Spectrometry and its Enzymelike C–H and C—C Oxidation Reactions. *Nature Chem*. **2011**, *3*, 788.
(23) Bigi, M. A.; Reed, S. A.; White, C. Diverting Non-Haem Iron Catalysed Aliphatic C–H Hydroxylations Towards Desaturations. *Nature Chem*. **2011**, *3*, 216.
(24) Bigi, M. A.; Reed, S. A.; White, M. C. Directed Metal (Oxo) Aliphatic C−H Hydroxylations: Overriding Substrate Bias. *J. Am. Chem. Soc*. **2012**, *134*, 9721.
(25) Gormisky, P. E.; White, C. Catalyst-Controlled Aliphatic C−H Oxidations with a Predictive Model for Site-Selectivity. *J. Am. Chem. Soc*. **2013**, *135*, 14052.
(26) White, M. C. Adding Aliphatic C-H Bond Oxidations to Synthesis. *Science* **2012**, *335*, 807.
(27) Nam, W.; Lee, Y.-M.; Fukuzumi, S. Tuning Reactivity and Mechanism in Oxidation Reactions by Mononuclear Nonheme Iron(IV)-Oxo Complexes. *Acc. Chem. Res*. **2014**, *47*, 1146.
(28) Kotani, H.; Suenobu, T.; Lee, Y.-M.; Nam, W.; Fukuzumi, S. Photocatalytic Generation of a Non-Heme Oxoiron(IV) Complex with Water as an Oxygen Source. *J. Am. Chem. Soc*. **2011**, *133*, 3249.
(29) Tsudaka, T.; Ohkubo, K.; Fukuzumi, S, Photocatalytic Oxidation of Iron(II) Complexes by Dioxygen using 9-Mesityl-10-methylacridinium Ions. *Chem. Commun*. **2016**, *52*, 6178.
(30) McQuilken, A. C.; Matsumura, H.; Dürr, M.; Confer, A. M.; Sheckelton, J. P.; Siegler, M. A.; McQueen, T. M.; Ivanovic-Burmazovic, I.; Moënne-Loccoz, P.; Goldberg, D. P. Photoinitiated Reactivity of a Thiolate-Ligated, Spin-Crossover Nonheme $\{FeNO\}^7$ Complex with Dioxygen. *J. Am. Chem. Soc*. **2016**, *138*, 3107.
(31) Canals, M.; Gonzalez-Olmos, R.; Costas, M.; Company, A. Robust Iron Coordination Complexes with N-Based Neutral Ligands as Efficient Fenton-Like Catalysts at Neutral pH. *Environ. Sci. Technol*. **2013**, *47*, 9918.
(32) Codolá, Z.; Gómez, L. ; Kleespies, S. T.; Que Jr., L. ; Costas, M.; Lloret-Fillol, J. Evidence for an Oxygen Evolving Iron–Oxo–Cerium Intermediate in Iron-Catalysed Water Oxidation. *Nature Commun*. **2015**, *6*, 1.
(33) Grau, M.; Kyriacou, A.; Martinez, F. C.; de Wispelaere, I. M.; White, A. J. P.; Britovsek, G. J. P. Unraveling the Origins of Catalyst Degradation in Non-Heme Iron-Based Alkane Oxidation. *Dalton Trans*. **2014**, *43*, 17108.

(34) Chao, Z.; YingPing, H.; YanFen, F.; LiRong, J.; LiMing, L.; Lau, K. T. Visible Light-Induced Degradation of Organic Pollutants using Fe(II) Supported on Silica Gel as an Effective Catalyst. *Chinese Sci. Bull*. **2008**, *53*, 1497.
(35) Honda, J.; Teratani, Y.; Kobayashi, Y.; Nagamune, T.; Sasabe, H.; Hirata, A.; Ambe, F.; Endo, I. Light-induced Oxidation of Iron Atoms in a Photosensitive Nitrile Hydratase. *FEBS Lett*. **1992**, *305*, 177.
(36) Caiazza, N. C.; Lies, D. P.; Newman, D. K. Phototrophic Fe(II) Oxidation Promotes Organic Carbon Acquisition by Rhodobacter capsulatus SB1003. *App. Environ. Microb*. **2007**, *73*, 6150.
(37) Makhlynets, O. V.; Rybak-Akimova, E. V. Aromatic Hydroxylation at a Non-Heme Iron Center: Observed Intermediates and Insights into the Nature of The Active Species. *Chem. Eur. J*. **2010**, *16*, 13995.
(38) Mukherjee, A.; Carnswick, M.A.; Chakrabarti, M.; Paine, T.K.; Fujisawa, K.; Münck, E.; Que Jr., L., Oxygen Activation at Mononuclear Nonheme Iron Centers: A Superoxo Perspective. *Inorg. Chem*., **2010**, *49*, 3618.
(39) Proshlyakov, D. A.; Henshaw, T. F.; Monterosso, G. R.; Ryle, M. J.; Hausinger, R. P. Direct Detection of Oxygen Intermediates in the Non-Heme Fe Enzyme Taurine/R-Ketoglutarate Dioxygenase. *J. Am. Chem. Soc*. **2004**, *126*, 1022.
(40) Roelfes, G.; Vrajmasu, V.; Chen, K.; Ho, R. Y. N.; Rohde, J.-U.; Zondervan, C.; Crois, R. M. I.; Schudde, E. P.; Lutz, M.; Spek, A. L.; Hage, R.; Feringa, B. L.; Munck, E.; Que, Jr., L. End-on and Side-on Peroxo Derivatives of Non-Heme Iron Complexes with Pentadentate Ligands: Models for Putative Intermediates in Biological Iron/Dioxygen Chemistry. *Inorg. Chem*. **2003**, *42*, 2639.
(41) Oddon, F.; Chiba, Y.; Nakazawa, J.; Ohta, T.; Ogura, T.; Hikichi, S., Characterization of Mononuclear Non-Heme Iron(III)-Superoxo Complex with a Five-Azole Ligand Set. *Angew. Chem. Int. Ed*., **2015**, *54*, 7336.
(42) Mori, K.; Kagohara, K.; Yamashita, H. Synthesis of Tris(2,2'-Bipyridine)Iron(II) Complexes in Zeolite Y Cages: Influence of Exchanged Alkali Metal Cations on Physicochemical Properties and Catalytic Activity. *J. Phys. Chem. C* **2008**, *112*, 2953.
(43) Carter, M. T.; Rodriguez, M.; Bard, A. Voltammetric Studies of the Interaction of Metal Chelates with DNA. 2. Tris-Chelated Complexes of Cobalt(III) and Iron(II) with 1,10-Phenanthroline and 2,2'-Bipyridine. *J. Am. Chem. Soc*. **1989**, *111*, 8901.

Chapter 4

Using Molecular Fe(bpmcn)Cl_2 for Controlled Growth of an Amorphous FeOOH Electrocatalyst for Water Oxidation

4.1 Introduction

In addition to the reactivity of Fe(bpmcn)Cl_2 under acidic conditions and exposure to visible light and oxygen, we also wanted to probe the stability of this complex toward neutral and basic conditions. It has been reported in the literature that non-heme iron complexes with similar structure to Fe(bpmcn)Cl_2 undergo decomposition starting at pH 9 during water oxidation with sodium persulfate as a sacrificial oxidant in water.[1] The proposed decomposition pathway was the dissociation of Fe^{3+} from the ligand in the presence of OH^- to form amorphous FeOOH, a known electrocatalyst for the oxygen evolution reaction that is stable up to pH 14. However, the morphology of this solid material was not discussed. A key aspect to electrocatalyst and solid-state synthesis is influence over morphology, which allows for some control over surface area, hole concentration at the surface, and ultimately high current generation per unit surface area of an electrode. In fact, some reports on FeOOH synthesis involve $FeCl_2$ and small L-type ligands such as *N*-methylimidazole, NH_3, poly(vinyl pyrrolidone), and others,[2,3,4] while others have used ferrocene,[5] and some only use $FeCl_2$ under typical buffered conditions at or above pH 4.[6–9] The importance of growing FeOOH electrcatalyst with control over deposition that yield high photocurrents ($j \geq 10$ mA cm^{-2}) at low overpotentials ($\eta_{OER} \leq 600$ mV) is to ultimately coat visible-light absorbing semiconductor electrodes such as WO_3 or $BiVO_4$ that that inherently require high overpotentials, have low selectivity for water oxidation, or have poor stability under neutral to basic conditions. This coating of FeOOH would be used to increase the properties of the photoanode discussed above, particularly at higher pH.[6,9]

Although some FeOOH electrodes in the literature achieve 10 mA cm^{-2} at pH 14 with overpotentials below 600 mV, there has not been much investigation in the role of the ligand on morphology of the FeOOH electrocatalyst and, thus, current generated from electrocatalytic OER. However, growth mechanisms that have generated the lowest overpotentials for OER have

involved organic ligands, particularly Cp (X-type η^3 ligand) and amine-based L-type ligands. We therefore want to probe how an L-type η^4 ligand such as the bpmcn ligand in $[Fe(bpmcn)(H_2O)_2]^{2+}$ can control morphology of FeOOH growth as compared to $[Fe(H_2O)_6]^{2+}$ under basic pH. We explore both the morphology of FeOOH growth in solution as a function of pH, and determine the morphology of FeOOH from the $Fe(bpmcn)Cl_2$ complex via electrochemical deposition at pH 13. The structure of $Fe(bpmcn)Cl_2$ is shown in Scheme 4.1.

Scheme 4.1. Chemical structure of $Fe(bpmcn)Cl_2$ with C_{2V} symmetry.

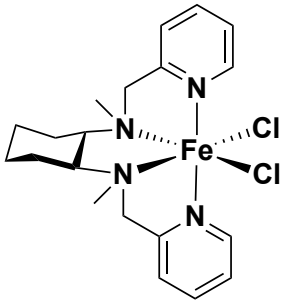

$Fe(bpmcn)Cl_2$

4.2 Experimental Section

General considerations. Iron(II) chloride tetrahydrate (99.99% trace metals basis) and sodium hydroxide were purchased through Sigma Aldrich. $FeCl_2 \cdot 4H_2O$ was stored under N_2 prior to use. $Fe(bpmcn)Cl_2$ was synthesized as described in Chapter 3 of this thesis, and as found in the literature.[10,11] Hydrochloric acid (Certified ACS Plus, 36.5 – 38.0% (w/w)) was purchased through Fisher Scientific. 18.2 MΩ water was used for all experiments in this chapter to prevent any contamination. pH was measured with a Fisher Scientific™ accumet™ AE150 pH Benchtop Meter. Scanning electron microscopy images were collected on a JEOL-7800FLV scanning electron microscope equipped with an Oxford X-Man^N silicon drift detector (Oxford Instruments) and a (Oxford NordlysMax2) detector. Fluorine-doped tin oxide coated glass slides were cut into 1 cm x 3 cm rectangles, then scrubbed by hand with Fisherbrand Sparkleen® detergent before being sonicated in 18.2 MΩ H_2O, ethanol, acetone, and hexanes for 15 minutes each. The slides were then washed with hexanes and dried over a stream of N_2 prior to electrochemical deposition. Slides were stored covered in plastic petri dishes to prevent dust build-up. Powder X-ray Diffractograms were collected on a Bruker D8 Advance diffractometer equipped with a graphite monochromator, a Lynx-Eye detector, and parallel beam optics using Cu Kα radiation (λ =

1.54184 Å). Raman spectroscopy was collected on a Reinshaw inVia spectrometer with a 532 nm laser and RenCam CCD detector.

a-FeOOH precipitation from NaOH in air. 0.01 M solutions of either $[Fe(H_2O)_6]^{2+}$ or $[Fe(bpmcn)(H_2O)]^{2+}$ were prepared at a scale of 10.0 mL, and pH was adjusted to the appropriate level with small additions of either HCl or NaOH (1 M or 6 M). It is important to note that the solubility of $Fe(bpmcn)Cl_2$ in water does not allow for a higher concentration at room temperature and increased ionic strength of the solution results in lower solubility of the complex. Solutions were then allowed to sit in the dark for 3 days and observed by eye to test for precipitation. Any solutions that contained particulates that could be collected were analyzed with a scanning electron microscope and PXRD.

OER activity of a-FeOOH powders precipitated from base. Powders collected from the precipitation at pH 11 and pH 13 were suspended in a carbon-based (CB) slurry. Briefly, 5 mg of a-FeOOH was added to a vigorously stirring solution of 1.0 mL THF containing 1 mg of acetylene carbon black and 11.25 µL Nafion® 117 solution (5% in low aliphatic alcohols and water). The solution was then sonicated for 20 minutes before drop-casting 50µL onto a clean FTO substrate masked to expose 1 cm^2 with electrical tape. The film was allowed to dry in air overnight, then films were exposed to a pH 14 NaOH solution with the a-FeOOH/CB film as the working electrode, a Pt disk as the counter electrode, and Ag/AgCl as the reference electrode. LSVs were conducted at 5 mV s^{-1} starting at OCP. Given the brief exposure to the solution, we do not believe the Ag/AgCl was negatively affected by the high pH.

a-FeOOH electrodeposition from $Fe(bpmcn)Cl_2$ precursor. 25 mL of a 0.01 M $Fe(bpmcn)Cl_2$ solution was prepared with 0.1 M NH_4Cl as an electrolyte solution. It is important to note that the solubility of $Fe(bpmcn)Cl_2$ in water does not allow for a higher concentration at room temperature, and increased ionic strength of the solution results in lower solubility of the complex. This solution was degassed with N_2 (for at least 15 minutes) prior to the addition of $Fe(bpmcn)Cl_2$, then degassed for an additional 30 minutes to thoroughly remove oxygen and prevent FeOOH precipitation in solution. The solution was then brought to pH 13 with 1 M NaOH while maintaining a stream of N_2 over the solution at which point the solution turns an opaque orange. A cleaned FTO film

masked to expose 1 cm^2 of area with electrical tape, and clipped with alligator clips was placed in the solution as the working electrode, with a Pt disk as the counter electrode and a Hg/HgO (1 M NaOH) reference electrode. A 0.4 V vs Hg/HgO bias was applied to the working electrode until sufficient charge was passed (0.025 – 0.12 C). During electrodeposition, the solution was slowly purged with N_2 via a needle to prevent FeOOH formation in the solution, but not to perturb the solution to a degree that would cause stirring of the solution. Once the electrode was removed from solution, the film was immediately washed thoroughly with 18.2 MΩ H_2O, then ethanol to remove any unreacted $Fe(bpmcn)(OH)_2$ or unbound FeOOH. The film was dried over a stream of N_2 prior to storage.

Electrocatalytic Water Oxidation with FeOOH films. Films of FeOOH|FTO were submerged in pH 14 NaOH with a Pt disk counter electrode and a Hg/HgO reference electrode. Linear sweep voltammetry (LSV) scans were performed starting from open circuit potential (OCP) and scanned toward positive potentials at a rate of 5 mV s^{-1}. Electrochemical potential was adjusted to RHE scale with Eqn. 4.1.

$$E(\mathrm{V})_{\mathrm{RHE}} = E(\mathrm{V})_{\mathrm{Hg/HgO}} + 0.098\ \mathrm{V} + 0.059\mathrm{pH} \qquad \text{Eqn. 4.1}$$

Any scans that were treated with *i*R compensation were adjusted using the measured resistance of the FTO slide used, which was typically ~26 Ω.

4.3 Morphology and Electrochemical Activity of FeOOH from $Fe(bpmcn)Cl_2$ in Solution

Precipitation of 0.01 M $Fe(bpmcn)Cl_2$ from aqueous conditions under air was observed to begin near pH 5, but did not produce enough powder for characterization until pH 11, or closer to stoichiometric amounts of $[OH^-]$ were present in solution. However, enough particulates could be gathered for solutions at pH 11 and pH 13 NaOH with 0.01 M $Fe(bpmcn)Cl_2$. Powder X-ray diffraction shows these are mostly amorphous materials, with broad diffraction peaks near 28 º-2θ and 32 º-2θ, consistent with the production of an amorphous iron oxide material with poor crystallinity similar in structure to goethite (α-FeOOH, Figure 4.1).[2]

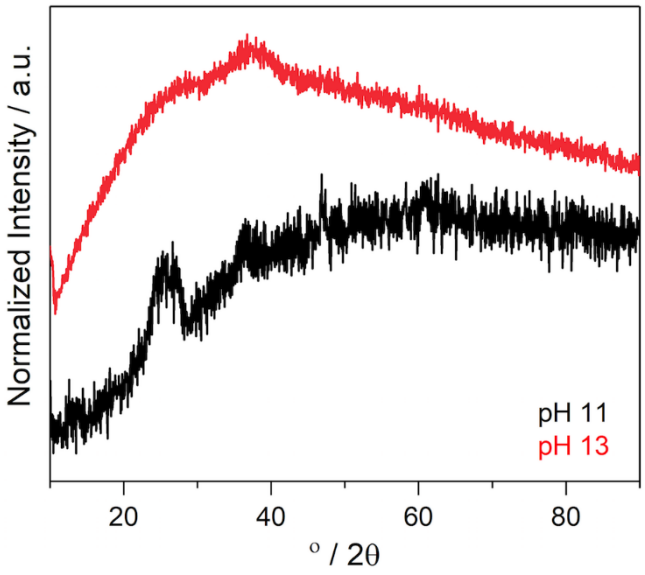

Figure 4.1. Powder X-ray diffractograms of Fe(bpmcn)Cl_2 precipitated as a-FeOOH from (black) pH 11 and (red) pH 13 solutions.

To confirm the morphology of this material and the chemical composition, we examined these powders under scanning electron microscopy (SEM) and qualitatively analyzed the chemical composition by Energy-Dispersive X-Ray Spectroscopy (EDS). As shown below in Figure 4.2, SEM images show aggregation of nanoparticles, and show particles with urchin-like morphology, stemming from an initial nucleation site in the center and continuing with anisotropic growth of the material from the central nucleation site. On the other hand, particles precipitated from Fe(bpmcn)Cl_2 at pH 13 and $FeCl_2$ at pH 11 and 13 are aggregations of smaller particles with no clear anisotropic morphology. This implies that Fe(bpmcn)Cl_2 in pH 11 solution exposed to air may produce particles at a slow enough rate that influence over morphology is observed. In order to examine the true size of the aggregated particles from precipitation of $FeCl_2$ precipitate from pH 11, and Fe(bpmcn)Cl_2 and $FeCl_2$ at pH 13, higher resolution SEM images will be needed. Based on measurements made with ImageJ software, the average particle size of a-FeOOH precipitate from Fe(bpmcn)Cl_2 at pH 11 is (350 ± 60) x (70 ± 10) nm. This gives us an aspect ratio of 4.84 ± 0.06, where aspect ratio is calculated with the equation described in Eqn. 4.2

$$AR = l/w \qquad \text{Eqn. 4.2}$$

where AR is the aspect ratio, and l & w are the average length and width of the particles measured in nm, respectively.

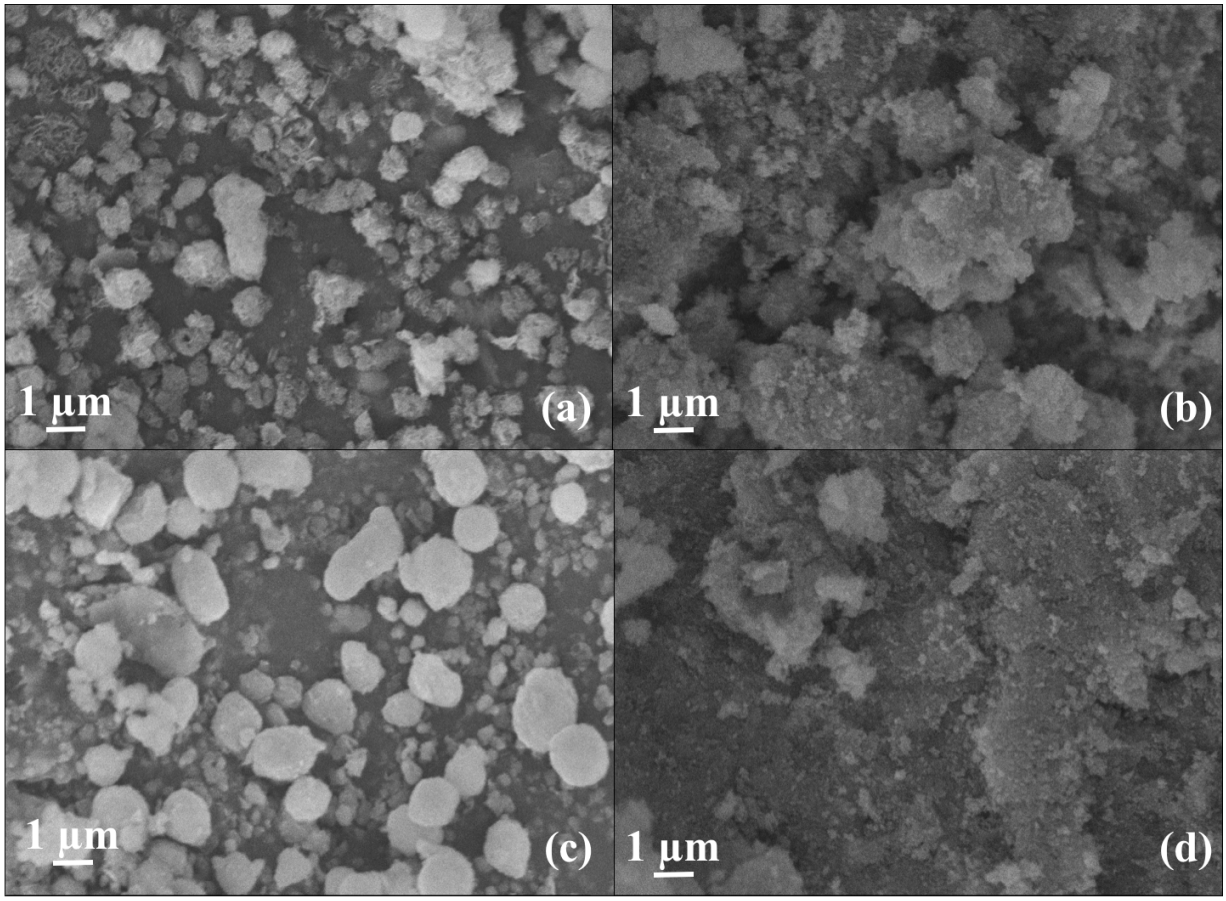

Figure 4.2. SEM images of particles precipitated in a pH 11 solution from (a) $Fe(bpmcn)Cl_2$ and (b) $FeCl_2$, and particles precipitated in a pH 13 solution from (c) $Fe(bpmcn)Cl_2$ and (d) $FeCl_2$.

To confirm the existence of a-FeOOH, Raman spectroscopy was taken of both powders precipitated from pH 11 and pH 13 with a 532nm laser at 10% power (Figure 4.3). Although Raman-active vibrations match well with the reference Raman spectra of α-FeOOH, a crystalline form of iron oxide known as goethite,[12] Raman shifts between 500 – 700 cm^{-1} seem broadened compared to the crystalline reference. A table of the Raman shifts along with literature values and assignments are outlined in Table 4.1.

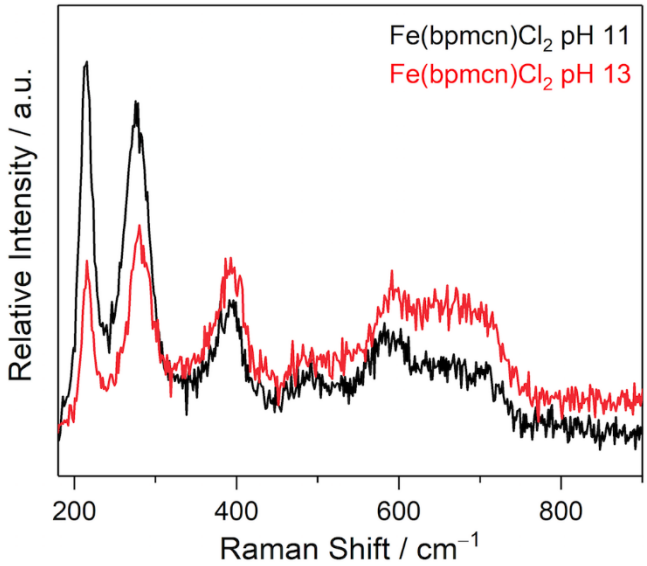

Figure 4.3. Raman spectra of FeOOH particles precipitated from (black) pH 11 and (red) pH 13, confirming both materials are identical in structure, and have similar chemical structure to goethite (α–FeOOH), with broadened vibrational responses compared to the reference between 500 – 700 cm^{-1} and 1100 – 1500 cm^{-1}.

Table 4.1. Raman shifts of a-FeOOH precipitated from $Fe(bpmcn)Cl_2$ in pH 11 and 13, compared to the known Raman shifts of crystalline goethite, α-FeOOH.

Experimental (cm^{-1})	**Literature (cm^{-1})**	**Assignment**
215	223	*Fe–O sym. str.*
279	297	*Fe–OH sym. bend*
396	392	*Fe–O–Fe/OH sym. str.*
492	484	*Fe–OH assym. str.*
582	564	*Fe–OH assym. str.*
670	674	*Fe–O sym. str.*

The similarities in Raman spectra between goethite and the a-FeOOH material and the amorphous PXRD pattern indicates that the *local structures* are very similar, yet our a-FeOOH shows no long-range ordered crystalline domains. This broadening of the Raman signals has been observed previously both in a-FeOOH and in amorphous Si.[2,13], in which these amorphous materials have similar bonding and vibrational modes to those of either goethite or crystalline Si, respectively. Given no crystalline signal from the a-FeOOH via PXRD, we propose the a-FeOOH

produced from room temperature precipitation from Fe(bpmcn)Cl_2 at basic pH grows in a similar, yet amorphous structure to goethite, which is shown in Figure 4.4.[14]

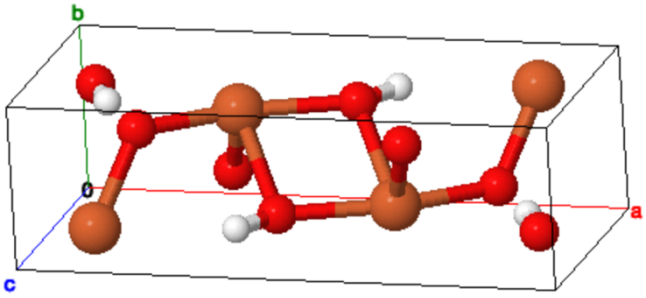

Figure 4.4. Crystal structure of α-FeOOH (goethite), taking an orthorhombic crystal structure with a = 9.913 Å, b = 3.013 Å, c = 4.580 Å, α = β = γ = 90º and space group P_{nma}. Here, Fe atoms are represented by brown spheres, while O and H atoms are represented by red and white, respectively. Figure generated with JSmol.

We also propose the chemical reaction that takes place during precipitation involves the use of O_2(aq) to oxidize the Fe(bpmcn)Cl_2, followed by a subsequent precipitation of $Fe(OH)_3$ and finally deprotonation of one of the hydroxyl groups to for a-FeOOH, leaving the free ligand in solution (Eqn. 4.3). In support of this reaction, mass spectrometry collected of the 0.01 M Fe(bpmcn)Cl_2 solutions of pH 11 and pH 13 reveal a large signal at m/z^+ = 325, which matches with the protonated bpmcn ligand [bpmcn-H^+] = 325 (Figure C1 and C2).

$$4Fe(bpmcn)(OH)_2 + O_2 \rightarrow 4FeOOH(s) + 4bpmcn + 2H_2O \qquad \text{Eqn. 4.3}$$

To understand the electrochemical activity of this material toward OER, slurries of these powders were created with acetylene carbon black and Nafion® 117 as a conductive contact to the FeOOH particles, and drop-casted onto a 1 cm^2 exposed area of an FTO slide. This film was then exposed to a pH 14 solution of NaOH, and linear sweep voltammetry (LSV) was used to characterize the electrochemical reactivity toward water oxidation. As shown in Figure 4.5, these films are shown to be electrochemically active in basic conditions. However, overpotential is high due to poor electrical contact of the FeOOH@Carbon film to the FTO surface.

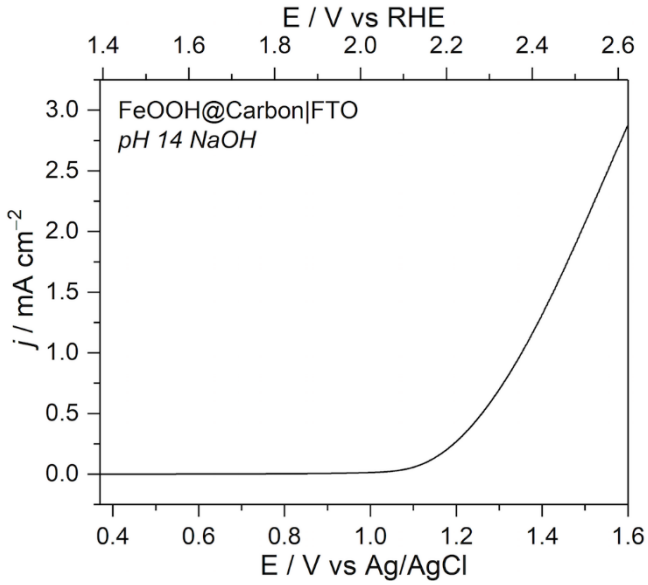

Figure 4.5. Linear sweep voltammogram of a-FeOOH embedded in carbon black and Nafion® 117 on a FTO slide, with a scan rate of 5 mV s^{-1}.

The data collected in Figure 4.5 shows that the a-FeOOH is electrochemically active for OER. To improve the electrochemical response, electrochemical deposition of a-FeOOH from Fe(bpmcn)Cl_2 was pursued to replace O_2 as the sacrificial oxidant with a potentiostat, allowing better contact with the FTO and reducing overall resistance in the anode.

4.4 Electrochemical Deposition of a-FeOOH from Fe(bpmcn)Cl_2 onto FTO

Since Fe(bpmcn)Cl_2 can be slowly oxidized in the presence of oxygen to a-FeOOH as described in Eqn. 4.3, and this resulting powder was measured to be electrochemically active for water oxidation, an electrochemical deposition route was pursued from a Fe(bpmcn)Cl_2 precursor. Starting from similar deposition conditions as reported in the literature[2], a 0.01 M solution of Fe(bpmcn)Cl_2 in 0.1 M NaCl at pH 13 under N_2 was used, applying a 0.4 V vs Hg/HgO bias until 0.12 C was passed. The electrochemical half-reaction at the surface is outlined in Eqn. 4.4.

$$Fe(bpmcn)(OH)_2 + OH^- \rightarrow FeOOH + bpmcn + H_2O + e^- \qquad \text{Eqn. 4.4}$$

The first step is believed to be the oxidation of $Fe^{II}(bpmcn)(OH)_2$ via Eqn. 4.5

$$Fe^{II}(bpmcn)(OH)_2 \rightarrow [Fe^{III}(bpmcn)(OH)_2]^+ + e^- \qquad \text{Eqn. 4.5}$$

Fe^{3+} is known to be highly unstable under basic conditions and form $Fe(OH)_3$ in solution in the presence of OH^-.[15] It is believed that a polymerization of $Fe(OH)_3$ then occurs in solution to form $[Fe(OH)_2]_n^+$. The mechanism for this reaction is proposed to be the following chemical reaction, similar to what has been reported for $FeCl_2$.[15]

$$[Fe(OH)_2]_I^+ + Fe^{III}(bpmcn)(OH)_2 \rightarrow [Fe(OH)_2]_{n+1}^+ + bpmcn \qquad \text{Eqn. 4.6}$$

where the polymer forms in solution to the point that a colloidal suspension of FeOOH is formed that ultimately develops a low enough zeta potential (ζ) to precipitate out of solution as a-FeOOH, and nucleate directly at the sight of oxidation on the surface.

$$[Fe(OH)_2]_n^+ + nOH^- \rightarrow [FeO(OH)]_n + nH_2O \qquad \text{Eqn. 4.7}$$

SEM images of the resulting FeOOH|FTO films show high aspect ratio films (Figure 4.6), but with a more uniform coating compared to the precipitate found when forming a-FeOOH from $Fe(bpmcn)Cl_2$ in solution at pH 11 or pH 13 in the presence of O_2 (see Figure 4.2). Side-angle view suggests a platelet-like morphology of the film.

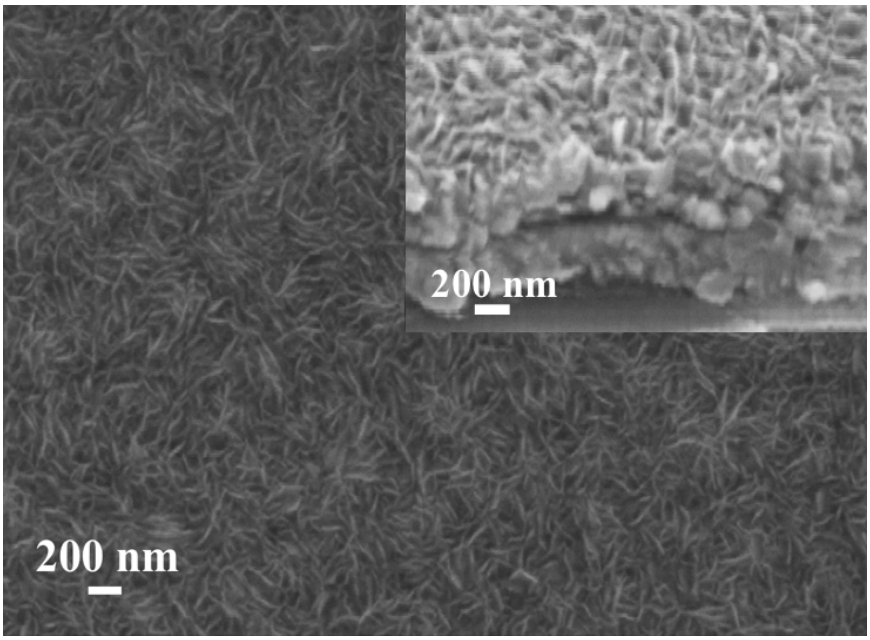

Figure 4.6. SEM image of a-FeOOH|FTO electrodeposited from a 0.01 M $Fe(bpmcn)Cl_2$ solution at pH 13 with 0.1 M NaCl electrolyte, using a Pt disk counter electrode and Hg/HgO (1 M NaOH) reference electrode. Electrodeposition conducted at 0.4 V vs Hg/HgO (1 M NaOH) until 0.02 C passed. Inset is a 45º angle view of the film, showing platelet morphology.

Average width of these disordered array of platelets is 21 ± 5 nm. In comparison to the high aspect ratio particles precipitated from pH 11 under air, these particles have widths that are 50 nm thinner, and observable lengths of 240 ± 80 nm.

Electrochemical activity of the a-FeOOH|FTO film shown in Figure 4.6 in pH 14 NaOH confirms electrocatalysis of the OER. Compensating for *i*R loss from the FTO with a resistance measured as 27.5 Ω, we achieve 10 mA cm^2 with an overpotential as low as 500 mV (Figure 4.7), with an optimal film deposition charge of 0.075 C/cm^2.

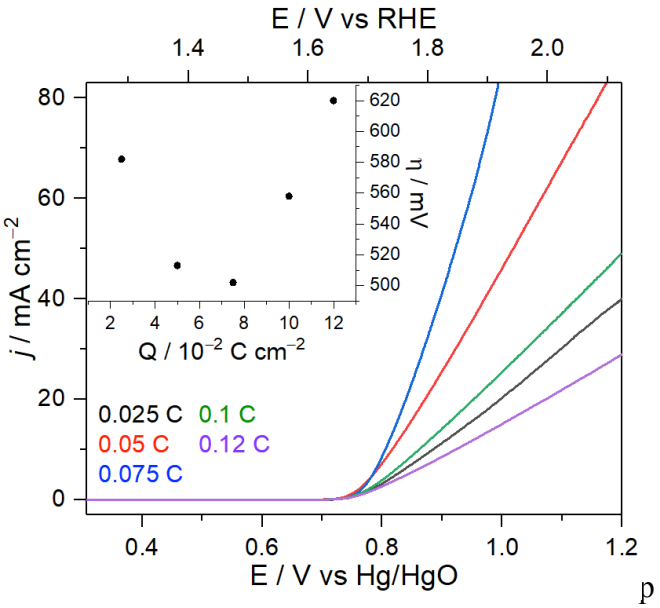

Figure 4.7. LSV of a-FeOOH|FTO with 1 cm^2 exposed surface area in pH 14 NaOH with a Pt disk counter electrode, Hg/HgO (1 M NaOH) reference electrode, and a 5 mV s^{-1} scan rate. Data is represented as *i*R compensated with 27.5 Ω resistance for the FTO film, and LSV scans of films grown from deposition charge passed of (black) 0.025 C, (red) 0.05 C, (blue) 0.075 C, (green) 0.1 C, and (purple) 0.12 C. Electrochemical potential was converted to the RHE scale using Eqn. 4.1.

Compared to other examples of a-FeOOH films, some report overpotentials as low as 480 mV with undoped a-FeOOH and as low as 420 mV overpotential with Ni-doped a-FeOOH.[5–7] While these films are comparable in overpotential for undoped a-FeOOH, proper optimization of these films in terms of concentration of Fe(bpmcn)Cl$_2$, electrolyte concentration, and temperature of deposition must be done to reach overpotentials closer to ~400 mV for the OER.

However, it is important to note that the solubility of Fe(bpmcn)Cl$_2$ in water can only reach 0.01 M at room temperature in 0.1 M electrolyte. Further, increasing electrolyte concentration

toward 1 M NaCl decreases the solubility of Fe(bpmcn)Cl_2 below 0.01 M. Therefore, temperature must also be explored as a variable to increase solubility of the precursor while also being able to change the electrolyte concentration. Depositions of FeOOH have electrolyte concentrations that range from 0.1 M to 3 M of chloride or perchlorate salts containing either sodium or ammonium cations, and Fe-based precursor concentrations from 0.02 M to 0.05 M.[2–5] With that in mind, future experiments must also explore the role of pyridyl and/or amine-based η^4 L-type ligands to replace the bpmcn ligand to understand effects on morphology and overpotential for the OER under basic conditions.

4.5 Conclusions

a-FeOOH was successfully synthesized from basic conditions both in solution when exposed to air, and from the electrochemical deposition from a Fe(bpmcn)Cl_2 precursor at room temperature. Morphology of the powders and films yield high aspect ratio particles, with platelet-like structures as low as 21 nm in width when electrodeposited onto a conductive FTO substrate, and a mostly amorphous structure with poor crystallinity close to that of goethite. While overpotentials at highly alkaline conditions show OER occurs at overpotentials around 500 mV, this may be reduced through optimization of electrodeposition conditions by changes in Fe(bpmcn)Cl_2 concentration, temperature of deposition, and replacements of the η^4 L-type ligand bpmcn with other pyridyl and/or amine-based ligands. It will be important to characterize the symmetry of new L_4FeCl_2 complexes and how that affects morphology and overpotential for reaching 10 mA cm^{-2} in pH 14 NaOH solutions.

4.6 References

(1) Hong, D.; Mandal, S.; Yamada, Y.; Lee, Y.-M.; Nam, W.; Llobet, A.; Fukuzumi, S., Water Oxidation Catalysis with Nonheme Iron Complexes under Acidic and Basic Conditions: Homogeneous or Heterogeneous? *Inorg. Chem.* **2013**, *52*, 9522 - 9531

(2) Chemelewski, W.D.; Lee, H.-C.; Lin, J.-F.; Bard, A.J., Mullins, C.B., Amorphous FeOOH Oxygen Evolution Reaction Catalyst for Photoelectrochemical Water Splitting. *J. Am. Chem. Soc.* **2014**, *136*, 2843 – 2850.

(3) Ishaq, S.; Sikora, A.; Scheidler, N.; Hambleton, C., Katz, J.E., Enhancement of Water Oxidation Photocurrent for Hematite Thin Films Electrodeposited with Polyvinylpyrrolidone, *J. Electrochem. Soc.* **2016**, *163*, F1330 – F1336.

(4) Spray, R.L.; Choi, K.-S., Photoactivity of Transparent Nanocrystalline Fe_2O_3 Electrodes Prepared via Anodic Electrodeposition, *Chem. Mater.* **2009**, *21*, 3701 – 3709.

(5) Chowdhury, D.R.; Spiccia, L.; Amritphale, S.S.; Paul, A.; Singh, A., A Robust Iron Oxhydroxide Water Oxidation Catalyst Operating Under Near Neutral and Alkaline Conditions, *J. Mater. Chem. A* **2016**, *4*, 3655 – 3660.
(6) Louie, M.W., Bell, A.T., An Investigation of Thin-Film Ni–Fe Oxide Catalysts for the Electrochemical Evolution of Oxygen, *J. Am. Chem. Soc.* **2013***, 135,* 12329 – 12337.
(7) Chemelewski, W.D.; Rosenstock, J.R.; Mullins, C.B., Electrodeposition of Ni-doped FeOOH oxygen evolution reaction catalsyts for photoelectrochemical water splitting, *J. Mater. Chem. A* **2014**, *2*, 14957 – 14962.
(8) Seabold, J.A.; Choi, K.-S., Efficient and Stable Photo-Oxidation of Water by a Bismuth Vanadate Photoanode Coupled with an Iron Oxyhydroxide Oxygen Evolution Catalyst, *J. Am. Chem. Soc.* **2012**, *134*, 2186 – 2192.
(9) Lhermitte, C.R.; Verwer, J.G.; Bartlett, B.M., Improving the Stability and Selectivity for the Oxygen-Evolution Reaction on Semiconducting WO_3 Photoelectrodes with a Solid-State FeOOH Catalyst, *J. Mater. Chem.* **2016**, *4*, 2960 – 2968.
(10) Esarey, S.L.; Holland, J.C., Bartlett, B.M., Determining the Fate of a Non-Heme Iron Oxidation Catalyst Under Illumination, Oxygen, and Acid, *Inorg. Chem.* **2016**, *55*, 11040 – 11049.
(11) Costas, M.; Que, L. Jr., Ligand Topology Tuning of Iron-Catalyzed Hydrocarbon Oxidation, *Angew. Chem. Int. Ed.* **2002**, *41*, 2179 – 2181.
(12) Legodi, M.A., de Waal, D., The Preparation of Magnetite, Goethite, Hematite, and Maghemite of Pigment Quality from Mill Scale Iron Waste, *Dyes and Pigments* **2007**, *74*, 161 – 168.
(13) Alben, R; Weaire, D.; Smith, J.E.; Brodsky, M.H., Vibrational Properties of Amorphous Si and Ge, *Phys. Rev. B* **1975**, *11*, 2271 – 2296.
(14) Crystallographic data (raw) from Gualtieri, A.; Venturelli, P.; In Situ Study of the Goethite-Hematite Phase Transformation by Real Time Synchrotron Powder Diffraction, *American Mineralogist* **1999**, *84*, 895 – 904.
(15) Flynn, C.M., Hydrolysis of Inorganic Iron(III) Salts, *Chem. Rev.*, **1984**, *84*, 31-41.

Chapter 5

Discussion-Centered General Chemistry Laboratories for Hands-On Teaching of the Scientific Method

5.1 Introduction.

This chapter now changes gears in order to focus on my time in chemical education, expanding on ways the University of Michigan Chemistry Department could educate its introductory chemistry students. The Department of Chemistry at the University of Michigan provides an opportunity for graduate students interested in pursuing careers in education to acquire experience developing new techniques to improve the learning experience for its students. This opportunity is offered through the Chemical Sciences at the Interface of Education | University of Michigan (CSEI|UM) Future Faculty Graduate Student Instructor (FFGSI) program, where the graduate student obtains a 25% appointment as a FFGSI, and 25% appointment as a Graduate Student Instructor (GSI) in a particular course offered through the department. Over the 2016 – 2017 academic year, I was given this opportunity through their general chemistry laboratory course, CHEM 125/126. In the UM Chemistry department, faculty and staff provide general chemistry laboratory instruction to more than 1500 students each year. This laboratory is structured as a 2-credit, one-semester course that is broken up into two parts: 1 hour per week for lecture, 1 hour per week for presentation-style teaching demonstrations presented by students to GSIs, and a 2-hour laboratory experiment written by the instructor that covers a variety of common general chemistry topics. During the fall semester, there are approximately 30 graduate students who serve as GSIs, and one primary instructor commonly occupied by a staff or faculty member with a position in the chemistry department. Currently, large lecture halls in a theater-like setting are used to relay information to students in a typical lecture containing >100 students per lecture, a style commonly found at larger universities. However, new formats such as a flipped classroom have been suggested in the literature as a means of transforming the classroom structure toward an improved learning experience.[1–7]. Although introductory courses in chemistry commonly implement smaller discussion or recitation groups to improve student-instructor interactions, this

strategy is not often applied to the chemistry laboratory. This choice of structure is commonly attributed to the interactive nature of the laboratory itself; however, discussion of the results *during the laboratory period* could give students the opportunity to discuss the data just collected in lab *with the instructor present.* At large institutions, the instructor inside the laboratory is often a graduate student instructor or teaching assistant. It is common and effective for undergraduate students to gain research skills in our department through joining a research lab as an undergraduate, where they are mentored under a graduate student or post-doctoral researcher in a research laboratory under the instruction of a principal investigator. To increase and improve our students' exposure to proper and necessary research skills that will prepare them for future courses or beyond, I proposed introducing these skills at the introductory level with the goal of easing the transition into a research-minded approach to scientific discovery. In this manner, they can then enter a research group with a deeper fundamental understanding of specific lab techniques qnd sound reasoning skills needed to succeed in a research laboratory.

It is common that general chemistry laboratories are used to solely teach students core concepts of chemistry and techniques that chemists use to answer scientific questions, I saw a greater potential to use the laboratory in a more constructive fashion. In this chapter, I propose using general chemistry as a course to teach students *how to think like scientific researchers at a fundamental level*, *how to interpret data, engage with theoretical understanding while conducting the experiment, and think critically on how to improve their procedures based on preliminary results collected in the lab*. This concept engages students in the protocols they follow, and thus gives students (a) the tools needed to write protocols on their own without guidance, and (b) the ability to answer a scientific question they have never been asked. Often, time spent engaging with students is a limiting factor with a lab setting, necessitating allocation for students to conduct the experiment, data collection, analyze and engage the collected data, challenge the students to think critically about their results in a thorough discussion, and present the findings in a way that shows adequate understanding of how research in the sciences should be conducted.

A flipped classroom in which lectures are typically provided as online lecture videos and the classroom is used as a discussion-centered learning environment surrounding direct engagement with material alongside the instructor has been tested on numerous occasions to improve the learning environment. This format allows students to engage the material and challenge their understanding in an efficient way compared to the more traditional format of

lecturing in-class and working on problems at home. This method has been shown to improve the learning experience for students, and has had a positive impact on their understanding of the material.[1–7] Although this method has been applied extensively to chemistry courses over the years, it has only recently emerged as a method that could be suitable for chemistry laboratories.[8,9] The few examples that are present in literature have shown promising results for students to more thoroughly engage the material and connect theory to experimental results. Several have also used pre-lab lecture videos in their classrooms to supplement the coursework completed in class.[10,11] I apply instructional videos in the laboratory as supplement to the lecture hall format, which provides an extra hour in-lab for class discussion of results, and one-on-one interaction with fellow students and the instructor of the lab. Essentially, the additional time may be used to analyze the collected data *as it was being collected in lab* and interpret the results to tie back to key concepts discussed in the pre-lab lecture video. *The learning goal of this study was to improve students' capacity to connect theory to experiment with exposure to all facets of the scientific method, and effectively use it to answer a new scientific question*. In this chapter, I will discuss 2 major points: 1) the impact on the students cognitive understanding of the material through understanding their ability to answer a new, challenging science question, and 2) the student disposition students had for this format. For first proof-of-concept and proper curriculum development, this new format was completed on a small scale with $n \sim 40$ students split between two sections.

5.2 Benefits of Discussion-Centered Format.

This study narrows the range of students from ~1500 students per year to ~40 ($n \sim 20$ per semester) to focus on developing the format properly for high student success. The small, more personal interactions between students and instructors allows for easier communication and observation of positive and negative feedback in a timely manner. It also allows the course easier control for the instructor and higher precision on the information that is conveyed to students. Although the small class sizes over two semesters does limit statistical analysis, the focus of this study was in the development of a discussion-style portion to our general chemistry laboratory course that would receive positive responses from students and intimately engage them with hypothesis-based problem solving, procedure development, and chemistry-specific technical skills. The scalability and bureaucratic hurtles of applying this format to the large scale of ~1500 students is out of the scope of this study; however, scalability was taken into consideration when

designing this course, and issues with scalability are discussed in the limitations section of this chapter.

5.3 Methodology

For this study, the Fall 2016 semester was composed of one section of 23 students ($n = 23$), while the winter 2017 semester was one section of 20 students ($n = 20$). Students were informed at the beginning of the semester and throughout formal assessments that their work would be used for research purposes, and gave consent prior to completing the assessments and assignments. No personally identifying information were recorded for online surveys, but names were written and removed after grading for any assessments and assignments used for this chapter. IRB approval was obtained for this study,[12] and students were made aware of any surveys or exams that would be used for the purposes of this study. Students gave explicit consent for this information prior to completing assignments.

The general format of the course was designed as a 4-hour session. Before attending lab, students were assigned to watch a 15- to 30-minute pre-lab lecture (made by the instructor), and complete a pre-lab assignment. During the first hour of the lab session, teaching demonstrations/presentations were completed by either one or two teams, which lasted 15-30 minutes each with time for questions. A brief overview of the lab experiment was then presented by the instructor, which included pointing out where chemicals were, safety hazards that needed to be made explicitly clear (when applicable), waste disposal concerns, and a brief overview how to use any instrumentation used that day. A concise description of each portion of the laboratory course is described below. First, I will outline the pieces of the course that remained constant throughout both semesters, then discuss the details that were different between semesters. Throughout the semester, the graduate student teaching assistant served both as the lecturer and the teaching assistant during the lab, and was responsible for writing assignments, exams, quizzes, and grading said assignments and exams.

Pre-laboratory videos: Videos were made using Camtasia 2.0 software, and were approximately 15-30 minutes in length. These included PowerPoint presentations with a video of the lecturer presented near the bottom left corner. Included in text and figures, drawings were also used where necessary. During these lecture videos, enough information was conveyed to inform the students

of the theory behind what the lab was based on, and introduce them to the techniques they would be responsible for performing for the lab. Pre-lab questions were spread out throughout the lecture to ensure the students were focused on the important topics to remember. Videos were edited and uploaded to YouTube with the Camtasia software. Videos were made available to students at least 3 days prior to the laboratory session.

Laboratory experiments: Lab protocols were given to students at least 3 days prior to the scheduled laboratory session. These experiments took a 2-hour format, where emphasis on practical application of chemical knowledge was placed on writing the procedures. Students were required to work in pairs of two or three and changes to these pairings occurred once during the middle of the term. The topics covered included (1) Measurements & Uncertainty, (2) Waters of Hydration on Metal Salts, (3) Gas Laws: Collecting gas over water, (4) Introduction to spectroscopy: UV-Vis & chemical Dyes, (5) Determining a Relative Rate Law, (6) Extraction of Caffeine, (7) The Equilibrium Constant, (8) Oxidation & Reduction Reactions, (9) The Nernst Equation & Galvanic Cells, and (10) Calorimetry: Exchanging energy as heat. The same labs were conducted in both sections, albeit in a different order between the Fall 2016 and Winter 2017 semesters.

Short communications: These were given to students 2 – 3 times before the full manuscript assignment to not only prepare them for the full manuscript, but also to get students to practice presenting their results in written format. These short communications were restricted to a maximum of 500 words, which did not include any tables, figures, or schemes that were created by the students. Correct citations were expected where appropriate, and a brief description were expected for the goals & hypothesis of the lab, an outline of the procedure, an organized presentation of final results, and a conclusion that tied back to the original hypothesis.

Full manuscript: One full manuscript (5-page maximum) was expected for the experiment "The Nernst Equation & Galvanic Cells." This manuscript had the typical format of a chemistry laboratory report, including a title, abstract, introduction, experimental section, results & discussion, conclusions, and references (properly formatted according to a guide given to the students). A detailed description of what was to be expected was given to students at the beginning

of the semester, which outlined both good and bad examples for many of the sections. These reports were structured around having students engage entirely with the material, including the technique, the data analysis, hypothesis writing, conclusions, conceptual questions surrounding their data, and future work proposed based on their experiments. Students were not graded on accuracy, but rather their presentation of the material, proper citation of literature values, and proper conclusions made about their individual/class data.

Post-semester survey: After the semester was over, students were given an online form (Google Forms) to fill out that asked a series of questions related to the material and style covered during their respective semesters. These were collected anonymously with no ties to the students, and were given to students after grades had been submitted. In addition, no grade was assigned to the students after the completion of this survey, and was completely voluntary. Question 1 collected demographic information, while for statements 2–10 students were asked to respond to on a scale of 1 (strongly disagree) – 5 (strongly agree) are listed as (1) What year were you when you took this course? (2) After taking this course this academic year, I feel that taking this course was the right decision for me, (3) After taking this course this academic year, I felt the pre-lab lectures were adequate to prepare me for the laboratory experiments, (4) After taking this course this academic year, I would recommend other students or my peers to take this section of CHEM 125/126, (5) After taking this course this academic year, I feel that I was more interested in pursuing scientific courses, (6) After taking this course this academic year, I felt like I was successfully taught the scientific method and have a good understanding of how it works, (7) After taking this course this academic year, I feel that the extra hour dedicated to discussion portions of this section were valuable to my overall learning experience for this course, (8) After taking this course this academic year, I feel the teaching demonstrations were useful in helping me grasp concepts of the labs and think critically about my data and/or class data, (9) After taking this course this academic year, I feel that I learned the basic techniques taught during the sections of this course, and (10)Compared only to other scientific courses I have taken, I would rank this section as one of the most valuable courses I have taken in the sciences.

Midterm exams*:* The midterm exam contained a mix of questions relating to theoretical understanding of the techniques, problem-solving skills, interpreting data, and making conclusions

based on the given results. No laboratory component was given for this exam, and was entirely short answer questions with calculations required for some of the questions.

Pre- and post-semester diagnostic quizzes: These quizzes were ungraded documentation to demonstrate to the instructor how prepared the students were for the semester, and how well they could apply their newly acquired skillset using the scientific method at the end of the semester. The questions were written to test how much they knew about the conceptual topics covered during the semester, as well as how well they could formulate hypotheses and write procedures based on a scientific question.

Teaching Demonstrations: 15-30 minute presentations were expected for each student to present either a difficult chemistry-related conceptual question to the class that was related to the previously conducted experiment the week prior, or give a presentation on their results and conclusions of a previous experiment they conducted in lab. The students were expected to demonstrate a deep knowledge of the topic by exploring a difficult concept within the topic of the previous lab experiment. Examples of topics covered during the teaching demonstrations in which a challenging problem was discussed were comparing the ideal gas law to the equations governing real gasses, discussing a recently published journal article on the extraction of citric acid from aqueous media,[13] and the various waters of hydration for sodium sulfate decahydrate, also known as Glauber's salt.[14] Example calculations were also expected to be presented during these teaching demonstrations, and a mix of "chalk-talks" and PowerPoint presentations were commonly used by the students. Students who gave presentations on their data from a previous experiment were required to give adequate background information to demonstrate good understanding of the topic, a brief outline of the experimental protocol, and a thorough interpretation of their data. A new scientific question that expands further on the results of their previous experiment was also expected in their presentation.

Lab Practical: This practical exam for both semesters involved probing the effect of ligands on the electrochemical potential of metal cations. The Fall 2016 practical focused on exploring the effect of neutral ligands around a central Zn^{2+} cation on the electrochemical reduction potential in a galvanic cell. For this comparison, students were told the week of the galvanic cells experiment

during the semester that the practical exam was based on that experiment, to ensure good note taking and proper preparation. During the exam, students were presented a question: how does the effect of ammonia surrounding Zn^{2+} change the electrochemical potential for the half reaction $Zn^{2+} + 2e^{-} \rightarrow Zn^{0}(s)$, given that E^{0}_{red} $(Zn^{2+/0}) = -0.76$ V? This question was presented to them on the day of the exam with no previous knowledge of the question. Hypotheses were expected to be drawn based on the scientific question presented, then a procedure was expected to be written during the 2-hour timeslot given for the exam. Students were then expected to complete the experiment they wrote a procedure for, and collect the necessary data to analyze in the context of their original hypothesis. Students were then asked a series of conceptual questions surrounding the original scientific question, including making conclusions about their original hypothesis. The measure of success for this exam was not based on accuracy, but rather their ability to formulate a hypothesis, create a procedure, conduct the procedure, analyze the collected data, and interpret the results in the context of their original hypothesis to make conclusions supported by data. Students had access to their notes, pre-lab videos, previous lab protocols, and any accessible website deemed credible during the exam.

The Winter 2017 practical focused on exploring the effect of both anionic and neutral ligands around a central Zn^{2+} cation on the electrochemical reduction potential in a galvanic cell. For this comparison, students were told two weeks before the practical exam that the topic covered would be the techniques and concepts surrounding galvanic cells and electrochemical cell and reduction potentials. During the exam, students were presented a question: what effect do the properties surrounding anionic and neutral ligands have on the electrochemical reduction potential of $Zn^{2+/0}$, given that E^{0}_{red} $(Zn^{2+/0})$ in a 0.1 M solution of $Zn(NO_3)_2 = -0.76$ V? This question was presented to them on the day of the exam with no previous knowledge of the question. Hypotheses were expected to be drawn based on the scientific question presented with only one independent variable identified, then a procedure was expected to be written during the 2-hour timeslot given for the exam. Students were then expected to complete the experiment they wrote a procedure for, and collect the necessary data to analyze in the context of their original hypothesis. Students were then asked a series of questions surrounding the original scientific question, including making conclusions about their original hypothesis. The measure of success for this exam was not based on accuracy, but rather their ability to formulate a hypothesis, create a procedure, conduct the procedure, analyze the collected data, and interpret the results in the context of their original

hypothesis to make conclusions. Students had access to their notes, pre-lab videos, previous lab protocols, and any accessible website deemed credible during the exam.

5.4 Measuring Student Success & Feedback to Format.

Although this course was structured to maintain exposure of students to common general chemistry techniques and concepts (gas laws, the Nernst equation, calorimetry, etc.), the primary learning goal of the course was to give students a hands-on experience using the scientific method from start to finish, and prepare them for the practical exam at the end of the semester. A successful term would yield high percentages of students correctly writing hypotheses and interpreting data during this practical, where they were asked to reiterate the scientific question posed in the text of the exam, write an original hypothesis, write and perform their own individual procedure, analyze their collected data, draw conclusions about their results in the context of their original hypothesis, support or reject their original hypothesis, and present their future work and a new question to answer if they were to continue exploring the topic covering the exam.

Pre-lab lecture videos. Students were on average positively receptive to the pre-lab lecture videos for both Fall 2016 and Winter 2017 semesters. Outside of students' opinion of the teaching style and presentation skills of the instructor, the accessibility and utilization of the videos during lab was obvious during the laboratory session. It was common to observe students referring to the video after data collection to re-engage with the theoretical concepts governing the chemical reactions or phenomena they were exploring for that experiment. This is quite unique to this format of chemistry laboratory, and quite different from the typical lecture-hall format the University of Michigan's Department of Chemistry currently utilizes.

Practical Exam Results Fall 2016. The practical exam was analyzed in sections ranging from students' ability to correctly identify variables for a hypothesis and write them in the correct format, thorough procedures that outline the experiment the student will conduct, and will collect data that directly supports or rejects their hypothesis, correct calculations and analysis of their data, and drawing correct conclusions from their results as they pertain to their original hypothesis. I was also interested to see if students could understand future work presented to them after

analyzing their data and running through the experiment. This exam focused solely on the effect of ammonia around Zn^{2+} on the reduction potential of $Zn^{2+/0}$, and did not involve other ligands.

Out of 23 students, 100% developed a working hypothesis that contained an independent variable, dependent variable, and written in such a way to demonstrate they would control the independent variable and measure the direct variable. One minor error associated with these hypotheses were that students stated the reduction potential would increase or decrease, rather than be more specific (more negative or more positive reduction potential). All students were also able to create a working procedure that would correctly answer the question set forth in the exam, and support or reject their hypothesis. However, many students left out key pieces of information, including concentrations of the half-cell electrolyte solutions (0.1 M $Zn(NO_3)$ and 0.1 M $Zn(NH_3)_4(NO_3)_2$) and not noting the necessity of a positive electrochemical cell potential (which electrode is anode or cathode). The latter mistake was commonly translated when reporting electrochemical cell potentials in the results section of the exam. Only 73% of students correctly set up their galvanic cells to read a positive E_{cell}, and only 27% correctly calculated the reduction potential of the $Zn(NH_3)_4^{2+} + 2e^- \rightarrow Zn^0(s) + 4NH_3(g)$ from their electrochemical cell potential, even if their E_{cell} was reported negative. This translates to a lower fundamental understanding of the technique used in this lab than expected. However, 73% of students could make a conclusion whether to support or reject their hypothesis given their calculated values (even if they were fundamentally incorrect results calculated). While students did not have a deep enough understanding of what values to expect using this characterization technique, most students were able to correctly draw conclusions from data regarding their hypothesis.

This misconception of electrochemistry seemed apparent in the follow-up questions surrounding the theory behind the observations they measured. ~65% of students correctly presented their data in figure form (plotting their reduction potentials on an electrochemical potential scale, determining why electrons flowed from the anode to the cathode in this specific system, etc.). The most common mistakes made were regarding the potential reaction between $Zn(NH_3)_4^{2+}$ and Al(s). While they were given the reduction potential of Al^{3+} to $Al^0(s)$, many students could not translate their reduction potential calculated in the exam for $Zn(NH_3)_4^{2+} + 2e^- \rightarrow Zn(s) + 4NH_3(g)$ to produce a net chemical reaction shown in Eqn. 5.1. The primary flaw seemed to be a disconnect between the signs of reduction potentials and the direction of electron flow from reducing agents to oxidizing agents.

$$3Zn(NH_3)_4^{2+} + 2Al(s) \rightarrow 3Zn^0(s) + 2Al(NH_3)_6^{3+} \quad E^0_{cell} = 0.62\ V \qquad \text{Eqn 5.1}$$

Although it was acceptable to show $Al^{3+} + 6NH_3(g)$ as a product, only 55% of students correctly identified this reaction in this specific question given their data collected.

Overall, this exam showed us that students taught with this format could write hypotheses and identify similar protocols to use for new experiments proposed. Students' capability for analyzing data and relating it back to theory were lacking behind expectations; however, many still did prove a tight grip on the material and their ability to use the scientific method effectively.

Practical Exam Results Winter 2017. The practical exam was analyzed in sections ranging from students' ability to correctly identify variables for a hypothesis and write them in the correct format, thorough procedures that outline the experiment the student will conduct, and will collect data that directly supports or rejects their hypothesis, correct calculations and analysis of their data, and drawing correct conclusions from their results as they pertain to their original hypothesis. I was also interested if students could think of new scientific questions and experiments that relate to the topic of the practical exam.

90% of students taking the exam correctly identified independent and dependent variables, and correctly formatted the hypothesis such to imply they would control the independent variable and measure the dependent variable. Only minor errors (such as claiming their independent variable would increase/decrease the electrochemical reduction potential of $Zn^{2+/0}$ instead of saying the potential would become more negative or positive). When writing procedures to gather data in support of their hypothesis, 60% of students laid out properly formatted protocols that identified all materials needed with important specifics listed, with only minor issues. The most common mistake for those that did not fit within this stipulation was a combination of ensuring a direct comparison of ZnL_n solutions with the same $Zn(NO_3)_2$ reference half-cell, and outlining specifics on details like anode and cathode, concentrations of solutions, and outlining the specific galvanic cells they would be building. Setting aside these common mistakes, 90% of students were still able to write procedures that would correctly support or reject their original hypothesis. However, it is important to note that only 60% of students wrote procedures that wrote procedures that could easily be reproduced by another person without missing crucial information.

85% of students correctly analyzed the data collected during their exam fully required. This included correctly reporting the reduction potentials of $Zn^{2+/0}$ in the presence of various ligands (anionic and neutral), and placing them on an electrochemical potential diagram with more negative potentials at the top and more positive potentials near the bottom. Few students made significant errors (3 out of 20), and the most common mistake was forgetting units on the reduction potentials. However, drawing conclusions from this data set was more challenging for students. Only 45% of students taking this exam correctly answered the questions related to describing the trends in data fully required. While 7/20 students correctly identified all necessary conclusions needed, 10/20 made significant errors in drawing conclusions based on their results reported. Although mistakes varied, many of them were common mistakes to be expected by an introductory student. These included generalizing trends without referring to their data to back up claims, and misinterpretations of what an "anionic ligand" vs "neutral ligand" meant, even though a pre-lab instructional video was given to students about that specific topic. This was also observed when students were asked to support or reject their hypothesis. Some data collected from students were very inconsistent, and no trend could be observed; however, many of these students still tried to make a conclusion about this data when there was no obvious trend to observe. This is also a common mistake that I would expect from an introductory student. Overall, 55% of students correctly supported or rejected their hypothesis, with 11/20 students doing so with no errors in explanation or presentation.

When it came to presenting a new scientific question related to electrochemical potentials and galvanic cells, 80% of students successfully identified a valid question and made valid hypotheses that were within reason of a general chemistry student. The most common mistake was over-generalizing the dependent variable of electrochemical reduction potentials (stating it would increase or decrease rather than becoming more negative or positive). Excluding this error, 16/20 students correctly proposed new future work that they were interested in learning regarding galvanic cells and the Nernst equation. Examples of topics given by students were exploring concentrations of neutral ligands in solution and how temperature of the solution affects the reduction potential of metal complexes surrounded by neutral ligands.

Overall, I believe this practical exam coupled with the proposed teaching format gives students not only the proper exposure to techniques, but also teaches them the scientific method effectively at the introductory level. This adds to the current method of teaching at the University

of Michigan without significantly altering the course load for students, yet still exposes them to more valuable information that they can take with them in other scientific courses or even the research lab. The average for this exam was an 81% ± 16%, implying the average student that leaves this section can correctly work through ~80% of the scientific method from start to finish (excluding oral presentation) independently given a topic that they are well familiar with.

Post-semester survey. The results of the post-semester survey for the Fall 2016 and Winter 2017 semesters students that responded are below. Overall, only n = 19 students responded from both sections, 9 students from the Fall 2016 section and 10 students from the Winter 2017 section.

Table 5.1. Post-semester survey response results for students taking the fall 2016 (9 respondents) and winter 2017 (10 respondents) semesters of general chemistry laboratory. Numbers correspond to perentage of respondents.

	Favorable 4 - 5 (F16 / W17)	*Neutral 3 (F16 / W17)*	*Unfavorable 1 - 2 (F16 / W17)*
Right decision	7 / 8	0 / 1	2 / 1
Pre-lab lecture videos	6 / 6	1 / 1	2 / 3
Recommend course to others	5 / 5	1 / 3	3 / 2
Pursuing other science courses	3 / 3	1 / 5	5 / 2
Scientific method skills	6 / 9	1 / 0	2 / 1
Discussion-section	5 / 7	2 / 2	2 / 1
Teaching Demonstrations	3 / 5	1 / 2	5 / 3
Learned Basic Techniques	5 / 8	1 / 1	2 / 1
Valuable science course	5 / 5	2 / 2	2 / 3

Students had a positive outlook on the second semester of this course, with 80% of students responding that taking this course was the right decision. For both sections, it seems that most

students would recommend this course to others (56% for F16, 50% for W17). Some students felt neutral to this idea, which could be due to uncertainty in how other students might respond to such a recommendation. It is important to note that both sections found the extra hour dedicated to a discussion session at the end of the lab experiment extraordinarily valuable. These sections were used to work out calculations and review data analyses with others, while also discussing the conceptual questions as a group. To be clear, these discussion sessions were not used to hand out answers. Rather, they were used as a time slot for the lab to operate similarly to a recitation section for the lab, where the teaching assistant would run over questions about the lab with the group *while still in the lab* and have the students discuss amongst the group what a possible answer may be, what types of data points students collected, or difficult concepts that many within the group needed to review with the teaching assistant. Specifically, all of those who responded favorably in the Fall 2016 section rated "strongly agree" that the discussion was valuable to their learning experience. For the winter 2017 term, 71% of those who showed favorable views of the discussion portion of the lab strongly agreed that it was valuable to their learning experience in this course.

5.5 Limitations to the Discussion-Centered Format.

There are a few points of this study that limit the scope and scalability that must be discussed. Although making pre-lab lecture videos as the sole delivery method of information to students may be unrealistic at a large-scale setting such as the University of Michigan, these videos can easily serve as supplementary information during labs and after class in addition to lecture hall style teaching. However, practitioners who teach courses of chemistry which have course and lab as one entity (i.e. separate credits are not assigned to lab and lecture), pre-lab videos may serve as a suitable addition to their classes to both prepare students for lab and not take valuable one-on-one time with students to lecture on the material in detail.

It must also be pointed out that the Winter 2017 semester was taught with more emphasis on hypothesis-writing, procedure-writing, and data interpretation than the Fall 2016 semester. This was because of feedback received from students both from the lab practical and end-of-term evaluations. Many students still lacked in core conceptual understanding of the material during the Fall 2016 semester about electrochemistry, even though a large emphasis of the course was structured around galvanic cells and redox chemistry. This was also during a semester where challenging problem solving was a core entity in the teaching demonstrations given by students.

It was decided for the Winter 2017 semester that more focus should be on data interpretation and thinking of unique scientific hypotheses that were testable in our laboratories. Although the change was in response to student feedback from the Fall 2016 semester to improve the learning experience for students in the Winter 2017 semester, it does limit the interpretation of how presentation-style problem solving impacts student learning.

The size of the course being limited to ~22 students per semester also limited the statistical analysis of this study and does not provide any statistical evidence suggesting a discussion-centered general chemistry laboratory increases student's reasoning skills compared to the traditional format adopted by the Department of Chemistry at the University of Michigan. However, it is important to remember the scope of this study was isolated to formulating this new format at UM, with statistical analysis of this technique to be completed once the correct format was developed and fundamental details of the format were put into practice and shown to be feasible at the small scale.

The larger point that this study reveals is that recitation or discussion-style settings of chemistry laboratories was positively received from students in improving their understanding of the scientific method when emphasis is placed on this during the labs. However, it is imperative that students pay individual attention to the material outside of a structured class time to challenge themselves on the material, as conceptual knowledge of the material did not seem to change much solely based on the different format. Presentations of the data did seem to introduce scientific communication to the students, but it did not add much to the overall learning goal for students to use the scientific method effectively and independently. Therefore, a discussion-style setting implemented within the large-scale chemistry laboratory settings is recommended, one that would focus less on oral presentations during a laboratory period. If this format were adopted at the larger scale, this study suggests that using the pre-lab instructional videos as supplementary guides and tutorials in addition to a more traditional lecture hall style is best. In addition, discussions could be instituted at the end of the lab experiment as a full 1-hour time slot, and smaller time (~5-10 minutes) could be allotted for presentations of challenging problems rather than the longer 15 – 30 minute presentations. Lastly, the implementation of the practical exam showed that at least 3 similar lab practicals are needed to accommodate multiple sections that meet throughout the week. It is important that students have two-weeks advance notice of the lab practical topic so that they can prepare sufficiently, and that only numerical values (e.g.—concentrations) or non-essential

chemical parameters (e.g.—spectator ions in this case) should be altered between each lab practical.

5.6 Conclusions

This study sought to develop a discussion-centered general chemistry laboratory in the Department of Chemistry at the University of Michigan that would increase students' participation in the scientific method, with an end-of-term lab practical as an evaluation tool. Surveys were also used to probe the level of acceptance students had for the various materials and structural entities developed in the study. It is suggested from the post-semester survey data and results of the lab practical from both sections that students had overall a positive response to the format. In the Winter 2017 semester, more emphasis was placed on hypothesis-based science, drawing conclusions specifically related to students' original hypothesis, and thinking of new ideas to test for future experiments. This was different from the Fall 2016 semester, which focused more on theoretical understanding of the material through oral presentations and difficult follow-up questions during discussion portions of the laboratory session. Students found the discussion portion of the laboratory to be paramount to their success, while presentation-style teaching demonstrations had a lesser, but still positive influence on students.

Although students were not experimenting with their own questions and designing their own experiments throughout the semester, they were constantly engaged with the idea while also exploring the common techniques learned in a general chemistry setting. The format allowed students to get acquainted with the scientific method slowly without over-burdening them with answering difficult experimental questions they only recently were exposed to. On the other hand, lab protocols that are structured to integrate previous concepts and techniques, and later labs that are allow students to explore their own scientific questions independently would match well with the learning goal of this study.

This new format gives students more time to review the material on their own outside of lab before attending lecture, moving at their own pace to engage the material, show stronger participation *during lab*, and an experience involving a productive and research-like lab environment. The material learned in this section was designed to translate the students to higher level science courses that do require them to think about their own scientific questions, designing

new hypotheses on topics that they have not yet explored, and even prepare them to join a lab as an undergraduate research assistant.

5.7 References

(1) Fautch, J.M., The Flipped Classroom for Teaching Organic Chemistry in Small Classes: Is It Effective?, *Chem. Educ. Res. Pract.* **2015**, *16*, 179.

(2) Flynn, A.B., Structure and Evaluation of Flipped Chemistry Courses: Organic & Spectroscopy, Large and Small, First to Third Year, English and French, *Chem. Educ. Res. Pract.* **2015**, *16*, 198.

(3) Eichler, J.F.; Peeples, J., Flipped Classroom modules for Large Enrollment General Chemistry Courses: a Low Barrier Approach to Increase Active Learning and Improve Student Grades, *Chem. Educ. Res. Pract.*, **2016**, *17*, 197.

(4) Reid, S.A., A Flipped Classroom Redesign in General Chemistry, *Chem. Educ. Res. Pract.* **2016**, *17*, 914

(5) Ryan, M.D.; Reid, S.A., Impact of the Flipped Classroom on Student Performance and Retention: A Parallel Controlled Study in General Chemistry, *J. Chem. Educ.* **2016**, 93, 13 – 23.

(6) Seery, M.K., Flipped Learning in Higher Education Chemistry: Emerging Trends and Potential Directions, *Chem. Educ. Res. Pract.* **2015**, *16*, 758 – 768.

(7) Smith, J.D., Student Attitudes Toward Flipping the General Chemistry Classroom, *Chem. Educ. Res. Pract.*, **2013**, *14*, 607 – 614.

(8) Fung, F.M., Using First-Person Perspective Filming Techniques for a Chemistry Laboratory Demonstraiton to Facilitate a Flipped Pre-Lab. *J. Chem. Educ.* **2015**, *92*, 1518 – 1521.

(9) Teo, T.W.; Tan, K.C.D., Yan, Y.K.; Teo, C.; Yeo, L.W., How Flip Teaching Supports Undergraduate Chemistry Laboratory Learning. *Chem. Educ. Res. Pract.* **2014**, *15*, 550 – 567.

(10) Smith, D.K., iTube, YouTube, WeTube: Social media Videos in Chemistry Education and Outreach. *J. Chem. Educ.* **2014**, *91*, 1594 – 1599.

(11) Keeney-Kennicutt, W.L.; Merchant, Z.H., Using Virtual Worlds in the General Chemistry Classroom. *ACS Symposium Series*, Chapter 8. Pedagogic Roles of Animations and Simulations in Chemistry Courses, **2013**.

(12) IRB number HUM00125248 Feb. 27, 2017.

(13) Datta, D.; Asci, Y.S.; Tuyun, A.F., Intensification of Citric Acid Extraction by a Mixture of Tioctylamine and Tridodecylamine in Different Diluents. *J. Chem. Eng. Data* **2015**, *60*, 960 – 965.

(14) Okorafor, O.C., Solubility and Density Isotherms for the Sodium-Water-Methanol System. *J. Chem. Eng. Data*, **1999**, *44*, 488 – 490.

Chapter 6
Conclusions and Potential Future Directions

6.1 Summary of Presented Work

The work presented herein quantifies stability ranges and conditions by which common anchoring groups and molecular dyes and catalysts can be used for molecular/solid-state photoanodes in solar water splitting cells. Specifically, 1) the common tether phosphonic acid is not suitable for neutral pH conditions by which many of molecular water oxidation catalysts such as Ru(bda)(pic)$_2$ and Fe(bpmcn)Cl$_2$ are more active for the OER. Instead, hydroxamic acid provides added stability throughout the pH range, despite the lower binding constant under acidic conditions compared to phosphonic acid. 2) Fe(bpmcn)Cl$_2$ has a distinct pH range for operation, and inert storage conditions by which long-term stability can be provided. Specifically, operating under highly acidic or basic conditions forces the decomposition of the complex through the dissociation of the Fe^{2+} or Fe^{3+} center, leaving either $[Fe(H_2O)_6]^{2+}$ in acidic conditions, or a-FeOOH under basic conditions. While this catalyst is most cost-effective compared to other common WOCs, its inherent instability under conditions typically observed during PEC water oxidation leave it non-ideal for a molecular/solid-state photoanode without redesigning the ligand for higher stability while maintaining OER activity. 3) Morphology of the a-FeOOH electrocatalyst can be influenced both during precipitation in base under air and electrochemically deposited, through the use of the η^4 bpmcn ligand bound to Fe^{2+} with C_{2V} symmetry.

6.2 Improving Adsorption and Stability of Molecular|Solid-State Photoanodes

In Chapter 2, I presented my work on the quantitative analysis of phosphonic acid and hydroxamic acid as viable anchoring groups for tethering $[Ru(bpy)_3]^{2+}$ to TiO_2 and WO_3. Although hydroxamic acid does suit better for binding molecular dyes or catalysts to the surface of TiO_2 over phosphonic acid in neutral and basic conditions, it is still not ideal for long-term stability of molecule|semiconductor interaction over time. With a binding constant ~10^3, the lifetime of the

photoanode in aqueous solution is a mere couple of hours prior to significant dissociation from the metal oxide surface. It is therefore paramount that a functional group that binds tightly to metal oxides with $K_B \geq 10^5$ while also maintaining adequate electron transfer from the molecular dye or catalyst to the semiconductor surface. One example that has been recently reported is silatrane and triethoxysilane, reported to have long-term stability for bound molecular dyes and catalysts to the surface of TiO_2 with a pH range from 2 to 11.[1,2] However, careful investigation into the binding constant and rates of adsorption/desorption as a function of pH have not been completed on this anchor, making it difficult to conclude the longevity of its possible interaction with a metal oxide surface both in the dark and under illumination during standard operation of a PEC cell. In addition, many report burying these complexes inside an insulating layer such as Al_2O_3, TiO_2, or ZnO improves stability of the molecule|solid-state interaction, but also suffer photocurrent loss and in some cases still continue to desorb the complexes over time during operation.[3]

It is worthy to consider depositing a solid-state layer to provide adequate stability of the molecular catalyst or dye to prevent dissociation from the surface. But, instead of using a molecule, use a solid-state electrocatalyst capable of both withstanding the harsh conditions of water oxidation while also serving as an electric contact between the electrolyte, the molecular dye or catalyst, and the metal oxide surface. Electrodeposition of a-FeOOH has already been shown to occur in conditions by which a molecular tether such as hydroxamic acid can be bound long enough for deposition of the metal oxyhydroxide to occur, both in Chapter 4 of this thesis and within the literature.[4,5,6] Therefore, it would be a synthetically simpler approach for increasing the stability of the molecular|solid-state photoanode by replacing insulating metal oxides with electrocatalytic metal oxyhydroxides active for the OER. However, it is worth mentioning that any electrodeposition of a-FeOOH should involve a photoelectrodeposition step at first, in order to ensure that deposition occurs at the molecular dye, where light absorption would take place. Photoelectrodeposition has been used in the past to coat $BiVO_4$ and WO_3 with FeOOH to ensure good electrical contact between the FeOOH film and the electrochemically active sites on the underlying metal oxide semiconductor.[4,5] This ensures that the molecular complex itself is indeed buried within the material deposited, while also providing good electrical contact to the material being deposited.

6.3 Taking Advantage of the $Fe^{III}–O_2^-$ Adduct in Oxidation Reactions

In Chapter 3, I discussed my work describing the dissociation of Fe^{2+} from the bpmcn ligand under highly acidic and basic conditions, and the inherent reactivity of the $Fe(bpmcn)Cl_2$ complex under illumination in the presence of O_2. Outside of WOCs, many chemists have used non-heme iron complexes in C–H activation of organic substrates and rely on sacrificial oxidants to do so.[7–10] Ideally, dissolved O_2 can be used as the oxidant instead of sacrificial oxidants with the help of visible light to provide the energy needed to drive the reaction, as discussed in the introduction of Chapter 3 with the formation of $Fe^{III}–O_2^-$. However, exploration must be done to probe the reactivity of the $Fe^{III}–O_2^-$ intermediate formed by illuminating $Fe(bpmcn)Cl_2$ in the presence of oxygen to understand its reactivity toward organic substrates with an activated C–H bond for oxidation, such as benzyl alcohol as a test substrate. Further, if the complex is reactive toward this substrate, it is crucial to understand the possible byproducts formed, and whether this complex can act catalytically under these conditions. If conditions are met to make this complex undergo catalytic C–H activation under illumination in the presence of O_2, it could serve as a starting point for zero-waste C–H oxidation. However, the first step in pursuing this possibility must include determining the decomposition products of oxidation with $Fe^{III}–O_2^-$. Given that this complex is already known to undergo oxidation at the C–N bond at the alpha-carbon of the pyridine ring in bpmcn, as shown in Chapter 3, it is possible that this complex could also serve to oxidize a substrate like benzyl alcohol to benzaldehyde under mild conditions. If the complex oxidizes the substrate stoichiometrically by ending at a product that contains ligands at the active site of the Fe-complex which are difficult to eliminate in a catalytic cycle. It would the be worth pursuing additives or conditions such as a strong acids or bases suitable for returning the complex to the active $Fe^{III}–O_2^-$ species if possible.

6.4 Ligand Dependence on and Optimization of a-FeOOH Electrodeposition Morphology and Film Thickness

In Chapter 4, I discussed my work highlighting the decomposition of $Fe(bpmcn)Cl_2$ to a-FeOOH, which was shown to be active for water oxidation under 600 mV overpotential at pH 14, with anisotropic growth of the particles in both precipitation reactions in solution in air, and electrodeposition onto FTO substrates. It is important to note that the reasoning behind anisotropic growth of a-FeOOH is still unclear. Possibilities include the slow release of $Fe(bpmcn)Cl_2$, leading

to slightly more crystalline growth and less nucleation. It is also possible that the bpmcn ligand serves as a chelating agent during particle growth, similar to other chelating agents in preparation methods for the synthesis of α-Fe_2O_3.[11,12] Further work must be done to understand the particular functionality of the ligand, including dynamic light scattering experiments to probe crystal growth dynamics, and zeta potential to measure particle size distributions and growth rate as a function of pH, concentration of Fe(bpmcn)Cl_2, and temperature.[13,14] It is also important to explore how the identity of the ligand, including the coordination number, functional groups chelated to the metal (pyridyl, amine, amide, alcohol, carboxylate, etc.), and symmetry of the complex affects growth of the particles. These variables could help identify key parameters that govern particle size, morphology, and crystallinity. Given it is still unclear what role the ligand plays in how a-FeOOH precipitates from Fe(bpmcn)Cl_2, these experiments may provide insight into how researchers can influence the growth of electrocatalysts such as NiOOH or FeOOH, two well-known electrocatalysts with high activity for water oxidation under low applied bias.[6,15]

6.5 Summary and Concluding Remarks

With the work I have presented in this thesis, I have demonstrated attention to detail regarding stability and practicality of molecular|solid-state photoanodes built from the ground up, starting at the anchor-metal oxide interaction and moving toward the chemical stability of the molecular complex tethered to the surface. This thesis stresses careful choice and design of the molecular|solid-state architectures in PEC cells to optimize the Faradaic efficiency of the photoanode for water oxidation with visible light for extended periods of time. While a few years ago, a lot of focus in the literature was spent on designing high photocurrent systems with these types of architectures, attention has now moved toward increasing the stability to maintain these high photocurrents (> 1 mA cm^{-2}) and high selectivity. This thesis adds to that story, and focuses the attention on the anchor itself in addition to carefully considering the conditions suitable for the chosen molecular dye or catalyst and the semiconductor on which it is to be anchored. As mentioned earlier, there have been attempts to bury complexes bound to surfaces with insulating materials to prolong the interactions between the molecular catalyst or dye to the surface; however, I propose that these insulating materials be replaced with solid-state electrocatalysts that serve both to prolong the molecular|solid-state interactions, and increase kinetic rates of reaction for water oxidation on the surface.

6.6 References

(1) Brennan, B.J.; Llansola, M.J.; Portolés, L.; Liddell, P.A.; Moore, T.A.; Moore, A.L.; Gust, D., Comparison of Silatrane, Phosphonic Acid, and Carboxylic Acid Functional Groups for Attachment of Porphoryin Sensitizers to TiO_2 in Photoelectrochemical Cells, *Phys. Chem. Chem. Phys.* **2013**, *15*, 16605 – 16614.

(2) Materna, K.L.; Crabtree, R.H.; Brudvig, G.W., Anchoring Groups for Photocatalytic Water Oxidation on Metal Oxide Surfaces, *Chem. Soc. Rev.* **2017**, *46*, 6099 – 6110.

(3) Wang, D.; Sheridan, M.V.; Shan, B.; Farnum, B.H.; Marquard, S.L.; Sherman, B.D.; Eberhart, M.S.; Nayak, A.; Dares, C.J.; Das, A.K.;Bullock, R.M.; Meyer, T.J., Layer-by-Layer Molecular Assemblies for Dye-Sensitized Photoelectrosynthesis Cells Prepared by Atomic Layer Deposition, *J. Am. Chem. Soc.* **2017**, *139*, 14518 – 14525.

(4) Seabold, J.A., Choi, K.-S., Efficient and Stable Photo-Oxidation of Water by a Bismuth Vanadate Photoanode Coupled with an Iron Oxyhydroxide Oxygen Evolution Catalyst, *J. Am. Chem. Soc.* **2012**, *134*, 2186 – 2192.

(5) Lhermitte, C.R.; Verwer, G.; Bartlett, B.M., Improving the Stability and Selectivity for the Oxygen-Evolution Reaction on Semiconducting WO_3 Photoelectrodes with a Solid-State FeOOH Catalyst, *J. Mater. Chem. A*, **2016**, *4*, 2960 – 2968.

(6) Chemelowski, W.D.; Lee, H.-C.; Lin, J.-F.; Bard, A.J.; Bullins, C.B., Amorphous FeOOH Oxygen Evolution Reaction Catalyst for Photoelectrochemical Water Splitting, *J. Am. Chem. Soc.*, **2014**, *136*, 2843 – 2850.

(7) Mühldorf, B.; Wolf, R. C—H Photooxygenation of Alkyl Benzenes Catalyzed by Riboflavin Tetraacetate and a Non-Heme Iron Catalyst. *Angew. Chem. Int. Ed.* **2016**, *55*, 427.

(8) Costas, M.; Que, Jr., L. Ligand Topology Tuning of Iron-Catalyzed Hydrocarbon Oxidations. *Angew. Chem. Int. Ed.* **2002**, *41*, 2179.

(9) Cussó, O.; Garcia-Bosch, I.; Ribas, X.; Lloret-Fillol, J.; Costas, M. Asymmetric Epoxidation with H_2O_2 by Manipulating the Electronic Properties of Non-heme Iron Catalysts. *J. Am. Chem. Soc.* **2013**, *135*, 14871.

(10) Nam, W.; Lee, Y.-M.; Fukuzumi, S. Tuning Reactivity and Mechanism in Oxidation Reactions by Mononuclear Nonheme Iron(IV)-Oxo Complexes. *Acc. Chem. Res.* **2014**, *47*, 1146.

(11) Ishaq, S.; Sikora, A.; Scheidler, N.; Hambleton, C.; Katz, J.E., Enhancement of Water Oxidation Photocurrent for Hematite thin Films Electrodeposited with Polyvinylpyrrolidone, *J. Electrochem. Soc.* **2016**, *163*, F1330 – F1336.

(12) Taffa, D.H.; Hamm, I.; Dunkel, C.; Sinev, I.; Bahnemann, D.; Wark, M., Electrochemical Deposition of Fe_2O_3 in the Presence of Organic Additives: A Route to Enhanced Photoactivity, *RSC Adv.* **2015**, *5*, 103512 – 103522.

(13) Bhattacharjee, S., DLS and Zeta Potential – What They Are and What They Are Not?, *J. Cont. Release* **2016**, *235*, 337 – 351.

(14) Berne, B.J., Pecora, R., *Dynamic Light Scattering: With Applications to Chemistry, Biology, and Physics,* Dover Publications, Inc.: Mineola, New York, 2000.

(15) Trotochaud, L.; Young, S.L.; Ranney, J.K.; Boettcher, S.W., Nickel-Iron Oxyhydroxide Oxygen-Evolution Electrocatalysts: The Role of Intentional and Incidental Iron Incorporation, *J. Am. Chem. Soc.* **2014**, *136*, 6744 – 6753.

Appendix A

Supporting Information for Chapter 2

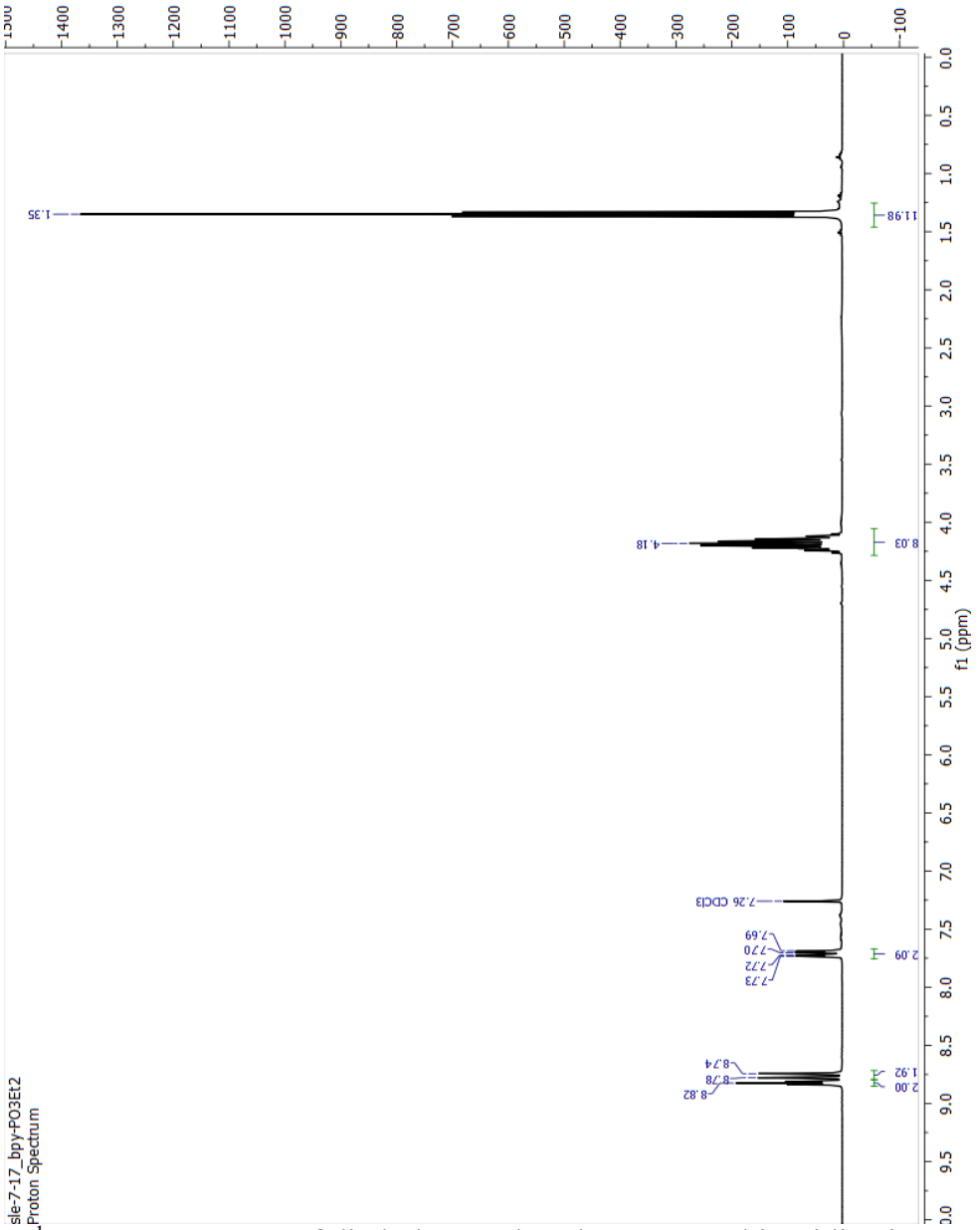

Figure A1. ^{1}H NMR spectrum of diethyl-4,4'-phosphonate-2,2'-bipyridine in $CDCl_3$

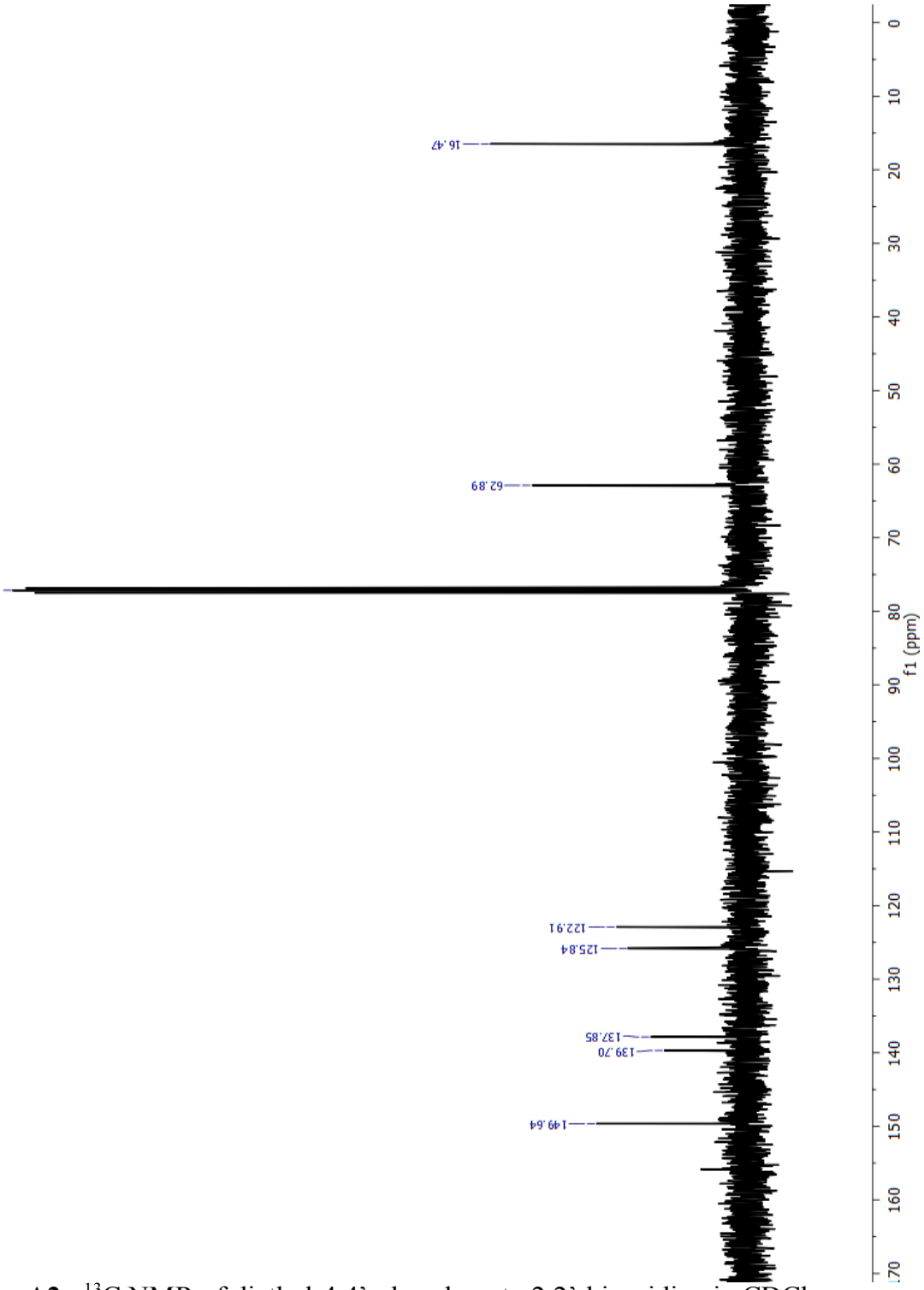

Figure A2. ^{13}C NMR of diethyl-4,4'-phosphonate-2,2'-bipyridine in $CDCl_3$

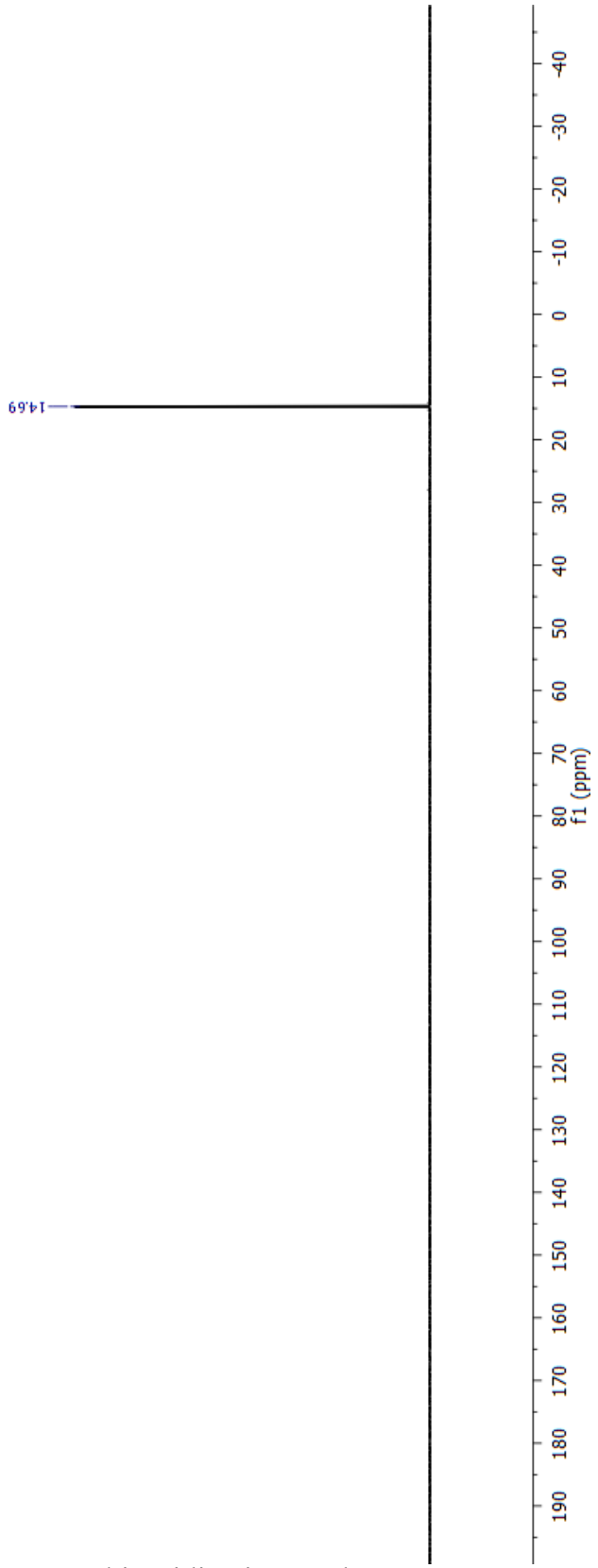

Figure A3. ^{31}P NMR of diethyl-4,4'-phosphonate-2,2'-bipyridine in $CDCl_3$

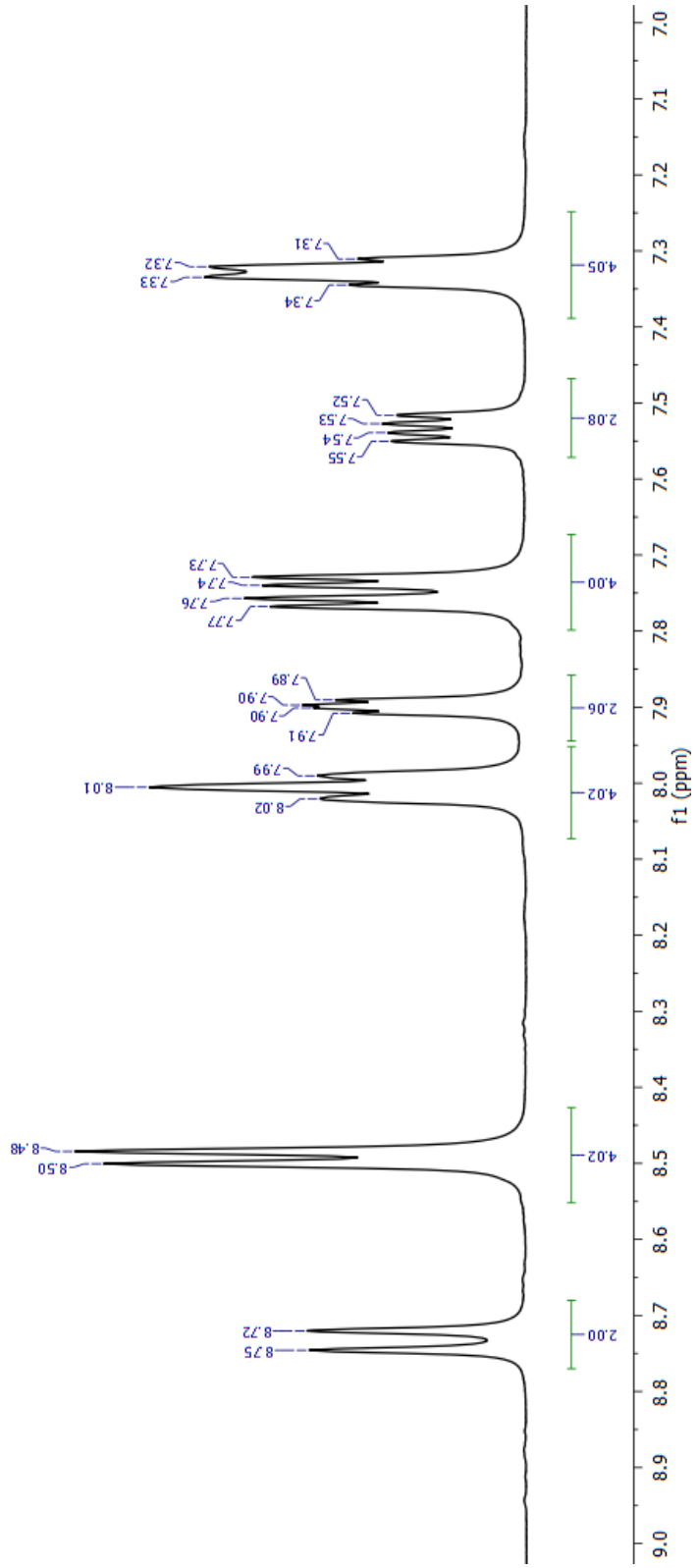

Figure A4. ^{1}H NMR spectrum of **Ru-P** in D_2O

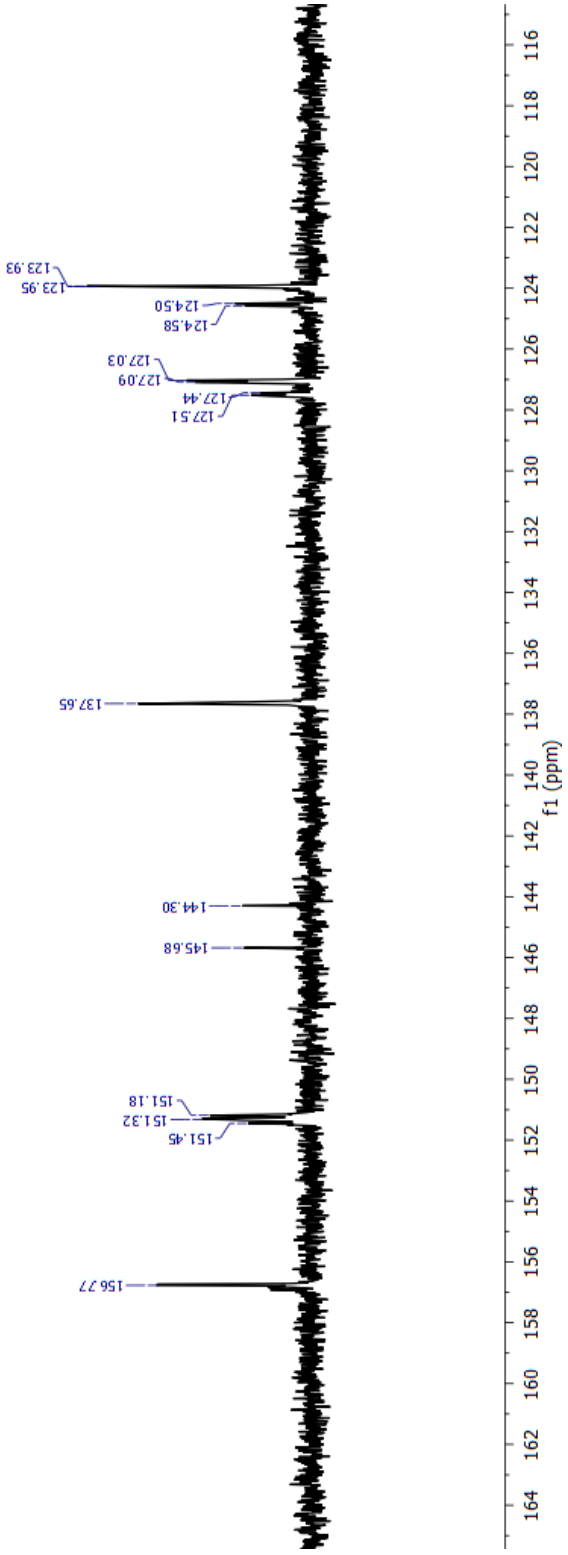

Figure A5. ^{13}C NMR of **Ru-P** in D_2O

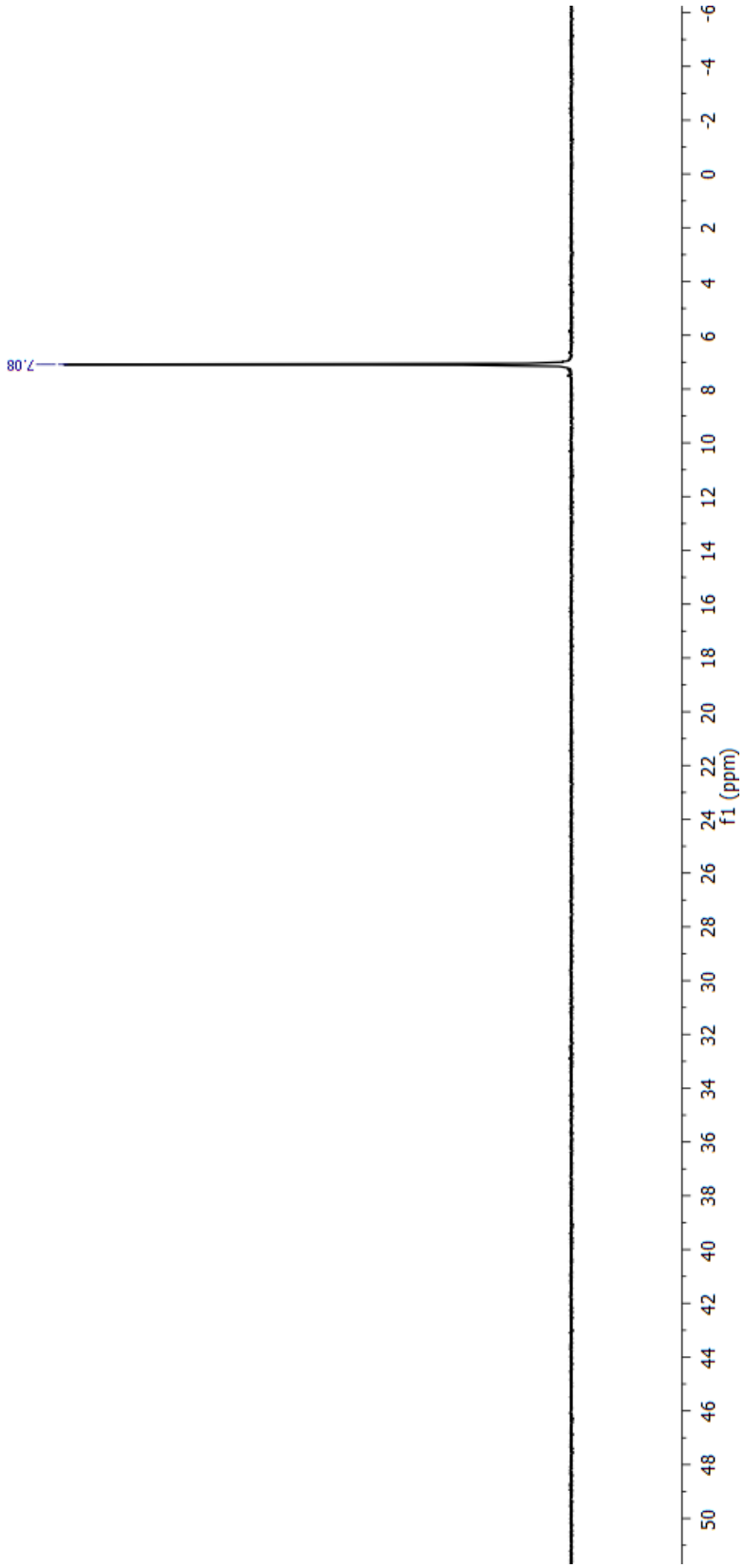

Figure A6. ^{31}P NMR of **Ru-P** in D_2O

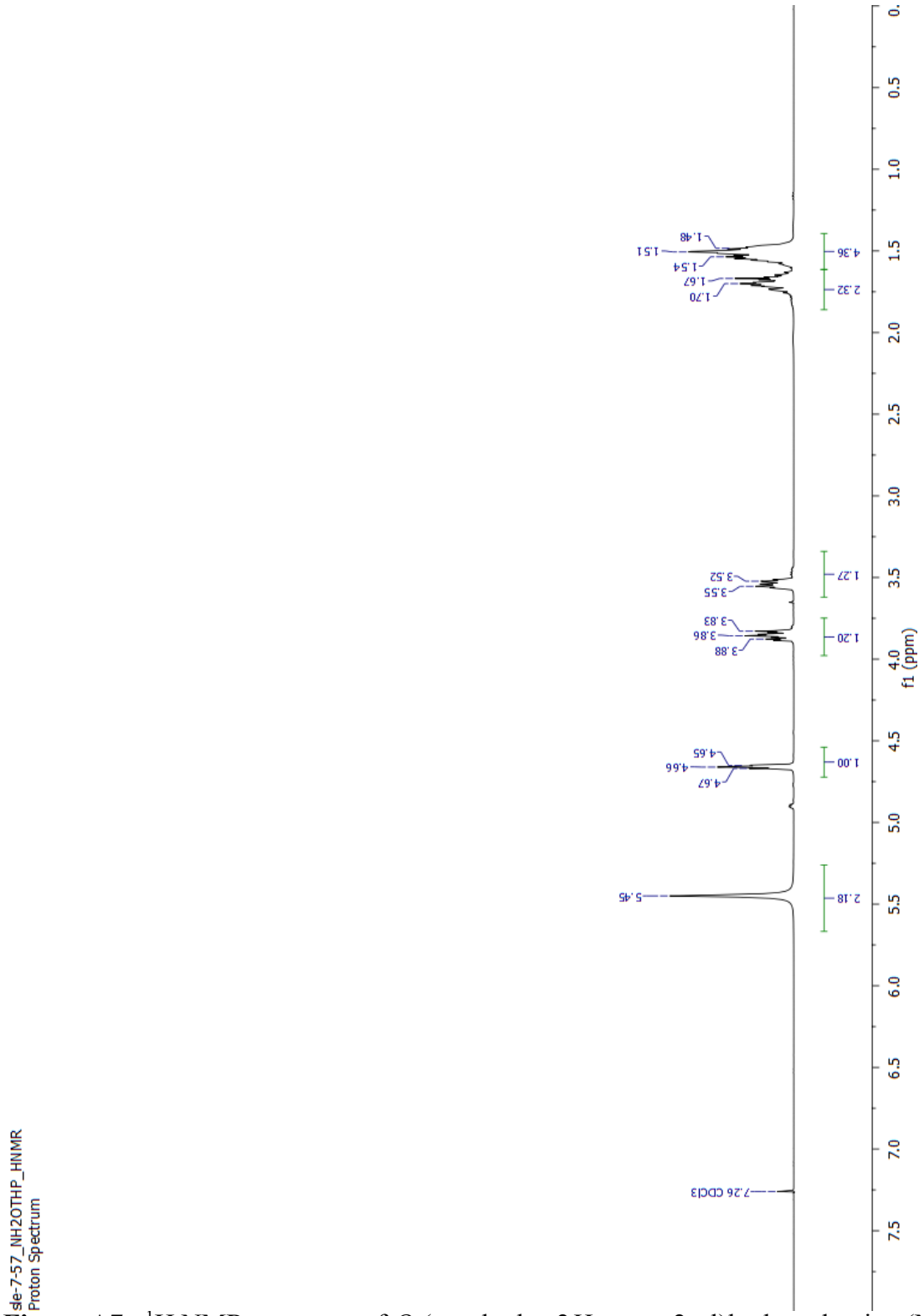

Figure A7. ^{1}H NMR spectrum of *O*-(tetrahydro-2*H*-pyran-2-yl)hydroxylamine (NH_2OTHP)

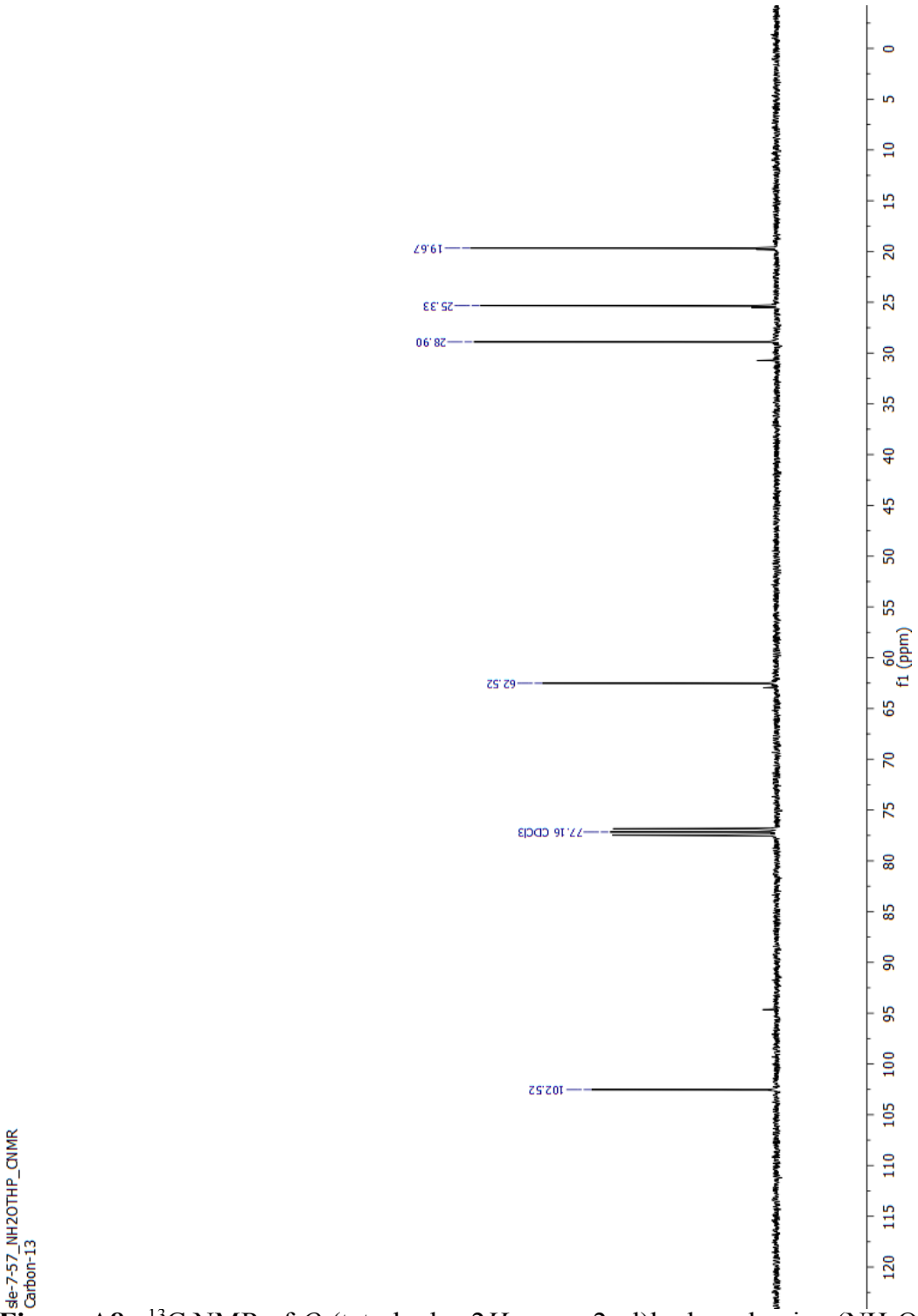

Figure A8. ^{13}C NMR of *O*-(tetrahydro-2*H*-pyran-2-yl)hydroxylamine (NH_2OTHP).

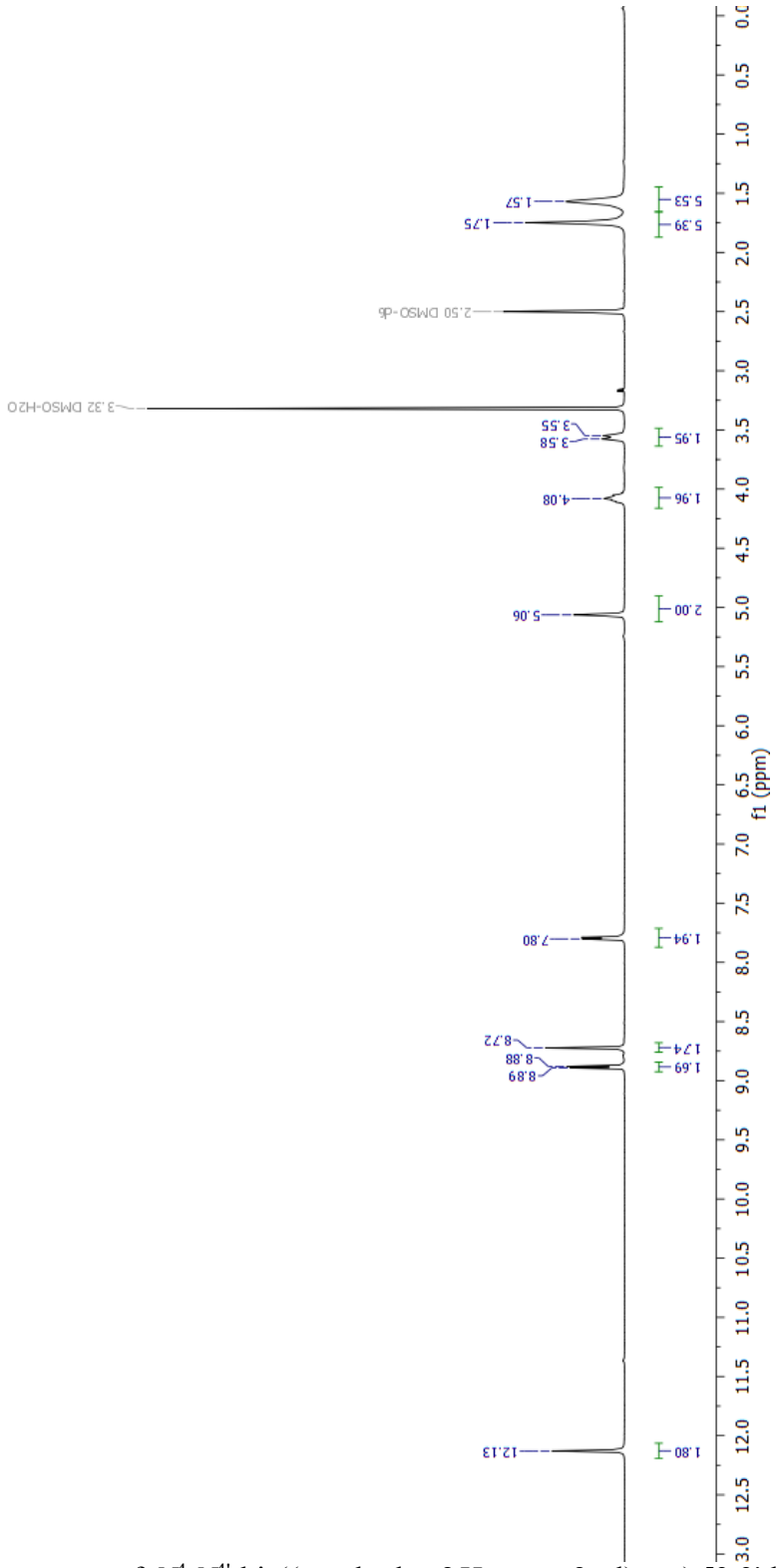

Figure A9. ^{1}H NMR spectrum of N^{4},$N^{4'}$-bis((tetrahydro-2*H*-pyran-2-yl)oxy)-[3,3'-bipyridine]-4,4'-dicarboxamide in d_6-DMSO.

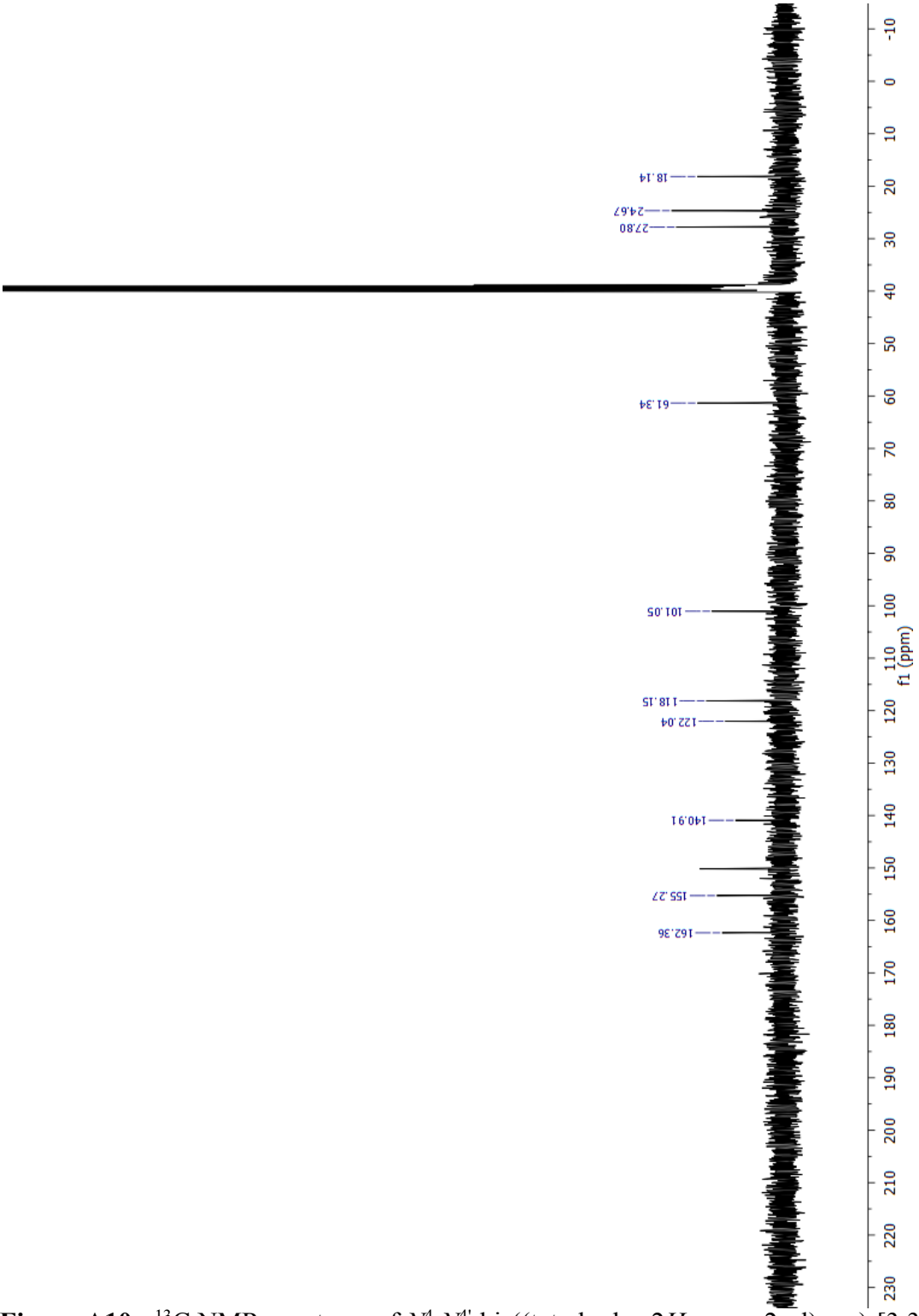

Figure A10. ^{13}C NMR spectrum of N^4,$N^{4'}$-bis((tetrahydro-2*H*-pyran-2-yl)oxy)-[3,3'-bipyridine]-4,4'-dicarboxamide in d_6-DMSO.

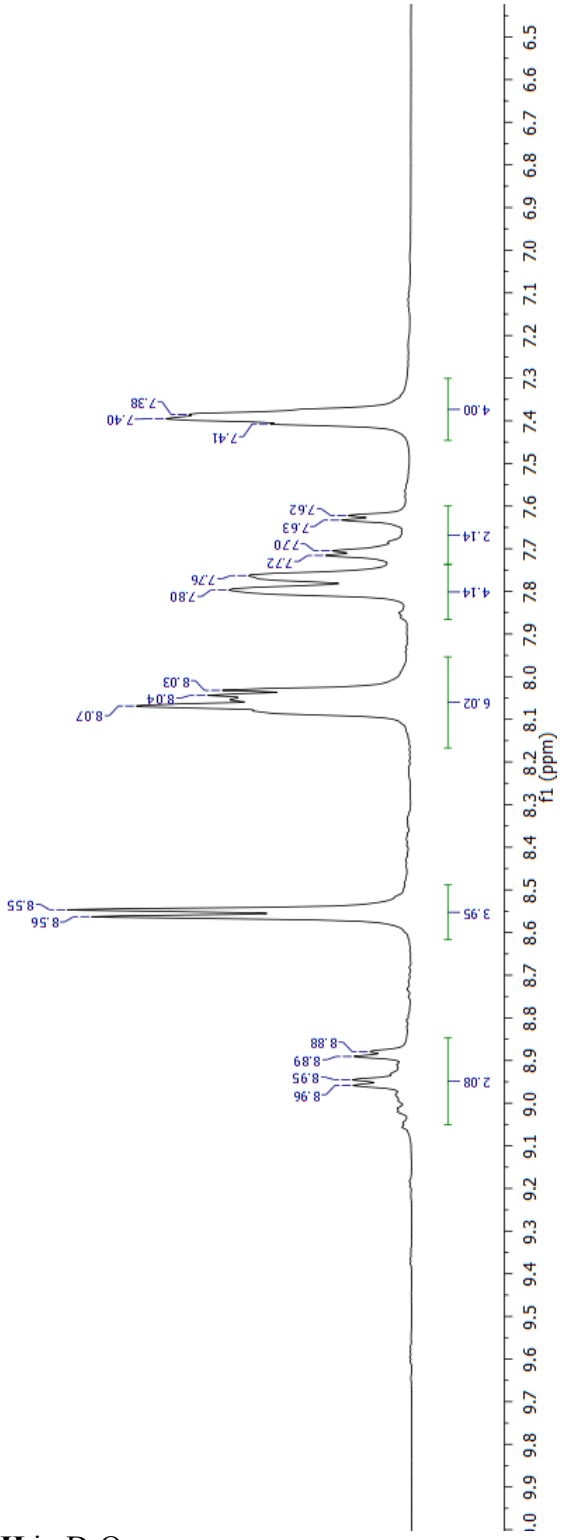

Figure A11. ^{1}H NMR spectrum of **Ru-H** in D_2O.

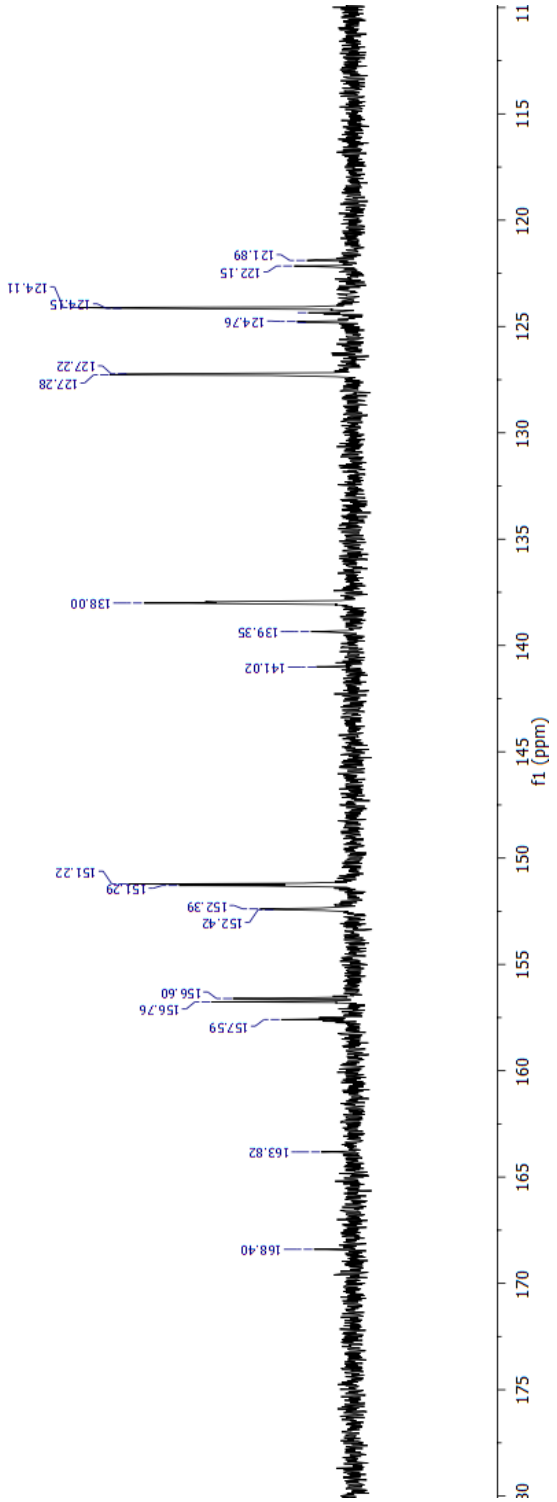

Figure A12. ^{13}C NMR of **Ru-H** in D_2O.

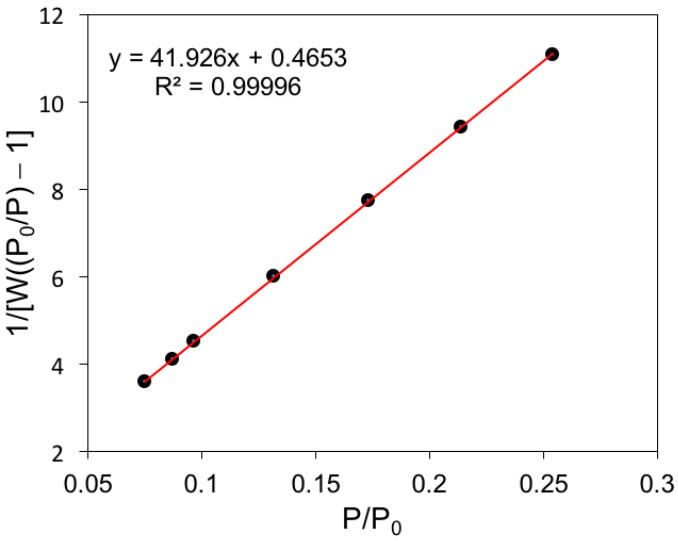

Figure A13. BET plot of TiO_2 anatase 25 nm particles from adsorption isotherm with N_2 gas.

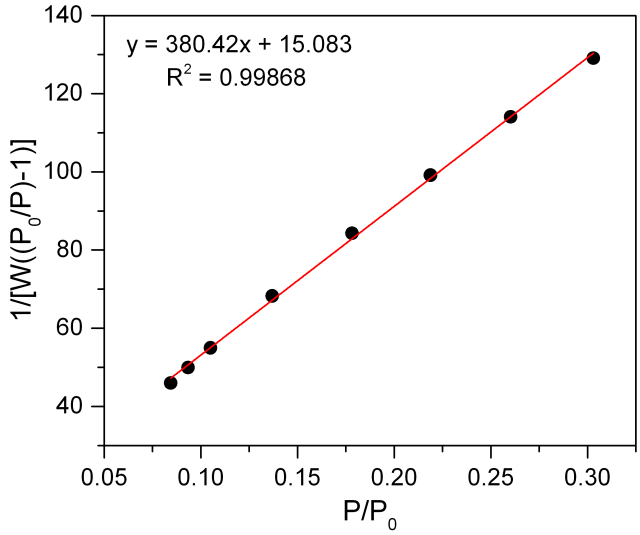

Figure A14. BET plot of WO_3 <100 nm particles from adsorption isotherm with N_2 gas.

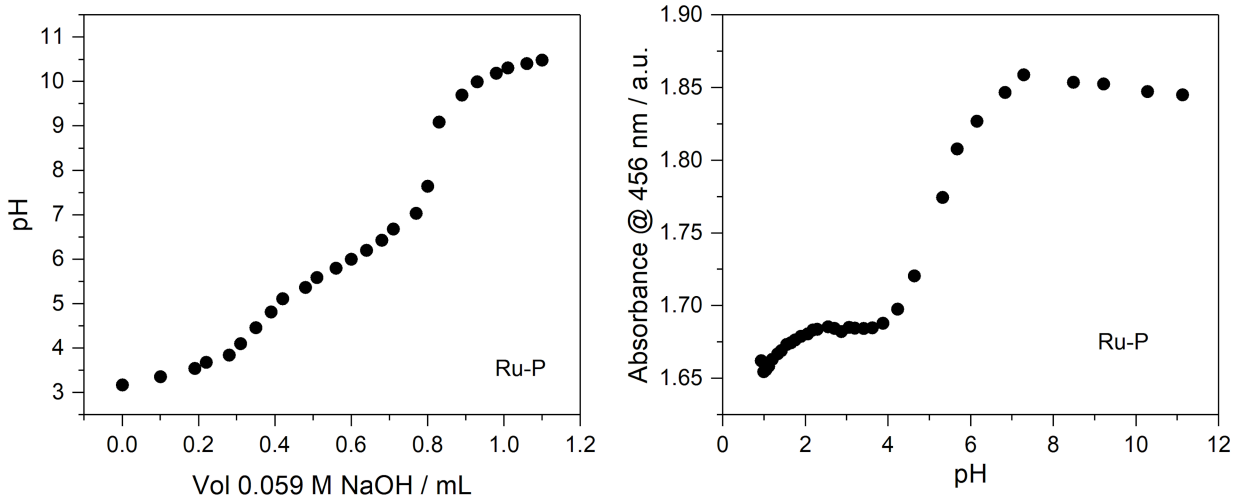

Figure A15. (Left) UV-Vis titration of Ru-P in 0.1 M HNO_3, titrating in small quantities of 10 M, 1 M, or 0.1 M NaOH to raise pH, with absorbance measured at 455nm. This plot was used to approximate the pK_a of the first acidic proton of the phosphonated 2,2'-bipyridine ligand bound to Ru^{II}. (Right) Acid-base titration plot of Ru-P to determine pKa_2, pKa_3, and pKa_4. It is noted that 0.3 mL of NaOH added in 100 mL solution (0.017 mmol) is equal to 1 equivalence versus the moles of Ru-P in solution (0.015 mmol), whereas 0.6 mL NaOH added in the 100 mL solution (0.035 mmol NaOH) is equal to 2 equivalence versus the moles of Ru-P in solution.

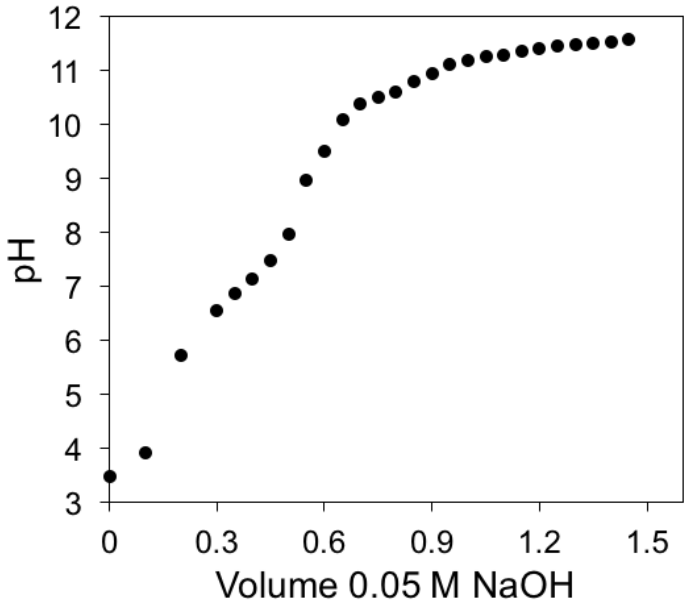

Figure A16. Acid-base titration plot of Ru-H to determine pKa_1 and pKa_2. It is noted that 0.3 mL of NaOH added in 100 mL solution (0.017 mmol) is equal to 1 equivalence versus the moles of Ru-P in solution (0.015 mmol), whereas 0.6 mL NaOH added in the 100 mL solution (0.035 mmol NaOH is equal to 2 equivalence versus the moles of Ru-H in solution.

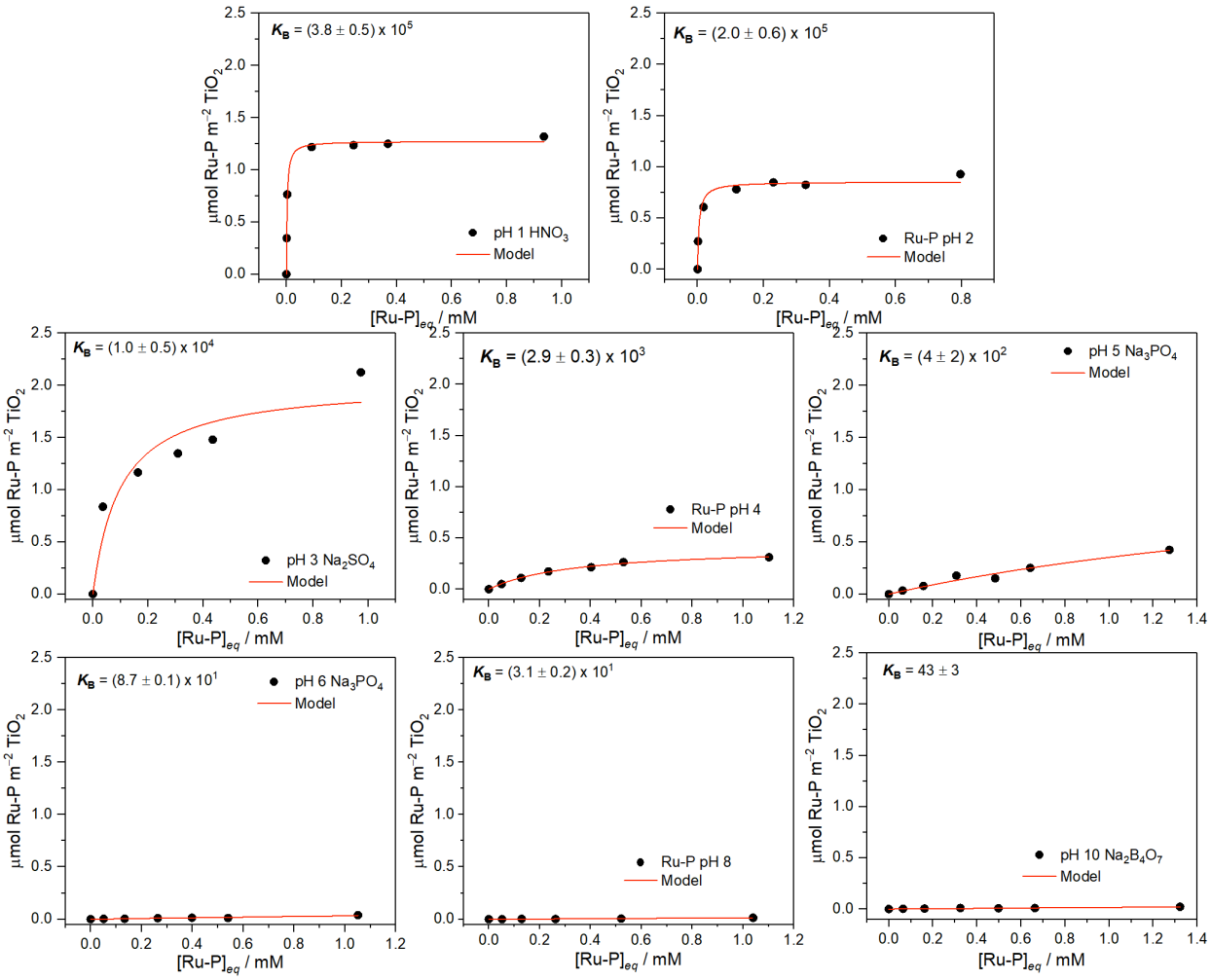

Figure A17. Langmuir plots of **Ru-P** on TiO_2 anatase in aqueous conditions at various pH.

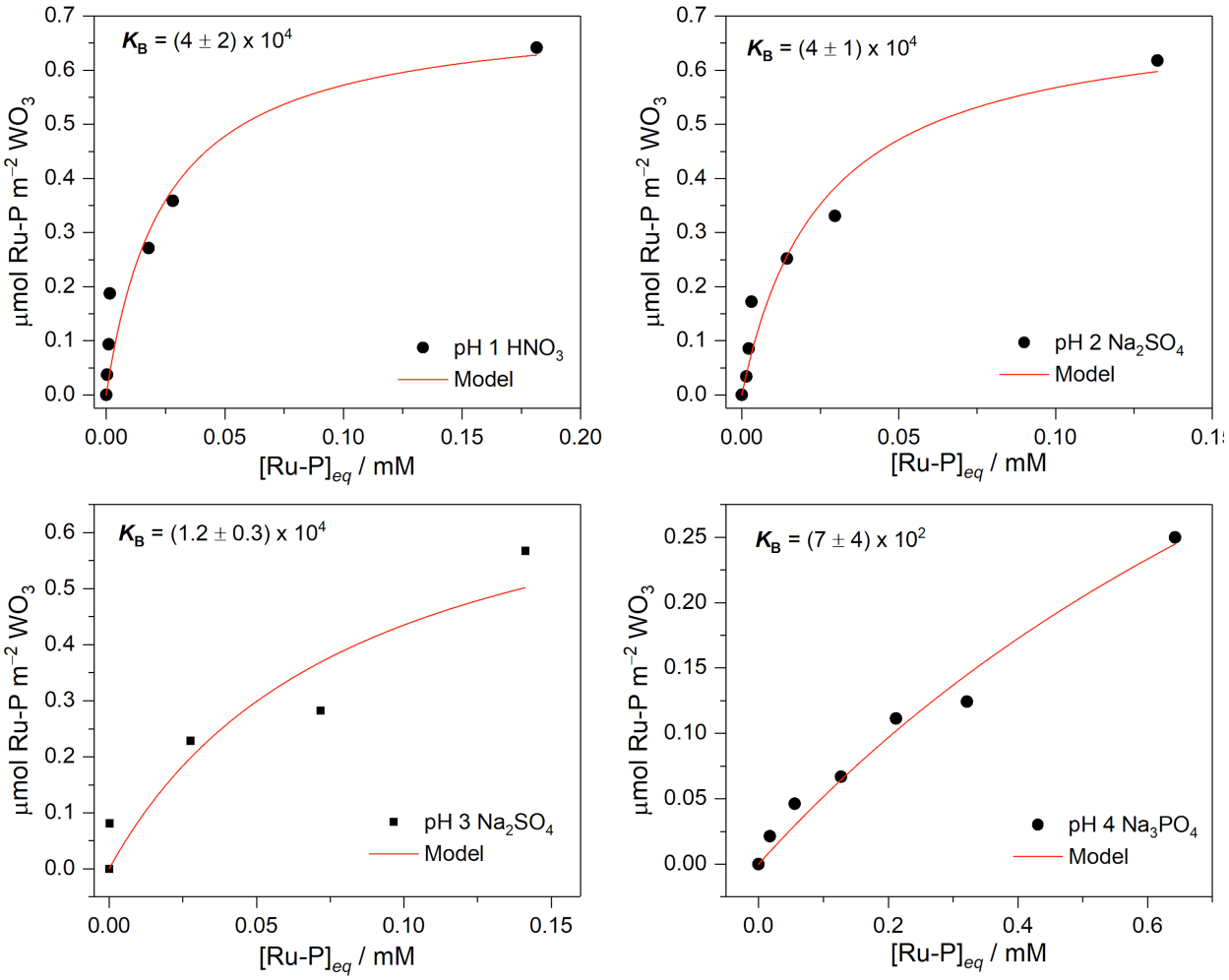

Figure A18. Langmuir plots of Ru-P on WO_3 in aqueous conditions at various pH.

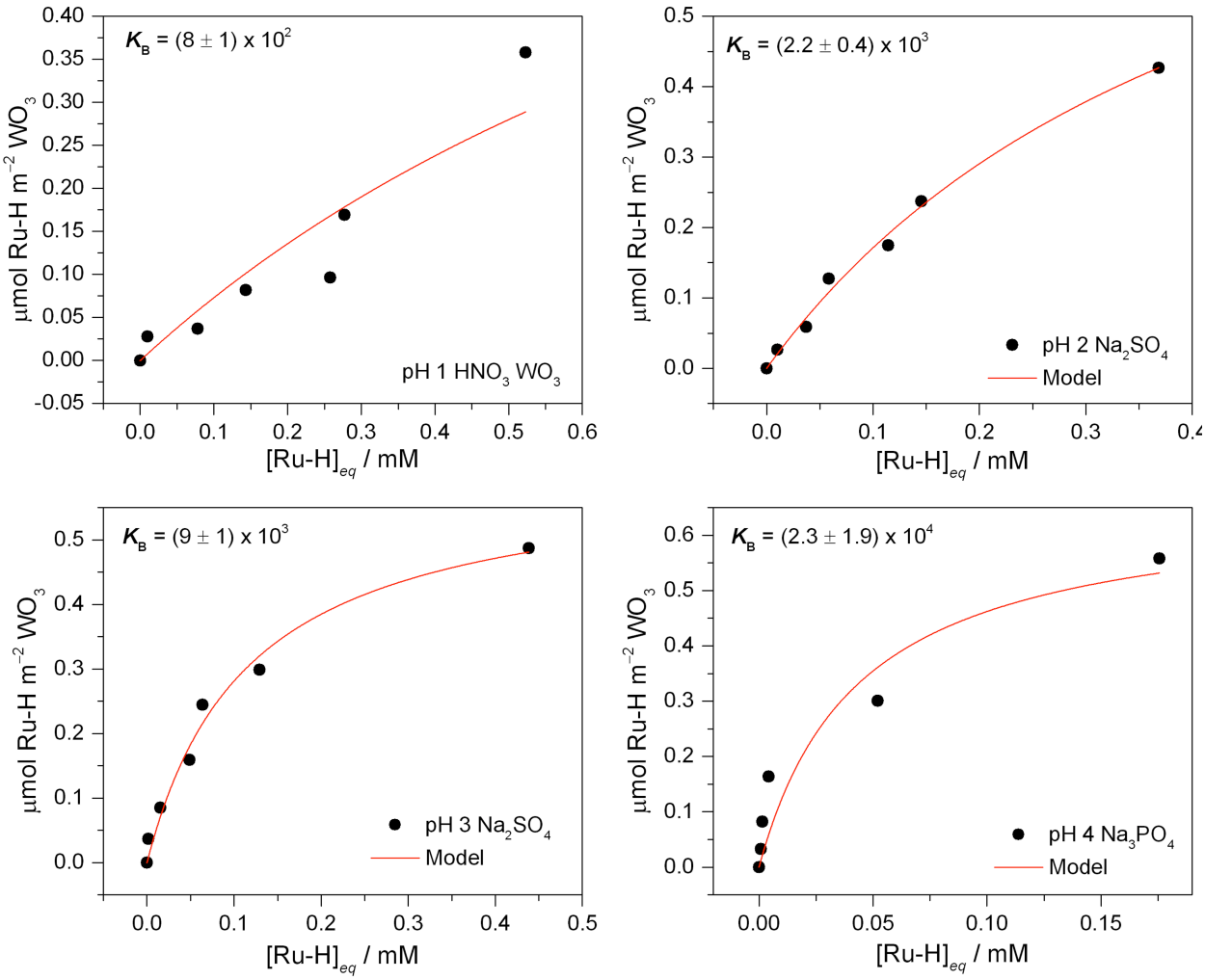

Figure A19. Langmuir plots of Ru-H on WO_3 in aqueous conditions at various pH.

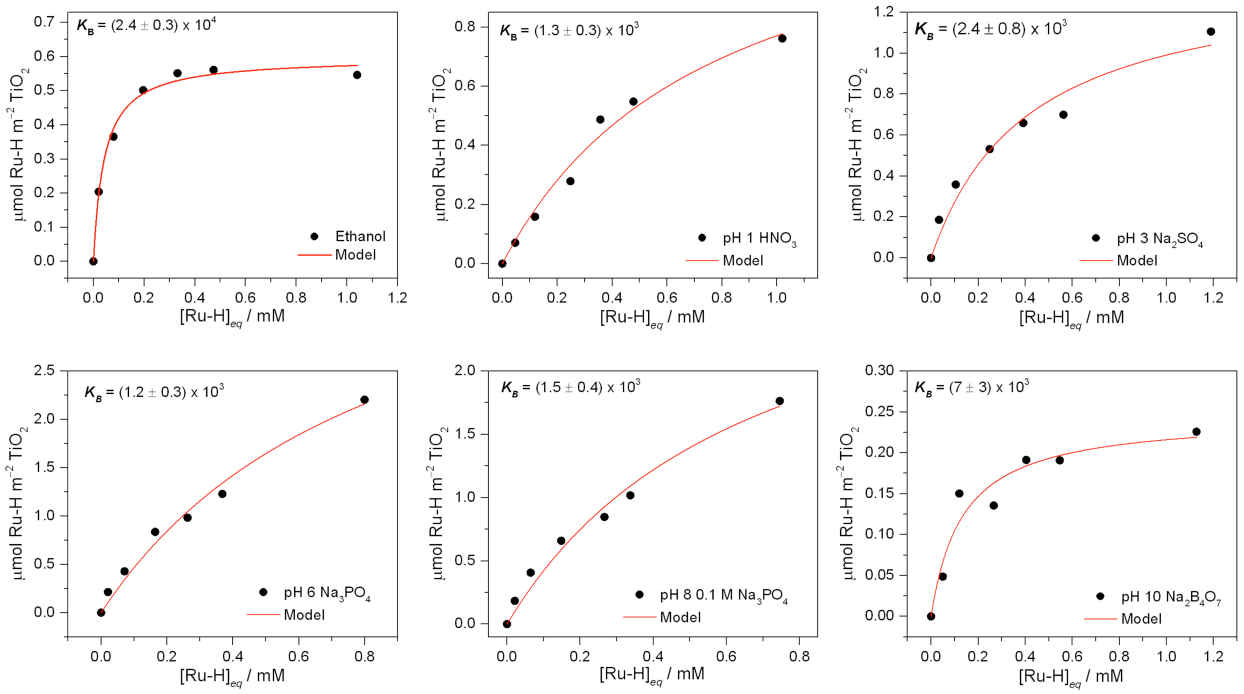

Figure A20. Langmuir plots of **Ru-H** on TiO_2 anatase in aqueous conditions at various pH.

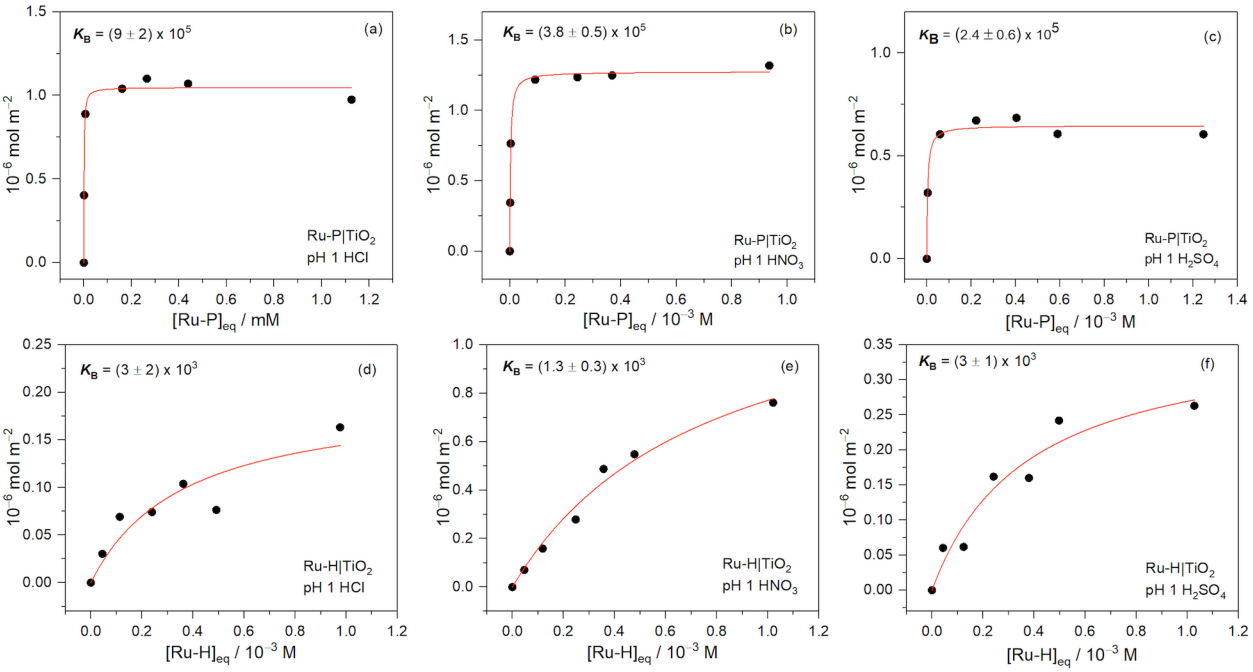

Figure A21. Langmuir plots of Ru-P|TiO_2 at pH 1 using (a) HCl, (b) HNO_3, and (c) H_2SO_4 as an acid, and Ru-H|TiO_2 at pH 1 using (d) HCl, (e) HNO_3, and (f) H_2SO_4 as an acid

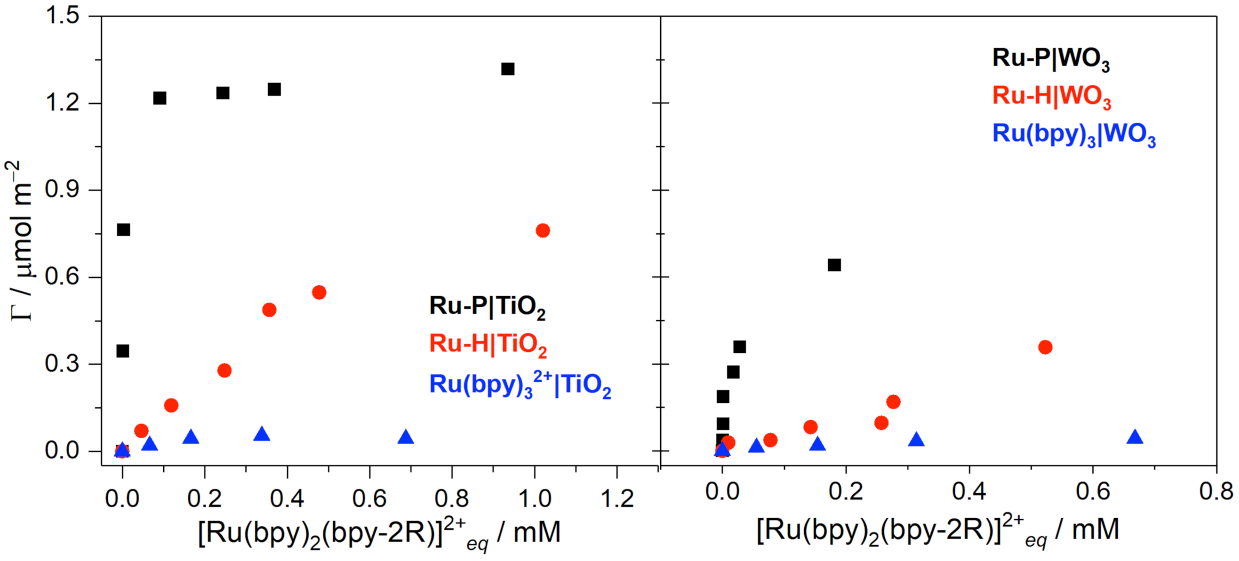

Figure A22. Langmuir plots of **Ru-P**, (black), **Ru-H** (red), and $[Ru(bpy)_3]^{2+}$ (blue) on TiO_2 (left) and WO_3 (right). Here, Γ is defined as the fractional surface coverage of Ru-P, Ru-H, or $[Ru(bpy)_3]^{2+}$ onto the surface of either TiO_2 or WO_3.

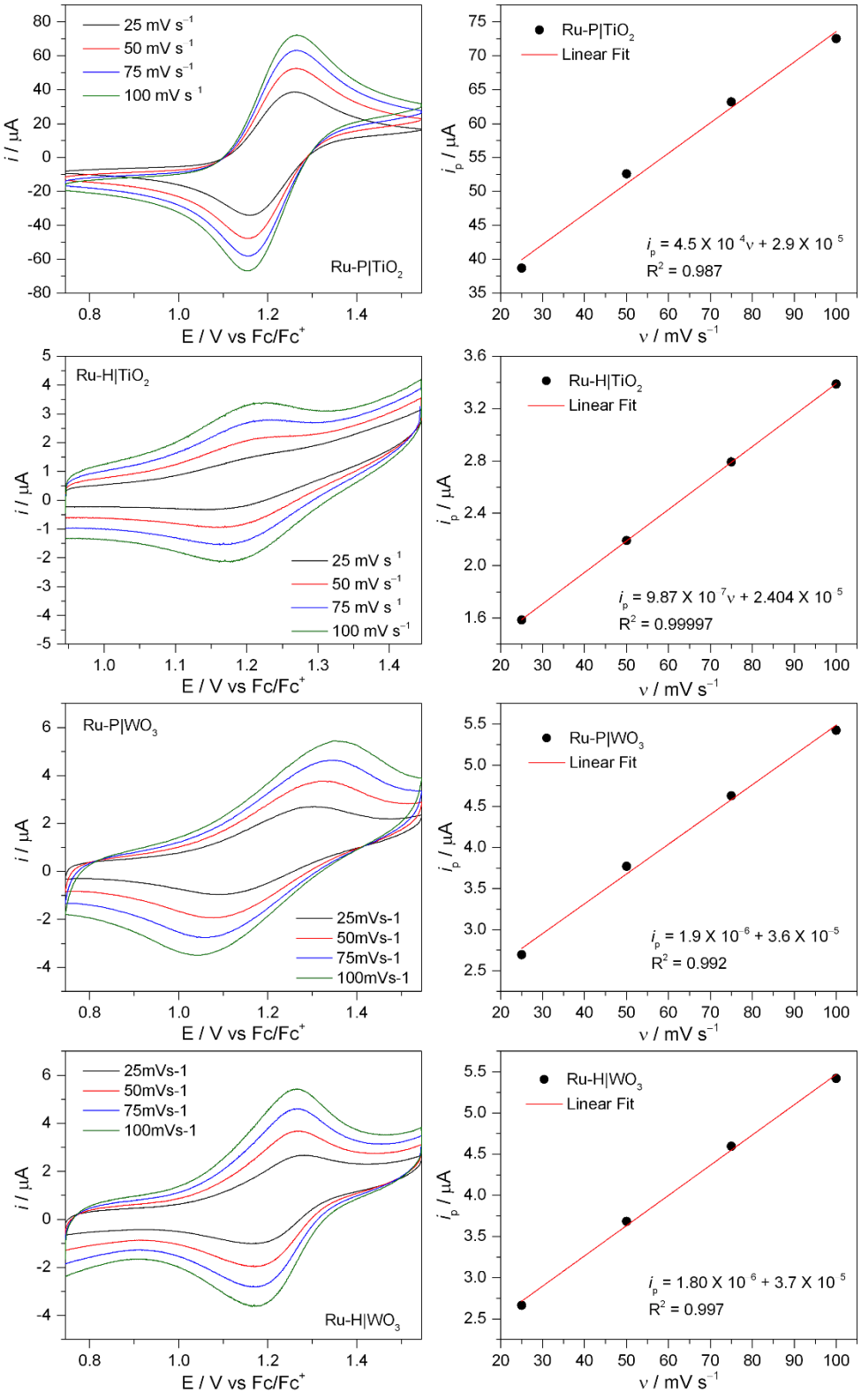

Figure A23. CV scans of Ru-R|TiO_2 or Ru-R|WO_3 films (left) at various scan rates, and linear plots of scan rate vs. anodic peak current, i_p.

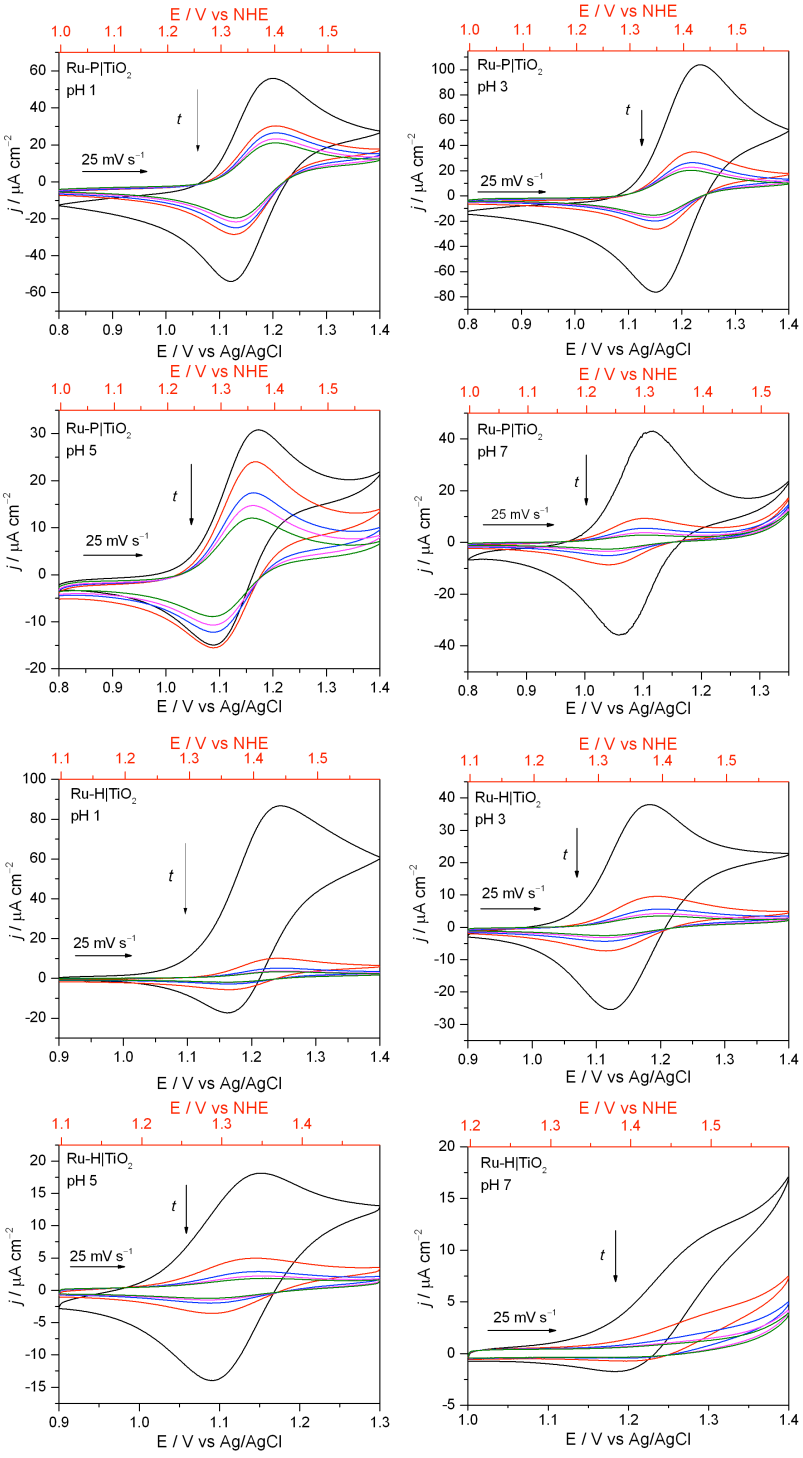
E / V vs NHE
Ru-P|TiO2
pH 1
25 mV s-1
t
j / µA cm-2
E / V vs Ag/AgCl
Ru-P|TiO2
pH 3
Ru-P|TiO2
pH 5
Ru-P|TiO2
pH 7
Ru-H|TiO2
pH 1
Ru-H|TiO2
pH 3
Ru-H|TiO2
pH 5
Ru-H|TiO2
pH 7

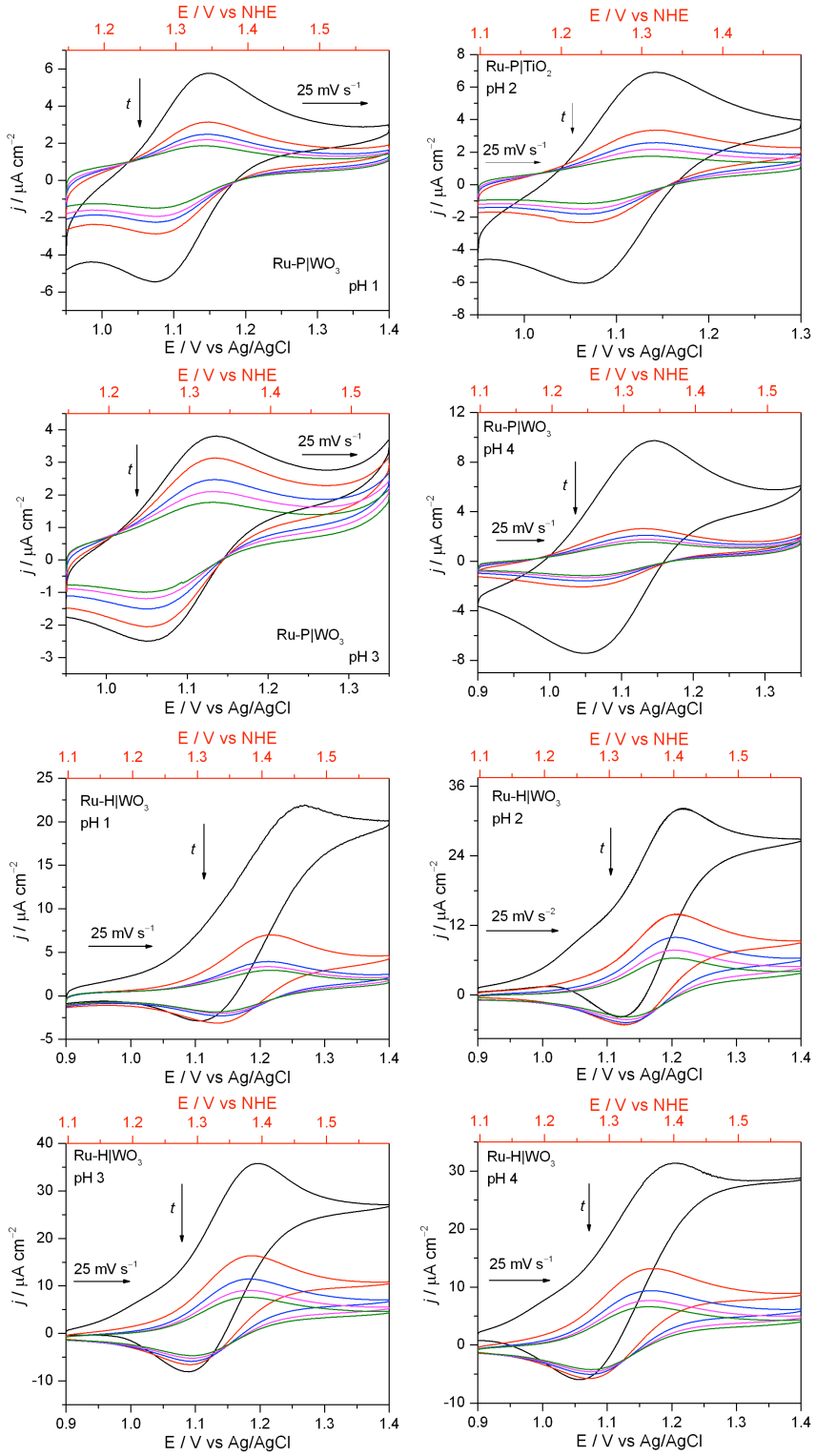

Figure A24. Cyclic voltammograms of Ru-R on either TiO_2 (pH 1, 3, 5, & 7) or WO_3 (pH 1 – 4)

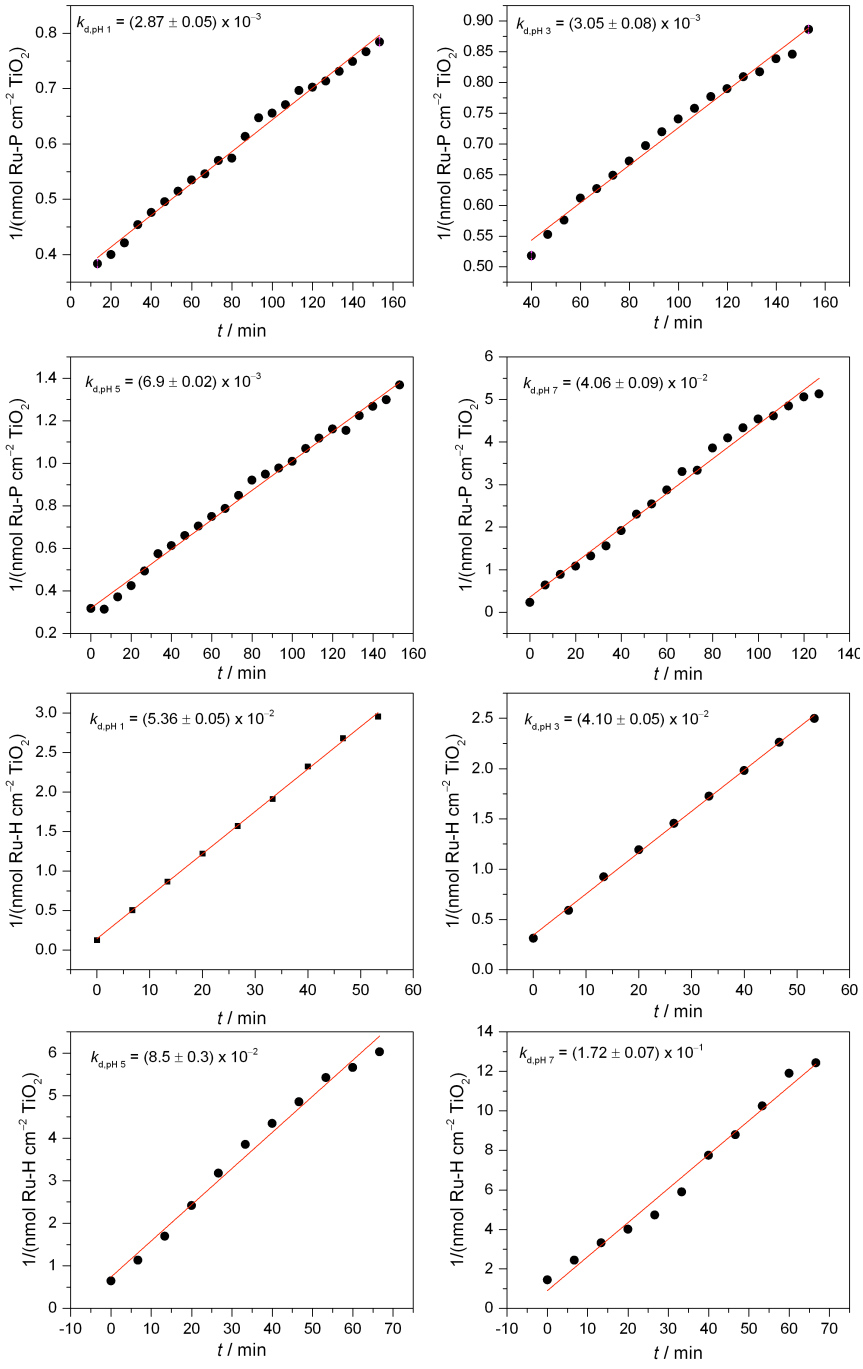
$k_{d,pH\ 1}$ = (2.87 ± 0.05) x 10^{-3}
$k_{d,pH\ 3}$ = (3.05 ± 0.08) x 10^{-3}
$k_{d,pH\ 5}$ = (6.9 ± 0.02) x 10^{-3}
$k_{d,pH\ 7}$ = (4.06 ± 0.09) x 10^{-2}
$k_{d,pH\ 1}$ = (5.36 ± 0.05) x 10^{-2}
$k_{d,pH\ 3}$ = (4.10 ± 0.05) x 10^{-2}
$k_{d,pH\ 5}$ = (8.5 ± 0.3) x 10^{-2}
$k_{d,pH\ 7}$ = (1.72 ± 0.07) x 10^{-1}
1/(nmol Ru-P cm^{-2} TiO_2)
1/(nmol Ru-H cm^{-2} TiO_2)
t / min

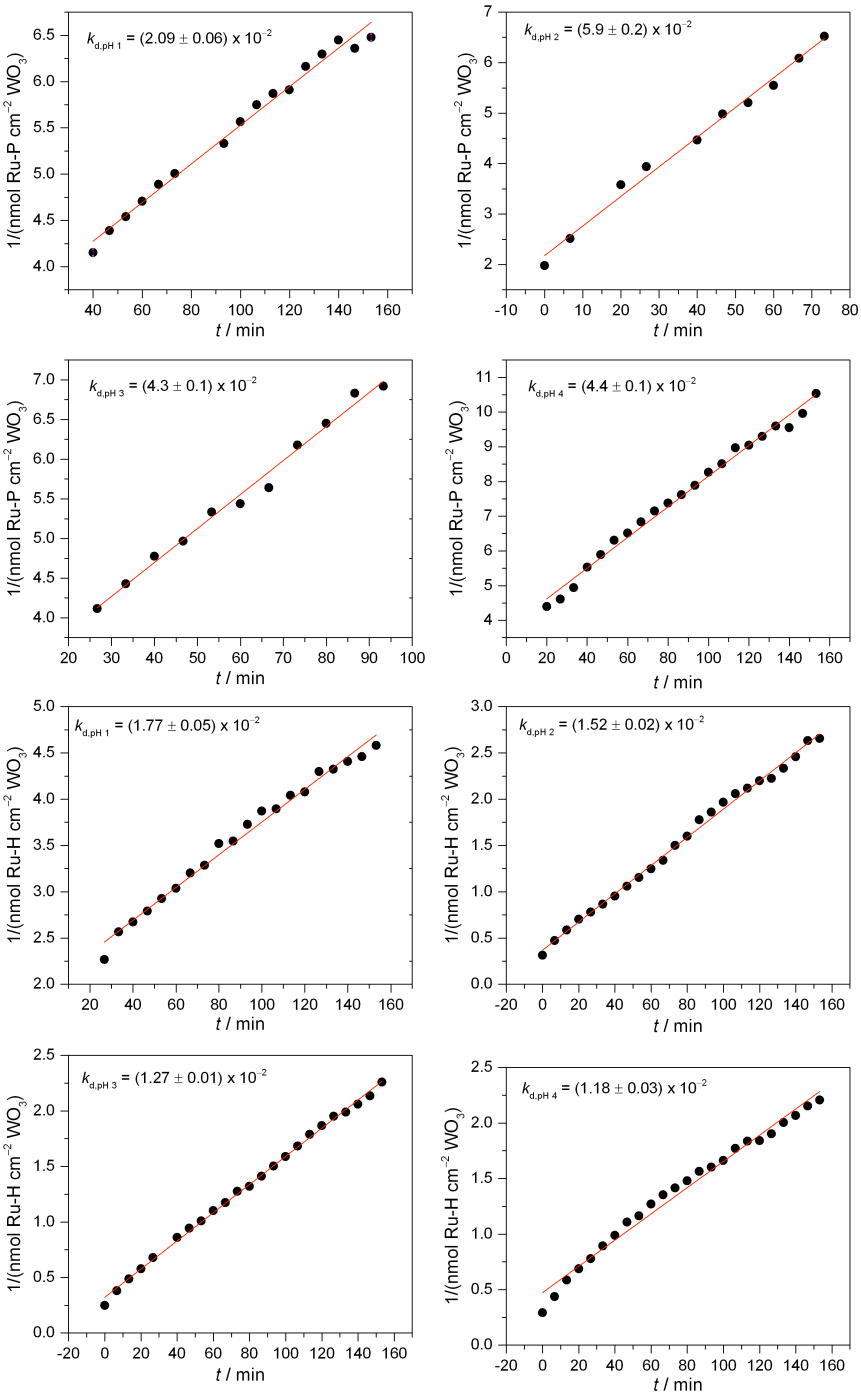

Figure A25. Second order rate plots for each cyclic voltammogram in Figure A20.

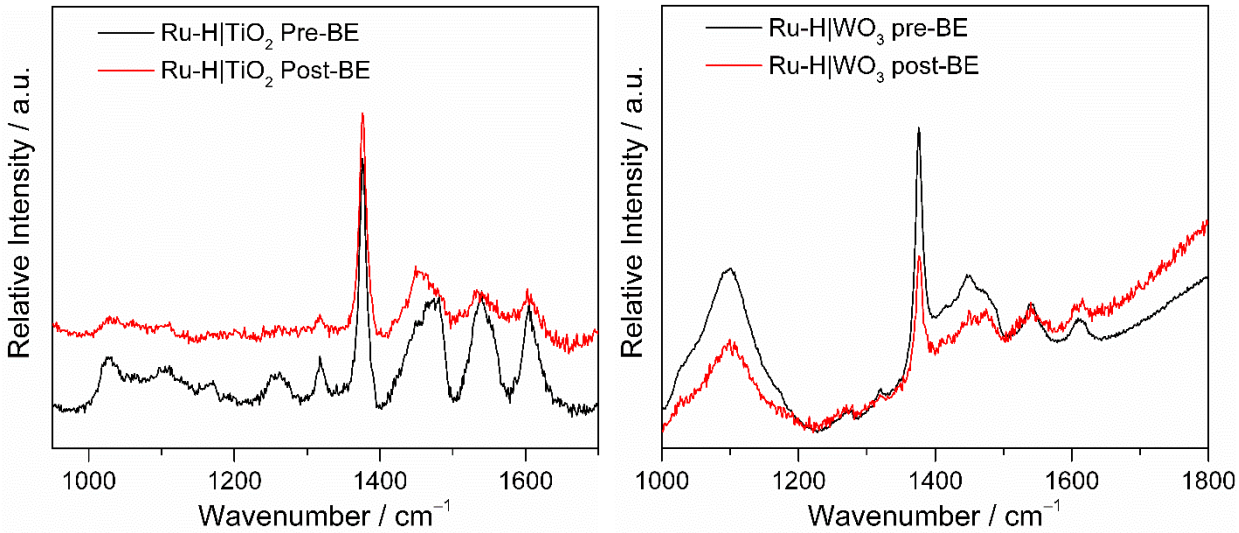

Figure A26. Raman spectra of Ru-H|TiO_2 (left) and Ru-2H|WO_3 (right) in a solution of 0.1 M $TBAPF_6$ in MeCN under no applied bias (black) and after applying 1.3 V vs Ag/Ag^+. Spectra collected with a 532nm laser inside a glass electrochemical cell with a CaF_2 window.

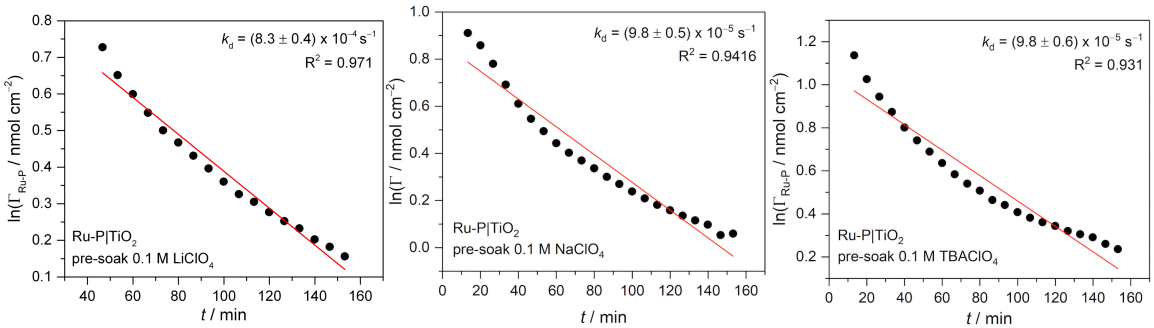

Figure A27. First-order rate plot of a Ru-P|TiO_2 film soaked (left) in 0.1 M $LiClO_4$ in ethanol prior to measuring desorption in pH 1 HNO_3, (middle) in 0.1 M $NaClO_4$ in ethanol, and (right) in 0.1 M $TBAClO_4$ in ethanol prior to measuring desorption in pH 1 HNO_3.

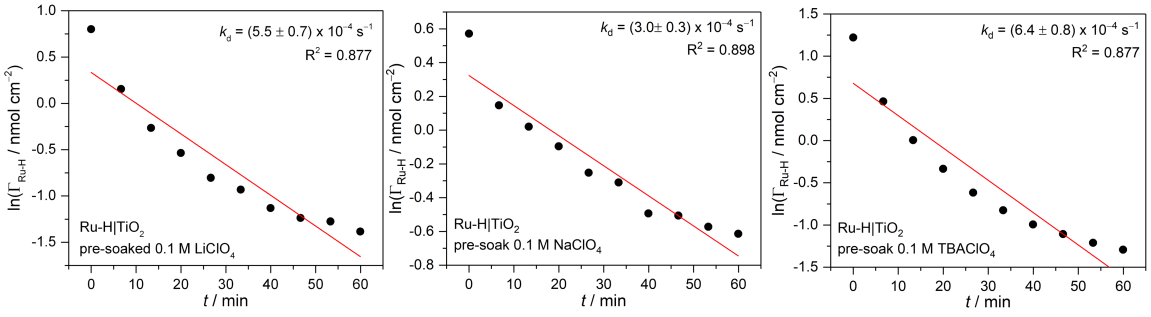

Figure A28. First-order rate plot of a Ru-H|TiO_2 film soaked (left) in 0.1 M $LiClO_4$ in ethanol prior to measuring desorption in pH 1 HNO_3, (middle) in 0.1 M $NaClO_4$ in ethanol, and (right) in 0.1 M $TBAClO_4$ in ethanol prior to measuring desorption in pH 1 HNO_3.

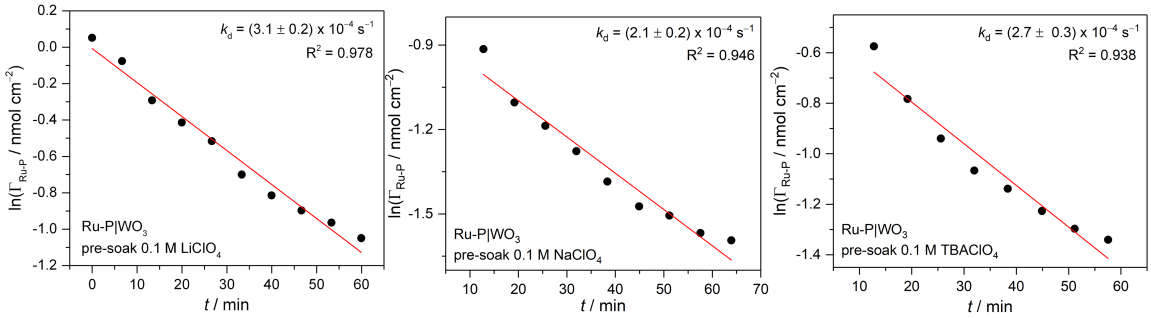

Figure A29. First-order rate plot of a Ru-P|WO_3 film soaked (left) in 0.1 M $LiClO_4$ in ethanol prior to measuring desorption in pH 1 HNO_3, (middle) in 0.1 M $NaClO_4$ in ethanol, and (right) in 0.1 M $TBAClO_4$ in ethanol prior to measuring desorption in pH 1 HNO_3.

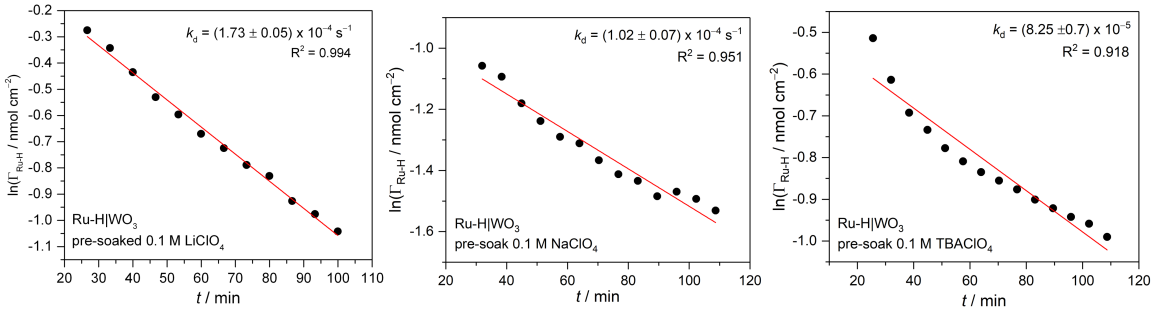

Figure A30. First-order rate plot of a Ru-H|WO_3 film soaked (left) in 0.1 M $LiClO_4$ in ethanol prior to measuring desorption in pH 1 HNO_3, (middle) in 0.1 M $NaClO_4$ in ethanol, and (right) in 0.1 M $TBAClO_4$ in ethanol prior to measuring desorption in pH 1 HNO_3.

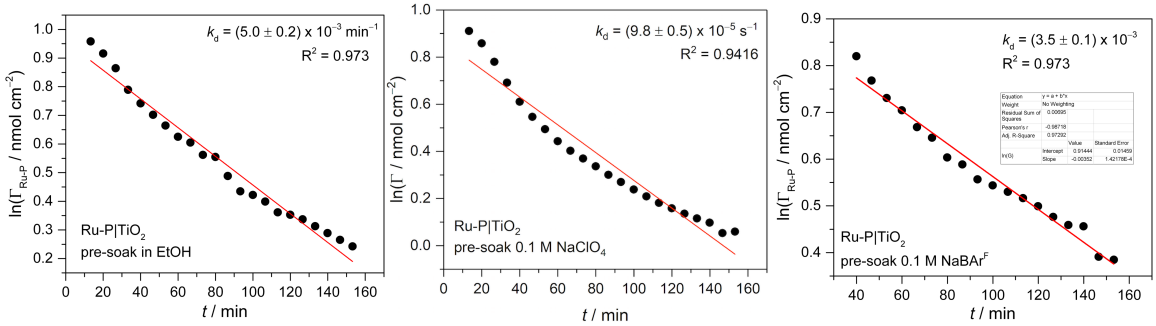

Figure A31. First-order rate plot of a Ru-P|TiO_2 film soaked (left) only in pure ethanol prior to measuring desorption in pH 1 HNO_3, (middle) in 0.1 M $LiClO_4$ in ethanol, and (right) in 0.1 M $NaBAr^F$ in ethanol prior to measuring desorption in pH 1 HNO_3.

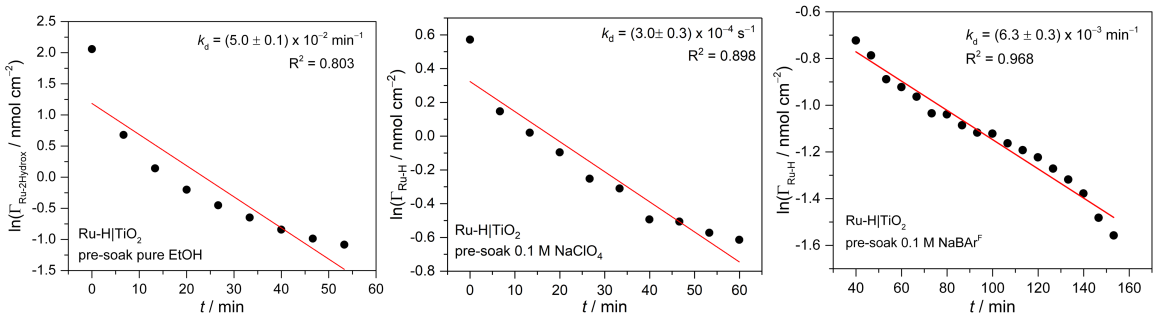

Figure A32. First-order rate plot of a Ru-H|TiO_2 film soaked (left) only in pure ethanol prior to measuring desorption in pH 1 HNO_3, (middle) in 0.1 M $LiClO_4$ in ethanol, and (right) in 0.1 M $NaBAr^F$ in ethanol prior to measuring desorption in pH 1 HNO_3.

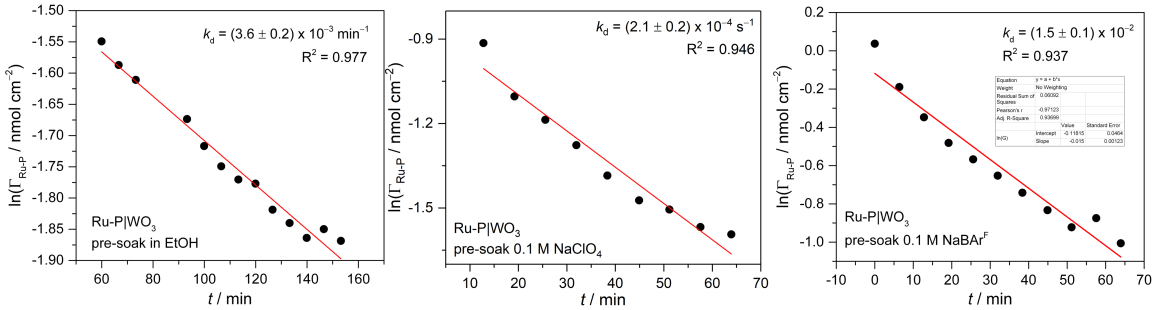

Figure A33. First-order rate plot of a Ru-P|WO_3 film soaked (left) only in pure ethanol prior to measuring desorption in pH 1 HNO_3, (middle) in 0.1 M $LiClO_4$ in ethanol, and (right) in 0.1 M $NaBAr^F$ in ethanol prior to measuring desorption in pH 1 HNO_3.

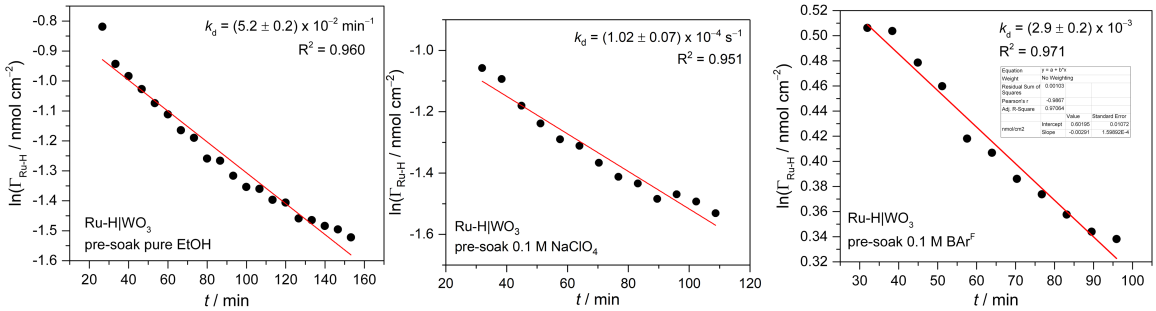

Figure A34. First-order rate plot of a Ru-H|WO_3 film soaked (left) only in pure ethanol prior to measuring desorption in pH 1 HNO_3, (middle) in 0.1 M $LiClO_4$ in ethanol, and (right) in 0.1 M $NaBAr^F$ in ethanol prior to measuring desorption in pH 1 HNO_3.

Table A1. R^2 and respective rate constants of desorption for **Ru-R** on TiO_2 and WO_3 with 0.1 M various metal salts in ethanolic soaking solutions derived from a 1st-order plot.

		Pure EtOH		0.1 M $LiClO_4$		0.1 M $NaBAr^F$	
	Anchor	R^2	k_D / s^{-1}	R^2	k_D / s^{-1}	R^2	k_D / s^{-1}
TiO_2	Ru-P	0.973	$(8.3 \pm 0.3) \times 10^{-5}$	0.971	$(8.3 \pm 0.3) \times 10^{-5}$	0.973	$(5.8 \pm 0.2) \times 10^{-5}$
	Ru-H	0.803	$(8.33 \pm 0.02) \times 10^{-4}$	0.877	$(5.5 \pm 0.7) \times 10^{-4}$	0.968	$(1.05 \pm 0.05) \times 10^{-4}$
WO_3	Ru-P	0.977	$(6.00 \pm 0.03) \times 10^{-4}$	0.978	$(3.1 \pm 0.2) \times 10^{-4}$	0.937	$(2.2 \pm 0.2) \times 10^{-4}$
	Ru-H	0.96	$(8.37 \pm 0.03) \times 10^{-2}$	0.994	$(1.7 \pm 0.5) \times 10^{-4}$	0.971	$(5 \pm 3) \times 10^{-5}$

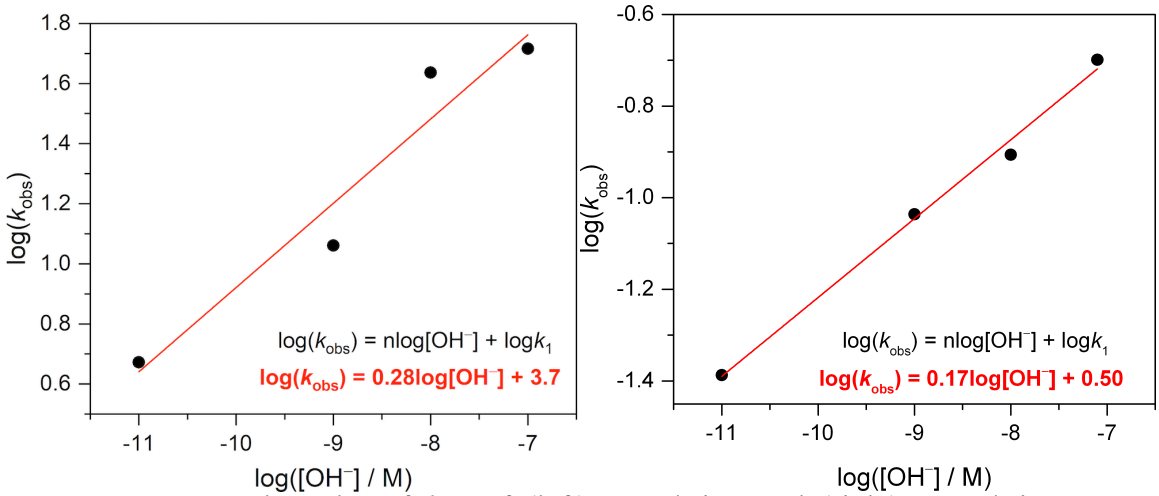

Figure A35. Log-log plot of k_{obs} of (left) **Ru-P**|TiO_2 and (right) **Ru-H**|TiO_2 vs [OH^-] for determining order of [OH^-] on the rate law of desorption.

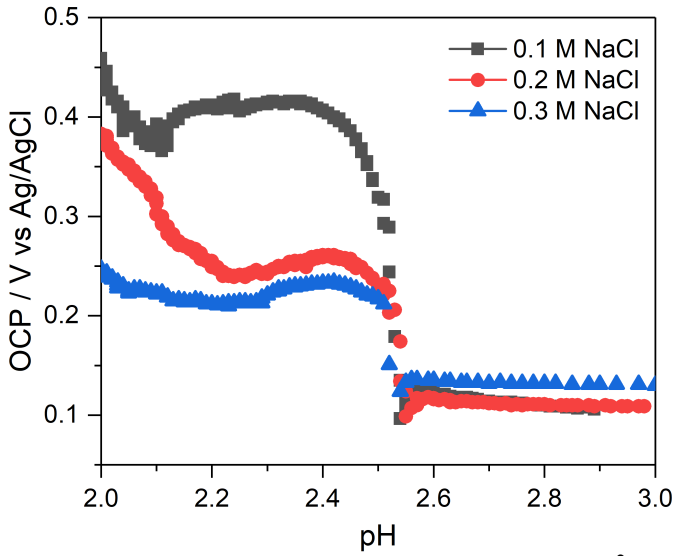

Figure A36. Potentiometric titration of a 1cm^2 electrode of TiO_2 in 200 mL of (black) 0.1 M, (red) 0.2 M, and (blue) 0.3 M NaCl at an initial pH = 2.0. 1 M NaOH was titrated at a rate of 1.00 mL h^{-1}.

Appendix B

Supporting Information for Chapter 3

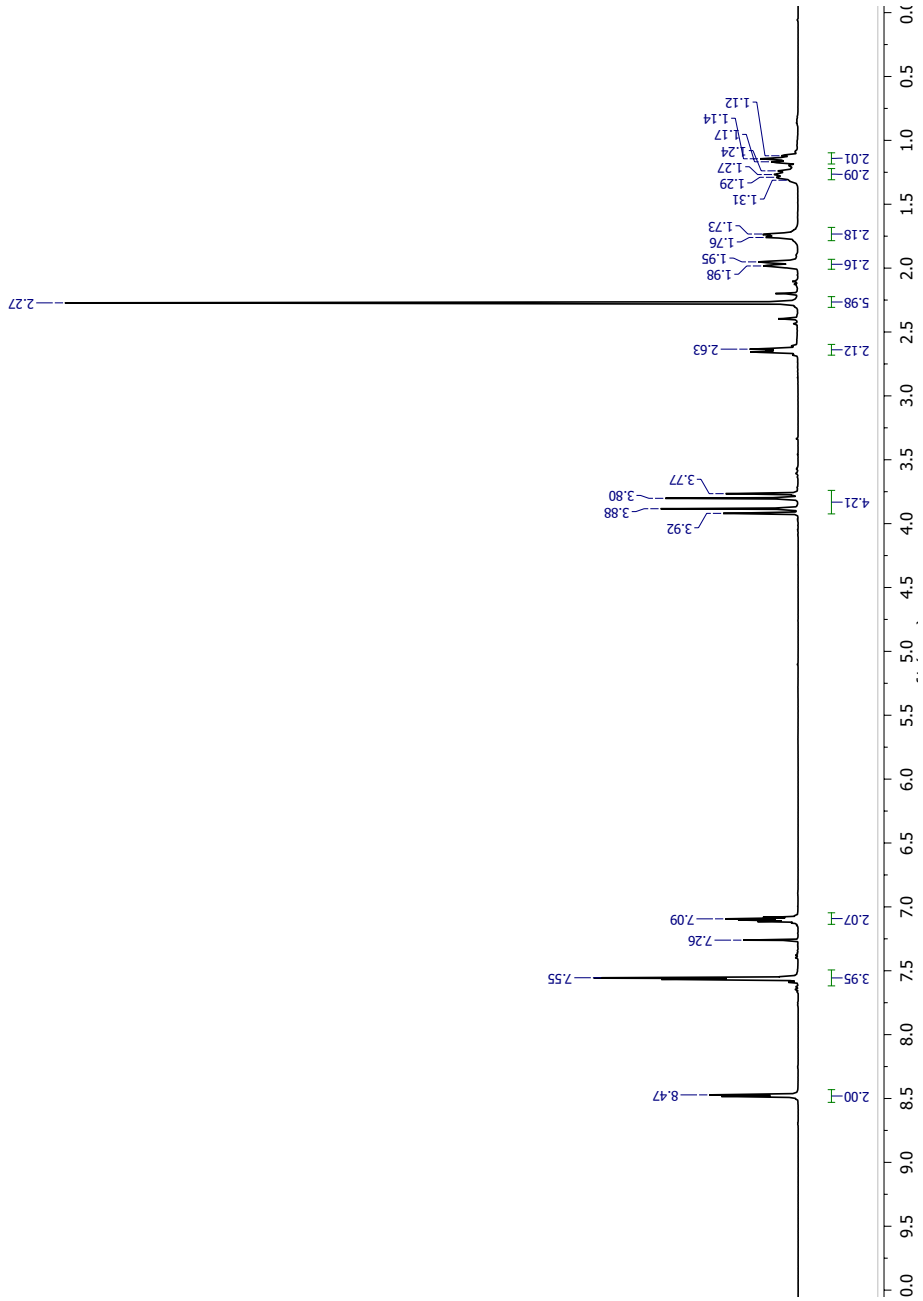

Figure B1. ^{1}H NMR spectrum of bpmcn ligand in $CDCl_3$

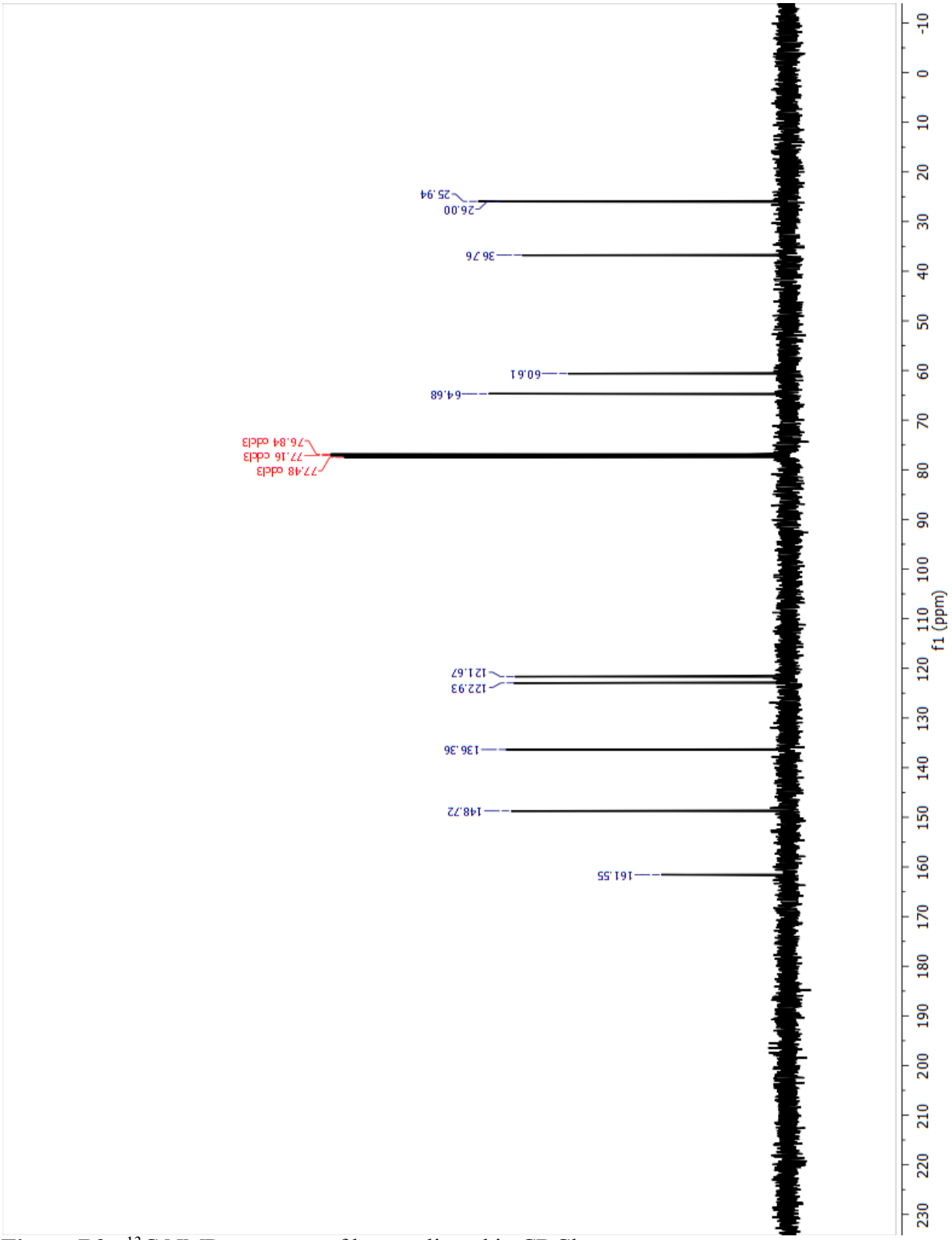

Figure B2. ^{13}C NMR spectrum of bpmcn ligand in $CDCl_3$

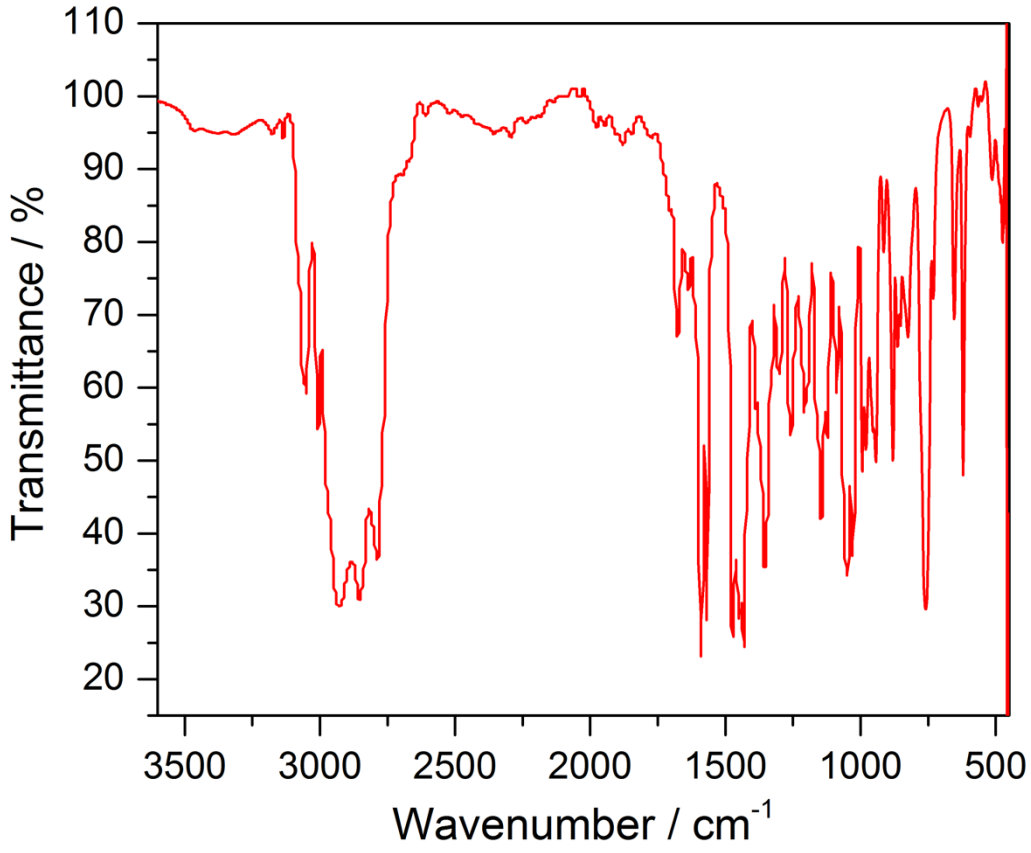

Figure B3. FTIR spectrum of the bpmcn ligand

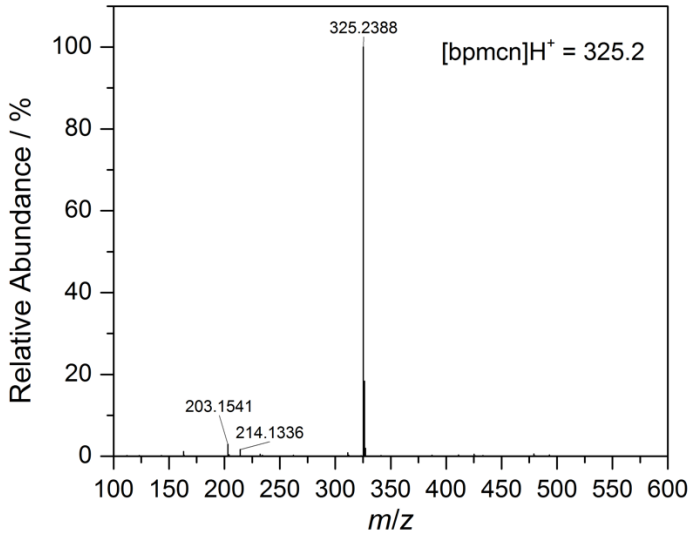

Figure B4. ESI-MS(+) spectrum of purified bpmcn ligand

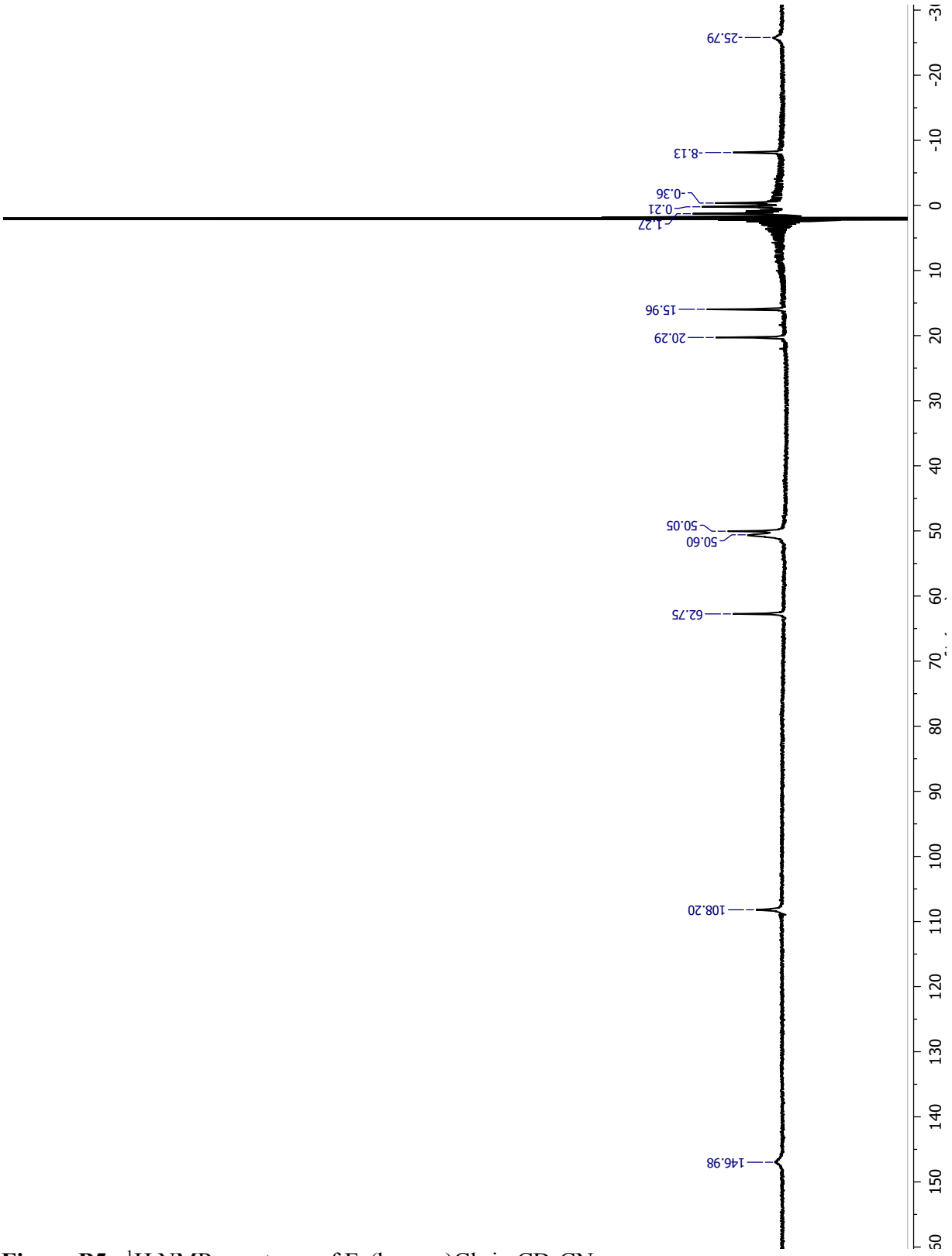

Figure B5. ^{1}H NMR spectrum of $Fe(bpmcn)Cl_2$ in CD_3CN

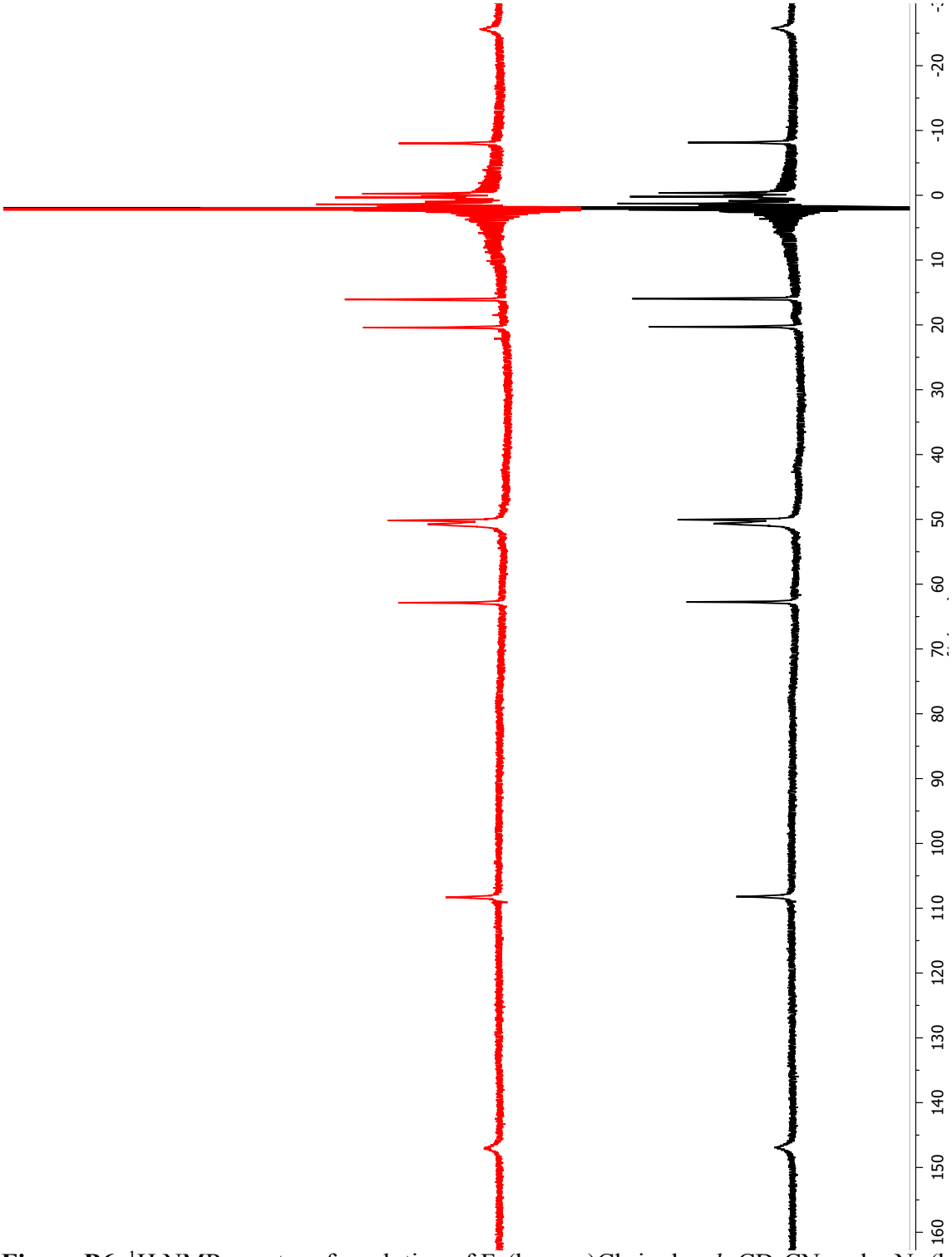

Figure B6. ^{1}H NMR spectra of a solution of $Fe(bpmcn)Cl_2$ in dry d_3-CD_3CN under N_2 (black) in the dark and (red) under 1 sun of illumination for t = 24 hours.

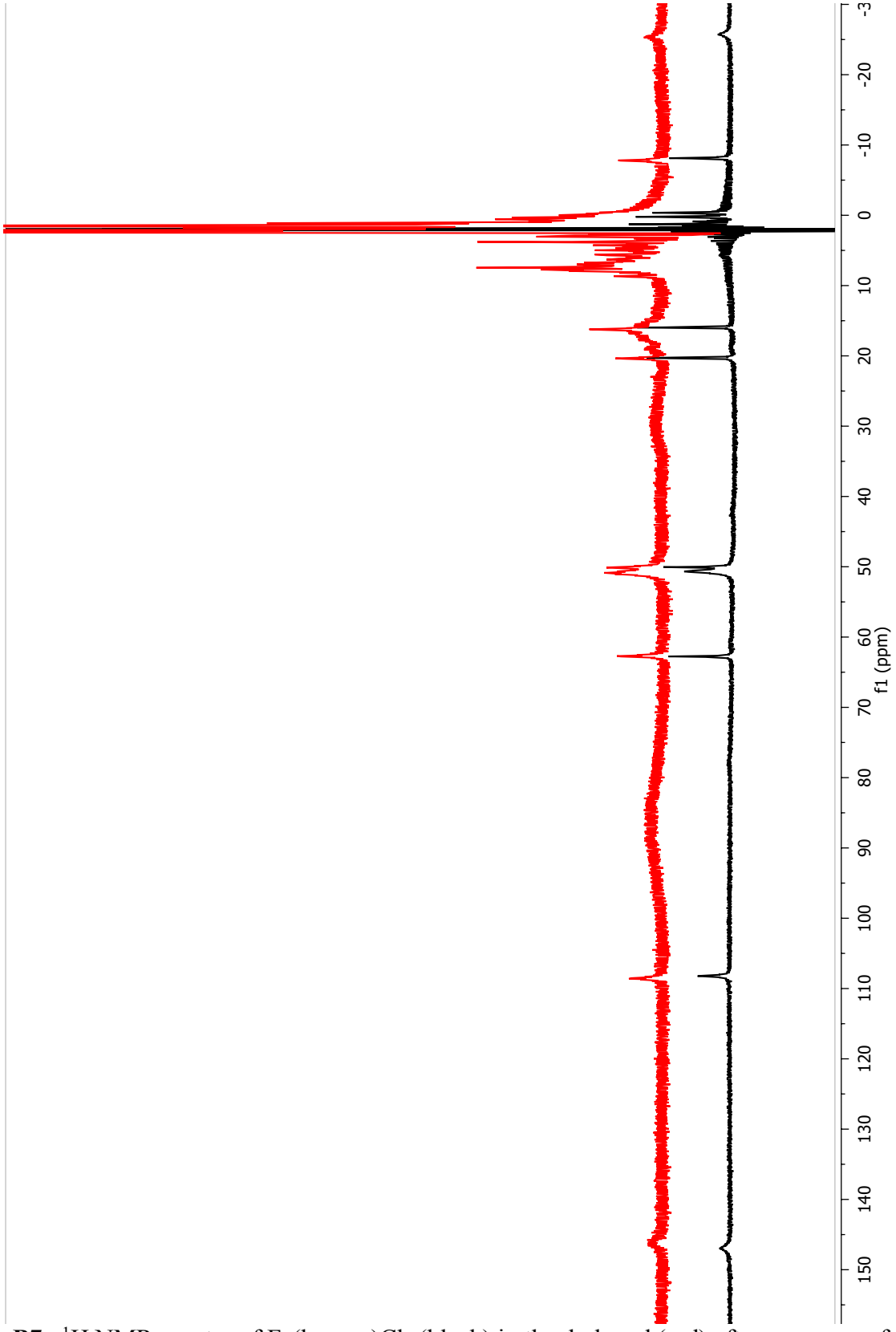

Figure B7. ^{1}H NMR spectra of Fe(bpmcn)Cl_2 (black) in the dark and (red) after exposure of 1 sun illumination under O_2 for 24 hours in dry acetonitrile.

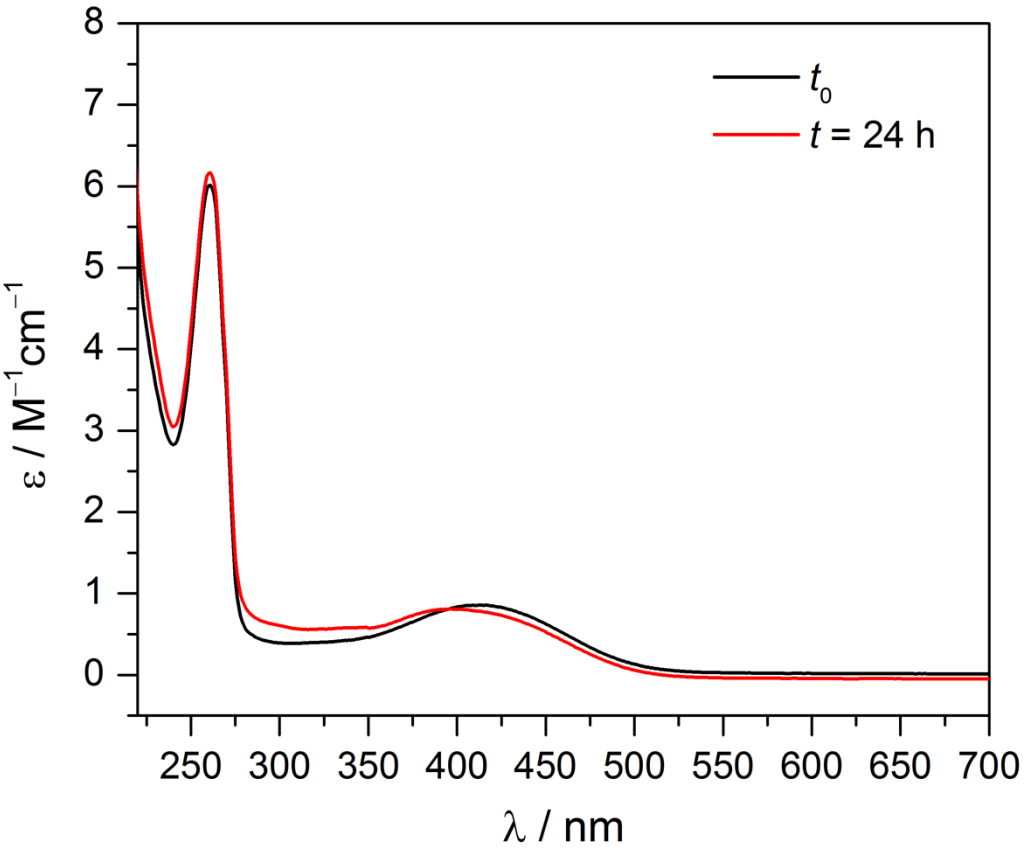

Figure B8. UV-Vis spectra of Fe(bpmcn)Cl_2 under O_2 (black) in the dark and (red) under illumination at 1.5 W with a Xe lamp and 550 nm cutoff filter equipped.

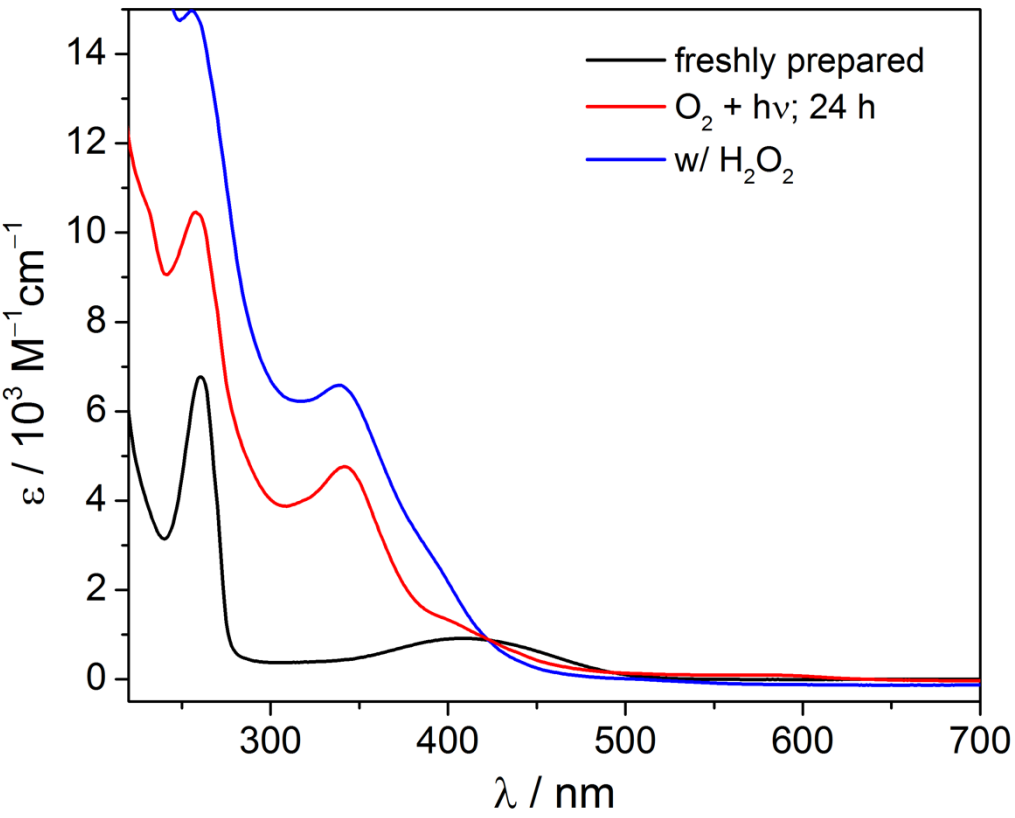

Figure B9. UV-Vis spectrum of 0.2mM Fe(bpmcn)Cl_2 (black) prior to and (red) after adding 5 µL of 30 wt-wt% H_2O_2 (added to a 10 mL solution of the iron complex), compared to (blue) 0.2 mM Fe(bpmcn)Cl_2 under 1 sun illumination for 24 hours.

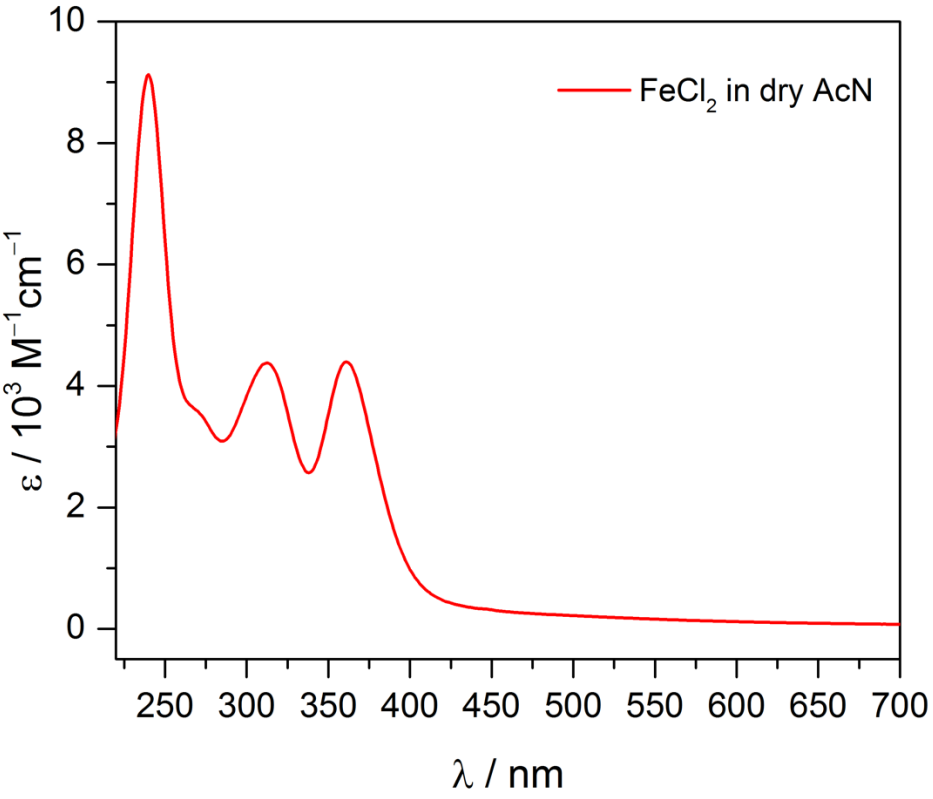

Figure B10. UV-Vis spectrum of $FeCl_2$ in dry acetonitrile under N_2. In dry acetonitrile, absorption bands appear for $FeCl_2$ at λ_{max} = 240 nm, λ_{max} = 312 nm, and λ_{max} = 361 nm

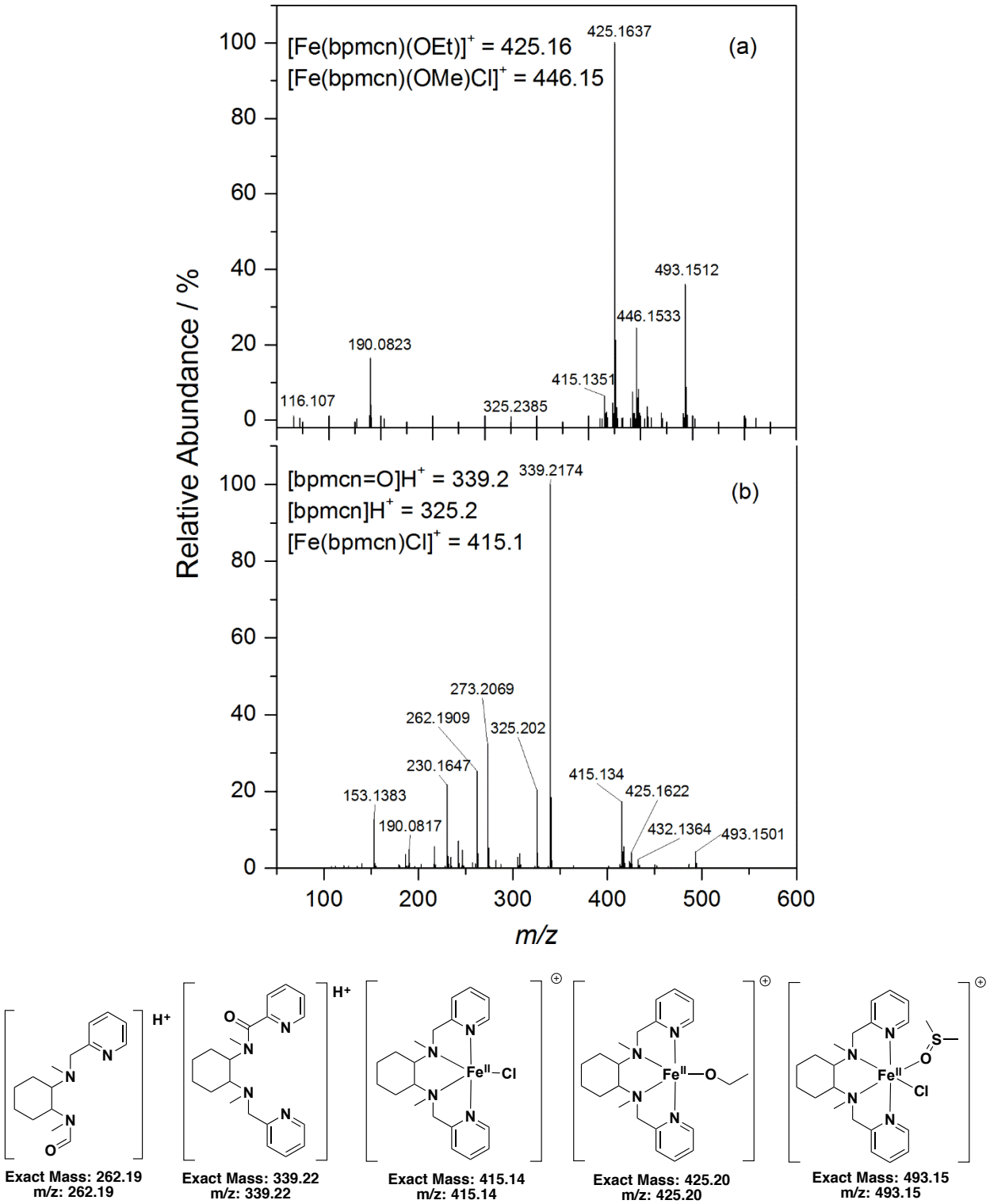

Figure B11. ESI-MS$^+$ spectra of Fe(bpmcn)Cl_2 (a) prior to and (b) after exposure to 1.5 W illumination with AM 1.5G filter for 48 hours under O_2.

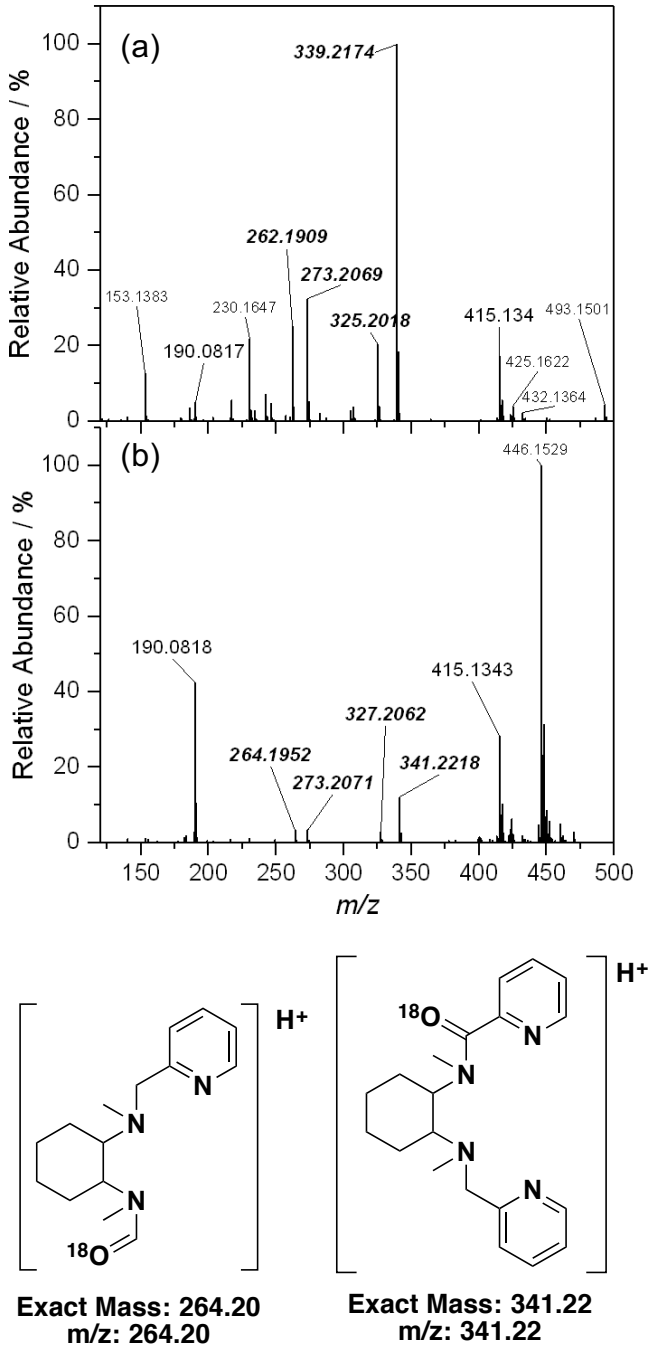

Figure B12. ESI-MS$^+$ spectra of Fe(bpmcn)Cl_2 exposed to 1.5 W illumination with AM 1.5G filter for 48 hours under (a) $^{16}O_2$ or (b) $^{18}O_2$

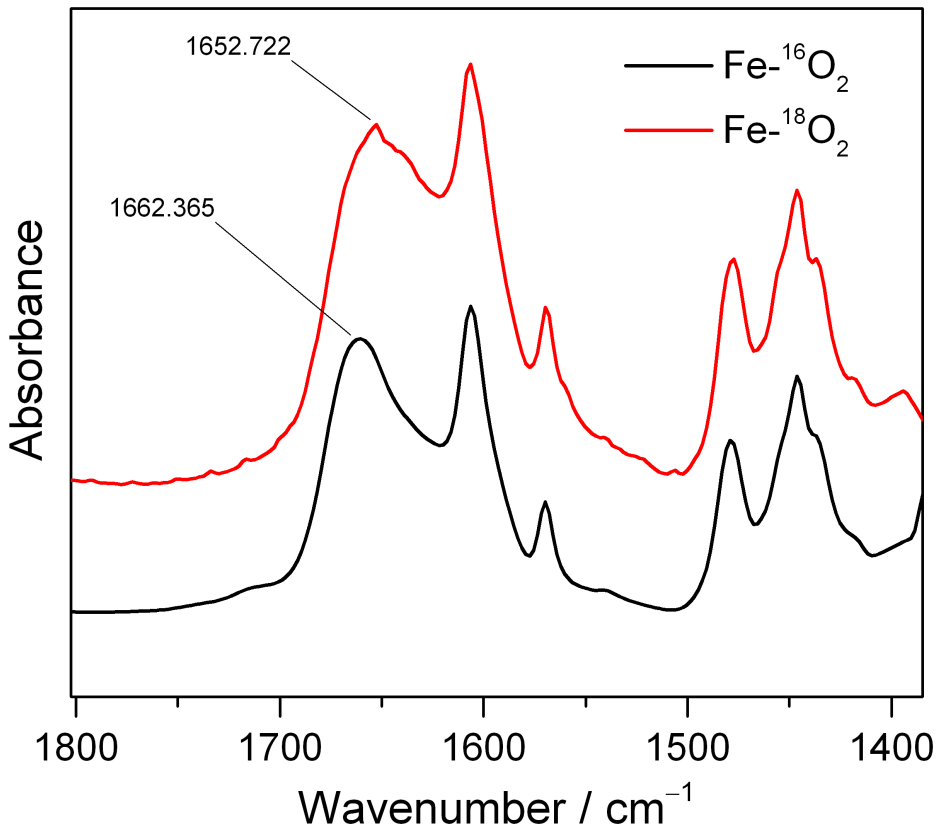

Figure B13. FTIR spectra of Fe(bpmcn)Cl_2 after illumination with 1.5W through an AM 1.5G filter in acetonitrile under (black) $^{16}O_2$ and (red) $^{18}O_2$. Note the region between 1600 – 1700 cm^{-1} where an amide bond typically appears in the IR spectrum.

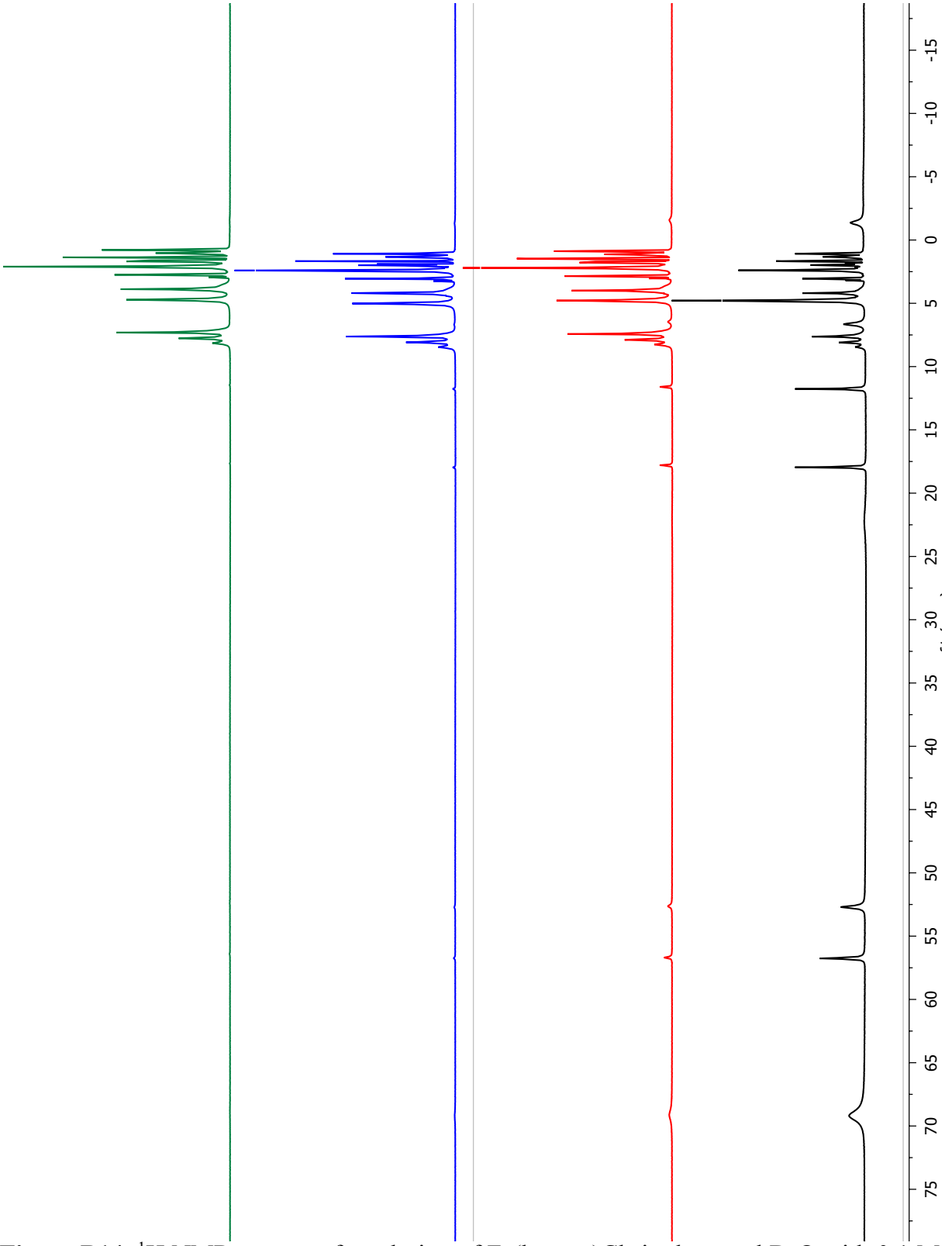

Figure B14. ^{1}H NMR spectra of a solution of Fe(bpmcn)Cl_2 in degassed D_2O with 0.1 M *d*-TFA (pH = 1) in the dark for t=0 minutes (black), 2 hours (red), 4 hours (blue), and 8 hours (green).

(b)

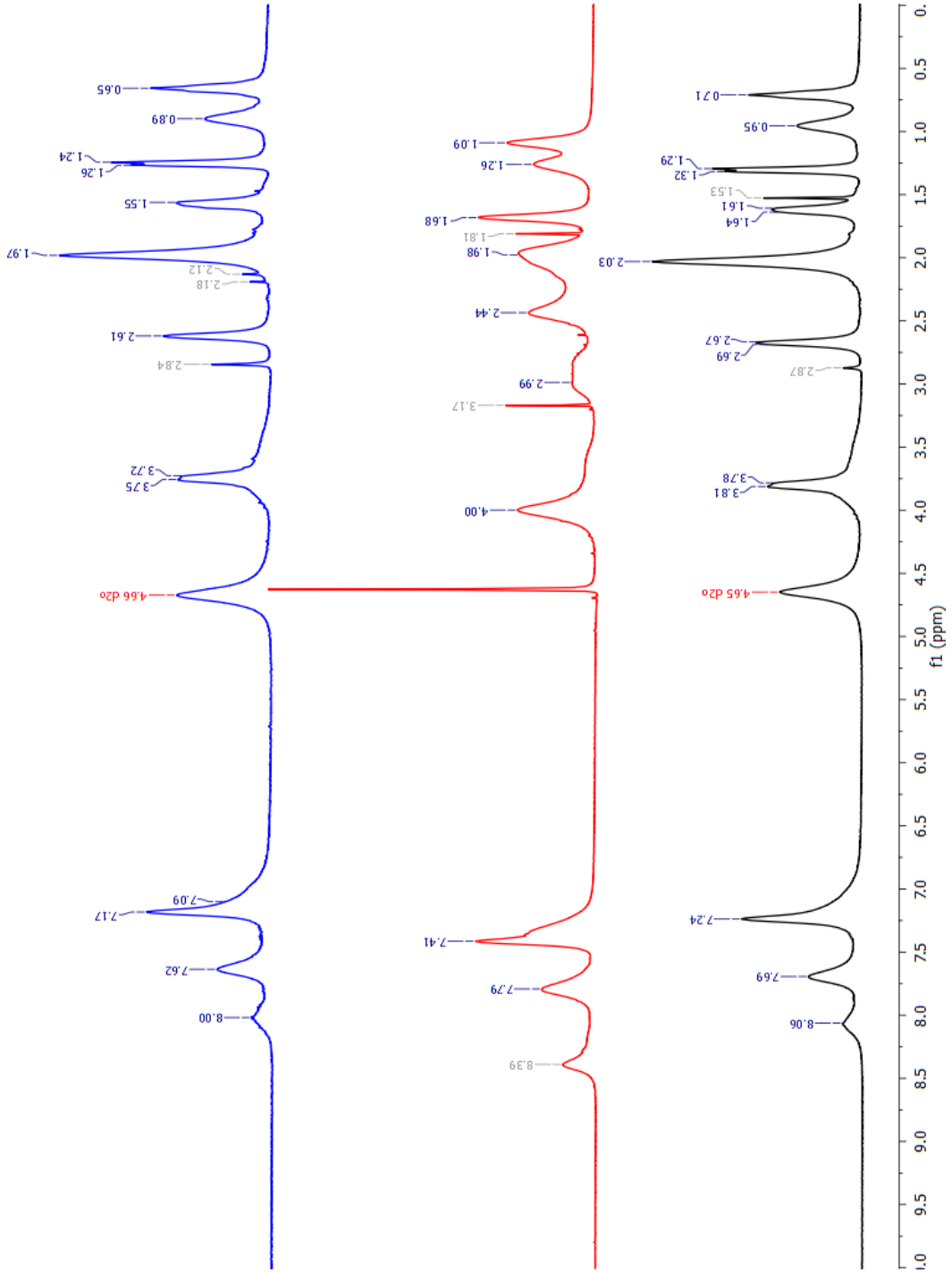

Figure B15. ^{1}H NMR spectra of (black) $Fe(bpmcn)Cl_2$ in 0.1 M *d*-TFA for 8 hours, (red) free bpmcn in 0.1M *d*-TFA, and (blue) $FeCl_2$ + bpmcn in 0.1M *d*-TFA.

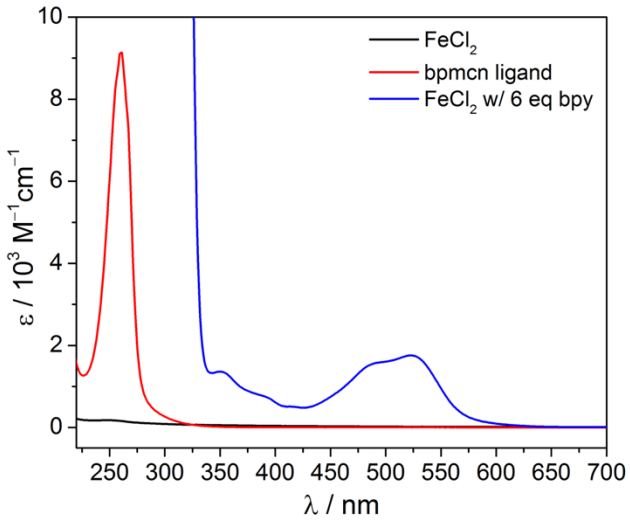

Figure B16. UV-Vis spectrum of (black) $FeCl_2(aq)$, (red) bpmcn ligand, and (blue) $FeCl_2$ with 6 equivalents of 2,2′ bpy in TfOH at pH 1 under N_2.

Appendix C

Supporting Information for Chapter 4

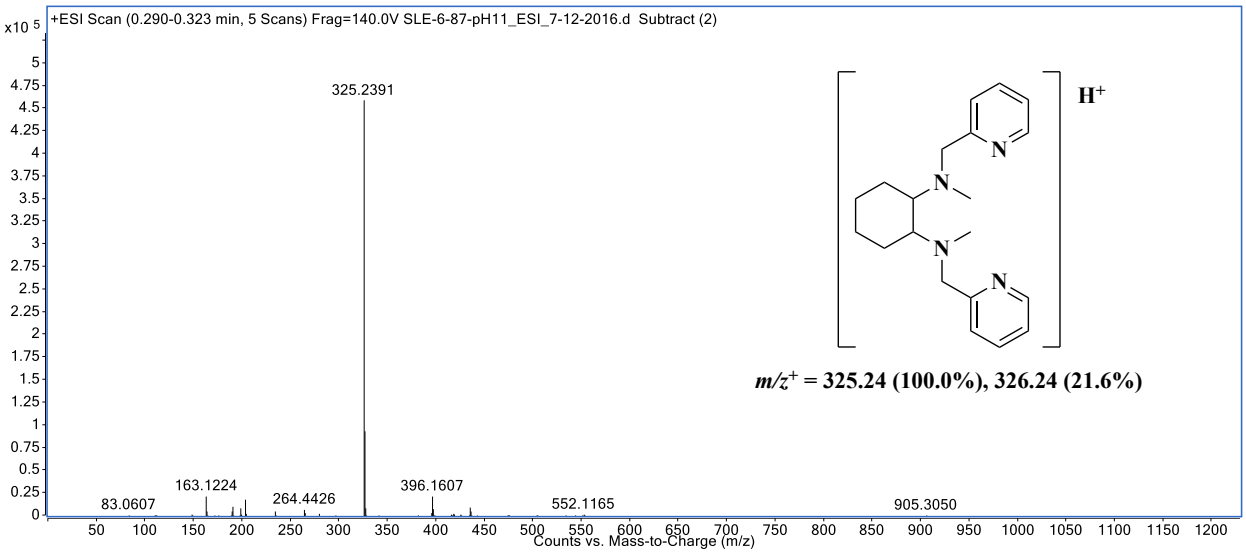

Figure C1. Mass spectrum of 0.01 M Fe(bpmcn)Cl_2 at pH 11 after exposure to air for 3 days.

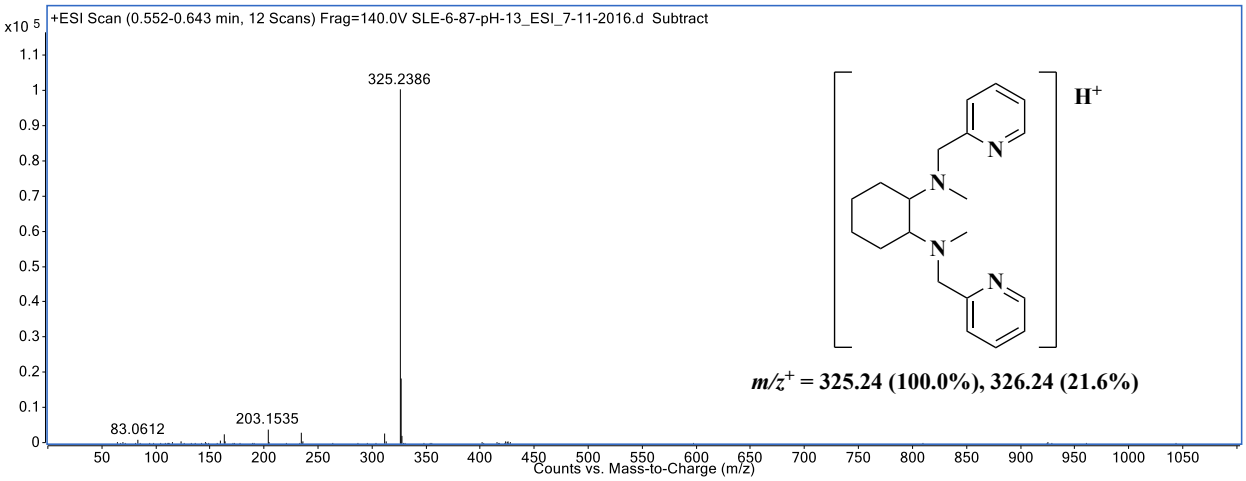

Figure C2. Mass spectrum of 0.01 M Fe(bpmcn)Cl_2 at pH 13 after exposure to air for 3 days.